The Development of Model Organic Decoupling Films for use on Strongly-Interacting Metal Surfaces

Thomas William White

A thesis submitted in partial fulfilment
of the requirements for the degree of
Doctor of Philosophy in Chemistry

Department of Chemistry
University of Warwick

2014

Contents

List of tables and figures

Chapter 1: Introduction

Figure 1.5 a) Concept model for the 'molecular Lander'. Adapted from reference [62]. b) and c) Side on views of an example Lander molecule in the gas-phase and adsorbed on a metal surface, respectively. Adapted from reference [30].

Figure 1.6 a) Schematic representation of the decoupling layer strategy. A thin layer of an insulating material is deposited onto the surface prior to adsorption of the molecular tecton. b) The 'multilayer approach' to decoupling, where a thick film of the organic species is deposited. The lower layers act as a decoupling layer.

Figure 1.7 a) Side-view schematic of a NaCl bilayer decoupling film. The substrate is shown in grey, the Na ions are blue, the Cl in green, and the decoupled molecules are shown as red dumbbells. b) Depiction of the 'carpet' growth of NaCl over Ge(001), adapted from reference [69]. The substrate atoms are shown with partially shaded circles, the fully shaded circles show the Cl^- ions within the NaCl structure.

Figure 1.8 a) and b) STM images of Pd atoms adsorbed on the NiAl(110) surface oxide film. The corresponding STS spectra of Pd atoms in each position are shown in c). Adapted from reference [68].

Figure 1.9 Three component model demonstrating the versatility of organic decoupling layers. The head and tail groups control the interaction between the decoupling layers and the substrate and overlayer adsorbates respectively. The backbone controls the thickness and the rigidity of the organic layer.

Figure 1.10 Schematics of the various ways in which alkanethiol films have been utilised as decoupling layers. In a), the functional species is deposited directly onto the alkanethiol film, whilst in b) the alkanethiol tail group is selected to specifically control the adsorption of the overlayer species. c) shows how a functional species can be functionalised with an alkanethiol chain prior to deposition on the metal surface.

Figure 1.11 Depiction of the bidentate bonding motif of the deprotonated carboxyl moiety on a close-packed Cu surface.

Figure 1.12 a) Schematic of benzoic acid. The blue, white and red represent carbon, hydrogen and oxygen respectively. b) STM images (left) and corresponding structures (right) of the benzoate structures on unreconstructed (top) and reconstructed (bottom) Cu(110) surfaces. Adapted from reference [108].

Figure 1.13 a) Schematic of formic acid (top) and acetic acid (bottom). b) STM image of the (2×2) formate structure on the Cu(110) surface. Adapted from reference [120]. c) STM image of the c(2×2) formate structure formed on the O-precovered Cu(110) surface. Adapted from reference [104]. d) STM image of the acetic acid chains obtained on the Cu(110) surface. Adapted from reference [130].

Figure 1.14 a) Schematic of oxalic acid. b) The tilting and bidentate adsorption geometries of oxalic acid identified on the Cu(110) surface. Adapted from reference [103]. c) STM image of the flat-lying oxalate structure reported on Cu(111). Adapted from reference [127].

Chapter 2: Experimental and theoretical methods

Figure 2.1 Schematic of the STM experiment. The tip is moved over the sample by the piezoactuators (orange box), whilst a voltage is applied between the tip and sample. The tunnel junction is depicted in the red circle.

Figure 2.2 Schematic of the tunnel junction, revealing the derivation of the different terms comprising Equation 2.5 and how the tunnel current decreases with increased tip-sample separation.

Figure 2.3 Depiction of the tip trajectory as it is scanned in constant height and constant current modes. The green line shows the position of the tip as it is scanned over the sample. In the bottom profiles, the measured current is displayed as a function of position, assuming a perfect feedback system.

Figure 2.4 a) Schematic of the LEED apparatus. The phosphor screen is shown at the rear of the LEED as the green line, the electron gun is the blue shape, and the retarding grids are shown as the black dashed lines. The electrons are shown as the

array of spots, the colour of which depends on their energy and direction. The blue electrons show the primary electron beam being fired at the sample, the red and green are the inelastically and elastically back-scattered electrons, respectively. b) Example LEED pattern of a clean Cu(110) surface.

Figure 2.5 a) Model demonstrating how the real space structure of a surface is depicted in reciprocal space in the LEED pattern. b) Demonstration of how a superstructure is shown in the LEED as a consequence of the reciprocal depiction. The red squares indicate the adsorbate positions (top image) and the additional spots they generate in the LEED pattern (lower image).

Figure 2.6 Mean free path of electrons as they travel through an inorganic lattice. Adapted from reference [13]. The black dots correspond to data points obtained from a variety of different materials.

Figure 2.7 a) Schematic of the XPS process. b) The photoemission process in terms of the electron energy levels.

Figure 2.8 Schematic depiction of a XPS spectrum, whereby the obtained spectrum is shown in red, the fitted peak in green, and the background in blue.

Figure 2.9 a) Schematic of the Auger emission process. b) Energy level depiction of the transitions involved in NEXAFS.

Figure 2.10 a) Schematic of TPA molecule (upper) and side view (lower). In the side view, the σ- and π-orbitals are shown by the green and orange dumbbell shapes, respectively. b) NEXAFS spectra taken of TPA on rutile TiO_2(110) at low molecular coverage. c) NEXAFS spectra taken of TPA on rutile TiO_2(110) at 1 monolayer coverage. The angles in b) and c) are the photon incidence angle with respect to the surface, as depicted by the inset of b). The σ- and π-signals are colour-coded using green and orange bands, respectively. Both b) and c) are adapted from reference [18].

Figure 2.11 Depiction of the cell dimensions used for the MM calculations.

Figure 2.12 a) Photograph of the LT-UHV-STM used in many of the experimental studies presented here. The three chambers have been highlighted with different colours; the loadlock in blue, the preparation chamber in green and the STM chamber in red.

Figure 2.13 a) Schematic of the evaporation of low vapour pressure molecules. b) Photo of the loaded OA doser, as mounted on chamber. c) Schematic of the OA doser. The blue boxes represent CF flanges. The two valves are labelled (1) and (2). LL represents the loadlock.

Chapter 3: Terephthalic acid on Cu(110) and Cu(111)

Table 3.1 Summary of the dimeric H-bond lengths reported for TPA on a number of different weakly-interacting surfaces and in bulk TPA crystals. The * indicates a H-bond length that has been corrected to use a TPA molecular length of ~7Å.

Figure 3.1. a) and b) plan views of the (110) and (111) surfaces. c) Molecular structure of TPA. d) STM image (adapted from reference [5]) and schematic of the TPA brickwork superstructure.

Figure 3.2 Examples of TP MO structures. a) STM images and structural models of the porous Fe-TP films obtained on Cu(001), adapted from reference [17]. b) STM image and structural model of the chiral Fe-TP 'flowers' fabricated on the Cu(110) surface, adapted from reference [16].

Figure 3.3 a) STM images and structural models of the TPA 1D chains and TP brickwork-like structure obtained on the Pd(111) surface. Adapted from reference [10]. b) STM images and corresponding models of the three temperature-dependent TPA phases observed on Cu(001). Adapted from reference [11].

Figure 3.4 a) and b) STM images of the (10×2) TPA structure. The blue dashed lines highlights the molecular rows, whilst the green highlights the adatom rows. a) I=800 pA, U=-1.5 V. b) I=800 pA, U=-1.2 V.

Figure 3.5 a) LEED pattern of the (10×2) TPA network on Cu(110). Two of the crystallographic spots are labelled. E=60 eV. b) c(5×2) LEED pattern as simulated by the LEEDpat3.0 software [28].

Figure 3.6 a) and b) C 1s and O 1s XPS spectra of the (10×2) TPA layer. The C 1s shows peaks at 284 eV and 288 eV, representing the aromatic and carboxylate carbons, respectively. The O 1s shows only a single, narrow peak, centred at 531 eV, arising from the chemically-identical O atoms in the carboxylate moiety.

Figure 3.7 a) and b) Structural model and simulated STM image of the lowest energy (10x2) TPA structure, as calculated by DFT. The simulated image was obtained using the DOS between the Fermi energy and a bias potential of 0.5 eV.

Figure 3.8 a), b) and c) STM image (I=800 pA, U=-1.2 V), model and simulated STM image of the (14×2) structure on Cu(110), respectively. The blue arrow in (a) shows the position of the Cu adatoms, imaged as a darker line.

Figure 3.9 a) and b) STM image and LEED pattern of the (6×2) TP phase on Cu(110). a) I=800 pA, U=-1.2 V. b) E=61 eV. c) and d) DFT-calculated lowest energy structure and simulated STM image of the (6×2) film.

Figure 3.10 a) and b) C 1s and O 1s XPS spectra, respectively, of the TPA multilayer film, measured at 190K. In the O 1s spectrum, the carboxylic peaks have been coloured red, the carboxylate green and the contaminant peak green.

Figure 3.11 a) Summary of the DFT-calculated free energies of formation per molecule for the three TP structures obtained on Cu(110). b) Schematic of the total adsorption energy with increasing TPA coverage. The red, green and blue profiles show the adsorption energies for the (10×2), (14×2) and (6×2) phases respectively. Dashed lines represent the energy the system would have if all molecules were in the same phase. Dash-dotted lines are a tentative (not calculated) representation of the energy for second layer molecules. The full line indicates the actual supramolecular configuration adopted by the system.

Figure 3.12 STM images of the TPA H-bonded network on the Cu(111) surface, after deposition onto a RT substrate. The blue arrow indicates the straight edge of the molecular island. a) I=50 pA, U=1.3 V. b) shows a zoomed-in image of the islands internal structure. The green oval highlights a single TPA molecule and the blue circle demonstrates a defect in the organic lattice. I=100 pA, U=-1.0 V.

Figure 3.13 Two STM images showing a) weakly-correlated or randomly-arranged, and b) strongly-correlated distribution of defects in the TPA lattice. The two images have been obtained from different sample preparations. The purple box indicates a short chain of defects. a) I=210 pA, U=1.4 V. b) I=33pA, U=-0.9V.

Figure 3.14 MM study of the TPA-TPA interactions. a) shows a schematic of the unit cell used in the MM calculations, revealing how the unit cell of the calculation was constructed to test the in-chain and inter-chain interactions. Vectors **a** and **b** define the size and shape of the unit cell which, for the case of a single TPA row, is shown by the red dashed lines. b) Potential energy profile calculated as a function of **a**. c) Potential energy surface as a function of $\mathbf{b}_x$ and $\mathbf{b}_y$ for a fixed value of **a**.

Figure 3.15 a) Model of the initial TPA arrangement on Cu(111) used in the DFT calculations. The green rectangle shows the space explored by the DFT calculations, corresponding to the DFT-calculated potential energy surface shown in (b).

Figure 3.16 a) Derivation of the $\mathcal{D}$ and $\mathcal{L}$ parameters and the definition of the $\mathcal{F}(x)$ and $\mathcal{G}(x)$ terms used to simulate the different interactions. b) Flow diagram showing how the proposed analytical model can be used to predict the effects of the interaction interplay. c) Illustration of the two chains of points used to depict the substrate and molecules in the algorithm. The blue dots indicate the positions of molecules, the red of the substrate.

Figure 3.17 a) The results of simulations using model $\mathcal{D}$ and $\mathcal{L}$ vales. The blue dots indicate the positions of molecules, the red of the substrate. The green and blue bars in c) indicate molecular separations that are smaller or longer than that given by the $\mathcal{L}$ parameter, respectively.

Figure 3.18 Calculated distribution of TPA molecules from the model described in the text. The red circles represent the positions of substrate lattice sites. The blue circles show the positions of the TPA molecules and define the lower boxes showing the intermolecular separations. These are reported in units of lattice parameters (top) and actual distances (bottom). The colour coding shows where the bonds are shorter (green) or longer (blue) than the separation predicted from the intermolecular interaction alone.

Figure 3.19 STM images of the TP structures fabricated by annealing the H-bonded TPA phase to 353K. a) shows an overview of the features found, including the terrace-bound structures and the 2D stripes observed at steps. I=70 pA, U=1.6 V. b) Zoomed in view of the terrace-bound structures, demonstrating the variety of motifs observed. I=40 pA, U=-1.4 V.

Figure 3.20 a) STM image of two TP monomers. The blue line illustrates the position of the line profile shown in c). A TP model has been overlaid on the upper feature. I=40 pA, U=-1.4 V. b) 3D representation of the image in a) to highlight the depressions at the ends of the TP molecules.

Figure 3.21 a) STM image of two TP trimers. The trimer on the right is overlaid with a structural model including a single Cu adatom. I=50 pA, U=-1.9 V. b) STM image of a TP tetramer and, inset, the same image with an overlay of a tentative model with two Cu adatoms. I=30 pA, U=-1.9 V.

Figure 3.22 a) Large-range STM image, showing 1D stripes (highlighted by blue boxes) and 2D islands (highlighted by green boxes). I=100 pA, U=-1.0 V. b) Zoomed in image of a 2D island; the profile along the blue line is shown in c). d) Zoomed in STM image, overlaid with TP models. c) and d) I=110 pA, U=-1.0 V.

Figure 3.23 a) Large-range STM image of Fe islands grown on the Cu(111) surface held at 248 K during deposition. I=100 pA, U=1.0 V. The green circles highlight multilayer-high Fe islands. b) and c) Zoomed in topography and current images of a single Fe island, respectively. The current image is shown to highlight the resolution

within the island, suggesting a (111)-like arrangement of the protrusions. The green arrows in b) shows the locations of steps within the island. I=1.3 nA, U=45 mV.

Figure 3.23 a) Large-range STM image of Fe islands grown on the Cu(111) surface held at 248 K during deposition. I=100 pA, U=1.0 V. The green circles highlight multilayer-high Fe islands. b) and c) Zoomed in topography and current images of a single Fe island, respectively. The current image is shown to highlight the resolution within the island, suggesting a (111)-like arrangement of the protrusions. The green arrows in b) shows the locations of steps within the island. I=1.3 nA, U=45 mV.

Figure 3.24 a) Large-range STM image of Fe deposited onto H-bonded TPA/ Cu(111) held at 248 K. I=40 pA, U=1.4 V. b) Zoomed in STM image of a TPA island after Fe deposition. Some protrusions consist of Fe adsorbed either on top or penetrating into the TPA lattice (blue circle), others correspond to single TPA molecules with enhanced contrast (green circle). I=40 pA, U=1.4 V.

Figure 3.25 a) Large-range and b) zoomed in STM images of the films in Figure 3.24 after annealing to 317 K. a) I=58 pA, U=-0.3 V. b). I=33 pA, U=0.4 V. The blue and green circles highlight trimer and tetramer motifs, respectively. The green line shows the line profile in c).

Figure 3.26 a) Large-range STM image of the films in Figure 3.24 after annealing to 383 K. I=33 pA, U=1.7 V. b) Zoomed-in STM image of the same sample, highlighting the apparent similarity to the MOCN-II structure shown in c) (figure taken from reference [15]). I=40 pA, U=-0.7 V. d) STM image of the same Fe-TPA structure after annealing to 403 K. I=58 pA, U=-0.5 V.

Chapter 4: Oxalic acid on Cu(110) and Cu(111)

Table 4.1 The most favourable geometries for the a) mono-deprotonated, b) fully-deprotonated and c) intact OA molecules with a (3×2) superstructure on the Cu(110) surface, as predicted by DFT simulations.

Table 4.2 Total adsorption energies, as predicted by DFT, of mono-deprotonated OA adsorbed in an upright geometry on the Cu(110) surface, using different molecular packings.

Figure 4.1. a) STM image of the OA film on the Cu(110) surface prior to annealing. Small ordered regions can be found amidst non-resolvable areas. I=120 pA, U=-1.1 V. b) STM image of the OA film after annealing to 398 K, showing the long-range (3×2) ordering. The blue circle highlights an interstitial OA molecule and the green lines highlights a domain boundary between two (3×2) domains. I=180 pA, U=-1.1 V. c) STM image of the OA film after annealing to 423 K, demonstrating clean areas (blue circle), potential decomposition products (purple circle) and isolated OA features (green circle). I=100 pA, U=1.1 V. d) LEED image of the (3×2) OA film. E=148eV, T≈RT.

Figure 4.2 a) LEED image of the 'disordered (3×2)' OA phase. E=63eV, T≈RT. b) Corresponding STM image. I=300 pA, U=-1.0 V.

Figure 4.3 Initially-assumed OA structure, viewed from above and along the [001] direction, based on the (3×2) structure found using STM and LEED and the upright orientation suggested in reference [1] from RAIRS studies.

Figure 4.4 a) Possible positions of the interstitial OA if it maintains the same adsorption site as the surrounding OA molecules. In either of the two positions, the molecule is no longer centred within the (3×2) cell. b) Alternative adsorption site compatible with the a symmetric c(3×2) configuration. c) and d) STM images of the OA (3×2) structure, imaged at positive and negative bias voltages, respectively. I=180 pA. e) Profiles of the two lines in a) and b), highlighting the apparent height differences in empty and filled state imaging.

Figure 4.5 a) Large scale STM image of the OA monolayer films. In the top terrace, the OA domains have been coloured to highlight the [001] orientation of the domain boundaries. I=210 pA, U=1.0 V. b) Model of the domain boundary shown in Figure 4.1b, demonstrating the staggered arrangement of the OA molecules.

Figure 4.6 a) and b) Sequential STM images of a domain boundary with a 3× periodicity along the [110] direction. The OA molecule highlighted with the blue arrow is seen to move one Cu lattice spacing to the left between the two scans. I=110 pA, U=1.2 V. c) Schematic representation of the diffusion barriers along the two principal crystallographic directions of the Cu(110) substrate.

Figure 4.7 a) and b) O 1s spectra of the OA monolayer and multilayer films, respectively. c) and d) C 1s spectra of the OA monolayer and multilayer films, respectively. The peak assignment is discussed in the text.

Figure 4.8 a) Top and side views of OA, showing the relative orientations of the σ- and π-states (orange and green, respectively). The NEXAFS spectra of the OA (3×2) monolayer, acquired with the photon incidence angle oriented along b) along the [001] direction and c) along the [110] direction. The photon polarisation vector of each scan are given with respect to the surface plane. In the two spectra, the σ- and π-transitions are highlighted by the green and orange bands, respectively.

Figure 4.9 Proposed adsorption geometry of the OA molecules, based on the results of the STM, LEED, DFT, XPS and NEXAFS measurements.

Figure 4.10 STM images showing the adsorption of OA on Cu(111) as a function of coverage. a-c) are adapted from reference [2], performed at 100 K. d-f) were obtained in this work. a) and d) show formation of formate. b) and e) The coexistence of the OA rhomboidal phase and formate. c) and f) Zoomed in STM images of the rhomboidal structure of the OA phase. d) I=100 pA, U=1.0 V. e) I=140 pA, U=-1.7 V. f) I=140 pA, U=-1.7 V. The crystallographic directions inset into d) only apply to d-f).

Figure 4.11 Model of the Cu-OA structure on Cu(111) as proposed by Faraggi *et al*. Image taken from reference [2].

Figure 4.12 a) STM image of the Cu(111) surface after exposure to 30 Langmuirs of OA. I=100 pA, U=-1.0 V. b) STM image acquired after annealing the sample shown

in a) to 398 K. The green oval highlights a chain of second layer OA. I=57 pA, U=1.0 V.

Figure 4.13 a) Zoomed in STM image of the OA ($\sqrt{3}\times\sqrt{3}$)R30^{o} monolayer phase on the Cu(111) surface. I=190 pA, U=-1.4 V. b) and c) Two sequential STM images of the same area, highlighting removal of individual molecules by the tip in b) and deposition of OA molecules onto the OA monolayer in c). The contrast in b) and c) been selected so that the on-top OA molecules could be better resolved. b) and c) I=19 pA, U= -1.4 V.

Figure 4.14 LEED image of the OA ($\sqrt{3}\times\sqrt{3}$)R30^{o} structure. E=105 eV, T=207 K.

Figure 4.15 Schematics of a potential a) flat-lying and b) vertically-standing OA monolayer on Cu(111) with a ($\sqrt{3}\times\sqrt{3}$)R30^{o} superstructure.

Figure 4.16 STM images of unidentified features obtained after OA monolayer preparation. a) Large area STM image I=140 pA, U=-1.4 V. b) and c) Sequential STM images of the porous OA structure, showing the dynamic nature of the structure. I=58 pA, U=-1.4 V.

Figure 4.17 Top-view models of a) the flat-lying OA film on the Cu(110) surface and b) the vertically-standing OA on the Cu(111) surface.

Chapter 5: Terephthalic acid on oxalic acid monolayers

Figure 5.1 a) STM image and model of the OA (3×2) monolayer film obtained on the Cu(110) surface. I=180 pA, U=-1.1 V. b) and c) STM images taken after TPA deposition onto the OA (3×2) film held at RT, showing the formation of [001]-oriented TPA stripes. The blue circle in c) indicates an unordered TPA structure. b) I=210 pA, U=-1.0 V. c) I=110 pA, U=-1.0 V.

Figure 5.2 a) STM image of two TPA chains on the OA (3×2) film. The green line marks the position of the profile shown in b). The blue arrow in a) highlights the local disorder in the OA film. I=110 pA, U=-1.0 V.

Figure 5.3 STM image of TPA on the OA (3×2) film after annealing to 423 K. Gaps are now found in the OA lattice, whilst the TPA have maintained the same apparent brightness with respect to the OA molecules. I=65 pA, U=-0.9 V.

Figure 5.4 Schematic of the TPA molecules penetrating through the OA film to adsorb on the bare surface. The TPA initially adsorbs on top of the OA film (top). The OA is then displaced, so that the TPA can adsorb directly on the metal surface (bottom). The increased local OA density is a consequence of the TPA 'squeezing' the OA out of the way. The OA molecules and Cu(110) substrate supports have been faded in the top left panel, to clarify the TPA molecule.

Figure 5.5 a) Schematic of proposed TPA manipulation on-top of the OA film by the STM tip. b) Model demonstrating how the lack of TPA mobility fits a model where OA is displaced and TPA is directly adsorbed onto the copper substrate.

Figure 5.6 STM images of TPA on the OA (3×2) film, held at approximately 140 K during TPA deposition to limit OA mobility. a) Large range STM image. I=83 pA, U=1.4 V. b) Zoomed-in STM image of what is thought to be a single TPA molecule, circled, highlighting that there is no disruption to the OA lattice. I=58 pA, U=-1.8 V.

Figure 5.7 STM images and model of the $(\sqrt{3}\times\sqrt{3})R30^{O}$ OA structure obtained on the Cu(111) surface. I=90 pA, U=-1.4 V. b-d) STM images acquired after TPA deposition onto the OA film held at RT. c) and d) show zoomed in images of the overlayer 2D islands and the 1D chains, respectively. b-c) I=14 pA, U=1.8V. d) I=100 pAm U=-0.9 V.

Figure 5.8 a-d) A series of sequentially-acquired STM images, showing overlayer 1D TPA chains on the OA/Cu(111) film. The chain highlighted in blue is disassembled by its interaction with the scanning tip, whilst that in green remains intact and can be used as a reference marker. The green arrows in b) and c) indicate the positions of the displaced TPA. All STM images taken at I=100 pA, U=-1.8 V.

Figure 5.9 a) Large area STM image of TPA deposited onto the OA/Cu(111) monolayer. The blue box corresponds to the approximate area shown in panel b). A

line-by-line flattening is applied to this image due to tip-switching events. I=100 pA, U=1.8 V. b) Zoomed-in image of the TPA island after manipulation of the TPA molecules. I=40 pA, U=-1.8 V. c) Zoomed-in image showing the OA exposed after TPA manipulation. I=40 pA, U=-1.8 V.

Figure 5.10 a) STM image of TPA on the vertically-standing OA film on the Cu(111), demonstrating the perpendicular orientations of TPA 2D-islands and 1D-chains. Inset are the substrate crystallographic directions. I=14 pA, U=1.8 V. The directions of the 2D-islands (upper) and 1D-chains (lower) are also shown. b-c) Proposed models for the TPA chains and islands on the OA lattice, based on the observed orientation and periodicity of the TPA. OA is shown as blue circles, the TPA as the orange ovals.

Declaration

I hereby declare that this thesis, submitted in partial fulfilment for the degree of Doctor of Philosophy, represents my own work and has not been previously submitted to this or any other institution for another qualification. Work was carried out between October 2009 and July 2013 under the supervision of Dr Giovanni Costantini.

Both Chapters 3 and 4 contain contributions from collaborators, which are outlined in each section. Part of the work in Chapter 3 can be found in a published article, as outlined in the list of publications on Page 202. The room temperature scanning tunnelling microscope measurements of terephthalic acid on Cu(110) were performed by Dr Yeliang Wang and the corresponding density functional theory simulations by Dr Stefano Fabris. All of the theoretical simulations of terephthalic acid on Cu(111), including the molecular mechanics, density functional theory and the development of the analytical algorithm, have been performed by Dr Natalia Martsinovich and Professor Alessandro Troisi. The density functional theory calculations of oxalic acid on Cu(110) were performed by Dr Sara Fortuna and Dr Stefano Fabris.

Thomas William White

2014

Acknowledgements

There are many people I have to thank for their help and contributions to this work. Firstly, my eternal thanks go to my supervisor, Dr Giovanni Costantini. Thank you for the opportunity to work with you on this project. It has been a real pleasure and I know I have learned a lot.

I would also like to thank the many collaborators who I am honoured to have worked with; Dr Natalia Martsinovich, Professor Ale Troisi, Dr Yeliang Wang, Professor Klaus Kern, Dr Sara Fortuna, Dr Stefano Fabris, Dr Sam Haq, Dr David Duncan and Professor Phil Woodruff, to name just a few. I hope I am lucky enough to work with you again at some point in the future.

To my group and office mates, thank you for all your help and friendship. It was a blast, and I will miss you guys!

My heartfelt thanks also go to my family; I might stop boring you now with 'molecules'. Probably not. Thank you for all the support and the love you have given me, particularly over the last few years. I am not sure I could have managed without you.

Finally, I guess I should acknowledge one last person. Thank you for believing in me sweetie.

Abstract

Many of the highlights in the surface science field in the last years have arisen from the study of organic molecules adsorbed upon, but physically decoupled from, metallic substrates. When adsorbed on bare surfaces like Cu, the strong interaction between the two can have a number of different effects on the chemistry, functionality and assembly of the adsorbates. These effects can be reduced or even prevented by incorporating an ultra-thin insulating film between the molecule and the metal, enabling the retention of the desired molecular properties. Previous studies have almost exclusively used films of inorganic material, such as alkali halides and metal oxides. In this work, an all-organic alternative approach has been developed, which should allow a greater degree of control over the nature of the decoupling film and its corresponding interactions.

To demonstrate the potential impact of the molecule-substrate interaction on the formation of molecular nanostructures, the adsorption and assembly of a prototypical molecular tecton, terephthalic acid (TPA), has been explored on Cu(110) and Cu(111). On Cu(110), the TPA is deprotonated and goes on to form a range of metal-organic or all-organic monolayer films. The exact structure obtained is determined by the total molecular coverage, which is rationalised by consideration of the TPA adsorption energies and the molecular density in each phase. On Cu(111), TPA adsorbs intact, and assembles into a brickwork-like structure

characterised by both uncharacteristically short and elongated hydrogen bonds. This unusual assembly is the result of the oft-cited, but in general poorly understood, ‘interplay of intermolecular and molecule-substrate interactions’. In a bid to understand the observed supramolecular assembly of TPA on Cu(111), a simple algorithm has been developed that is capable of predicting both its quantitative and qualitative aspects. Moreover, this analytical model can be readily expanded to more complex assemblies, such as those using more complex molecules and surfaces. In addition, the formation of Cu- and Fe-terephthalate complexes has been explored.

Oxalic acid (OA) monolayers have been investigated as prototype organic decoupling layers for the Cu(110) and Cu(111) surfaces. This molecule was chosen as, in previous work, it had been reported to adsorb in an upright orientation and assemble into a densely packed monolayer on Cu(110). In this work, a flat-lying, low density film has been obtained on Cu(110), which later proved to be incapable of supporting molecular ‘overlayers’ unless it was cooled to low temperature prior to the deposition of molecular overlayers. In contrast, a densely-packed, upright monolayer was obtained on Cu(111). This decoupling layers was effective even at room temperature, and moreover appears to plays a significant role in determining the assembly of the overlayer species. These studies indicate the potential of vertically standing organic films as both decoupling layers and also as a tool with which to directly modify and control the assembly of organic nanostructures.

Abbreviations

1D, 2D, 3D	1-, 2-, 3-dimensional
bcc	body-centred cubic
DOS	Density of electronic states
DFT	Density functional theory
fcc	face-centred cubic
H-bond	Hydrogen bond
HOMO	Highest occupied molecular orbital
LEED	Low-energy electron diffraction
LT	Low temperature
LUMO	Lowest unoccupied molecular orbital
MM	Molecular mechanics
MO	Metal-organic
NEXAFS	Near-edge X-ray adsorption fine structure
OA	Oxalic acid
PES	Potential energy surface
RAIRS	Reflection-adsorption infra-red spectroscopy
RT	Room temperature
SAM	Self-assembled monolayer
STM	Scanning tunnelling microscope
STS	Scanning tunnelling spectroscopy
TP	Terephthalate
TPA	Terephthalic acid
UHV	Ultra-high vacuum
vdW	van der Waals
XPS	X-ray photoemission spectroscopy

Chapter 1

Introduction

1.1 Surface engineering

The engineering of surfaces with specific, predetermined properties is an important research goal. For many applications, the focus is necessarily on the *nanoscale* attributes of the material, including both its 'functional' aspects – those properties that can, at least in principle, be utilised in various potential applications – and their nanoscopic structure. Ultimately, this will necessitate the consideration of single molecules and atoms in, or adsorbed upon, the surface layer. To work effectively at this size scale, a range of high-resolution manufacturing and

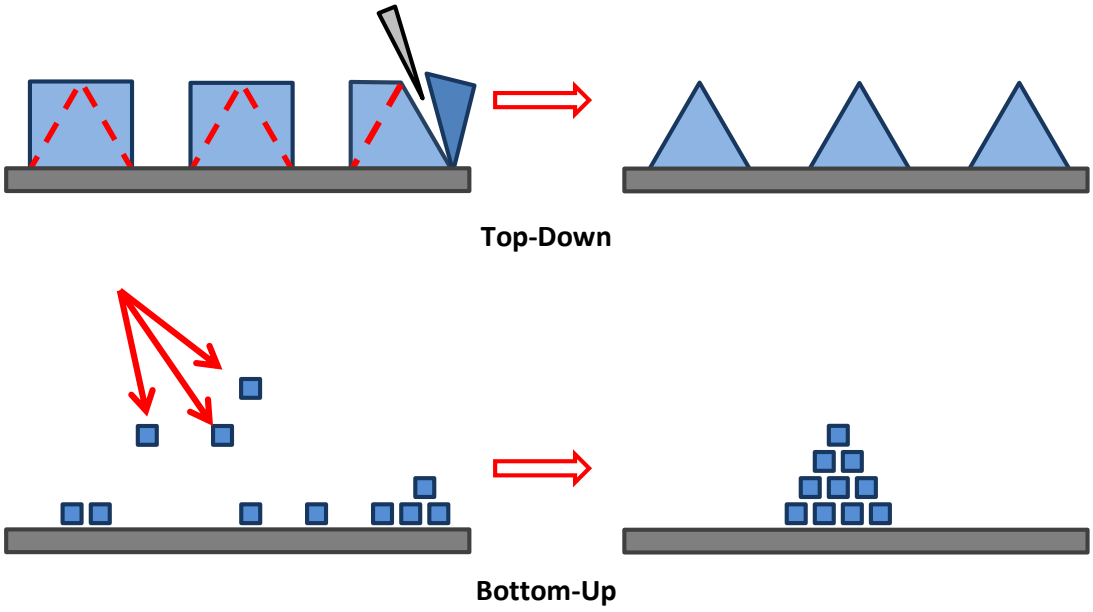

Figure 1.1 Schematic representation of the top-down and bottom-up approaches to the fabrication of nanostructures on surfaces. In the top-down approach, structure is imposed on a material 'from above' using classical techniques that add or remove material. In the bottom-up approach, the inherent interactions between smaller components are harnessed such that they assemble into the required structure.

characterisation techniques have been developed. Thanks to these techniques, it now possible to truly understand and even manipulate matter at the most fundamental levels.

A wide range of different techniques has been developed for the fabrication of functional nanostructures. These processes are normally categorised as either 'top-down' or 'bottom-up' [1]; the underlying concepts behind the two are depicted in Figure 1.1. Top-down procedures construct features using micro- and nanoscopic equivalents of traditional fabrication techniques like lithography, milling and stamping [2]. This approach has proven incredibly successful: In fact, much of the modern computer era owes its success to the use of top-down manufacturing in the semiconductor industry. However, they tend to become increasingly challenging at

smaller size scales and ultimately are unlikely to be feasible at sub-nanometre dimensions.

In contrast, the bottom-up approach aims to manufacture features through the piecing-together of smaller components, called ‘tectons’ [3]. This is directed by their fundamental interactions with one another, which, through careful consideration of the tecton’s composition and the fabrication conditions, can occur in an autonomous manner without the need for external stimuli. Such ‘self-assembly’ results in highly ordered structures with comparatively little manufacturing effort and thus is potentially an extremely powerful tool in surface engineering.

For self-assembly to be an effective route to nanostructure fabrication, it is essential that it is sufficiently versatile to construct functional materials into highly specific structures. In this respect, self-assembly of *molecular* tectons is perhaps the most attractive option. First, given the wealth of expertise developed over the last century, organic synthesis is now capable of manufacturing chemicals with a multitude of different functional properties. Second, supramolecular chemistry [3] has demonstrated how careful selection of the manner in which tectons interact and their molecular structure can grant an exquisite level of control over their assembly in a way unachievable with other materials. This is largely due to the variety of different intermolecular interactions available to organic molecules, which can be used with excellent effect to direct the assembly of 1-, 2- and 3-dimensional (1D, 2D, 3D) structures. Moreover, this also allows specific tailoring of the interactions to the tectons exact purpose within their given application. For example, where a high degree of uniformity is required, assembly through hydrogen bonds (H-bonds) and van der Waals (vdWs) forces are ideal, as their innate reversibility enables the self-repair of defects within the film [4]. If highly robust nanostructures are needed,

tectons that form intermolecular covalent bonds can be used [5]. In some scenarios, incorporation of metallic species may be essential, which can be readily achieved with coordination bonding [6]. All of these have been demonstrated for various molecules on different surfaces. Moreover, in some cases, multiple types of interaction are available, with the exact type being dependent on the precise experimental conditions used. For example, temperature [7,8] and deposition rate [9] are just two of the many important parameters that must be considered.

To successfully use molecular tectons in surface engineering, it is important that rational and reproducible design and fabrication protocols can be developed. Perhaps the simplest and most intuitive approach for this is one that simplifies the process into two key steps. First, the desired functional properties are considered and an appropriate molecular 'core' is designed and synthesised. Second, this core is functionalised with peripheral moieties that direct the molecules to self-assemble in the desired way. In this manner, all of the information required for the system to assemble into a functional nanostructure is programmed exclusively into the molecular species. However, for construction on solid substrates, this approach is normally unrealistic as it is usually impossible to neglect the influence of the surface and its corresponding interaction with the adsorbates. In the particular case of metal supports, whose conducting nature is an essential component of many applications, the interaction can be sufficient to completely transform the functional properties, the assembly and even the intrinsic structure of the tecton and the metal. Furthermore, its overall effect can often be difficult to predict, due to the large number of highly intertwined chemical and electronic processes by which it is determined. Consequently, effective surface engineering will ultimately demand a

detailed understanding of the molecule-substrate interaction, so that its effects can eventually be incorporated into the design process described above.

1.2 The role of the substrate

The molecule-substrate interaction can be highly complex as, depending on the particular system in question, it can encompass vdW, coulombic and covalent contributions. With respect to surface engineering, it is particularly critical to consider the strength of the interaction and its impact on the functional properties and assembly of the adsorbed tectons. Where it is very weak, the molecule is only slightly perturbed by the underlying metal. It therefore retains much of its gas-phase physical and electronic structure [10,11] and is likely to be still capable of its originally desired functional properties [12]. This is typically labelled physisorption. Conversely, where it is strong, the organic species is considered to be chemisorbed, which often results in substantial conformational, chemical and electronic modifications to both the molecule and the surface. Furthermore, molecular diffusion can also be compromised and the assembly of chemisorbed molecules can therefore be severely hindered. The distinction between these two labels is not well defined and is based rather arbitrarily on the magnitude of the interaction strength. Consequently, it is perhaps of greater use to consider the possible implications to the tecton and the substrate when the two interact strongly. In the following section, the different repercussions are outlined, where they are loosely defined as either ‘structural’ – those that concern the conformation and composition of the molecule and surface – or ‘electronic’. The effects on adsorbate assembly can be highly complex and vary from case to case. This will be explored in more detail in Chapter 3.

1.2.1 Adsorbate and substrate structural modifications

Unless a molecule is extremely weakly adsorbed or is significantly rigid, it will undergo distortions upon adsorption that optimise its interaction with the substrate. In the mildest cases, only very small conformational changes are likely to occur [13,14], which ultimately have little to no effect on the molecular assembly or its functional properties. In other instances, the effects can be profound. For example, as a candidate for conducting wires or interconnections in molecular computing systems, poly-aromatic molecules are promising. For their successful implementation, the species has to be adsorbed upon, but lifted from, a metal substrate, which can be achieved by incorporating bulky chemical moieties at their peripheries (see Section 1.4.1 for more details). However, the strong interaction between π-electron systems and metals can be sufficient to bend the aromatic moiety away from the desired height to one much closer to the surface [15]. In doing so, the adsorbate's electronic structure is significantly perturbed and is consequently no longer suitable for the role of a molecular wire.

The metal support is also not immune to adsorption-induced conformational changes, and these effects can often be quite radical. For example, where the molecule-surface interaction is sufficiently strong, metal atoms can be lifted out of the surface plane. Whilst this sounds relatively innocuous, the resulting stress can severely modify the assembly of the adsorbates [14,16]. In more extreme circumstances, the surface can even undergo radical reconstructions, resulting in a fundamentally different structure to that before molecular adsorption [17-19].

When sufficiently strong, the molecule-substrate interaction can also lead to chemical transformations in the adsorbate. In such cases, chemical bonds can be broken and sometimes additional bonds can be formed [20]. Moreover, chemical

modification of tectons are often not well defined, resulting in unpredictable products that can be difficult to identify even with exhaustive multidisciplinary studies [21-23]. While such reactions are the basis of the extensive success of reactive metal surfaces in heterogeneous catalysis [24,25], it should clearly be avoided when the goal is to transfer molecular functionality to a substrate.

On the other hand, controlled chemical reactions on surfaces can, in some situations, be a useful tool with which to fabricate the desired molecular species. For example, it has recently been demonstrated that the reactivity of metals and annealing treatments can be used to form covalent bonds between appropriate tectons, resulting in the formation of very large single-molecule species [5,20]. As adsorbates of such size cannot be easily prepared by other means, this is likely to become an important tool in surface engineering.

1.2.2 Electronic interactions between molecule and substrate

An adsorbed molecule will experience a number of electronic perturbations because of its proximity to a metallic surface. Perhaps the most difficult to predict *a priori* is the hybridisation of molecular and surface electronic states. When an organic tecton is adsorbed on a metal, the molecular and metallic electronic states are in close spatial proximity. If they are also sufficiently proximal in energy, the electronic structures of the two can mix, or 'hybridise'. Metal surfaces exhibit a large density of electronic states (DOS) over a wide energy range, and thus an adsorbate is always able to find electronic states with which to hybridise. The consequences for the molecule can be severe; the originally well-defined and localised molecular orbitals become spatially and energetically broadened [26-32], as depicted in Figure

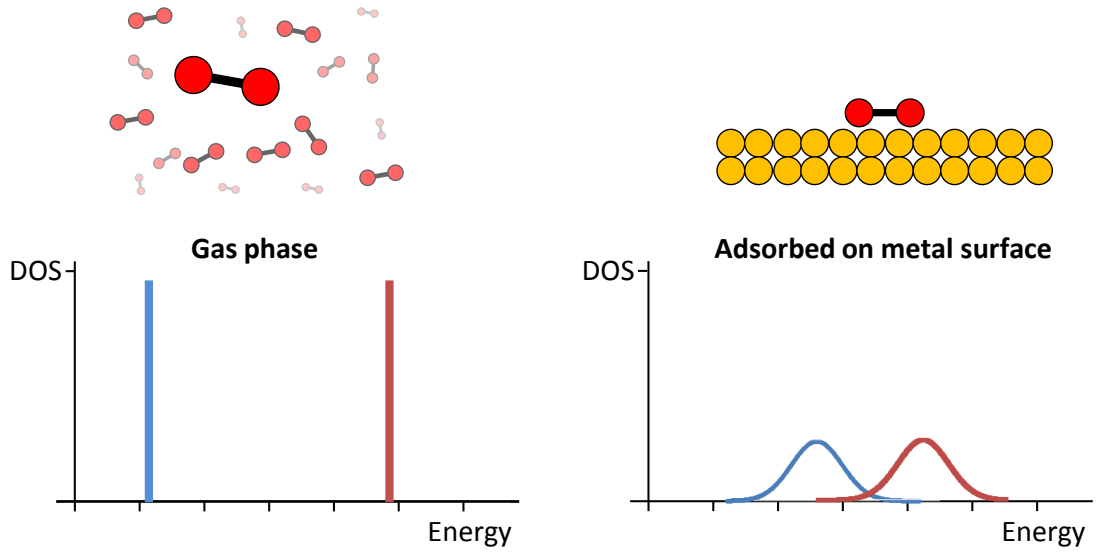

Figure 1.2 Schematic representation of the electronic structure of a molecule (red dumbbell shape) in the gas-phase (left) and adsorbed on a metal surface (right). In the gas phase, the electronic structure is energetically well-defined. In contrast, when adsorbed on the metal, the hybridisation of the molecular and metallic electronic states results in their energetic and spatial distributions being broadened.

1.2. In some cases this effect is relatively minor [11], but often the electronic structure can be transformed beyond recognition [33].

In addition to this hybridisation are two effects that can shift the energy of an adsorbate's electronic states. The first occurs upon electron transfer to or from the molecule. When a charge is localised above the substrate (i.e. within the tecton), the electron density within the metal surface is redistributed. This results in an 'image charge' in the metal that, in terms of electron distribution and polarisation response, is equivalent to an equal but opposite charge with respect to that in the adsorbed species [34], as illustrated in Figure 1.3a. The coulombic attraction between the two charges stabilises that in the adsorbate, resulting in a reduced ionisation potential and an increased electron affinity. The net result is that the highest-occupied and lowest unoccupied molecular orbitals (HOMO and LUMO, respectively), are typically shifted in energy towards the Fermi level, resulting in a reduction of the 'molecular

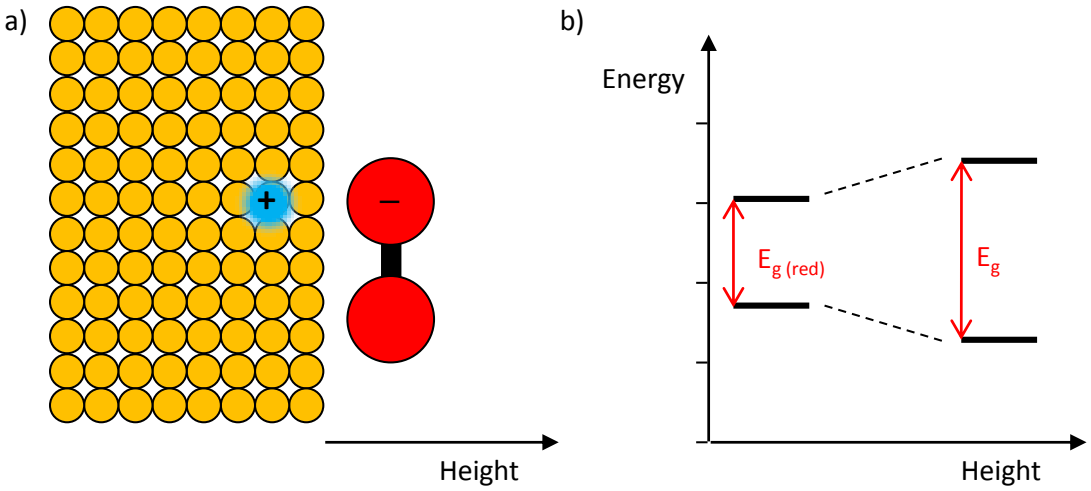

Figure 1.3 a) Schematic representation of the adsorbate charge screening on metal surfaces. b) The HOMO-LUMO gap, labelled E_g, as a function of the molecule-substrate separation.

band gap' in comparison to that observed in the gas phase, as illustrated in Figure 1.3b.

In addition to the image charge effect, the formation of interfacial dipoles can also affect a tecton's electronic structure. A number of different mechanisms can occur that generate a dipole across the metal interface upon adsorption of an adsorbate, including charge transfer, chemical interactions and the image charge effect [35]. The net result is a constant electric field in the area immediately above the metal in which the molecule resides. The electronic states of the adsorbate are rigidly shifted either upwards or downwards in energy by this potential, depending on its sign, which is in turn determined by the direction of the interfacial dipole.

1.3 Characterising sample surfaces

Defining the role of the substrate in the self-assembly of organic tectons can be highly challenging. Moreover, 'real-world' metal substrates are already extremely complex, making the task of understanding the fundamental aspects of surface engineering, in general, very difficult. With this in mind, surface science studies are

typically performed using model systems, whereby the complexity of the molecule-on-metal sample is reduced by using simple, well-defined interfaces and molecules, and precisely controlled experimental conditions. For example, many studies use highly crystalline substrates with low Miller index terminations, and make use of ultra-high vacuum (UHV) systems. The latter grants exquisite control over the constituents of the surface throughout the investigation. Furthermore, many studies use relatively simple prototype tectons so that their adsorption behaviour, functional properties and assembly can be readily understood within a limited number of experimental parameters.

Whilst model systems can greatly simplify the characterisation of functional surfaces, it is still often necessary to use a range of different experimental analysis techniques to construct a complete picture of a given sample. One of the most important techniques, particularly when studying molecular tectons, is the scanning tunnelling microscope (STM). Since its invention in 1982 [36], it has revolutionised the surface science field due to it being, until recently, the only technique capable of routinely imaging interfaces with sub-nm precision. This impact was recognised by its near-immediate award of the physics Nobel prize in 1986 [37]. A detailed description of the technique is presented in Chapter 2. However, while it is an incredibly powerful technique, it cannot necessarily provide all of the required information about a given sample. For example, STM does not directly provide details about the chemical state of an adsorbate, and thus many studies also make use of X-ray photoemission spectroscopy (XPS), which allows the exact chemical state of the surface constituents to be elucidated.

1.4 Controlling the molecule-substrate interaction

A very efficient way to control the effects of the molecule-substrate interaction is the introduction of a gap between the two. In doing so, the adsorbate is protected from structural and chemical transformations and is also electronically 'decoupled' from the substrate due to the reduced overlap of their relative wavefunctions. The magnitude of the separation is an important consideration; if the tecton is too close to the surface, some electronic interaction is still possible, whilst if the separation is too great, charge transfer to and from the adsorbate via electron tunnelling is prevented. It is therefore necessary to aim for separations between these two extremes, on the order of ~5 Å [31,38].

Perhaps the most succinct method for proving an adsorbate is fully decoupled is to quantitatively characterise its electronic structure. This can be achieved in a number of ways, but scanning tunnelling spectroscopy (STS), a technique directly integrated into the STM experiment [39], is a particularly powerful tool for this as it allows the simultaneous determination of a molecule's local environment and its electronic structure.

The effectiveness of the combined STM/STS approach in this respect has been demonstrated numerous times [32,40-46]. In one particular example, a thin layer of NaCl was used to decouple individual pentacene molecules from a Cu(111) surface [41]. When adsorbed on the bare metal, the STS spectrum of pentacene is featureless, due to the strong hybridisation of molecular and metallic electronic states [33]. However, when located on top of the NaCl film, the pentacene STS spectrum shows strong peaks in both the occupied and empty states region (Figure 1.4a). Imaging the pentacene by STM at a bias voltage corresponding to these two peaks results in the resolution of intramolecular contrast with features that strongly

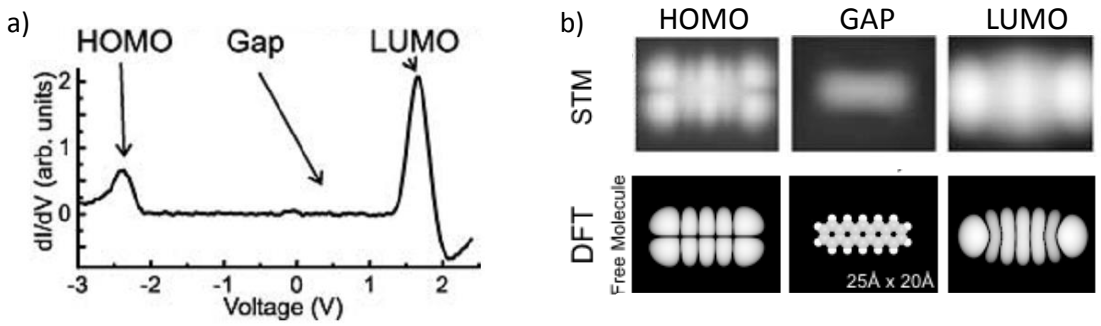

Figure 1.4 a) STS spectrum of pentacene adsorbed on top of a NaCl decoupling layer on Cu(111). b) STM images taken at the HOMO, Gap and LUMO voltages found in a). The DFT-calculated HOMO and LUMO of isolated pentacene are shown beneath, highlighting that the experimentally obtained images of the HOMO and LUMO exhibit similar spatial characteristics to the gas-phase species. Both images are adapted from reference [31].

resemble the HOMO and LUMO of the density functional theory (DFT)-calculated gas-phase pentacene molecules (Figure 1.4b).

Strictly, the peaks observed in the STS spectrum do not actually correspond to the HOMO and LUMO of pentacene, but in fact to its positive and negative ion resonances. The enhanced lifetime of the tunnelling electrons [41,47,48] in the pentacene results in polarization of the NaCl electronic structure underneath the molecule, which in turn stabilises a partial charge in the pentacene. The resonances of the pentacene are thus slightly shifted in energy towards the Fermi level in comparison to the gas-phase molecular orbitals, as the electrons do not tunnel into a neutrally charged species [49].

This effect can be used, in some circumstances, to control adsorbate charge states; for example, adsorbed adatoms [50-52] and molecules [38,46] have been reversibly switched between different charge states. This increased charge stability makes decoupled tectons promising candidates as bits for data storage applications, as switches in molecular electronics, and as activated precursors for tip-induced chemical reactions. STM-induced reactions are not exclusive to decoupled systems, but controlled current pulses are normally required to initiate reactions. On

decoupling films, charged adatoms have been bought into close proximity to molecules, which spontaneously react due to the charge on the adatom, forming a metal-organic (MO) complex [43,44,48].

One particularly important application for decoupled tectons is in controlled molecular luminescence. Luminescent molecules on conducting surfaces may prove to be highly efficient light sources; electrons can be pumped directly into the high-energy electron levels of adsorbates, resulting in an excited molecular state that can in turn decay, emitting a photon. Furthermore, as the emitted photon is dependent on the fluorescing transition, stimulated photon emission has been suggested as a useful tool in chemical characterisation [53,54]. However, emission from molecules on metal surfaces is often strongly quenched. The electronic coupling between the adsorbate and substrate electronic structures results in severe shifting and broadening of the molecular energy levels and, consequently, the electronic states of the molecule are often no longer capable of luminescence [55]. In addition, the close spatial proximity of a metal can strongly enhance the probability of non-radiative relaxation pathways that occur on a faster timescale than the photon emission mechanism [53]. In particular, charge transfer of the excited electron into the empty metallic states can annihilate the molecular excited state, while strong coupling of the emitter's dipole to surface plasmons may result in dissipation of the excitation into the substrate [56]. These quenching mechanisms can all be inhibited by decoupling the adsorbate from the metal [54,57-59].

In the following, two main types of decoupling strategy are discussed in detail, so that the 'ideal' characteristics of an effective decoupling strategy can be ascertained. Other methods do exist, such as the use of lateral intermolecular interactions, but these are usually very specific to the systems involved [60,61].

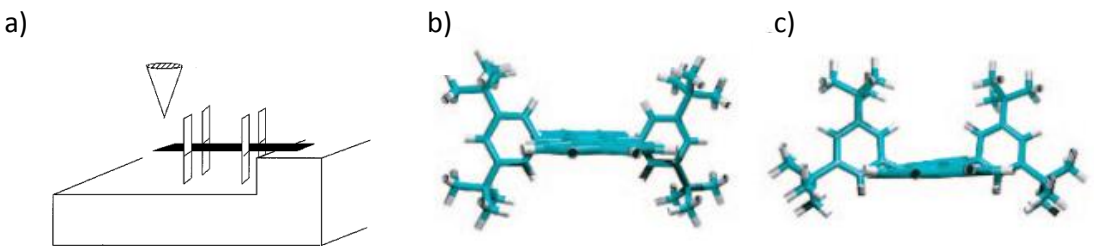

Figure 1.5 a) Concept model for the 'molecular Lander'. Adapted from reference [62]. b) and c) Side on views of an example Lander molecule in the gas-phase and adsorbed on a metal surface, respectively. Adapted from reference [30].

Consequently, the main schemes that are in principle applicable to a range of systems are presented below.

1.4.1 The 'Lander' approach to decoupling

Figure 1.5a shows the original concept behind the 'Lander' molecule [62], one of the earlier attempts at electronic decoupling that utilises a 'self-decoupling' approach. The Lander consists of a rigid core, from which the desired functional properties originate. The peripheries of the core are then functionalised with bulky moieties that act as 'legs', lifting the core from the surface, as illustrated in Figure 1.5b. The 'Lander' moniker comes from the specie's notional resemblance to the landing crafts used in interplanetary exploration [30].

Whilst the underlying principle of this approach is attractive, there remain a number of issues. One particularly difficult challenge to address is the way in which both adsorbate and the metal 'react' to the Lander core-surface separation. In a manner of speaking, both adsorbate and metal are working to negate the hard-won electronic decoupling. First, although the Landers are designed to be rigid enough to support the core, there is still often significant rotation and bending about the C-C bonds in the leg moieties [15]. The consequence of this, illustrated in Figure 1.5c, is that the molecular core is significantly closer to the surface than is desired and is

therefore not adequately electronically decoupled. Second, in some cases substrate adatoms can become trapped underneath the Lander [63,64], resulting in an effective local reconstruction directly underneath the core that acts to increase the molecule-substrate interaction. The final and perhaps greatest limitation of the Lander approach is that it imparts extremely strict limitations on the nature of the molecule. It must have significant rigidity if it is to maintain the electronic decoupling, as described above. This may preclude the inclusion of heteroatoms into the Lander, which are usually strongly attracted to the metal surface. Additionally, inclusion of the leg moieties can potentially cause significant modifications to the desired functional properties of the Lander core. Finally, the areas of the core where the legs are attached are effectively blocked, preventing the inclusion of other required peripheral functionalities, in particular those used to direct molecular assembly. In other words, the functional moieties that direct assembly can only be included at the molecule termini, where there are no bulky chemical groups, and consequently the Lander architecture limits directed molecular assembly to 1D [65,66].

1.4.2 Ultra-thin decoupling layers

An alternative approach is to use an ultra-thin film of insulating material – a 'decoupling layer' or 'decoupling film' – between the tecton film and the metal surface, as depicted in Figure 1.6a. The use of inorganic materials has proven highly successful in this respect. Such films can often be fabricated with the appropriate thicknesses and with sufficient band gaps [67], such that there is no electronic coupling of the molecular 'overlayer' with the decoupling film or with the surface [68]. Furthermore, the interaction between the overlayer and the decoupling film is often exceptionally weak, thus allowing the molecular assembly to proceed

Figure 1.6 a) Schematic representation of the decoupling layer strategy. A thin layer of an insulating material is deposited onto the surface prior to adsorption of the molecular tecton. b) The 'multilayer approach' to decoupling, where a thick film of the organic species is deposited. The lower layers act as a decoupling layer.

unperturbed and as directed by their intermolecular interactions alone. The most commonly used materials are alkali halides and metal oxides, both of which are discussed in more detail below.

It is also possible, at least in principle, to achieve a similar decoupling effect using a multiple-layer thick film of the molecular tecton, as depicted in Figure 1.6b. The first layer(s) act as a 'sacrificial' decoupling film, whilst later layers are sufficiently separated from the surface to be electronically decoupled [33,57,59]. However, this approach offers less control over the final product; the properties of the sacrificial layer and the interaction between the different layers are not necessarily well defined.

1.4.2.1 Alkali halide decoupling films

Of the possible alkali halide options, NaCl has been by far the most popular material choice for a decoupling layer. This is perhaps due to its simple internal structure and the relative ease with which suitably thick films can be fabricated on a range of different materials [31,69-74]. Furthermore, the growth of NaCl has been optimised such that exclusively bilayer films can be formed on some surfaces [31,75], which is an ideal thickness for a complete electronic decoupling.

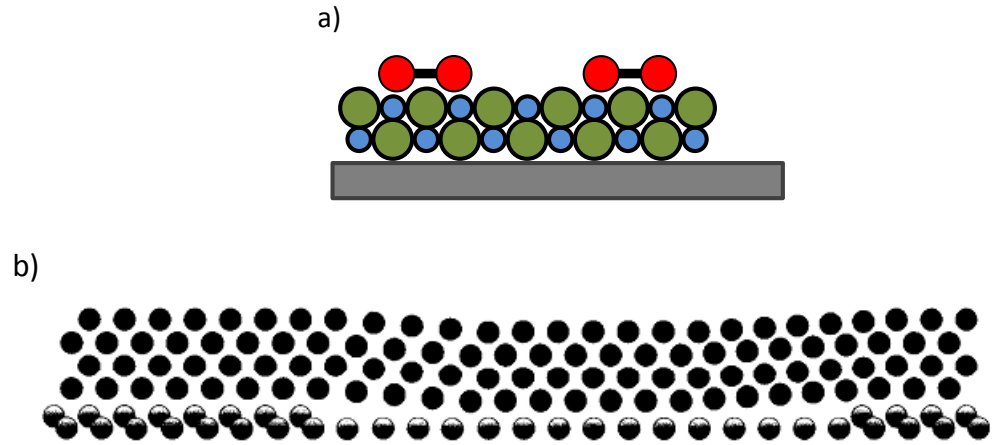

Figure 1.7 a) Side-view schematic of a NaCl bilayer decoupling film. The substrate is shown in grey, the Na ions are blue, the Cl in green, and the decoupled molecules are shown as red dumbbells. b) Depiction of the 'carpet' growth of NaCl over Ge(001), adapted from reference [69]. The substrate atoms are shown with partially shaded circles, the fully shaded circles show the Cl^- ions within the NaCl structure.

The strong attraction between the ions within alkali halide films plays a critical role in their growth behaviour on surfaces. First, regardless of the substrate symmetry, alkali halides almost always form (100)-terminated films (shown in Figure 1.7a). Only one example of a non-(100) film has been reported, which was only obtained after a considerably complex synthesis [76]. Second, alkali halide films exhibit a 'carpet-growth' regime: As the film grows laterally on substrate terraces, it will encounter steps, which it spreads over smoothly to continue growth on the following terrace [69]. This is illustrated in Figure 1.7b. In doing so, the alkali-halide maintains its (100)-termination. Finally, one study reported that when NaCl is deposited onto a particularly highly stepped surface, the underlying metal is forced to reconstruct in a way that provides a better epitaxy for the NaCl (100) facets [71,77].

It is perhaps unfortunate that other alkali halides have received very little attention in comparison to NaCl, as the electronic states of adsorbates on NaCl have been reported to be slightly broader than that expected [41]. This is not due to a residual molecule-substrate electronic coupling, but in fact arises from that between the molecular electronic states and phonons in the NaCl film [78]. In contrast, when RbI films are used, this broadening is not observed, allowing normally obscured electronic features to be revealed [42]. It is not clear if this effect extends to other alkali halide films due to their limited study.

1.4.2.2. Metal oxide decoupling films

Thin films of metal oxide on metals were originally studied as models for the substrates used to support catalytic metal dispersions [79]. As such films are both chemically inert and develop appropriately large band gaps within a few layers thickness [67], they are also suitable candidates for adsorbate decoupling. In fact, a number of studies have already demonstrated their effectiveness in this regard [54,58,80,81].

The most commonly used metal oxide decoupling film used is the surface oxide of NiAl(110). By annealing the (110) termination of a NiAl crystal in an O_2 atmosphere, approximately half of the substrate becomes covered with a 0.5 nm thick oxide layer [82]. The oxide has a highly complex structure and composition, which has remained controversial until recently [82-84]. Other oxides have been explored, but their preparation is typically more complex; metal atoms need to be deposited onto the sample using thermal deposition procedures whilst a background pressure of O_2 is maintained [74]. For films grown in this way, a lack of good epitaxy between the film and the underlying substrate can often result in imperfect

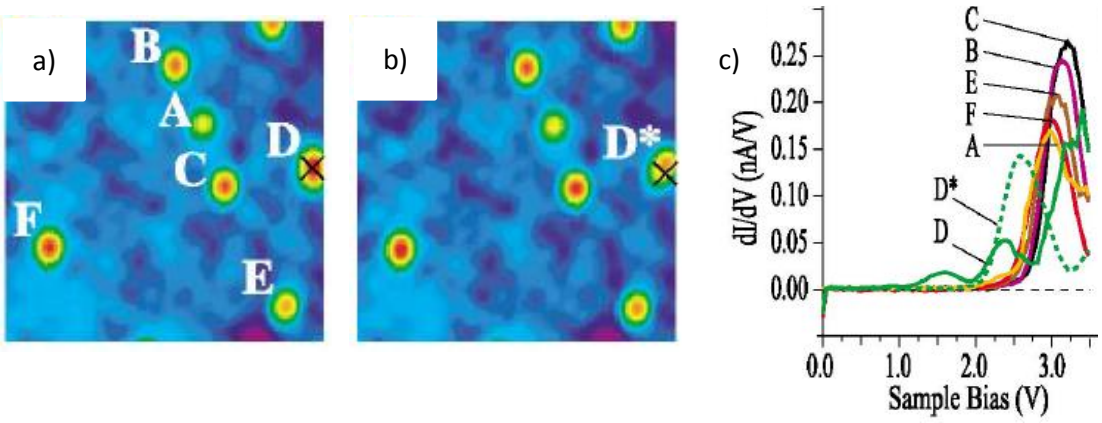

Figure 1.8 a) and b) STM images of Pd atoms adsorbed on the NiAl(110) surface oxide film. The corresponding STS spectra of Pd atoms in each position are shown in c). Adapted from reference [68].

growth [79]. In comparison, the NiAl(110) surface oxide has a reportedly low defect density and exhibits epitaxial growth along one direction [82].

The imperfections in oxide films are possibly their greatest limitation towards their widespread use. This is because defects usually interact relatively strongly with overlayer adsorbates, in turn modifying their functional properties. Even on the NiAl(110) surface oxide, the effect can be quite pronounced. For example, STS investigations of adatoms [68,80], metal clusters [85,86] and molecules [54] deposited onto this film reveal that the electronic states of the adsorbates can vary significantly, as shown by the STS spectra in Figure 1.8, depending on their position with respect to the film. This is taken as evidence for adsorbates coupling to different defects in the film, although this is challenging to prove given the difficulty encountered when trying to atomically resolve the surface of the oxide film with STM.

It is important to note that the use of inorganic layers in 'real world' applications will ultimately require that their growth conditions are well optimised.

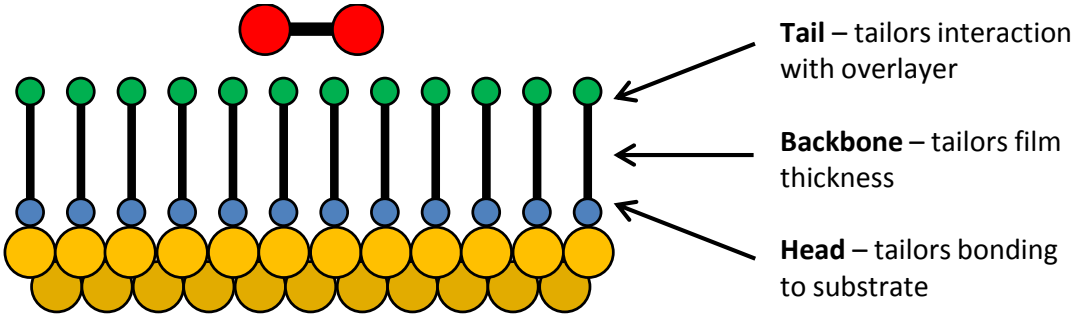

Figure 1.9 Three component model demonstrating the versatility of organic decoupling layers. The head and tail groups control the interaction between the decoupling layers and the substrate and overlayer adsorbates respectively. The backbone controls the thickness and the rigidity of the organic layer.

The low diffusion barriers of overlayer species, coupled with a preference for adsorbing on, or as near as possible to the metal surface [87-89] could result in differently decoupled adsorbates if non-uniform decoupling layers are used. This can be avoided by ensuring that the decoupling film covers the entire surface and is of uniform thickness.

1.4.3 Organic decoupling layers

As an alternative to inorganic decoupling layers, films of vertically-standing organic molecules are promising candidates [90]. In general, their properties are much more flexible, being easily tuned to their particular application through modifications to the molecular structure. To demonstrate this, the organic film can be considered in the context of a simple three-part model [91], which is illustrated in Figure 1.9.

At one terminus of the molecule is the ‘head group’ that binds to the metal. The strength of its interaction with the surface governs the films stability and the lateral mobility of each molecule within the film. Given the basic requirements of a decoupling film, it is desirable that the moiety binds sufficiently weakly such that the film can self-assemble with a low defect density, whilst still being adequately

anchored to prevent lateral displacement by overlayer adsorbates. Consequently, the head group has to be specifically tailored to the substrate being used.

At the other terminus is the ‘tail group’, which points away from the metal. The ‘organic surface’ created by a densely packed decoupling layer will consist of entirely this moiety, and therefore it determines the ultimate interaction with any overlayer adsorbates. With this approach, it should be possible to directly control the adsorption and assembly of overlayer species. For example, by using weakly interacting moieties, any perturbations to the overlayer assembly can be limited, if not prevented, allowing tecton-defined assembly to occur. In contrast, moieties that interact strongly with other organic molecules could be utilised in order to systematically modify overlayer assembly.

The final part of the model is the ‘molecular backbone’, which binds the two termini together. The backbone defines the thickness of the decoupling film and, consequently, the separation and resulting electronic interaction between the overlayer and the metal surface. It is also partially responsible for determining the packing of the molecular film. For example, long linear backbones in a vertically-standing monolayer can result in a highly crystalline film structure due to strong vdW attractions [91]. It may also be possible to modify the monolayer’s structure by including assembly-directing moieties into the backbone. However, it is important to note that the film packing is dependent on a number of factors, including the identity of the head and tail groups, and steric influences.

By far the most well-known example of vertically standing organic films are alkanethiol monolayers on Au(111). Their prominence is such that the term ‘self-assembled monolayer’ and its acronym ‘SAM’, which strictly refers to any single-

layer thick film that grows via self-assembly, have become almost exclusively synonymous with alkanethiol films on the Au(111) surface.

1.4.3.1 Alkanethiol decoupling films

Alkanethiol SAMs have been extensively investigated for a number of different possible applications, including organic electronics [92] , molecular switches [93], biocompatible surfaces [94,95], as insulating, functionalised supports [96,97], and many more [98]. They are an excellent example of the three-part model described above; the thiol moiety is the head group, the carbon chain is the backbone, and the tail group is whatever moiety is placed at the other molecule terminus. The vertically-standing geometry is achieved when a sufficiently high coverage is reached [99], a process driven by the strong thiol-metal bond. The vdW interactions between vertically-standing chains result in a densely-packed, highly-crystalline monolayer structure [91]. The alkanethiol head group actually interacts strongly with a number of different noble metals, and yet the vast majority of studies using alkanethiol SAMs have used the Au(111) surface. This is largely due to the high stability of Au(111) under ambient-environment conditions and because alkanethiol films can be easily prepared using solution processing [91,100], allowing their investigation outside of UHV conditions.

In the context of alkanethiol decoupling layers, two main strategies have been developed. The first, depicted in Figure 1.10a, is analogous to the inorganic decoupling films; the overlayer molecules are deposited on top of a pre-prepared SAM. In this approach, the tail moiety can be selected such that it selectively binds to, or inhibits the adsorption of, the overlayer species (Figure 1.10b). This has proven particularly successful in controlling the adhesion of biomolecules [94].

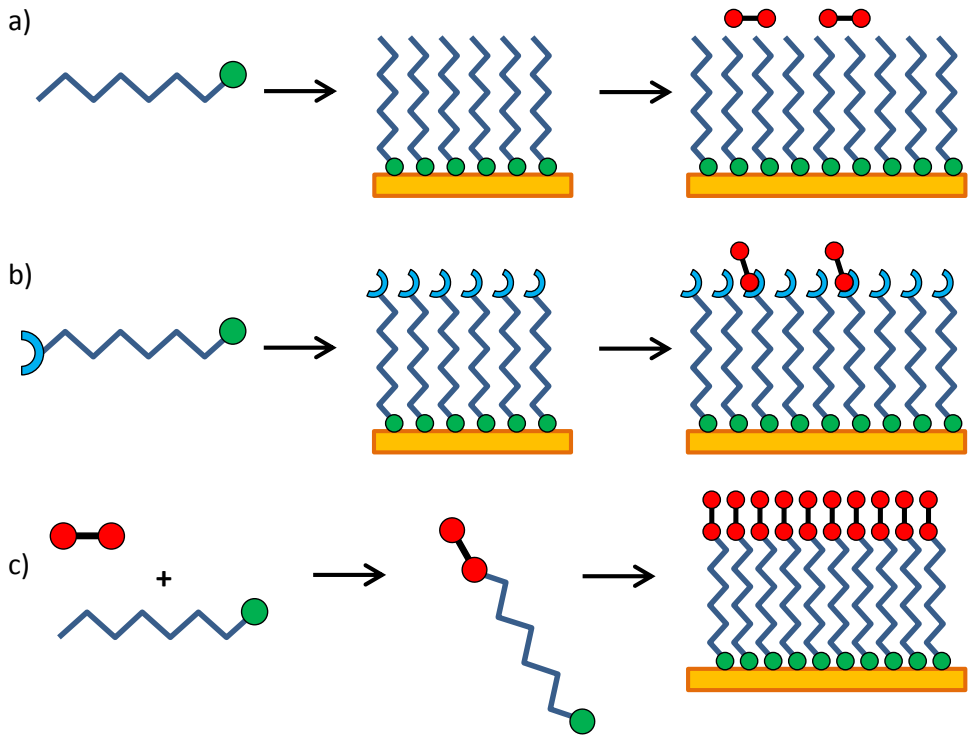

Figure 1.10 Schematics of the various ways in which alkanethiol films have been utilised as decoupling layers. In a), the functional species is deposited directly onto the alkanethiol film, whilst in b) the alkanethiol tail group is selected to specifically control the adsorption of the overlayer species. c) shows how a functional species can be functionalised with an alkanethiol chain prior to deposition on the metal surface.

Alternatively, in an approach conceptually similar to the molecular Lander system, the functional species is first functionalised with alkanethiol chains before their deposition onto the metal. The resulting SAM tail group is terminated with the functional moiety, as illustrated in Figure 1.10c [93,101]. In this way, the molecule is tethered directly to the surface.

1.5 Carboxylic acids on copper surfaces

Carboxylic acids have been suggested as a possible contender to alkanethiols due to their strong affinity for metal surfaces, in particular Cu. Moreover, a number of different carboxyl species have been reported to adsorb in an upright orientation on Cu, given suitable experimental conditions [90,102-105]. For a perpendicular

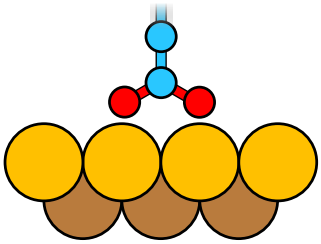

Figure 1.11 Depiction of the bidentate bonding motif of the deprotonated carboxyl moiety on a close-packed Cu surface.

geometry to be formed the acid moiety must first be deprotonated, which can readily occur when adsorbed upon sufficiently reactive Cu substrates. The resulting carboxylate moiety can then form a strong bidentate bond to the Cu, preferring adsorption along close-packed directions which closely match the O-O distance in the carboxylate moiety [102]. The resulting adsorption geometry is illustrated in Figure 1.11. When coupled with the use of rigid molecular backbones, this adsorption geometry should result in a strong correlation between the packing of vertically standing carboxylate films with the atomic-scale structure of the surface they are adsorbed upon.

The adsorption of a range of different carboxylic acids has already been investigated on Cu surfaces. A brief overview of their findings is given in the following, where the acids are simply classified as either ‘benzyl’ or ‘non-benzyl’, depending on the structure of the molecular backbone.

1.5.1 Benzyl acids on copper surfaces

The simplest benzyl carboxylic acid is benzoic acid, shown in Figure 1.12a. In the context of the three-part model described in Section 1.4.3, the tail group of a vertically standing benzoate is in fact a C-H moiety, which is likely to interact only very weakly with overlayer adsorbates. The benzyl backbone raises an interesting

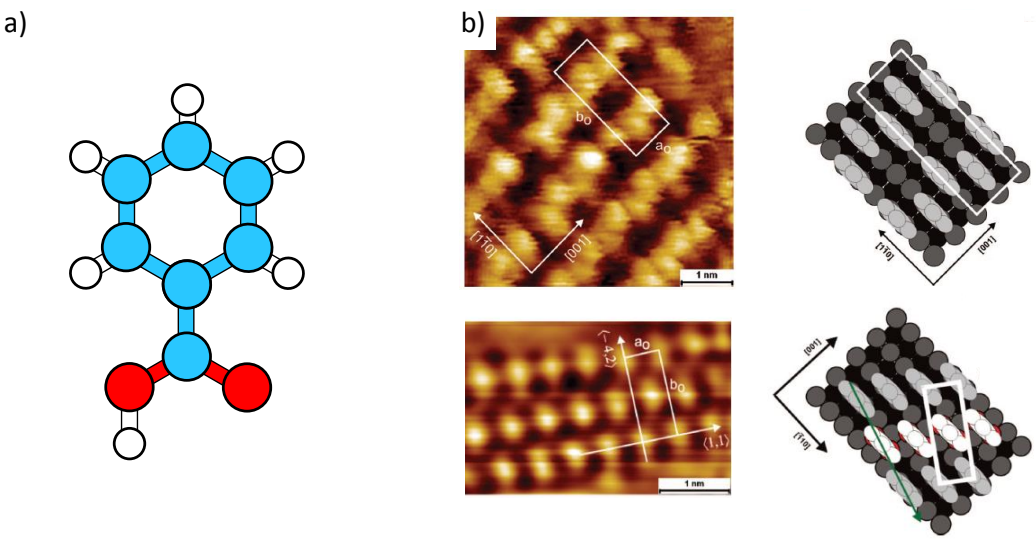

Figure 1.12 a) Schematic of benzoic acid. The blue, white and red represent carbon, hydrogen and oxygen respectively. b) STM images (left) and corresponding structures (right) of the benzoate structures on unreconstructed (top) and reconstructed (bottom) Cu(110) surfaces. Adapted from reference [108].

possibility in terms of enhancing the molecular packing of the decoupling layer; the highly conjugated backbone should cause the molecule to remain significantly rigid whilst the π-π interactions between neighbours should help to order the molecular film.

Vertically standing benzoate films have been reported on both the Cu(110) and Cu(111) surfaces. On Cu(110), two different upright phases are obtained, which differ in their molecular packing. In the first, the benzoates form a staggered-chain geometry [106], as revealed by the STM images and models in Figure 1.12b. The upright orientation was experimentally demonstrated using reflection-adsorption infra-red spectroscopy (RAIRS) [106] and an electron-stimulated ion angular distribution technique [107]. The second structure is obtained by annealing the first to high temperature, which also induces a reconstruction of the Cu substrate [108]. The resulting film is more densely packed, but its onset is accompanied by molecular

desorption that exposes regions of bare surface. The upright adsorption geometry is inferred, most likely, from their appearance in the STM images.

In all, only the first of the two phases – which has a c(8×2) superstructure – is an appropriate choice as a decoupling layer. However, its fabrication is in fact reasonably complex, involving a number of different phases that are formed prior to the c(8×2). At low molecular coverage, RAIRS and STM measurements indicate that the benzoate adsorb in a flat-lying geometry in a structure containing both benzoate and coordinated Cu adatoms [106,109]. Upon completion of this phase, additional molecules adsorb in an upright geometry in gaps in the flat-lying phase, and then subsequently *on top* of the flat-lying monolayer. The structure of this on-top layer is directed, or 'templated', by the flat-lying underlayer. Only when sufficient coverage is reached do the molecules reorganise into the c(8×2) phase, where all benzoates are adsorbed perpendicular to the surface.

The assembly of benzoic acid on Cu(111) has been studied comparatively less than on Cu(110), but does appear to be relatively simpler. RAIRS and Raman spectroscopy reveal that, at all coverages, benzoic acid is deprotonated and adsorbs perpendicularly to the surface [110, 111]. The difference in adsorption behaviour has been rationalised based on the relative concentration of adatoms on the two Cu faces at a given temperature, which appears to be critical for stabilising the flat-lying adsorption geometry.

The propensity of benzoate to adsorb in a flat-lying orientation on Cu(110) would complicate its use in a decoupling film. Similar benzene-containing acids, such as terephthalic acid (TPA) [90] have been suggested as alternatives, but, as will be demonstrated in Chapter 3, these can also form complex flat-lying phases. Moreover, the inclusion of the benzene moiety in the backbone makes the molecule

relatively long and therefore the decoupling film relatively thick [102,112]. This may prove to limit charge transfer to and from overlayer species.

1.5.2 Non-benzyl acids on copper

Formic and acetic acid, shown in Figure 1.13a, are perhaps the two shortest and simplest carboxylic acids and are also possible prototype molecules with which to make decoupling layers. Both molecules are readily deprotonated when adsorbed upon room temperature (RT) Cu substrates, although there is some evidence that the low reactivity and the reduced adatom population of Cu(111) at RT makes deposition more challenging [110,113]. A wide range of different techniques has been used to probe their adsorption geometry. For example, an upright orientation has been confirmed for formate on Cu(110) and Cu(111) using RAIRS and near-edge X-ray adsorption fine structure (NEXAFS) measurements [114-116], whereas photoelectron diffraction and normal incidence X-ray standing wavefield adsorption have established a similar arrangement for acetate [117,118]. In this geometry, the two films have thicknesses more appropriate for decoupling layers, approximately 3.8 Å and 4.5 Å respectively [118,119].

On Cu(110), formic acid forms $[1\bar{1}0]$-oriented rows, separated by 2× the $[001]$ periodicity [120]. No molecular resolution has been achieved of this structure, but it is believed the formate also form a 2× periodicity along the $[1\bar{1}0]$ direction. This results in an overall (2×2) superstructure, which is shown in Figure 1.13b. A more densely-packed c(2×2) structure, depicted in Figure 1.13c, is obtained when the surface is pre-dosed with O [121]. The O-(2×1) structure resulting from this pre-dosing [122] is thought to provide two benefits: Firstly, reaction between the released formic acid protons and the O results in the formation and desorption of

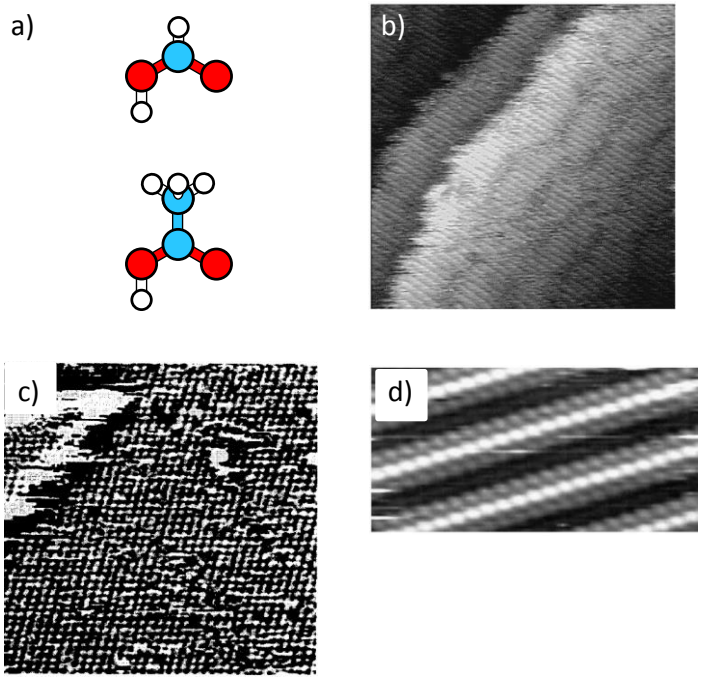

Figure 1.13 a) Schematic of formic acid (top) and acetic acid (bottom). b) STM image of the (2×2) formate structure on the Cu(110) surface. Adapted from reference [120]. c) STM image of the c(2×2) formate structure formed on the O-precovered Cu(110) surface. Adapted from reference [104]. d) STM image of the acetic acid chains obtained on the Cu(110) surface. Adapted from reference [130].

H_2O, providing a greater energetic benefit towards formic acid adsorption and deprotonation [120]. Secondly, the O-(2×1) structure contains Cu adatoms, which are released by the removal of the O atoms. These adatoms are 'consumed' by the formate [123,124], suggesting that the more densely-packed formate layer is adsorbed upon a reconstructed substrate, as was reported for the benzoate/Cu(110) system [108].

Adsorption of formic acid on the Cu(111) surface is reported to not be favourable at RT. To circumvent this, it is possible to first physisorb the molecule at low temperature (LT) and then anneal to higher temperatures to induce deprotonation [116,125]. Alternatively, formate can be synthesised directly on the substrate through decomposition of larger species [126,127] or through the chemical reaction of CO_2 and H_2 [25,128]. At low coverages, the formate arrange in 1D

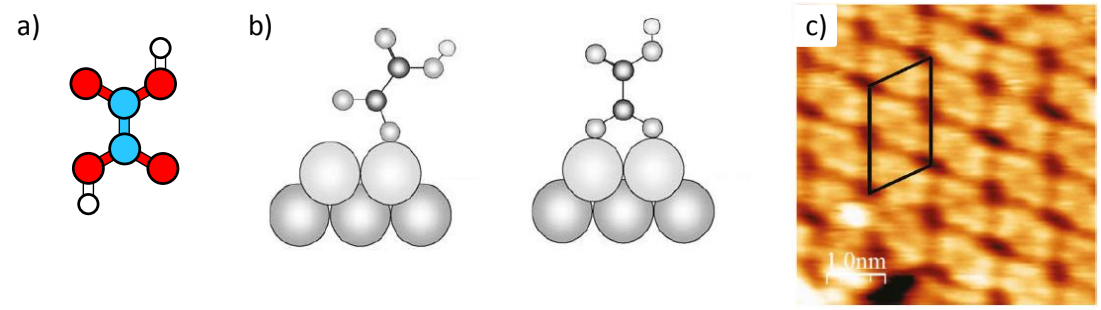

Figure 1.14 a) Schematic of oxalic acid. b) The tilting and bidentate adsorption geometries of oxalic acid identified on the Cu(110) surface. Adapted from reference [103]. c) STM image of the flat-lying oxalate structure reported on Cu(111). Adapted from reference [127].

chains, similar to those reported on Cu(110). At higher density, a range of different 2D structures can be constructed, depending on the formate coverage and the presence of pre-adsorbed O [25].

In comparison to formic acid, acetic acid has received comparably less attention. Only its assembly on Cu(110) has been studied in detail, where again the substrate adatoms are used to create a local reconstruction. On a clean surface, the acetate initially adsorb in stripes oriented along the $[1\bar{1}2]$ directions (critically, not a main crystallographic direction), which are three molecules wide [105,129] (Figure 1.13d). When deposited onto an O pre-treated Cu(110), deposition of acetic acid results in the formation of wider molecular stripes and eventually a densely packed film with c(2×2) symmetry [105].

The dense c(2×2) phases of the formate and acetate monolayers are both strong candidates for organic decoupling layers. However, both structures require pre-adsorbed O on the surface else only low density monolayers are formed. In contrast, oxalic acid (OA), shown in Figure 1.14a, has been demonstrated using low-energy electron diffraction (LEED) to pack in a dense c(2×2) superstructure on Cu(110) without the need for pre-adsorbed O [103]. RAIRS measurements show that OA also adsorbs in an approximately upright orientation; at low coverage, a tilted

unidentate-bonding motif is reported, whilst at saturation coverage a vertical, bidentate adsorption geometry is obtained (Figure 1.14b). Moreover, the RAIRS measurements suggest that the OA does not adsorb in a flat-lying orientation prior to the formation of an upright phase. An additional benefit of OA is that the resulting carboxylic-terminated organic surface should interact relatively strongly with overlayer adsorbates [130,131], thus making it an excellent starting point with which to explore organic decoupling layers and their potential effect of overlayer self-assembly.

Perhaps the only potential disadvantage to using OA monolayers as decoupling films is that a radically different assembly has been reported on Cu(111) [126]. This phase is discussed in detail in Chapter 4, but a short summary is in order. Initial adsorption results in decomposition of OA into formate chains that are localised at steps. Further deposition reveals a structure with rhomboidal symmetry, containing fully-deprotonated OA in a flat-lying monolayer, which is shown in Figure 1.14c. The OA is reported to be stabilised by MO bonding with Cu adatoms.

From the above, it is hopefully clear that whilst a number of different organic species could make suitable decoupling layers, OA is a strong candidate with which to begin. Therefore, it is the aim of this work to investigate its use in this direction. Firstly, the assembly of OA on the Cu(110) and Cu(111) surfaces will be investigated in detail, with a focus on the OA adsorption geometry. After this, the ability of OA films to support overlayers will be addressed by depositing a prototype organic overlayer on top.

1.6 Structure of thesis

This thesis is split into six chapters, with this introduction being the first. In Chapter 2, the different experimental and theoretical techniques used in this work are described in detail. The following three chapters present their findings:

In Chapter 3, the adsorption and assembly of TPA, an archetypal organic tecton, has been explored on both the Cu(110) and Cu(111) surfaces, at coverages where only flat-lying phases are observed. These systems have been studied to demonstrate how the substrate can play a dominant role in adsorbate assembly. Furthermore, these measurements act as a reference for later studies of TPA on top of OA decoupling layers, to understand if and how the assembly of the overlayer is modified by the overlayer-decoupling layer interaction.

In Chapter 4, the adsorption and assembly of OA on Cu(110) and Cu(111) is described. The structures of the two films obtained correlate strongly with that of the metal surfaces, whereas the local adsorption geometries appear to be very different. The two decoupling layers also exhibit a number of localised phenomena that have a direct impact on their effectiveness at supporting overlayers. This will be discussed further in Chapter 5, where the results of TPA deposition on top of the OA films are presented.

Finally, in Chapter 6, the conclusions of the three results chapters are summarised and a series of future experiments are outlined that should provide more detail and scope to the work in this thesis.

1.7 Chapter 1 references

1. Barth, J.V., G. Costantini, and K. Kern, *Engineering atomic and molecular nanostructures at surfaces.* Nature, 2005. **437**(7059): p. 671-679.
2. Gates, B.D., et al., *New Approaches to Nanofabrication: Molding, Printing, and Other Techniques.* Chemical Reviews, 2005. **105**(4): p. 1171-1196.
3. Lehn, J.-M., *Supramolecular Chemistry—Scope and Perspectives Molecules, Supermolecules, and Molecular Devices (Nobel Lecture).* Angewandte Chemie International Edition in English, 1988. **27**(1): p. 89-112.
4. De Feyter, S. and F.C. De Schryver, *Two-dimensional supramolecular self-assembly probed by scanning tunneling microscopy.* Chemical Society Reviews, 2003. **32**(3): p. 139-150.
5. Franc, G. and A. Gourdon, *Covalent networks through on-surface chemistry in ultra-high vacuum: state-of-the-art and recent developments.* Physical Chemistry Chemical Physics, 2011. **13**(32): p. 14283-14292.
6. Barth, J.V., *Fresh perspectives for surface coordination chemistry.* Surface Science, 2009. **603**(10–12): p. 1533-1541.
7. Pawin, G., et al., *A Surface Coordination Network Based on Substrate-Derived Metal Adatoms with Local Charge Excess.* Angewandte Chemie International Edition, 2008. **47**(44): p. 8442-8445.
8. Matena, M., et al., *Aggregation and Contingent Metal/Surface Reactivity of 1,3,8,10-Tetraazaperopyrene (TAPP) on Cu(111).* Chemistry – A European Journal, 2010. **16**(7): p. 2079-2091.
9. Sirtl, T., et al., *Control of Intermolecular Bonds by Deposition Rates at Room Temperature: Hydrogen Bonds versus Metal Coordination in Trinitrile Monolayers.* Journal of the American Chemical Society, 2012. **135**(2): p. 691-695.
10. Brown, D.E., D.J. Moffatt, and R.A. Wolkow, *Isolation of an Intrinsic Precursor to Molecular Chemisorption.* Science, 1998. **279**(5350): p. 542-544.
11. Soe, W.H., et al., *Direct Observation of Molecular Orbitals of Pentacene Physisorbed on Au(111) by Scanning Tunneling Microscope.* Physical Review Letters, 2009. **102**(17): p. 176102.
12. Bazarnik, M., et al., *Light driven reactions of single physisorbed azobenzenes.* Chemical Communications, 2011. **47**(27): p. 7764-7766.
13. Classen, T., et al., *Hydrogen and Coordination Bonding Supramolecular Structures of Trimesic Acid on Cu(110).* The Journal of Physical Chemistry A, 2007. **111**(49): p. 12589-12603.
14. Fuhr, J.D., et al., *Interplay between Hydrogen Bonding and Molecule–Substrate Interactions in the Case of Terephthalic Acid Molecules on Cu(001) Surfaces.* The Journal of Physical Chemistry C, 2012. **117**(3): p. 1287-1296.
15. Zambelli, T., et al., *Conformations of a long molecular wire with legs on a Cu(100) surface.* Chemical Physics Letters, 2001. **348**(1-2): p. 1-6.
16. Tseng, T.-C., et al., *Charge-transfer-induced structural rearrangements at both sides of organic/metal interfaces.* Nat Chem, 2010. **2**(5): p. 374-379.
17. Leibsle, F.M., et al., *Molecularly induced step faceting on Cu(110) surfaces.* Surface Science, 1995. **343**(3): p. L1175-L1181.
18. Munoz-Marquez, M.A., et al., *N-induced pseudo-(100) reconstruction of Cu(111): One layer or more?* Surface Science, 2005. **582**(1-3): p. 97-109.

19. Nenchev, G., et al., *Self-assembly of methanethiol on the reconstructed Au(111) surface.* Physical Review B, 2009. **80**(8): p. 081401.
20. Grill, L., et al., *Nano-architectures by covalent assembly of molecular building blocks.* Nature Nanotechnology, 2007. **2**(11): p. 687-691.
21. Arachchilage, A.P.W., et al., *Photoelectron spectra and structures of three cyclic dipeptides: PhePhe, TyrPro, and HisGly.* The Journal of Chemical Physics, 2012. **136**(12): p. 124301.
22. Moreton, B., et al., *Dissociation and hierarchical assembly of chiral esters on metallic surfaces.* Chemical Communications, 2013. **49**(58): p. 6477-6479.
23. de Oteyza, D.G., et al., *Direct Imaging of Covalent Bond Structure in Single-Molecule Chemical Reactions.* Science, 2013. **340**(6139): p. 1434-1437.
24. Francis, S.M., et al., *Methanol Oxidation on Cu(110).* Surface Science, 1994. **315**(3): p. 284-292.
25. Fujitani, T., et al., *Scanning Tunneling Microscopy Study of Formate Species Synthesized from CO2 Hydrogenation and Prepared by Adsorption of Formic Acid over Cu(111).* The Journal of Physical Chemistry B, 2000. **104**(6): p. 1235-1240.
26. Chavy, C., C. Joachim, and A. Altibelli, *Interpretation of STM images: C60 on the gold (110) surface.* Chemical Physics Letters, 1993. **214**(6): p. 569-575.
27. Fisher, A.J. and P.E. Blöchl, *Adsorption and scanning-tunneling-microscope imaging of benzene on graphite and MoS_2.* Physical Review Letters, 1993. **70**(21): p. 3263-3266.
28. Joachim, C., et al., *Electronic Transparence of a Single C60 Molecule.* Physical Review Letters, 1995. **74**(11): p. 2102-2105.
29. Pascual, J.I., et al., *Seeing molecular orbitals.* Chemical Physics Letters, 2000. **321**(1–2): p. 78-82.
30. Moresco, F. and A. Gourdon, *Scanning tunneling microscopy experiments on single molecular landers.* Proceedings of the National Academy of Sciences of the United States of America, 2005. **102**(25): p. 8809-8814.
31. Repp, J. and G. Meyer, *Scanning tunneling microscopy of adsorbates on insulating films. From the imaging of individual molecular orbitals to the manipulation of the charge state.* Applied Physics a-Materials Science & Processing, 2006. **85**(4): p. 399-406.
32. Villagomez, C.J., et al., *A local view on hyperconjugation.* Chemical Physics Letters, 2007. **450**(1–3): p. 107-111.
33. Smerdon, J.A., et al., *Monolayer and bilayer pentacene on Cu(111).* Physical Review B, 2011. **84**(16): p. 165436.
34. Bardeen, J., *Electron Correlation and Screening Effects - In Relation to Surface Physics.* Surface Science, 1964. **2**: p. 381-388.
35. Ishii, H., et al., *Energy level alignment and interfacial electronic structures at organic metal and organic organic interfaces.* Advanced Materials, 1999. **11**(8): p. 605-625.
36. Binnig, G., et al., *Surface Studies by Scanning Tunneling Microscope.* Physical Review Letters, 1982. **49**(1): p. 57-61.
37. Binnig, G. and H. Rohrer, *Scanning Tunneling Microscopy—from Birth to Adolescence (Nobel Lecture).* Angewandte Chemie International Edition in English, 1987. **26**(7): p. 606-614.

38. Wu, S.W., N. Ogawa, and W. Ho, *Atomic-Scale Coupling of Photons to Single-Molecule Junctions.* Science, 2006. **312**(5778): p. 1362-1365.
39. Hipps, K.W., *Scanning Tunneling Spectroscopy (STS)*, in *Handbook of Applied Solid State Spectroscopy*, D.R. Vij, Editor. 2006, Springer US. p. 305-350.
40. Wu, S.W., et al., *Control of Relative Tunneling Rates in Single Molecule Bipolar Electron Transport.* Physical Review Letters, 2004. **93**(23): p. 236802.
41. Repp, J., et al., *Molecules on insulating films: Scanning-tunneling microscopy imaging of individual molecular orbitals.* Physical Review Letters, 2005. **94**(2): p. 026803.
42. Liljeroth, P., J. Repp, and G. Meyer, *Current-Induced Hydrogen Tautomerization and Conductance Switching of Naphthalocyanine Molecules.* Science, 2007. **317**(5842): p. 1203-1206.
43. Liljeroth, P., et al., *Single-Molecule Synthesis and Characterization of Metal−Ligand Complexes by Low-Temperature STM.* Nano Letters, 2010. **10**(7): p. 2475-2479.
44. Mohn, F., et al., *Reversible Bond Formation in a Gold-Atom–Organic-Molecule Complex as a Molecular Switch.* Physical Review Letters, 2010. **105**(26): p. 266102.
45. Gross, L., et al., *High-Resolution Molecular Orbital Imaging Using a p-Wave STM Tip.* Physical Review Letters, 2011. **107**(8): p. 086101.
46. Swart, I., T. Sonnleitner, and J. Repp, *Charge State Control of Molecules Reveals Modification of the Tunneling Barrier with Intramolecular Contrast.* Nano Letters, 2011. **11**(4): p. 1580-1584.
47. Qiu, X.H., G.V. Nazin, and W. Ho, *Vibronic States in Single Molecule Electron Transport.* Physical Review Letters, 2004. **92**(20): p. 206102.
48. Repp, J., et al., *Imaging bond formation between a gold atom and pentacene on an insulating surface.* Science, 2006. **312**(5777): p. 1196-1199.
49. Halasinski, T.M., et al., *Electronic Absorption Spectra of Neutral Pentacene (C22H14) and Its Positive and Negative Ions in Ne, Ar, and Kr Matrices.* The Journal of Physical Chemistry A, 2000. **104**(32): p. 7484-7491.
50. Repp, J., et al., *Controlling the Charge State of Individual Gold Adatoms.* Science, 2004. **305**(5683): p. 493-495.
51. Olsson, F.E., et al., *Multiple Charge States of Ag Atoms on Ultrathin NaCl Films.* Physical Review Letters, 2007. **98**(17): p. 176803.
52. Gross, L., et al., *Measuring the Charge State of an Adatom with Noncontact Atomic Force Microscopy.* Science, 2009. **324**(5933): p. 1428-1431.
53. Rossel, F., M. Pivetta, and W.-D. Schneider, *Luminescence experiments on supported molecules with the scanning tunneling microscope.* Surface Science Reports, 2010. **65**(5): p. 129-144.
54. Qiu, X., G. Nazin, and W. Ho, *Vibrationally resolved fluorescence excited with submolecular precision.* Science, 2003. **299**(5606): p. 542-546.
55. Avouris, P. and B.N.J. Persson, *Excited states at metal surfaces and their non-radiative relaxation.* The Journal of Physical Chemistry, 1984. **88**(5): p. 837-848.
56. Barnes, W.L., *Fluorescence near interfaces: The role of photonic mode density.* Journal of Modern Optics, 1998. **45**(4): p. 661-699.

57. Ćavar, E., et al., *Fluorescence and Phosphorescence from Individual C60 Molecules Excited by Local Electron Tunneling.* Physical Review Letters, 2005. **95**(19): p. 196102.
58. Wu, S.W., G.V. Nazin, and W. Ho, *Intramolecular photon emission from a single molecule in a scanning tunneling microscope.* Physical Review B, 2008. **77**(20): p. 205430.
59. Kabakchiev, A., et al., *Electroluminescence from Individual Pentacene Nanocrystals.* ChemPhysChem, 2010. **11**(16): p. 3412-3416.
60. Gopakumar, T.G., et al., *Coverage-Driven Electronic Decoupling of Fe-Phthalocyanine from a Ag(111) Substrate.* Journal of Physical Chemistry C, 2011. **115**(24): p. 12173-12179.
61. Franke, K., et al., *Reducing the molecule-substrate coupling in C-60-based nanostructures by molecular interactions.* Physical Review Letters, 2008. **100**(3): p. 036807.
62. Gourdon, A., *Synthesis of "Molecular Landers".* European Journal of Organic Chemistry, 1998. **1998**(12): p. 2797-2801.
63. Rosei, F., et al., *Organic Molecules Acting as Templates on Metal Surfaces.* Science, 2002. **296**(5566): p. 328-331.
64. Gross, L., et al., *Trapping and moving metal atoms with a six-leg molecule.* Nat Mater, 2005. **4**(12): p. 892-895.
65. Yu, M., et al., *Self-assembly of hydrogen-bonded chains of molecular landers.* Chemical Communications, 2010. **46**(30): p. 5545-5547.
66. Yu, M., et al., *Supramolecular Architectures on Surfaces Formed through Hydrogen Bonding Optimized in Three Dimensions.* ACS Nano, 2010. **4**(7): p. 4097-4109.
67. Schintke, S., et al., *Insulator at the ultrathin limit: MgO on Ag(001).* Physical Review Letters, 2001. **87**(27): p. 276801.
68. Nilius, N., T.M. Wallis, and W. Ho, *Influence of a Heterogeneous Al_2O_3 Surface on the Electronic Properties of Single Pd Atoms.* Physical Review Letters, 2003. **90**(4): p. 046808.
69. Schwennicke, C., J. Schimmelpfennig, and H. Pfnür, *Morphology of thin NaCl films grown epitaxially on Ge(100).* Surface Science, 1993. **293**(1–2): p. 57-66.
70. Hebenstreit, W., et al., *Atomic resolution by STM on ultra-thin films of alkali halides: experiment and local density calculations.* Surface Science, 1999. **424**(2-3): p. L321-L328.
71. Fölsch, S., et al., *Self-Organized Patterning of an Insulator-on-Metal System by Surface Faceting and Selective Growth: NaCl/Cu(211).* Physical Review Letters, 2000. **84**(1): p. 123-126.
72. Sun, X., et al., *NaCl multi-layer islands grown on Au(111)-(22 x √3) probed by scanning tunneling microscopy.* Nanotechnology, 2008. **19**(49): p. 495307.
73. Le Moal, E., et al., *Misfit driven azimuthal orientation of NaCl domains on Ag(100).* Surface Science, 2009. **603**(16): p. 2434-2444.
74. Bennewitz, R., *Structured surfaces of wide band gap insulators as templates for overgrowth of adsorbates.* Journal of Physics-Condensed Matter, 2006. **18**(26): p. R417-R435.
75. Fölsch, S., A. Helms, and K.H. Rieder, *Epitaxy of ionic insulators on a vicinal metal substrate: KCl and RbI on Cu(211).* Applied Surface Science, 2000. **162–163**(0): p. 270-274.

76. Hebenstreit, W., et al., *Bulk Terminated NaCl(111) on Aluminum: A Polar Surface of an Ionic Crystal?* Physical Review Letters, 2000. **85**(25): p. 5376-5379.
77. Mauch, I., G. Kaindl, and A. Bauer, *Formation of NaCl stripes on Cu(100).* Surface Science, 2003. **522**(1–3): p. 27-33.
78. Repp, J., et al., *Scanning Tunneling Spectroscopy of Cl Vacancies in NaCl Films: Strong Electron-Phonon Coupling in Double-Barrier Tunneling Junctions.* Physical Review Letters, 2005. **95**(22): p. 225503.
79. Freund, H.-J. and G. Pacchioni, *Oxide ultra-thin films on metals: new materials for the design of supported metal catalysts.* Chemical Society Reviews, 2008. **37**(10): p. 2224-2242.
80. Heinrich, A.J., et al., *Single-Atom Spin-Flip Spectroscopy.* Science, 2004. **306**(5695): p. 466-469.
81. Wu, S.W., et al., *Conductance Hysteresis and Switching in a Single-Molecule Junction.* The Journal of Physical Chemistry C, 2008. **112**(14): p. 5241-5244.
82. Libuda, J., et al., *Structure and defects of an ordered alumina film on NiAl(110).* Surface Science, 1994. **318**(1–2): p. 61-73.
83. Stierle, A., et al., *X-ray Diffraction Study of the Ultrathin Al_2O_3 Layer on NiAl(110).* Science, 2004. **303**(5664): p. 1652-1656.
84. Kresse, G., et al., *Structure of the ultrathin aluminum oxide film on NiAl(110).* Science, 2005. **308**(5727): p. 1440-1442.
85. Hansen, K.H., et al., *Palladium Nanocrystals on Al_2O_3: Structure and Adhesion Energy.* Physical Review Letters, 1999. **83**(20): p. 4120-4123.
86. Nilius, N., N. Ernst, and H.J. Freund, *Photon Emission Spectroscopy of Individual Oxide-Supported Silver Clusters in a Scanning Tunneling Microscope.* Physical Review Letters, 2000. **84**(17): p. 3994.
87. Ramoino, L., et al., *Layer-selective epitaxial self-assembly of porphyrins on ultrathin insulators.* Chemical Physics Letters, 2006. **417**(1-3): p. 22-27.
88. Bombis, C., et al., *Hydrogen-Bonded Molecular Networks of Melamine and Cyanuric Acid on Thin Films of NaCl on Au(111).* Small, 2009. **5**(19): p. 2177-2182.
89. Cañas-Ventura, M.E., et al., *Stabilization of bimolecular islands on ultrathin NaCl films by a vicinal substrate.* Surface Science, 2009. **603**(15): p. 2294-2299.
90. Martin, D., R. Cole, and S. Haq, *Creating a functionalized surface: The adsorption of terephthalic acid onto Cu(110).* Physical Review B, 2002. **66**(15): p. 155427.
91. Love, J.C., et al., *Self-Assembled Monolayers of Thiolates on Metals as a Form of Nanotechnology.* Chemical Reviews, 2005. **105**(4): p. 1103-1170.
92. Bock, C., et al., *Improved morphology and charge carrier injection in pentacene field-effect transistors with thiol-treated electrodes.* Journal of Applied Physics, 2006. **100**(11): p. 114517.
93. Simao, C., et al., *A robust molecular platform for non-volatile memory devices with optical and magnetic responses.* Nature Chemistry, 2011. **3**(5): p. 359-364.
94. Prime, K.L. and G.M. Whitesides, *Self-Assembled Organic Monolayers: Model Systems for Studying Adsorption of Proteins at Surfaces.* Science, 1991. **252**(5009): p. 1164-1167.
95. Mrksich, M. and G.M. Whitesides, *Using self-assembled monolayers to understand the interactions of man-made surfaces with proteins and cells.*

Annual Review of Biophysics and Biomolecular Structure, 1996. **25**: p. 55-78.
96. Silien, C., et al., *Electrodeposition of Palladium onto a Pyridine-Terminated Self-Assembled Monolayer.* Langmuir, 2011. **27**(6): p. 2567-2574.
97. Zhang, X.L., et al., *Fluorescence decay of quasimonolayered porphyrins near a metal surface separated by short-chain alkanethiols.* Applied Physics Letters, 2008. **92**(22): p. 223118-223118.
98. Schreiber, F., *Self-assembled monolayers: from 'simple' model systems to biofunctionalized interfaces.* Journal of Physics-Condensed Matter, 2004. **16**(28): p. R881-R900.
99. Poirier, G.E. and E.D. Pylant, *The Self-Assembly Mechanism of Alkanethiols on Au(111).* Science, 1996. **272**(5265): p. 1145-1148.
100. Xu, S., et al., *In situ studies of thiol self-assembly on gold from solution using atomic force microscopy.* Journal of Chemical Physics, 1998. **108**(12): p. 5002-5012.
101. Han, M., et al., *Light-driven molecular switches in azobenzene self-assembled monolayers: effect of molecular structure on reversible photoisomerization and stable cis state.* Chemical Communications, 2010. **46**(20): p. 3598-3600.
102. Pascal, M., et al., *Quantitative structural determination of the high coverage phase of the benzoate species on Cu(1 1 0).* Surface Science, 2001. **492**(3): p. 285-293.
103. Martin, D., R. Cole, and S. Haq, *Investigating the adsorption of oxalic acid onto Cu(110) to create a chemically functionalised surface.* Surface Science, 2003. **539**(1-3): p. 171-181.
104. Bowker, M., et al., *The adsorption and decomposition of formic acid on Cu{110}.* Surface Science, 1996. **349**(2): p. 97-110.
105. York, S.M., et al., *STM, FTIR and quantum chemical calculation studies of acetate structures on Cu(110) surfaces.* Surface Science, 2003. **522**(1-3): p. 34-46.
106. Frederick, B.G., et al., *Evolution of Lateral Order and Molecular Reorientation in the Benzoate/Cu(110) System.* Surface Review and Letters, 1996. **03**(04): p. 1523-1546.
107. Lee, J., O. Kuzmych, and J.T. Yates, *Adsorption and geometry of the chemisorbed benzoate species on Cu(110).* Surface Science, 2005. **582**(1-3): p. 117-124.
108. Lennartz, M.C., et al., *Cu-Adatom-Mediated Bonding in Close-Packed Benzoate/Cu(110)-Systems.* Langmuir, 2008. **25**(2): p. 856-864.
109. Dougherty, D.B., P. Maksymovych, and J.T. Yates, Jr., *Direct STM evidence for Cu-benzoate surface complexes on Cu(110).* Surface Science, 2006. **600**(19): p. 4484-4491.
110. Perry, C.C., et al., *Face specificity and the role of metal adatoms in molecular reorientation at surfaces.* Surface Science, 1998. **409**(3): p. 512-520.
111. Ivanecky, J.E., C.M. Child, and A. Campion, *Surface-chemistry of polyimide precursors on Cu(111).* Surface Science, 1995. **325**(3): p. L428-L434.
112. Atodiresei, N., K. Schroeder, and S. Blügel, *Density-functional theory study on the arrangement of adsorbed formate molecules on Cu(110).* Physical Review B, 2007. **75**(11): p. 115407.

113. Lin, N., et al., *Two-dimensional adatom gas bestowing dynamic heterogeneity on surfaces.* Angewandte Chemie-International Edition, 2005. **44**(10): p. 1488-1491.
114. Hayden, B.E., et al., *An iras study of formic acid and surface formate adsorbed on Cu(110).* Surface Science, 1983. **133**(2–3): p. 589-604.
115. Puschmann, A., et al., *Structure determination of the formate intermediate on Cu(110) by use of X-ray-Adsorption Fine-Structure Measurements.* Physical Review Letters, 1985. **54**(20): p. 2250-2252.
116. Baber, A.E., et al., *Assisted Deprotonation of Formic Acid on Cu(111) and Self Assembly of 1D Chains.* Physical Chemistry Chemical Physics, 2013. **15**(29): p. 12291-12298.
117. Weiss, K.U., et al., *Chemical-shift photoelectron diffraction from molecular adsorbates.* Physical Review Letters, 1992. **69**(22): p. 3196-3199.
118. Johnston, S.M., et al., *The structure of acetate and trifluoroacetate on Cu(111).* Surface Science, 2001. **477**(2-3): p. 163-173.
119. Gomes, J.R.B. and J.A.N.F. Gomes, *Adsorption of the formate species on copper surfaces: a DFT study.* Surface Science, 1999. **432**(3): p. 279-290.
120. Poulston, S., et al., *STM study of formic acid adsorption on Cu(110).* Physical Review B, 1997. **55**(19): p. 12888-12891.
121. Bowker, M., et al., *The adsorption and decomposition of formic acid on Cu(110).* Surface Science, 1996. **349**(2): p. 97-110.
122. Kern, K., et al., *Long-range spatial self-organization in the adsorbate-induced restructuring of surfaces - Cu(110)-(2x1)O.* Physical Review Letters, 1991. **67**(7): p. 855-858.
123. Bowker, M., et al., *A combined STM/molecular beam study of formic acid oxidation on Cu(110).* Journal of Molecular Catalysis A: Chemical, 1998. **131**(1–3): p. 185-197.
124. Bennett, R.A., S. Poulston, and M. Bowker, *Elevated temperature scanning tunneling microscopy study of formic acid adsorption and reaction on oxygen (2x1) covered Cu(110).* Journal of Chemical Physics, 1998. **108**(16): p. 6916-6922.
125. Sotiropoulos, A., et al., *A structural study of formate on Cu(111).* Surface Science, 2000. **444**(1–3): p. 52-60.
126. Faraggi, M.N., et al., *Role of Deprotonation and Cu Adatom Migration in Determining the Reaction Pathways of Oxalic Acid Adsorption on Cu(111).* The Journal of Physical Chemistry C, 2011. **115**(43): p. 21177-21182.
127. Otero, R., et al., *Molecular Self-Assembly at Solid Surfaces.* Advanced Materials, 2011. **23**(44): p. 5148-5176.
128. Nakamura, J., et al., *X-ray photoelectron spectroscopy and scanning tunnel microscope studies of formate species synthesized on Cu(111) surfaces.* Journal of Vacuum Science & Technology A, 1997. **15**(3): p. 1568-1571.
129. Haq, S. and F.M. Leibsle, *Acetate on Cu(110): evidence for long-range intermolecular interactions and molecular-induced restructuring of a metal surface.* Surface Science, 1996. **355**(1–3): p. L345-L349.
130. Herdt, G.C., D.R. Jung, and A.W. Czanderna, *Penetration of deposited Ag and Cu overlayers through alkanethiol self-assembled monolayers on gold.* Journal of Adhesion, 1997. **60**(1-4): p. 197-222.
131. Zhu, Z., et al., *Controlling Gold Atom Penetration through Alkanethiolate Self-Assembled Monolayers on Au{111} by Adjusting Terminal Group*

Intermolecular Interactions. Journal of the American Chemical Society, 2006. **128**(42): p. 13710-13719.

Chapter 2

Experimental and theoretical methods

This chapter describes the various experimental and theoretical techniques used in this work. Firstly, the fundamental aspects of the different characterisation methods are explained. After this, the fabrication procedures utilised to synthesise the different organic structures are outlined, alongside a detailed description of the experimental apparatus used for the majority of this work. Where appropriate, the specific devices and their relevant parameters are also listed. In some cases, such as the RT-STM characterisation of TPA on Cu(110) and the various synchrotron-based measurements, different systems have been utilised, but their underlying working principles are the same.

All of the experimental procedures outlined in this work have been performed in UHV, defined as a pressure $<1\times10^{-9}$ mbar. Whilst this imparts strict conditions and requires cumbersome experimental apparatus, it does also grant numerous benefits, many of which are critical for the study of the fundamental properties of molecule-on-metal systems. Perhaps the most important motivation is the need to maintain a high level of control over the sample cleanliness. In a first approximation [1], it can be estimated that the impingement rate of gaseous species onto a sample in UHV is approximately 3×10^{10} cm^{-2} s^{-1}, in comparison to 3×10^{23} cm^{-2} s^{-1} obtained under ambient conditions. Assuming that all impinging molecules stick to the surface, a sample would become completely saturated within 7 ns in air, whilst in UHV this time is extended to ~20 hours. Thus, UHV makes it possible to perform experimental measurements without serious time constraints and without the threat of rapid sample contamination. The LT-UHV-STM utilised in much of this work incorporates cryoshields about the STM head, which reduce the local pressure about the sample even further through cryo-pumping, granting sample standing times of several weeks. In addition to this, UHV conditions allow the use of cryogenic temperatures and a range of electron spectroscopy techniques.

This work contains the results of a number of different complementary characterisation techniques, which together combine to give a much clearer understanding of molecular assembly than would be possible with any single method alone. For example, STM is an excellent tool with which to identify the symmetry and dimensions of periodic and aperiodic nanostructures, alongside granting insight into localised and dynamic features and processes. However, it is, in many ways, a limited technique; it does not necessarily provide, for example, direct evidence of the adsorbate's chemical state, although often some inferences are possible. This can be

particularly challenging when studying reactive surfaces and in cases where chemical modifications of the adsorbate are possible. Furthermore, STM images can often be difficult to interpret and thus the molecular adsorption geometry is not always clear. Consequently, XPS and NEXAFS measurements, which provide information about the chemistry and orientation of adsorbates, are often combined with STM experiments. In addition, there is much that can be gained through theoretical approaches, which often provide information not directly available or easily obtained through experimental methods. Moreover, they are often the only means by which complex observations can be understood, and therefore are an essential part of many surface science investigations.

2.1 Scanning tunnelling microscopy

The STM [2,3] has, beyond doubt, revolutionised surface science. Its ability to directly image interfaces in real-time and real-space is one that cannot be overstated in its usefulness. This is demonstrated by some of its earliest successes, whereby some of the most challenging contemporary issues were resolved, including the atomic structure of the highly complex Si(111)-(7×7) reconstruction [4] and the physical chemistry underpinning behind the (2×1) reconstruction of certain metal (110) surfaces [5]. In this work, STM has been used primarily to probe the local structure of molecular assemblies.

2.1.1 Background

The 'heart' of the STM experiment, shown in Figure 2.1, is the *tunnel junction*; an ultra-sharp metallic tip that is bought to within a few Å of a conducting surface [6]. At this distance, electrons can quantum mechanically 'tunnel' back and forth across the gap and, if a bias is applied between the tip and the sample (in this

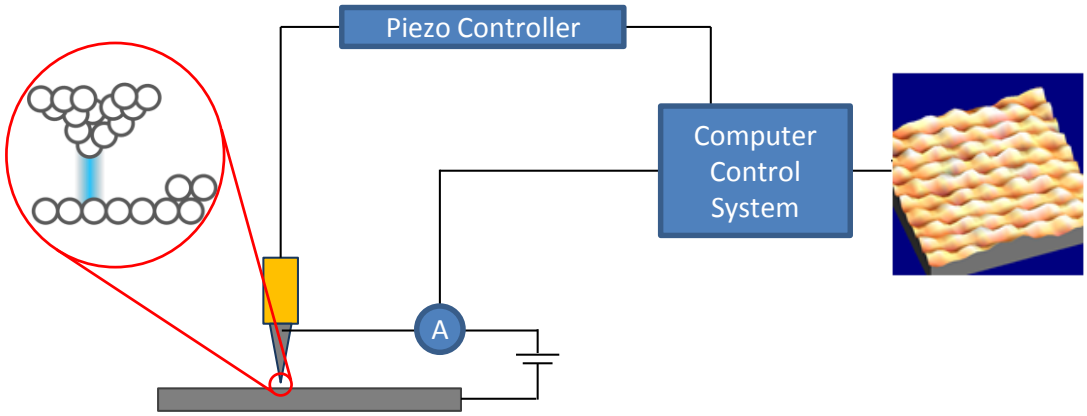

Figure 2.1 Schematic of the STM experiment. The tip is moved over the sample by the piezoactuators (orange box), whilst a voltage is applied between the tip and sample. The tunnel junction is depicted in the red circle.

case, the bias is applied to the sample whilst the tip is held at ground), tunnelling in one direction is favoured. This results in a net measurable current, given by

$$I = \frac{4\pi e}{\hbar}\int_{-\infty}^{\infty}[f(E_F - eU + \mathcal{E}) - f(E_F + \mathcal{E})].\rho_s(E_F - eU + \mathcal{E}).\rho_T(E_F + \mathcal{E}).|\mathcal{M}|^2 d\mathcal{E} \quad (2.1)$$

where $\rho_s(E)$ and $\rho_T(E)$ are the DOS of the surface and the tip at energy E. U is the bias applied across the tunnel junction. $\mathcal{M}$ is the tunnelling matrix element, which defines the wavefunctions of the tip and the sample and their overlap. $f(E)$ is the Fermi Dirac distribution function, which describes the perturbation to the DOS arising from the non-zero measurement temperature. At the characteristic temperatures of STM experiments, the contributions from $f(E)$ are negligible, and therefore the tunnel current can be approximated with:

$$I \sim \frac{4\pi e}{\hbar}\int_{0}^{eU}\rho_s(E_F - eU - \mathcal{E}).\rho_T(E_F + \mathcal{E}).|\mathcal{M}|^2\ d\mathcal{E} \quad (2.2)$$

$\mathcal{M}$, being dependent on the structure of the tip and its resulting wavefunction, is difficult to determine. If the tip is assumed to be perfectly sharp (i.e. terminating in a single atom), tunnelling can be approximated with a 1D tunnelling model [7], giving

$$I \sim \frac{4\pi e}{\hbar} \int_0^{eU} \rho_s(E_F - eU - \mathcal{E}).\rho_T(E_F + \mathcal{E}).\ e^{-2\kappa Z}\ d\mathcal{E} \qquad (2.3)$$

where κ is a constant that describes the decay of an electrons wavefunction with increasing distance from the surface (typically ~1 $Å^{-1}$) and Z is the tip-sample separation. By further assuming that the tip DOS remains constant over the voltage range of interest, Equation 2.3 can be further simplified to give:

$$I \sim \int_0^{eU} \rho_s(E_F - eU - \mathcal{E}).e^{-2\kappa Z}\ \ d\mathcal{E} \qquad (2.4)$$

Here, only electrons in the energy window $E_F - eU$ are capable of tunnelling. Outside of this, the electrons can only tunnel into filled states, which is prohibited by the Pauli exclusion principle. With this in mind, Equation 2.4 demonstrates that the tunnel current is approximately dependent only on the tip-surface separation, the sample DOS and the applied voltage.

The tunnel current is used to construct an image of the interface by scanning the tip over it and recording the current at each point. If the sample DOS is homogeneous, as is the case for pristine metals, the current only varies with the tip-sample separation and therefore the image is a true representation of the sample topography. For molecule-on-metal systems, the DOS does not remain constant and therefore any observed contrast differences are a combination of both electronic and topographic effects. This can make measuring absolute heights in STM experiments

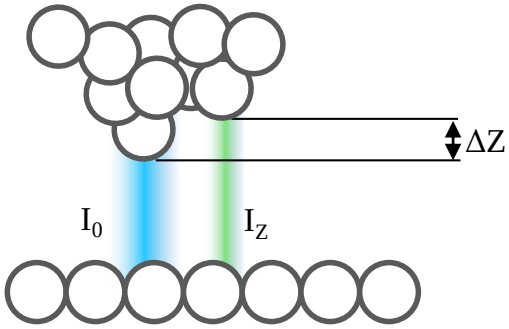

Figure 2.2 Schematic of the tunnel junction, revealing the derivation of the different terms comprising Equation 2.5 and how the tunnel current decreases with increased tip-sample separation.

particularly difficult. For example, in the most extreme cases, an adsorbate can sufficiently reduce the local DOS such that it is imaged as a depression, even though it is in fact adsorbed on top of the surface [8].

The extremely high spatial resolution of the STM measurement arises from the exponential decrease of the tunnelling current with the tip-sample separation. It can be shown that the tunnel current attenuation with increasing tip-sample separation is given by

$$\frac{I_0}{I_Z} = e^{-2\kappa\Delta Z} \tag{2.5}$$

where I_0/I_Z is the ratio of tunnel currents obtained at an initial and increased tip-sample separations, illustrated by the blue and green current channels in Figure 2.2, and ΔZ is the corresponding change in tip-sample separation. The result is that an increase in Z by the length of one single atom reduces the tunnelling current by a factor of approximately 100. Consequently, for a reasonably sharp tip, the current is essentially limited to the outermost atom, thereby allowing resolution of atomic scale features on the surface.

2.1.2 Measurement methodology

To bring the STM tip within an appropriate distance from the surface, two types of approach mechanism are typically used. The first is a 'coarse' approach, which allows the tip to be bought as close as is optically possible to the sample in a rapid fashion. After this, a computer-controlled 'fine' approach is utilised, whereby the tunnel current is continuously monitored to prevent tip-sample 'crashes' – where the tip makes physical contact with the sample, most likely damaging both. Once tunnelling is achieved, the tip is scanned over the surface to construct a STM image. Piezoelectric actuators give sub-Å precision of the tip position with respect to the sample. These are constructed from piezoelectric materials, which undergo physical extensions and contractions when a voltage difference is applied across the material. However, as the maximum spatial operating range of such materials is typically very limited, the coarse control mechanism is usually used to move the tip on a macroscopic scale.

The typical tunnelling conditions employed in STM imaging are around U=±0.1 – ±2.0 V and I=10 pA – 1 nA. As the current is very small and therefore susceptible to electrical noise, it is passed through a preamplifier before being sent to the STM controller. This converts the signal to a voltage and amplifies it by typically around 10^9 V A^{-1}. To maximise the signal-to-noise ratio, the preamplifier is situated as close as possible to the tunnel junction to limit signal degradation before amplification.

Imaging can be performed in one of two feedback modes, which are illustrated in Figure 2.3. In *constant-height* mode (Figure 2.3a), the tip is kept at a constant height during scanning whilst the varying current is measured and used to construct an image of the sample. As no feedback is required during scanning,

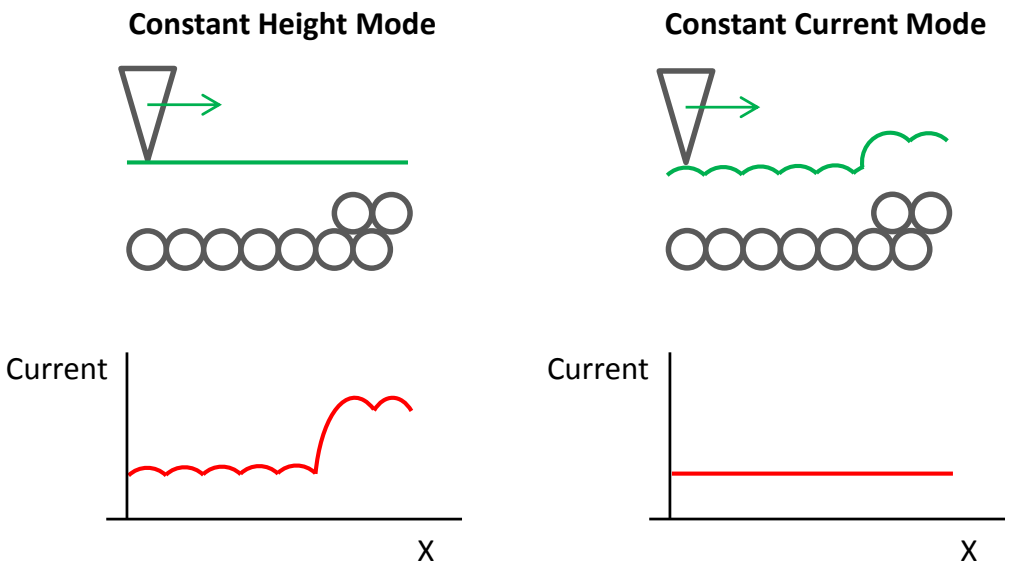

Figure 2.3 Depiction of the tip trajectory as it is scanned in constant height and constant current modes. The green line shows the position of the tip as it is scanned over the sample. In the bottom profiles, the measured current is displayed as a function of position, assuming a perfect feedback system.

imaging can be rapid. However, it is only feasible on extremely flat surfaces and for stable tunnel junctions, due to the possibility of crashing the tip into the sample. This can be particularly difficult when not scanning at low temperatures, due to the potential for thermal drift. In addition, as the current depends exponentially with the tip-sample separation (Equation 2.5), estimating the apparent heights of features can be more challenging, as illustrated in Figure 2.3a. In contrast, when the STM is operated in c*onstant-current* mode, the tip-sample separation remains approximately constant (assuming a homogeneous DOS), as depicted in Figure 2.3b. This is achieved by using a feedback system, which maintains a constant current by varying the tip height during scanning. Whilst this is a slower method of imaging, it is the most commonly used method as it should prevent tip crashes.

The mobility of isolated organic adsorbates at RT is often high, preventing their imaging with STM. This can be overcome by either imaging self-assembled structures, whereby the mobility is limited by the resulting intermolecular

interactions, or by imaging at low temperatures. The latter case is preferable, due to the relative ease with which it is possible to investigate single molecules. Furthermore, as the extension coefficients of the piezoelectric actuators are reduced at LT, the signal-to-noise ratio is also improved.

In this work, two different STMs systems have been used. The STM measurements performed on TPA on Cu(110) were taken using a variable temperature UHV-STM, operated at RT, in a home-built vacuum chamber, by Dr Yeliang Wang, now at the Chinese Academy of Sciences. All others were performed using a commercial Besocke type [9] LT-STM, held at 77 K. Both STMs were operated in constant current mode. A detailed description of the LT-STM system is provided in Section 2.6. All STM images in this work have been analysed with the WSxM free software [10]. Unless stated otherwise, the only image processing used is a single plane flattening, achieved by subtracting a global plane from each image. All measured distances are quoted with errors of one standard deviation.

2.2 Low-energy electron diffraction

LEED is a very powerful technique for analysing conductive surfaces. Its development constitutes an integral part of modern physics; the observation of a LEED pattern was part of the first experimental evidence of the wave nature of electrons [11], earning its inventors the 1937 Nobel Prize in physics. However, it was not until the 1960s that LEED became commonly used in surface science research [12]. Since then, it has become a critical tool for the rapid characterisation of periodic features on conducting surfaces.

Figure 2.4a shows a schematic of the LEED experiment. The electron gun in the centre (blue box) emits low-energy electrons (10-300 eV) towards the sample,

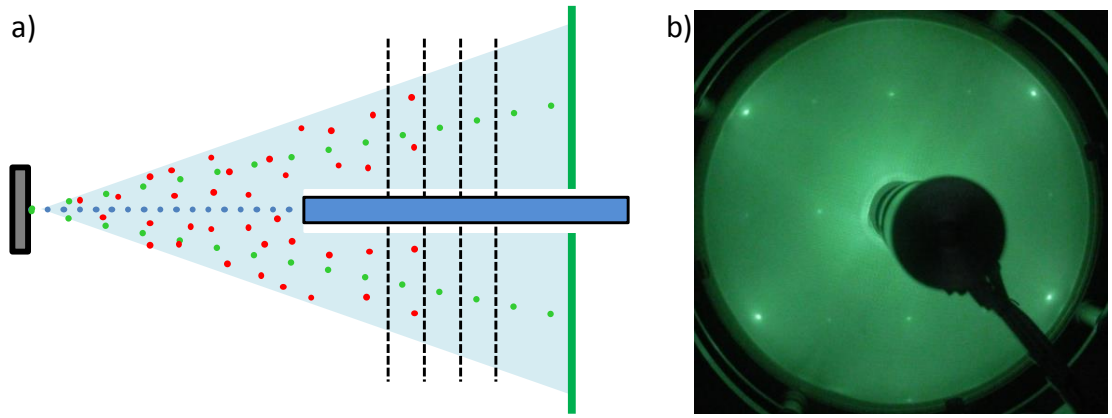

Figure 2.4 a) Schematic of the LEED apparatus. The phosphor screen is shown at the rear of the LEED setup as the green line (on the right in the drawing), the electron gun is the blue shape, and the retarding grids are shown as the black dashed lines. The electrons are shown as the array of spots, the colour of which depends on their energy and direction. The blue electrons show the primary electron beam being fired at the sample, the red and green are the inelastically and elastically back-scattered electrons, respectively. b) Example LEED pattern of a clean Cu(110) surface.

which are focused into an approximately 2 mm^2 spot using a series of electrostatic lenses. The electrons interact with the surface and are back-scattered towards the LEED optics. The symmetry and periodicity of the 'scatterers' can be reconstructed from the diffraction pattern of the elastically-scattered electrons, which can be directly visualised using a phosphorescent screen. An example LEED pattern is shown in Figure 2.4b. As not all electrons interact elastically with the surface, a series of retarding grids intercept the electrons before they reach the screen and filter out those that have lost energy.

As the LEED pattern is constructed from diffracted electrons, the pattern is a *reciprocal space* depiction of the surface. The result is demonstrated in Figure 2.5a; for a substrate with rectangular symmetry and lattice parameters a_1 and a_2, the observed LEED pattern dimensions are proportional to $1/a_1$ and $1/a_2$, respectively. This is an important consideration when analysing LEED patterns of adsorbate superstructures; the real-space periodicity of adsorbates is always larger than that of

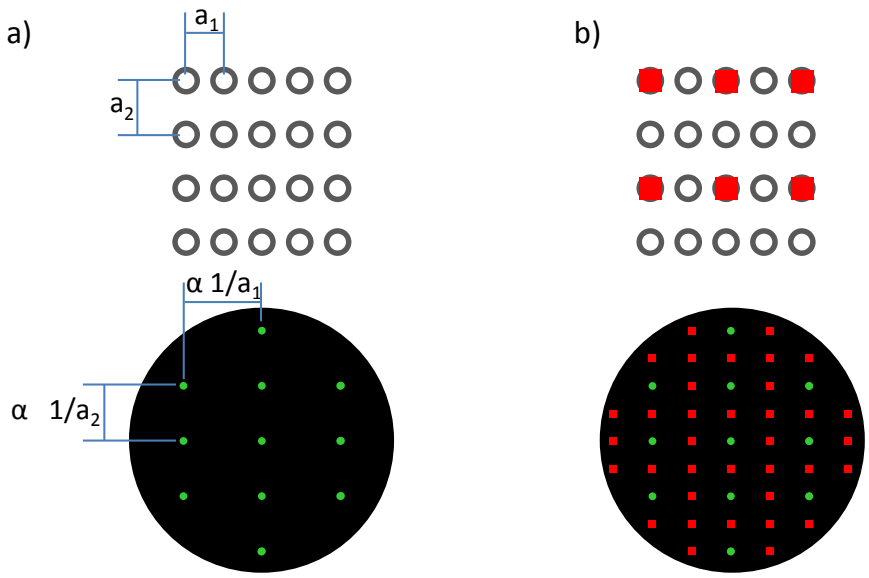

Figure 2.5 a) Model demonstrating how the real space structure of a surface is depicted in reciprocal space in the LEED pattern. b) Demonstration of how a superstructure is shown in the LEED as a consequence of the reciprocal depiction. The red squares indicate the adsorbate positions (top image) and the additional spots they generate in the LEED pattern (lower image).

the substrate, and thus the corresponding LEED pattern periodicity is *smaller*, as shown in Figure 2.5b. The LEED spots from such superstructures are therefore usually referred to as 'fractional order spots'.

LEED is a particularly useful technique in surface science due to its intrinsic surface sensitivity. The mean free path of an electron travelling through a crystal lattice is dependent on its energy, whilst being mostly independent of the material. This led to the development of the 'universal curve' shown in Figure 2.6. At the energies used in the LEED experiment, this distance is on the order of 1 nm or approximately 3-4 atomic layers [13]. This is due to the potential for inelastic interactions between the travelling electron and the crystal lattice, which in general remove kinetic energy from the electron. Consequently, LEED is extremely surface sensitive; an electron is highly unlikely to penetrate deeply into the crystal bulk and

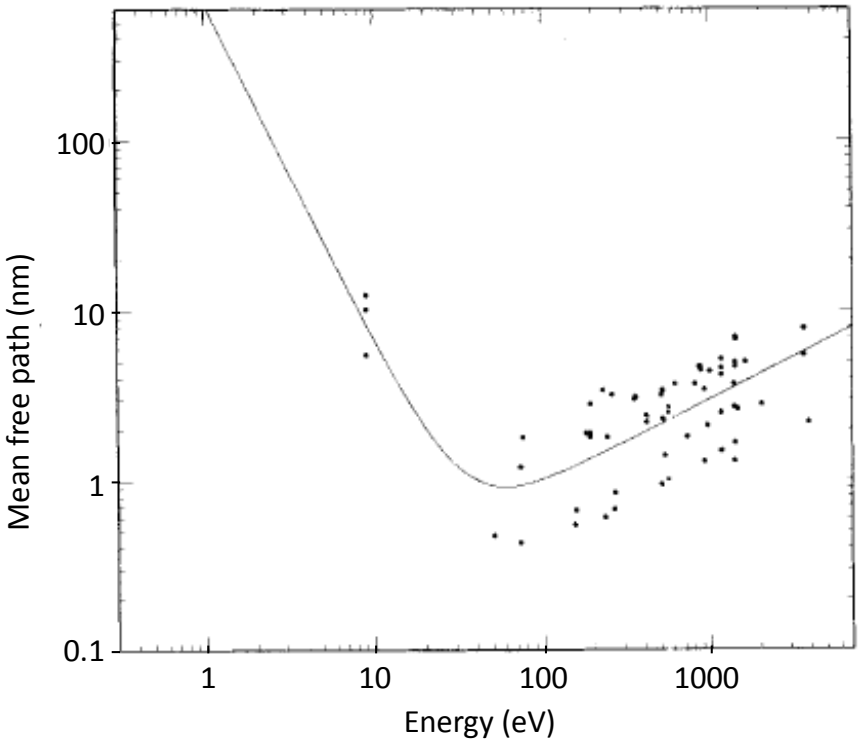

Figure 2.6 Mean free path of electrons as they travel through an inorganic lattice. Adapted from reference [12]. The black dots correspond to data points obtained for a variety of different materials.

also escape without losing any kinetic energy, and therefore avoid being filtered out by the suppressor grid.

2.3 X-ray photoemission spectroscopy

XPS is a photon-in, electron-out spectroscopic technique that allows the chemical composition of a sample surface to be characterised. Figure 2.7 depicts the photoemission process; the surface is irradiated with monochromatic photons that are absorbed by the core-level electrons of the sample constituents. This leads to their ejection from the sample with a kinetic energy given by

$$KE = h\upsilon - \phi - E_B \tag{2.6}$$

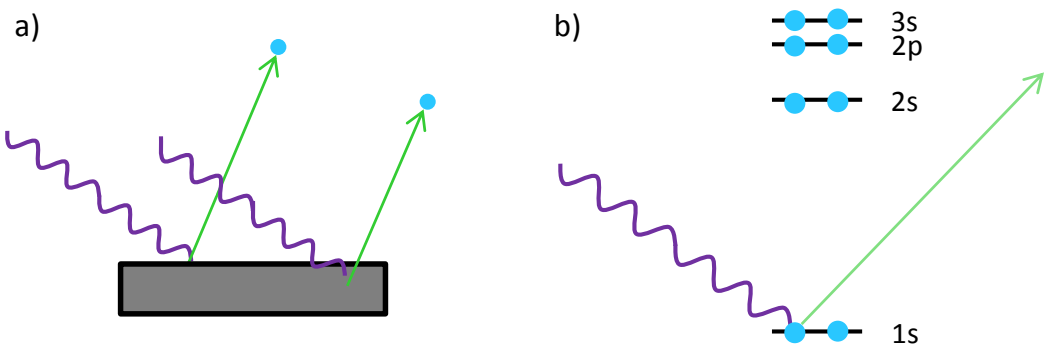

Figure 2.7 a) Schematic of the XPS process. b) The photoemission process in terms of the electron energy levels.

where KE is the photoelectron kinetic energy, $h\upsilon$ is the incident photon energy, ϕ is the work function and E_B is the binding energy of the electrons. Critically, the binding energy is characteristic of the element from which it is ejected and depends also on the chemical environment of that atom. This means that a binding energy spectrum can be used as a distinct 'chemical fingerprint' of the sample, allowing precise identification of its constituents and of their binding state. For example, O 1s electrons have a binding energy of approximately 530 eV, whereas the C 1s are around 280-290 eV. In TPA, which has two C environments, the C 1s spectrum reveals two peaks centred at 285 and 288 eV for the aromatic and carboxyl moieties, respectively [14,15].

Like LEED, XPS is an intrinsically surface sensitive technique due to the small mean free path of low-energy electrons, as was demonstrated in Figure 2.6. However, here the inelastically-scattered electrons are not filtered out by electrostatic lenses, but instead become part of the background signal. This background is not constant for all binding energies. Instead, each peak exhibits a so-called Shirley step [16], schematically depicted in Figure 2.8. This step, which exhibits a greater intensity on the high binding energy side of each peak, arises from

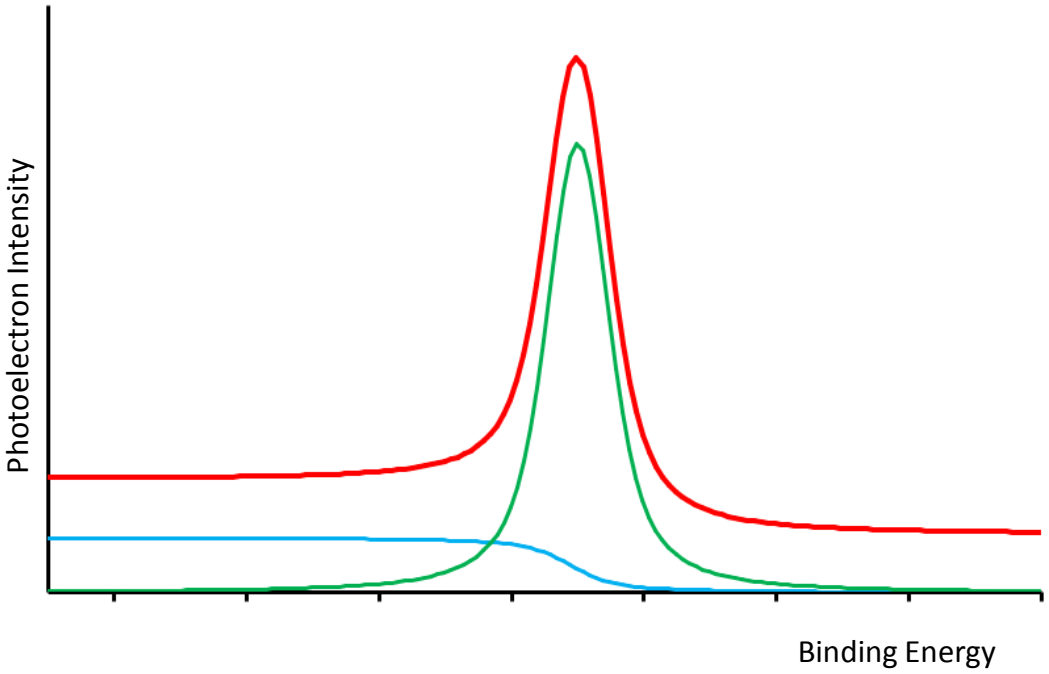

Figure 2.8 Schematic depiction of a XPS spectrum, whereby the obtained spectrum is shown in red, the fitted peak in green, and the background with Shirley step in blue.

the propensity of photoelectrons to lose rather than gain kinetic energy when interacting with atoms in the sample.

The XPS measurements of TPA on Cu(110) in Chapter 3 of this work were performed at the VUV beamline at the ELLETRA synchrotron, Italy. Those of OA adsorbed on Cu(110) in Chapter 4 were performed at the I09-SISA beamline at the Diamond Light Source, UK, in collaboration with Professor Phil Woodruff from the University of Warwick and Dr David Duncan from the Technische Universität München. In both cases, the O 1s and C 1s spectra were recorded using ~700 and 400 eV photons, respectively. Fitting of all XPS data was achieved using the XPSmania software, developed by Dr Francesco Bruno (ALOISA Beamline staff, CNR-IOM, Trieste, 2007). The binding energies of the spectra were calibrated with respect to the Fermi energy. For this, separate spectra of the Fermi step were taken, which, after subtraction of a linear background, were fitted with a Fermi Dirac

distribution. An additional Gaussian function was added to this distribution to account for instrumental resolution. The binding energy-corrected core level data was then fitted using one or multiple Voigt-type peaks [17]. A step-like Shirley background was added to each peak, with an intensity proportional to the peak area. To again compensate for the instrument's resolution, the peaks were convoluted with a Gaussian peak, whose shape was determined from the fit of the Fermi step spectrum. For spectra with multiple peaks, the shape of each peak was kept fixed by using identical full-width at half-maximum values for the Gaussian and Lorentzian contributions (the Gaussian component of the Voigt line shape is in addition to that arising from the instrumental resolution). The global peak shape and Shirley proportionality constant, and the individual peak binding energies and intensities were varied in an iterative process until convergence of the fitting error. Additional details are given in the text, where appropriate.

2.4 Near-edge X-ray adsorption fine structure spectroscopy

In XPS, electrons are emitted because the excitation energy is greater than the sum of their binding energy and the sample work function. If the photon has less energy than that needed for photoemission, the electron can instead be excited to a higher energy unoccupied, but still bound, state. In a NEXAFS experiment, the energy of the incident photon is varied. When the energy matches that of an electronic transition, the photon is adsorbed which, as long as the core hole is less than 10 keV deep [1], ultimately causes the ejection of an electron through the Auger emission process. This, in short, occurs when the core hole left by the excitation is refilled by relaxation of an electron from a higher energy level. The energy difference between these two states is transferred to a further electron, which is then

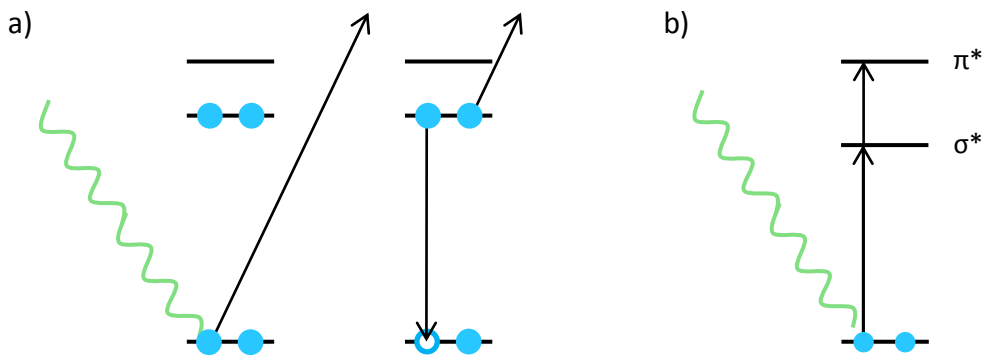

Figure 2.9 a) General schematic of the Auger emission process. The filled circles represent electrons, whilst empty circles represent an electron hole. b) Energy level depiction of the transitions involved in NEXAFS measurements.

ejected from the atom as depicted in Figure 2.9a [1]. As the energy of the photoelectron comes solely from an electronic transition, its kinetic energy does not vary with photon energy. By monitoring the emission of these 'Auger electrons' as a function of photon energy, it is possible to ascertain the energy of the electronic transition, which is characteristic of the unoccupied state filled by the initial excitation.

It is also possible to selectively enhance or suppress excitations to states with particular symmetries by using linearly-polarised light. For example, if an adsorbate has unoccupied states aligned parallel to the surface, excitation to these states is most efficient when the polarisation vector of the incoming photon is aligned in the same direction. As the two end-states have different energies (Figure 2.9b), the transition efficiencies can be monitored as a function of both photon energy and polarisation vector.

In summary, NEXAFS allows the orientation of adsorbed species with respect to the surface to be determined. This is clearly demonstrated in the case of TPA on rutile TiO_2 [18]. Figure 2.10a depicts the atomistic structure of TPA and, in

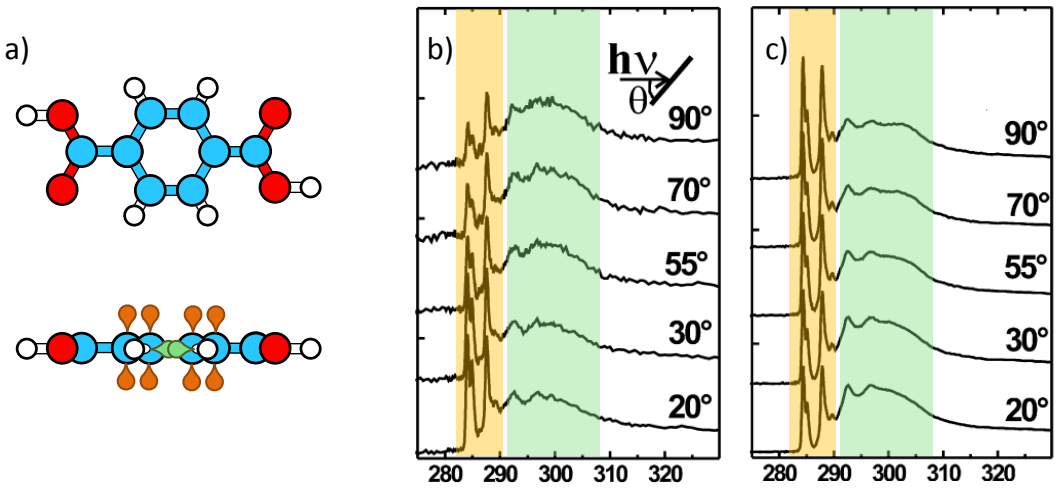

Figure 2.10 a) Schematic of TPA molecule (upper) and side view (lower). In the side view, the σ- and π-orbitals are shown by the green and orange dumbbell shapes, respectively. b) NEXAFS spectra taken of TPA on rutile TiO_2(110) at low molecular coverage. c) NEXAFS spectra taken of TPA on rutile TiO_2(110) at 1 monolayer coverage. The angles in b) and c) are the photon incidence angle with respect to the surface, as depicted by the inset of b). The σ- and π-signals are colour-coded using green and orange bands, respectively. Both b) and c) are adapted from reference [18].

the lower panel, the relative orientations of its σ- and π-states. At low molecular coverages, TPA adsorbs flat against substrate, resulting in the σ*-states being aligned parallel to the surface whilst the π*-orbitals are oriented perpendicularly. The NEXAFS spectrum, shown in Figure 2.10b, reveal two types of feature; a broad band characteristic of transitions to σ*-states (highlighted in green) and the sharp π-transitions found at lower photon energy (orange). When the X-rays are incident on the flat-lying TPA at normal incidence (corresponding to a photon polarisation vector that is parallel to the surface), electronic transitions to σ*-states are favoured whilst those to π*-states are suppressed, which is reflected in the spectra shown in Figure 2.10b. If the TPA coverage is increased, the organic film is reorganised so that the TPA is aligned perpendicular to the surface. The corresponding NEXAFS spectrum is shown in Figure 2.10c, where the relative intensities of the σ- and π-transitions are reversed for a given angle with respect to that shown in Figure 2.10b.

The NEXAFS measurements in this work were performed in collaboration with Professor Phil Woodruff and Dr David Duncan at the I09-SISA beamline at the Diamond Light Source, UK. The NEXAFS spectra were compiled from several, individual scans of the O-KLL Auger peak, taken with different photon energies (525-560 eV), using code written by Dr David Duncan.

2.5 Theoretical methods

The complexity associated with even the simplest molecule-on-metal system can be extreme. Notwithstanding this, theoretical approaches can provide an abundance of information that can prove critical in surface science investigations. To make this possible, calculations are performed using certain simplifications that ultimately make simulations manageable by reducing the total number of variables that need to be considered.

Molecular mechanics (MM) embodies this approach, whereby the chemical bonds in molecules are effectively simulated as springs, which can be readily modelled using variations of Hooke's law [19]. In this manner, very large ensembles of molecules can be investigated rapidly and inexpensively, at the cost of a 'complete picture' of all the associated properties. For example, in this work, MM has been used to investigate the nature of the intermolecular interactions in the TPA brickwork phase and how modification of its lattice parameters affects the total energy, which is described in detail in Section 3.2.1.1.

Unfortunately, its intrinsic simplifications result in MM being unsuited for the investigation of, for example, electronic properties. Given their importance in molecular adsorption on metal surfaces, it is necessary in such cases to use an *ab initio* approach. Here, the aim is to understand a molecular ensemble by solving its

many-electron Schrödinger equation. Given that an analytical solution is not possible for anything except a one-electron system, techniques have been developed that can make accurate estimates of the solution through a number of assumptions and simplifications, some of which are outlined below.

DFT [20,21] is such a method, whereby the electrons and their complex many-body interactions are reduced to a single functional; the *electron density*. This vastly reduces the number of variables that need to be calculated, as instead of simulating the motion and interactions of each electron, only the spatial variance of the electron density needs to obtained. This simplification is possible by considering the electron motion within the framework of the Born-Oppenheimer approximation, whereby the atomic nuclei are effectively stationary on the timescale of electron movements. The electrons therefore effectively interact only with a stationary potential field, defined by the positions of the atomic nuclei. It can be shown that the ground state electron density is unique to that particular potential field, allowing it to be calculated using energy minimisation processes. In doing so, the electrons contributions to the total energy can be calculated.

The electron density calculated by DFT allows the DOS to be readily evaluated. Given that the STM tunnel current depends largely on the sample DOS (Equation 2.4), DFT calculations can provide additional insight into the images obtained by STM. In particular, DFT is an excellent tool with which to *simulate* STM images, which is typically performed in the framework of the Tersoff-Hamann approach. Here, the tip apex is approximated with a s-wave orbital [22]. In doing so, the tunnel current can be estimated using:

$$I \sim \int_0^{eU} \rho_s\left(\vec{R}_0, \mathcal{E}\right) d\mathcal{E} \qquad (2.7)$$

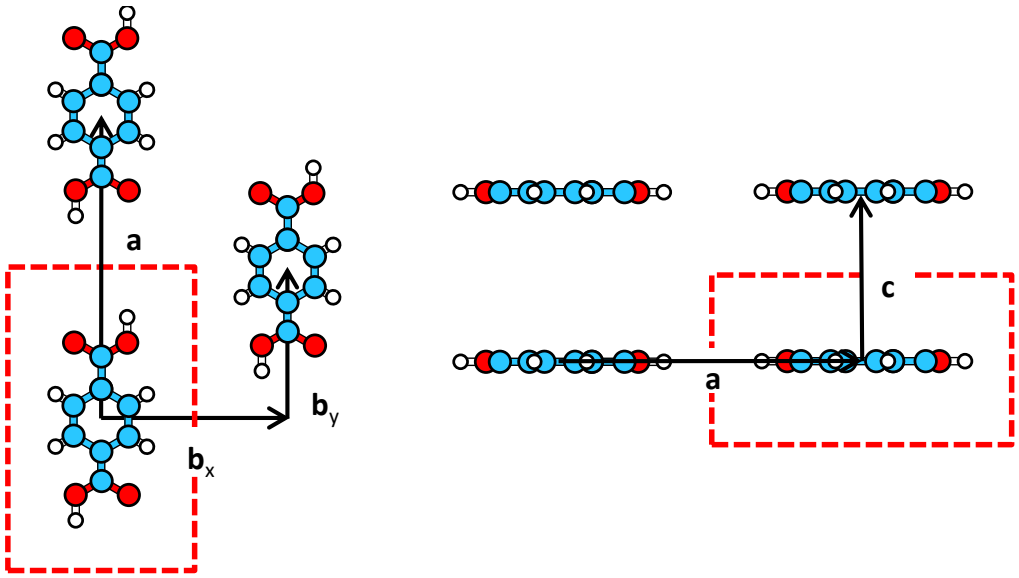

Figure 2.11 Depiction of the cell dimensions used for the MM calculations.

where $\rho_s(\vec{R}_0, \mathcal{E})$ is the sample DOS at the position of the tip apex, $\vec{R}_0$. With this in mind, a simulated STM image is obtained by calculating the spatial variance of the DOS within a given energy window.

2.5.1 Methods - molecular mechanics

The MM calculations were performed by Dr Natalia Martsinovich and Professor Alessandro Troisi from the University of Warwick, using the MM3 force field [23,24] in the Tinker software [25]. This has been adapted so as to correctly simulate the energy of the dimeric H-bonds between TPA carboxylic moieties, as calculated from DFT [26]. The interaction potential for gas-phase TPA was calculated by establishing a unit cell with dimensions **a**×**b**×**c**, containing only one TPA species, which is illustrated by the red box in Figure 2.11. In the following calculations, these dimensions were varied so as to simulate the different intermolecular separations. To calculate the intra-chain interactions, isolated 1D

chains were established by setting large **b** and **c** values. The size of **a** was then gradually increased in 0.05Å steps, and the total energy was calculated. The interactions between the chains were similarly investigated; **a** was initially set at its calculated lowest energy value whilst $\mathbf{b}_x$ and $\mathbf{b}_y$ were varied. Confirmation of the lowest **a**, $\mathbf{b}_x$ and $\mathbf{b}_y$ values was obtained by simultaneously varying all three parameters about their most favourable positions and observing no changes in their lowest energy values.

2.5.2 Methods - density functional theory

The DFT calculations of TPA on Cu(110), which were not dispersion-corrected, were performed by Dr Stefano Fabris, based at the Theory@ELLETRA group and SISSA. These employed the exchange and correlation energy functionals expressed in the Perdew-Burke-Ernzerhof generalized gradient approximation [27]. All calculations were performed with the Quantum-ESPRESSO computer package [28]. A 3-layer metal slab were used to model the Cu(110) surface, where the two lowermost layers were kept fixed during the structural relaxations. The STM images were simulated by integrating the sample DOS between the Fermi energy and a bias potential of 0.5 eV.

The dispersion-corrected DFT calculations of TPA on Cu(111) and Au(111) were performed by Dr Natalia Martsinovich and Professor Alessandro Troisi using the SIESTA code [29]. The metal surfaces were simulated using 3-layer metal slabs with a fixed bottom layer. Dispersion-correction was applied to molecule-metal interactions, and the relevant dispersion parameters on the Cu and Au surfaces were obtained from reference [30] and [31], respectively. The simulations were performed by first positioning the TPA molecule over a hexagonal close-packed hollow site on

the relevant substrate with the TPA long symmetry axis aligned along the $[11\bar{2}]$ crystallographic direction. To obtain the potential energy surface (PES) described in Section 3.2.1, the adsorption energy E_{ads} of the TPA was calculated in various positions on the metal. The adsorbate was moved parallel to the Cu(111) and Au(111) surfaces in 0.25 and 0.5 Å steps, respectively, so that the entire substrate unit cell is explored. In each position, E_{ads} was calculated using:

$$E_{ads} = E_{Total} - (E_{Surface} + E_{TPA}) \quad (2.8)$$

where $E_{Surface}$ and E_{TPA} are the energies of the clean metal surface and the isolated TPA molecule, respectively, and E_{Total} is the energy calculated for the total system (i.e. with the TPA adsorbed on the substrate).

The DFT calculations of the OA on Cu(110) system described in Section 4.1.2, which also did not include dispersion-corrections, were performed by Dr Sara Fortuna, now at the Department of Medical and Biological Sciences at the University of Udine, and Dr Stefano Fabris. These also used the Perdew-Burke-Ernzerhof generalized gradient approximation functional for the exchange and correlation energies [32], by means of the Quantum ESPRESSO distribution [28,33]. The Cu(110) substrate was simulated using a 5-layer deep Cu slab, with either (3×2) or (2×2) unit cells in the lateral (i.e. parallel to the surface) directions. During the structural relaxations, the lowermost two layers were kept fixed at their bulk-like coordinates. A wide variety of molecular adsorption geometries were investigated, including parallel, perpendicular and tilted orientations. The adsorption energies where calculated in a similar manner to that expressed in Equation 2.8, albeit that an additional term E_H, the energy associated with a single proton, has to be included to compensate for deprotonation. Furthermore, as some supercells contained multiple

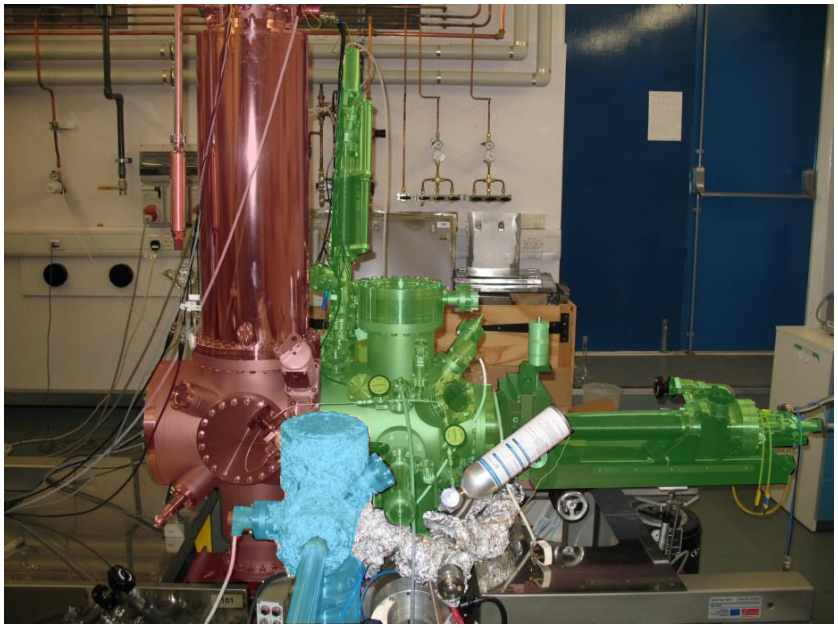

Figure 2.12 a) Photograph of the LT-UHV-STM used in many of the experimental studies presented here. The three chambers have been highlighted with different colours; the loadlock in blue, the preparation chamber in green and the STM chamber in red.

adsorbed OA species and varying degrees of deprotonation, it is necessary to incorporate scaling constants, leading to:

$$E_{ads} = E_{Total} + xE_H - (E_{Surface} + yE_{OA}) \quad (2.9)$$

where x and y are integers incorporated to calculate the effect of multiple adsorbates in the unit cell and effects of deprotonation.

2.6 Fabrication of molecule-on-metal films

2.6.1 UHV system

Figure 2.12 shows the UHV chamber used for the STM and LEED measurements of TPA on Cu(111) in Chapter 3, of OA on Cu(110) and Cu(111) in Chapter 4 and of TPA on OA films in Chapter 5. The instrument is a commercial

system purchased from Createc GmbH. The chamber is split into three separate compartments, which are highlighted in Figure 2.12 with different colours.

The first part of the chamber, shown in blue, is the loadlock. This is pumped using a series of pumps; a 300 l s^{-1} turbomolecular pump, backed by an 80 l s^{-1} turbomolecular pump, backed by a membrane pump. The base pressure of this chamber is approximately 1×10^{-9} mbar. The loadlock is intended for rapid introduction of samples into the main chambers, but is also needed for pumping the Ar gas used for substrate cleaning, purging of the Ar delivery line, and for the deposition of OA (see Section 2.6.3).

The second compartment is a preparation chamber, coloured green, which is fitted with a variety of instruments for sample cleaning and fabrication. These include; i) a manipulator for sample transfer and for making electrical connections to the substrate heater, ii) a leak valve for Ar inlet coupled to an ion gun for sputtering, iii) a sample storage rack, iv) LEED optics for checking surface cleanliness and for characterisation of molecular films, v) a mass spectrometer for identifying residual gases in the chamber, vi) 2× 4-cell evaporators (Dodecon GmbH) for the deposition of molecules onto samples, and vii) a metal evaporator (Createc GmbH) for the deposition of metal atoms onto samples. The three evaporators are connected to the preparation chamber via gate valves and linear transfer mechanisms, allowing them to be retracted and isolated from the chamber into a separately-pumped manifold. This facilitates rapid exchange of evaporants without the need to break the vacuum in the preparation chamber. The chamber is pumped by an ion pump fitted with a Ti sublimation pump, obtaining a base pressure of approximately 2×10^{-10} mbar.

The final aspect of the apparatus is the STM chamber, highlighted in red, containing the cryostat and STM head. This chamber is also pumped by an ion pump

and Ti sublimation pump, giving a base pressure of 1×10^{-10} mbar. The cryostat consists of two cryogen tanks; an outer 14 l tank, filled exclusively with liquid N_2, and an inner 4 l tank, which can be filled with either liquid N_2 or He. Throughout the course of this work, the inner cryostat is filled exclusively with liquid N_2. The STM head is suspended from the inner cryostat by springs, and is fitted with eddy current dampening for vibration isolation. It is also surrounded by two cryoshields, mounted to the internal and external tanks of the cryostat.

2.6.2 Sample cleaning

Sample cleaning is performed by multiple cycles (typically ~3) of Ar^+ sputtering and annealing. During sputtering, the surface is bombarded with accelerated Ar^+ ions, resulting in the ejection of substrate atoms. In this manner, it is possible to remove the outermost substrate layers. The process also causes significant damage to the surface, and thus annealing treatments are applied to repair this damage by giving the substrate atoms sufficient thermal energy to become mobile and ultimately reform a crystalline interface.

Sputtering is performed using an Ar pressure of 5×10^{-5} mbar and an acceleration voltage of 1 keV. The measured drain current is 14 mA cm^{-2}. During the sputtering cycles, the preparation chamber is pumped only by the turbomolecular pumps of the loadlock. After each sputtering, the metal crystal is annealed to 870 K for 5 minutes. This is achieved using a small button heater on the sample holder, onto which the crystal is securely mounted by a Ta clamp. The annealing time is limited to prevent excessive heat transfer to the sample holder and its soldered electrical connections. Temperature monitoring is achieved by a thermocouple that is spot welded to the Ta clamp.

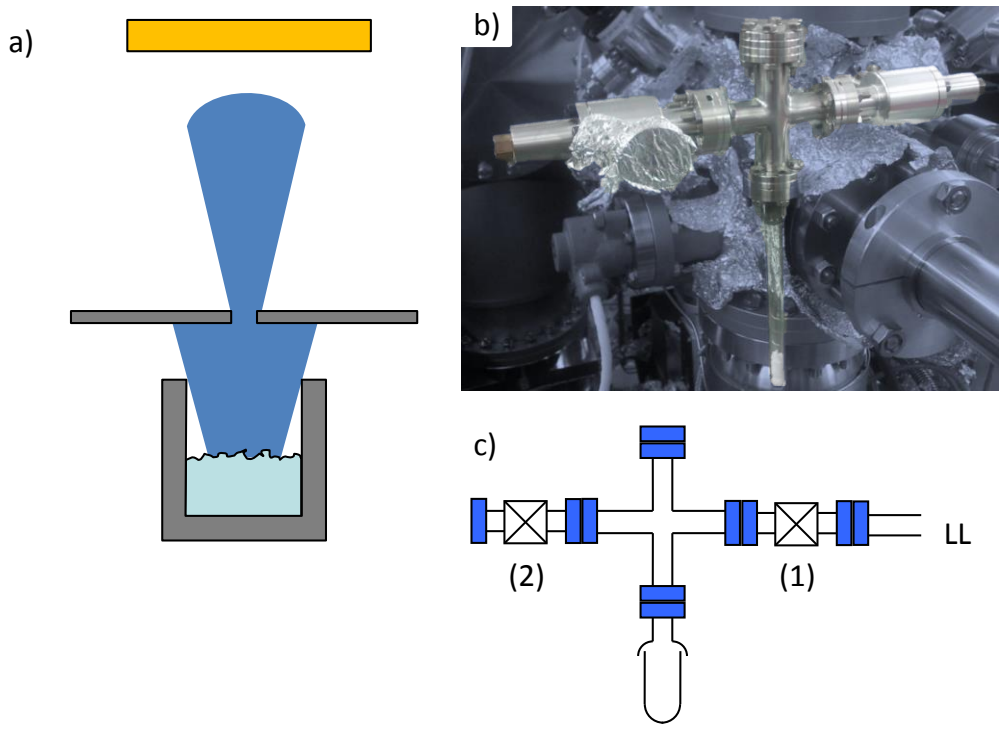

Figure 2.13 a) Schematic of the evaporation of low vapour pressure molecules. b) Photo of the loaded OA doser, as mounted on chamber. c) Schematic of the OA doser. The blue boxes represent CF flanges. The two valves are labelled (1) and (2). LL represents the loadlock.

2.6.3 Adsorbate deposition

Deposition of TPA was achieved using standard thermal evaporation in vacuum [34]. The process is depicted in Figure 2.13a; in essence, a crucible containing the TPA is heated to 450 K, resulting in its sublimation and the formation of a molecular beam. The sample is placed in the path of this beam for deposition. The deposition time, typically around 5-15 minutes, is controlled by means a rotary shutter in the molecular beam path. The TPA was thoroughly outgassed in UHV for several hours at 440 K prior to use.

OA has a comparatively high vapour pressure [35] and therefore cannot be stored in vacuum or be deposited as above. To circumvent this, an integral part of

this work has involved the design, testing and implementation of a gas dosing system, which is shown in Figure 2.13b and c. The OA powder is situated inside a kovar glass tube so that it does not make direct contact with the metal walls of the doser, which could potentially lead to decomposition. Kovar glass is used due to its similar thermal expansion characteristics as the stainless steel to which it is bonded. The doser has two valves, labelled (1) and (2), which lead to the loadlock and atmosphere, respectively.

The doser is first loaded with OA powder and then fitted to the chamber. It is then evacuated through (2) using an auxiliary pumping stage. Prior to use, the doser is cleaned by baking the metallic parts to approximately 373 K, whilst the crucible was kept at RT to limit OA sublimation. At the end of baking, the powder was gently outgassed by heating with a heat gun. In addition to this, the doser is purged briefly into the loadlock prior to each deposition by briefly opening (1). Deposition was achieved by exposing a freshly cleaned Cu surface to OA vapour through valve (1). The deposition time, typically around 5 minutes, was varied to control the exposure. The loadlock pressure varied from approximately 1×10^{-8} – 1×10^{-6} mbar throughout deposition, which returned to the initial base pressure after approximately 5-10 minutes upon closing (1).

The experimental conditions for Fe deposition were first calibrated using a quartz crystal microbalance mounted in a separate chamber. A Fe bar was bombarded with electrons accelerated by 750 V from a W filament, to which a 2.15 A current was applied. The emission current was first manually stabilised for 5 minutes prior to deposition. Deposition time was limited to ~5 s under these conditions, again controlled by a shutter mounted in front of the evaporator.

2.7 Chapter 2 references

1. Woodruff, D.P. and T.A. Delchar, *Modern Techniques of Surface Science*. 1986: Cambridge University Press, Cambridge.
2. Binnig, G., et al., *Surface Studies by Scanning Tunneling Microscope.* Physical Review Letters, 1982. **49**(1): p. 57-61.
3. Binnig, G. and H. Rohrer, *Scanning Tunneling Microscopy—from Birth to Adolescence (Nobel Lecture).* Angewandte Chemie International Edition in English, 1987. **26**(7): p. 606-614.
4. Binnig, G., et al., *7 × 7 Reconstruction on Si(111) Resolved in Real Space.* Physical Review Letters, 1983. **50**(2): p. 120-123.
5. Binnig, G., et al., *(111) facets as the origin of reconstructed Au(110) surfaces.* Surface Science Letters, 1983. **131**(1): p. L379-L384.
6. Chen, C.J., *Introduction to scanning tunneling microscopy*. Vol. 227. 1993: Oxford University Press New York.
7. Lang, N.D., *Spectroscopy of single atoms in the scanning tunneling microscope.* Physical Review B, 1986. **34**(8): p. 5947-5950.
8. Lang, N.D., *Apparent size of an atom in the scanning tunneling microscope as a function of bias.* Physical Review Letters, 1987. **58**(1): p. 45-48.
9. Besocke, K., *An easily operable scanning tunneling microscope.* Surface Science, 1987. **181**(1-2): p. 145-153.
10. Horcas, I., et al., *WSXM: A software for scanning probe microscopy and a tool for nanotechnology.* Review of Scientific Instruments, 2007. **78**: p. 013705.
11. Davisson, C. and L.H. Germer, *The scattering of electrons by a single crystal of nickel.* Nature, 1927. **119**: p. 558-560.
12. Van Hove, M.A., W.H. Weinberg, and C.-M. Chan, *Low-energy electron diffraction. Springer-verlag berlin heidelberg,*. 1986. **6**.
13. Seah, M.P. and W.A. Dench, *Quantitative electron spectroscopy of surfaces: a standard data base for electron inelastic mean free paths in solids.* Surface and Interface Analysis, 1979. **1**(1): p. 2-11.
14. Canas-Ventura, M.E., et al., *Coexistence of one- and two-dimensional supramolecular assemblies of terephthalic acid on Pd(111) due to self-limiting deprotonation.* Journal of Chemical Physics, 2006. **125**(18): p. 184710.
15. Classen, T., et al., *Hydrogen and Coordination Bonding Supramolecular Structures of Trimesic Acid on Cu(110).* The Journal of Physical Chemistry A, 2007. **111**(49): p. 12589-12603.
16. Shirley, D.A., *High-Resolution X-ray Photoemission Spectrum of Valence Bands of Gold.* Physical Review B, 1972. **5**(12): p. 4709-4714.
17. Tougaard, S., *Accuracy of the non-destructive surface nanostructure quantification technique based on analysis of the XPS or AES peak shape.* Surface and Interface Analysis, 1998. **26**(4): p. 249-269.
18. Rahe, P., et al., *Transition of Molecule Orientation during Adsorption of Terephthalic Acid on Rutile TiO2(110).* Journal of Physical Chemistry C, 2009. **113**(40): p. 17471-17478.
19. Hehre, W.J., *A guide to molecular mechanics and quantum chemical calculations*. 2003: Wavefunction Irvine, CA.
20. Hohenberg, P. and W. Kohn, *Inhomogeneous Electron Gas.* Physical Review, 1964. **136**(3B): p. B864-B871.

21. Kohn, W., *Nobel Lecture: Electronic structure of matter-wave functions and density functionals.* Reviews of Modern Physics, 1999. **71**(5): p. 1253-1266.
22. Tersoff, J. and D.R. Hamann, *Theory and Application for the Scanning Tunneling Microscope.* Physical Review Letters, 1983. **50**(25): p. 1998-2001.
23. Allinger, N.L., Y.H. Yuh, and J.H. Lii, *Molecular Mechanics - The MM3 Force-Field for Hydrocarbons .1.* Journal of the American Chemical Society, 1989. **111**(23): p. 8551-8566.
24. Lii, J.H. and N.L. Allinger, *Directional hydrogen bonding in the MM3 force field: II.* Journal of Computational Chemistry, 1998. **19**(9): p. 1001-1016.
25. Ponder, J.W. and F.M. Richards, *An efficient Newton-like method for molecular mechanics energy minimization of large molecules.* Journal of Computational Chemistry, 1987. **8**(7): p. 1016-1024.
26. Martsinovich, N. and A. Troisi, *Modeling the Self-Assembly of Benzenedicarboxylic Acids Using Monte Carlo and Molecular Dynamics Simulations.* The Journal of Physical Chemistry C, 2010. **114**(10): p. 4376-4388.
27. Perdew, J.P., K. Burke, and M. Ernzerhof, *Generalized gradient approximation made simple.* Physical Review Letters, 1996. **77**(18): p. 3865-3868.
28. Giannozzi, P., et al., *QUANTUM ESPRESSO: a modular and open-source software project for quantum simulations of materials.* Journal of Physics-Condensed Matter, 2009. **21**(39): p. 395502.
29. *http://departments.icmab.es/leem/siesta last accessed 26 November 2013*.
30. Grimme, S., *Semiempirical GGA-type density functional constructed with a long-range dispersion correction.* Journal of Computational Chemistry, 2006. **27**(15): p. 1787-1799.
31. Jalkanen, J.-P., et al., *A computational study of the adsorption of small Ag and Au nanoclusters on graphite.* Journal of Physical Chemistry A, 2007. **111**(49): p. 12317-12326.
32. Perdew, J.P., K. Burke, and Y. Wang, *Generalized gradient approximation for the exchange-correlation hole of a many-electron system.* Physical Review B, 1996. **54**(23): p. 16533-16539.
33. Scandolo, S., et al., *First-principles codes for computational crystallography in the Quantum-ESPRESSO package.* Zeitschrift Fur Kristallographie, 2005. **220**(5-6): p. 574-579.
34. Arthur, J.R., *Molecular beam epitaxy.* Surface Science, 2002. **500**(1-3): p. 189-217.
35. Bradley, R.S. and S. Cotson, *The Vapour Pressure and Lattice Energy of Hydrogen-bonded Crystals. II Alpha-anhydrous and Beta-anhydrous Oxalic Acid and Tetragonal Pentaerythritol.* Journal of the Chemical Society, 1953(JUN): p. 1684-1688.

Chapter 3

Terephthalic acid on Cu(110) and Cu(111)

In this chapter, the assembly of TPA on Cu(110) and Cu(111) is addressed. This is to both highlight the potential effects of the molecule-substrate interaction and its consequences on the design and construction of supramolecular structures on metal surfaces, and to provide a reference for later studies utilising OA decoupling layers. These two surfaces, shown in Figure 3.1a and b, have been chosen as they both interact strongly with organic species but exhibit significantly different reactivities and atomistic structures. These differences will ultimately prove to have a significant effect on the assembly behaviour of TPA.

When TPA, shown in Figure 3.1c, is deposited onto metal substrates, it adsorbs in a flat-lying geometry due to the interaction between its π-electrons and the

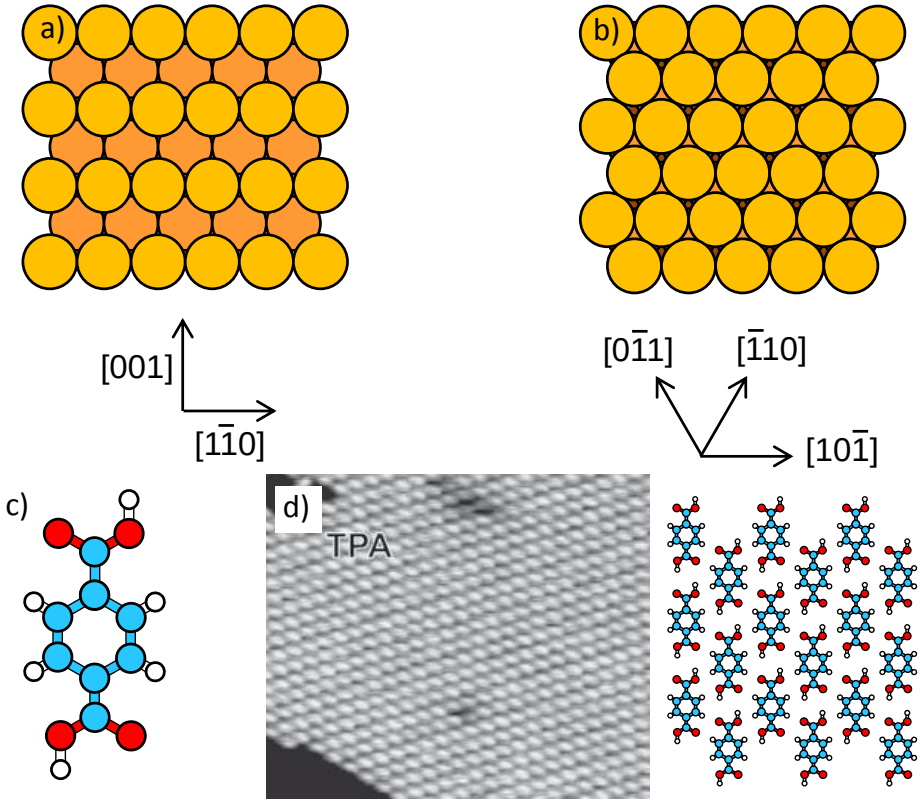

Figure 3.1 a) and b) plan views of the (110) and (111) surfaces. c) Molecular structure of TPA. d) STM image (adapted from reference [5]) and schematic of the TPA brickwork superstructure.

surface [1]. The nature of its assembly depends strongly on its chemical state. If deposited onto relatively inert, weakly-interacting substrates such as Ag(111), Au(111) and Pt(111), TPA will remain intact. In almost all such cases, it assembles into the so-called brickwork structure, illustrated in Figure 3.1d: Dimeric H-bonds form between carboxyl moieties on different molecules, resulting in the development of 1D chains [2-7]. These chains in turn stack laterally in an offset manner through weak dispersion forces [8].

When deposited onto reactive surfaces, the carboxyl moieties can be deprotonated, which increases the strength of the molecule-substrate interaction [9]. The resulting terephthalate (TP) are no longer capable of forming the 'normal' H-bonds, thus precluding the formation of the brickwork phase described above.

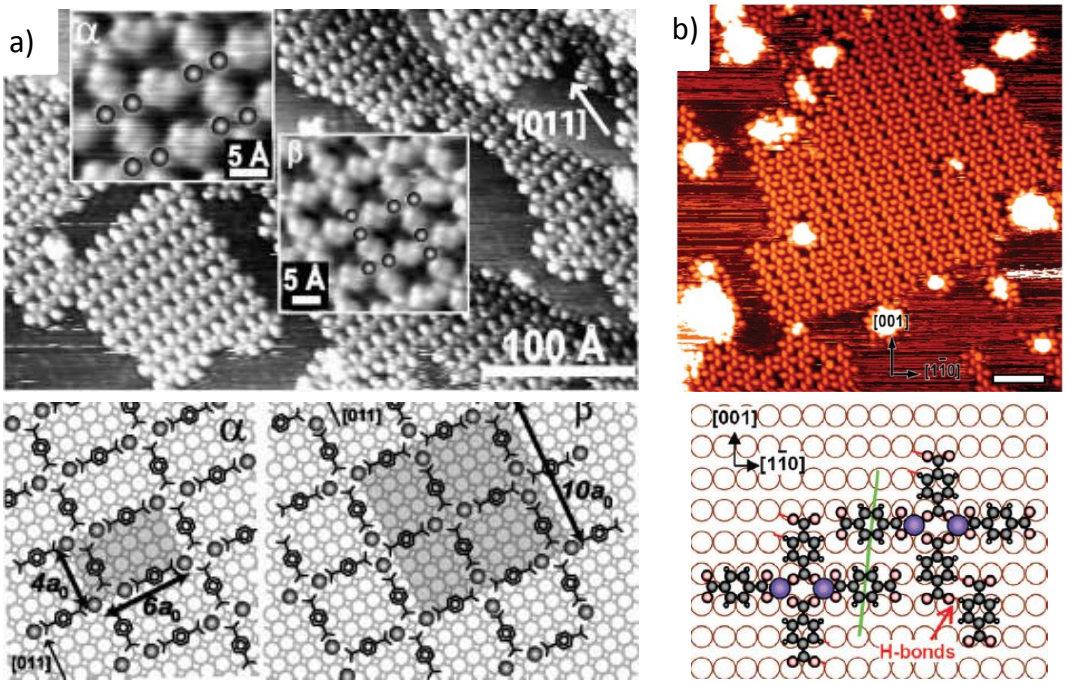

Figure 3.2 Examples of TP MO structures. a) STM images and structural models of the porous Fe-TP films obtained on Cu(001), adapted from reference [17]. b) STM image and structural model of the chiral Fe-TP 'flowers' fabricated on the Cu(110) surface, adapted from reference [16].

However, deprotonation does open up two further intermolecular bonding possibilities. By interacting with the aromatic protons in neighbouring molecules, *ionic* H-bonds can be formed [9-11]. Alternatively, MO complexes can be constructed through coordination to metal adatoms. These adatoms can be provided from the substrate itself [12] or from external sources, resulting in so-called 'intrinsic' [13] or 'extrinsic' [14-17] MO structures. In many cases, TP appears to favour rectangular, porous motifs via coordination to adatoms pairs, as illustrated in Figure 3.2.

One important exception reported to the above behaviour is the case of TPA on Pd(111) [10]. The reactivity of Pd results in partial deprotonation of the adsorbate, generating a mixture of fully protonated and fully deprotonated species. The intact TPA assembles into spatially isolated 1D chains that exhibit no lateral

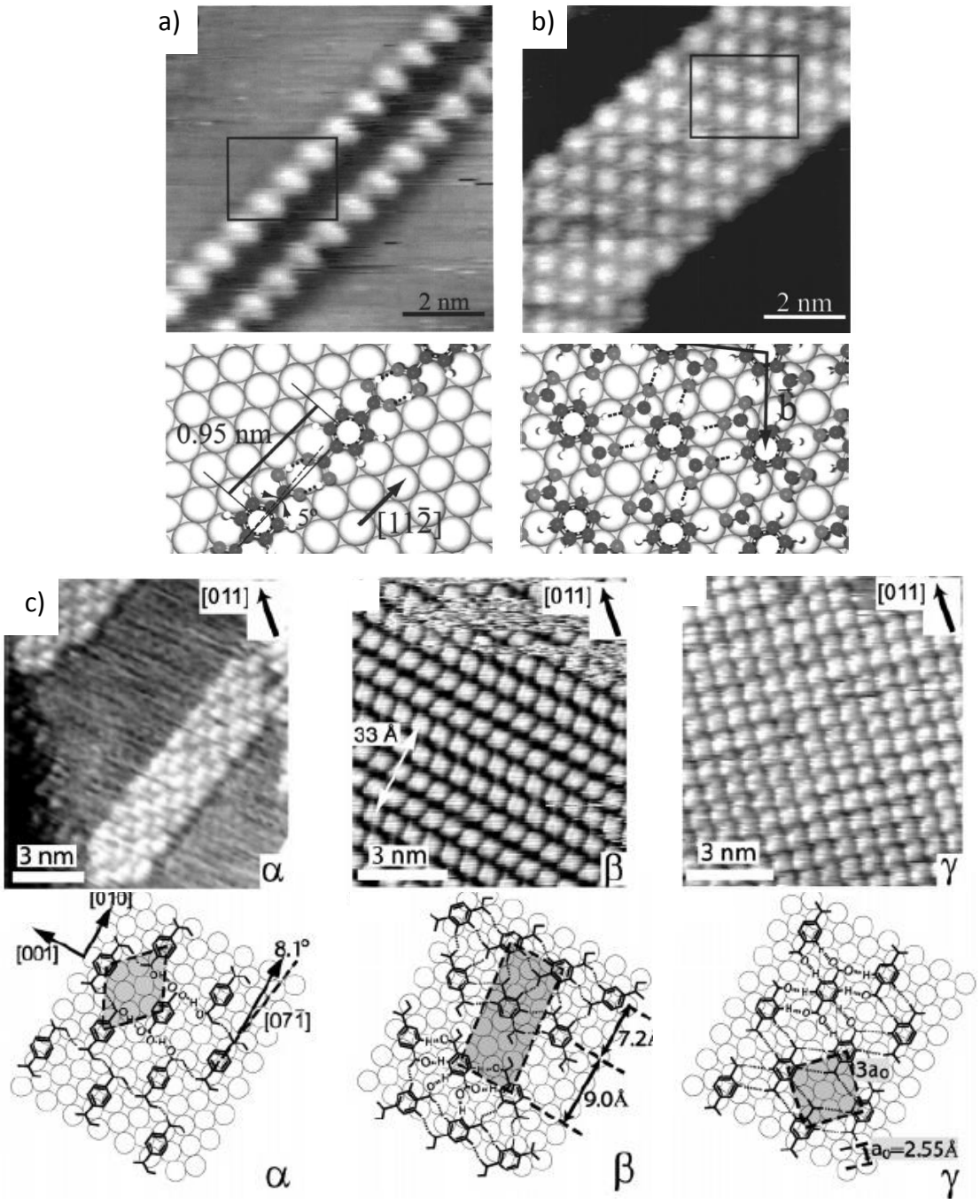

Figure 3.3 STM images and structural models of the TPA a) 1D chains and b) TP brickwork-like structure obtained on the Pd(111) surface. Adapted from reference [10]. c) STM images and corresponding models of the three temperature-dependent TPA phases observed on Cu(001). Adapted from reference [11].

stacking (Figure 3.3a). The TP combine into a supramolecular structure very similar to the brickwork pattern. However, in this motif, the TP interact via ionic H-bonds

between neighbouring ‘chains’, as shown in Figure 3.3b.

The assembly of TPA has also been extensively explored on the Cu(001) surface as a function of both temperature and molecular coverage [9,11,18]. XPS reveals that TPA remains intact when deposited onto a LT substrate, but gradually deprotonates when the temperature is increased above RT. STM measurements, shown in Figure 3.3c, demonstrate two irreversible phase changes as the sample is heated. At LT, the brickwork-like α structure is observed, characterised by H-bonds between TPA in neighbouring chains. At RT, partial deprotonation results in a mixture of fully- and mono-deprotonated TP. The two species are incorporated into a new assembly, labelled the β-phase, which is stabilised by a mixture of normal and ionic H-bonds. Complete deprotonation occurs at 388 K, inducing the formation of the closely packed γ-phase, which is reported to be stabilised by a complex surface-mediated assembly mechanism [9,19]. A further phase was later identified when a sufficiently high TPA coverage was produced: After a complete monolayer of the γ motif is formed, additional molecules can be incorporated into the first layer by compressing the TP film into a more densely-packed one with a c(3×5) superstructure [20].

Previous LEED and RAIRS characterisation of TPA on Cu(110) revealed that it initially adsorbs in a flat-lying geometry, is fully deprotonated and assembles into a *p*(10×2) superstructure [21]. At high molecular coverage, this reorganises into a densely-packed vertically-standing film, where only one carboxyl moiety is deprotonated. The latter phase has also been further investigated with DFT [22]. Some ambiguity remained regarding the exact chemical transformation involved in this process: Does the TPA regain a proton during reorganisation, or does the film retain a flat-lying, fully-deprotonated templating layer similar to that observed in the

growth of benzoate on Cu(110) [23]? A comparable upright geometry of TPA on Cu(001) has also recently been reported, where vertically-standing TPA is observed to be adsorbed on top of the c(3×5) TP superstructure described above [18].

In the first part of this chapter, the assembly of TPA on Cu(110) is characterised as a function of coverage and, to some degree, temperature. The reactivity of Cu(110) and its abundance of adatoms at RT [24] result in the formation of a number of different flat-lying MO phases, whose exact structure can be tuned through careful control of the molecular coverage. The transitions between these phases is rationalised by the DFT-calculated free energies of adsorption for TPA in the different structural motifs. The second part of the chapter is devoted to the assembly of TPA on Cu(111). At RT, it adsorbs intact and assembles into a brickwork-like structure, where the molecular separations are either uncharacteristically compressed or elongated. An analytical model is presented that reveals this arises from an interplay between the molecule-molecule and adsorbate-substrate interactions that govern the self-assembly process. In addition, the formation of different metal-TP complexes has been investigated, revealing a variety of structures that illustrate the effects of different adatoms on MO complex formation.

3.1 TPA on Cu(110)

The work presented in this section is the result of a collaboration with Dr Yeliang Wang, who performed the RT-UHV-STM measurements, and Dr Stefano Fabris, who implemented the DFT calculations [25]. The XPS measurements were performed at the VUV beamline at the ELETTRA synchrotron in Trieste, Italy.

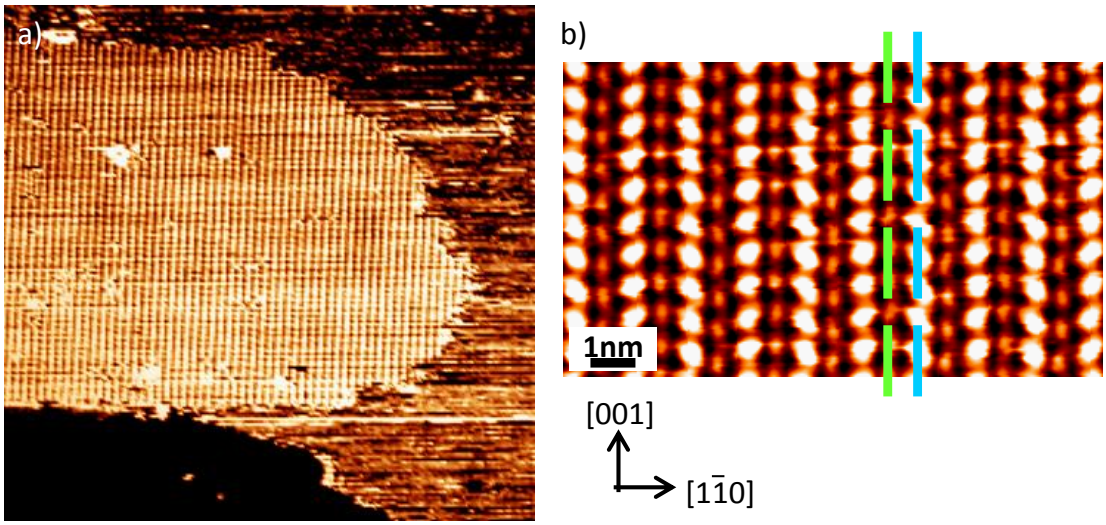

Figure 3.4 a) and b) STM images of the (10×2) TPA structure. The blue dashed lines highlights the molecular rows, whilst the green highlights the adatom rows. a) I=800 pA, U=-1.5 V. b) I=800 pA, U=-1.2 V.

3.1.1 The (10×2) structure

Figure 3.4 shows typical STM images obtained after depositing small amounts (less than 1 monolayer) of TPA onto the Cu(110) surface at RT. Large, compact islands are observed, which become larger and fewer upon annealing to 450 K. Increasing the TPA coverage results in the islands growing larger and more numerous, until the substrate is entirely covered.

A distinctive characteristic of this phase is the appearance of its internal structure, which, as shown in Figure 3.4b, consists of alternating bright and dark rows oriented along the [001] direction. The former, marked by the blue dashed line, consist of 7.2±0.6 Å long elliptical protrusions that form an angle of ±50° with respect to the [001] direction. Within each row, the features have only one orientation. These protrusions are assigned as individual, flat-lying TPA, since their size and shape match those obtained in previous STM measurements [2,10,11,16]. The darker rows, denoted by the green dashed line, consist of Cu adatoms, in line

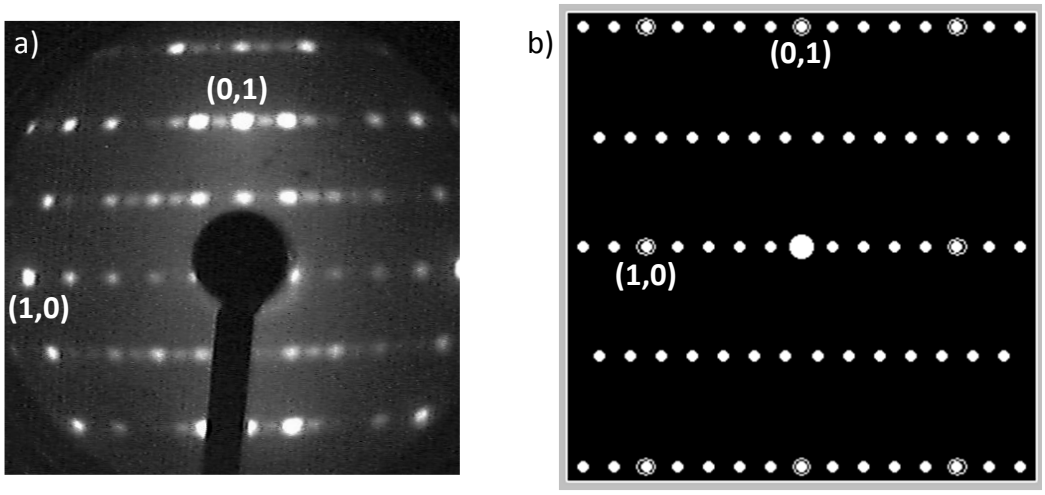

Figure 3.5 a) LEED pattern of the (10×2) TPA network on Cu(110). Two of the crystallographic spots are labelled. E=60 eV. b) c(5×2) LEED pattern as simulated by the LEEDpat3.0 software [28].

with previous experiments [13,26,27] and with the DFT calculations described below.

Along the $[1\bar{1}0]$ direction, the separation between successive molecular or Cu adatom rows is 12.7±0.2 Å, which corresponds to 5× Cu lattice spacings. Given that the TPA rows alternate in orientation, the total unit cell must contain two TPA and two Cu adatom rows. Therefore, the total periodicity along the $[1\bar{1}0]$ direction is 10× Cu lattice spacings. Along the [001] direction, the separation between equivalent protrusions is 7.2±0.2 Å, corresponding to double the lattice spacing along the [001] direction. Therefore, the total unit cell of the molecular superstructure is (10×2).

This assignment is, at least in principle, supported by LEED characterisation of the molecular film. Previous LEED measurements reported a *p*(10×2) LEED pattern for the flat-lying phase [21]. In this work, the obtained LEED pattern, shown in Figure 3.5a, is considerably complex and its analysis is not straightforward. The incident electron beam can be scattered by both molecules and adatoms, which have

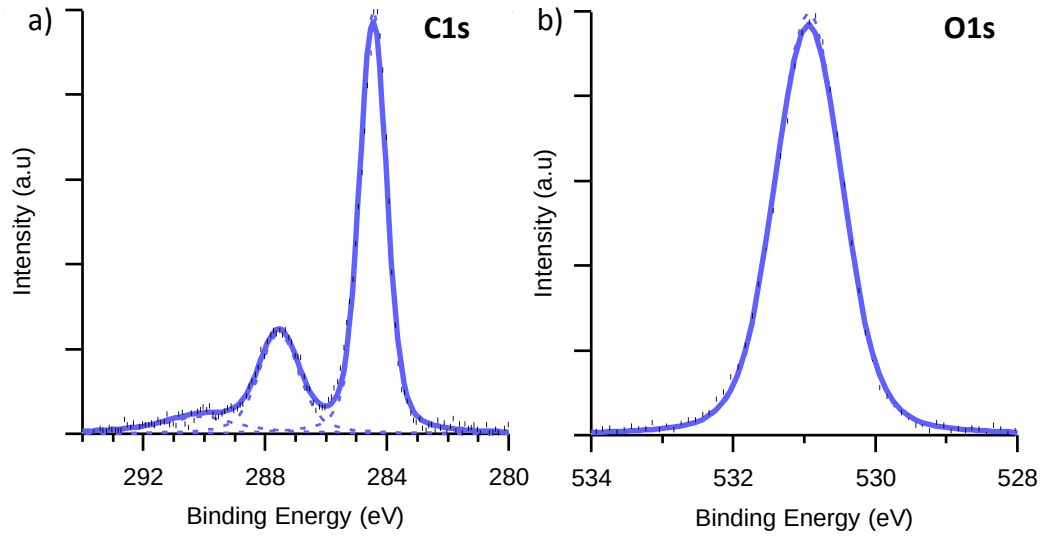

Figure 3.6 a) and b) C 1s and O 1s XPS spectra of the (10×2) TPA layer. The C 1s shows peaks at 284 eV and 288 eV, representing the aromatic and carboxylate carbons, respectively. The O 1s shows only a single, narrow peak, centred at 531 eV, arising from the chemically-identical O atoms in the carboxylate moiety.

slightly different superstructures; the TP are arranged in a (10×2) array, whilst the adatoms are in a c(10×2). Furthermore, these sublattices will scatter the electrons with different intensities, complicating the analysis. Finally, as the LEED spot on the sample is comparatively large (~2 mm), it is possible that the observed pattern also incorporates different molecular structures (see the following sections), which could result in different periodicities along the $[1\bar{1}0]$ direction. It is perhaps for these reasons that the observed LEED pattern is more complex than expected. It seemingly consists of two patterns with different intensities; a c(5×2) array of brighter spots and a (10×2) of dimmer spots. A simulated c(5×2) LEED pattern is shown in Figure 3.5b [28]. The LEED pattern is, however, clearly compatible with a 2× periodicity along the [001] direction, and possibly also with the 10× periodicity along the $[1\bar{1}0]$.

The STM data described above suggests that the TPA forms a MO structure with Cu adatoms, strongly suggesting the adsorbates are deprotonated to form TP. Confirmation of this is obtained from XPS measurements, which reveal

characteristic ‘chemical fingerprints’ of TP in both the C 1s and O 1s spectra [9-11]. The C 1s spectrum shown in Figure 3.6a exhibits two peaks, which are centred at approximately 284 eV and 288 eV. Previous XPS measurements of benzyl carboxylic acids have shown that the peak at 284 eV corresponds to the aromatic C atoms and that at 288 eV to those in the carboxyl moiety [10,11,13,29]. This assignment is supported by the relative intensities of the two peaks, which are indicative of the number of emitters from which the signal arises. The two peaks have a ratio of 3:1, as expected for an intact TPA C backbone. The energy of the carboxyl peak is sensitive to the protonation state of the carboxyl moiety; for example, XPS previous measurements on similar molecule-on-metal systems indicate that deprotonation shifts the energy of the carboxyl peak from approximately 289 eV to 288 eV [10,13,29-31]. The observed binding energy of the carboxyl peak here therefore supports the assertion that TPA is fully deprotonated on the Cu(110) surface at RT.

The O 1s spectrum shown in Figure 3.6b also confirms this conclusion. A single, narrow peak (full-width at half-maximum is ~1.1 eV) is observed, centred at 531eV. If the TPA were protonated, two peaks would be observed for the two inequivalent O atoms in the carboxylic moiety [11,30,32]. Such peaks are separated by approximately 1.3-1.5 eV but are often resolved as a singular broad peak with a full-width at half-maximum of ~2.5 eV [33-35]. The peak demonstrated here cannot, however, be resolved into two sufficiently separated peaks due to its relative narrowness, and thus is assigned unambiguously as a carboxylate O signal. The O 1s spectrum therefore supports the conclusions from the C 1s spectrum; the molecules are fully deprotonated, becoming TP, when adsorbed on the Cu(110) surface at RT.

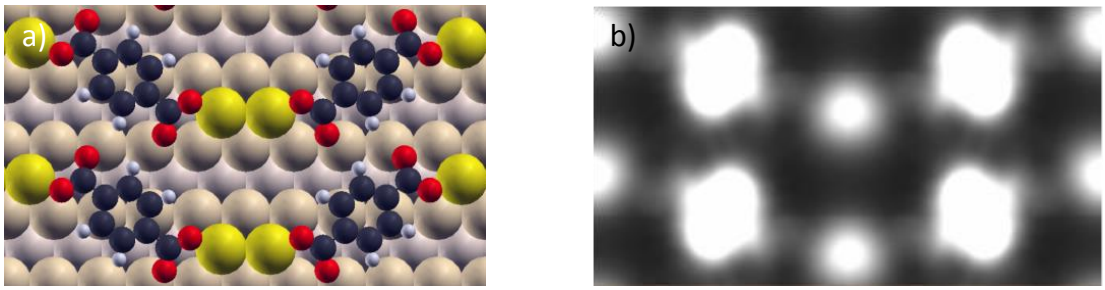

Figure 3.7 a) and b) Model and simulated STM image of the lowest energy (10x2) TPA structure, as calculated by DFT. The simulated image was obtained using the DOS between the Fermi energy and a bias potential of 0.5 eV.

Based on the STM, LEED and XPS results, first-principles DFT calculations were performed to determine the most favourable atomistic configuration compatible with the experimental data. Figure 3.7a shows the lowest energy structure for an ordered MO supramolecular film with a (10×2) supercell that is consistent with the experimental data. The TP are arranged in a flat-lying geometry interacting with Cu adatoms *dimers*. Along the [001] direction, ionic H-bonds are formed between the O atoms that are not coordinated with adatoms and neighbouring aromatic protons. The simulated STM image, Figure 3.7b, is in close agreement with the STM data.

This structure corresponds to a TP coverage of ~1 nm^{-2}. In the sub-monolayer regime, where the coverage is <1 nm^{-2}, annealing to 450 K causes no modifications to the islands internal structure. However, a new phase can be generated by first increasing the TPA coverage beyond a complete monolayer (i.e. beyond the coverage where the (10×2) covers the entire surface) and annealing to 450 K. The additional adsorbates are initially bound weakly on top of this layer, resulting in a high lateral mobility that inhibits their characterisation with STM. If the sample is then annealed, the multilayer film is organised into a new, single layered structure with a molecular density of approximately 1.5 nm^{-2}.

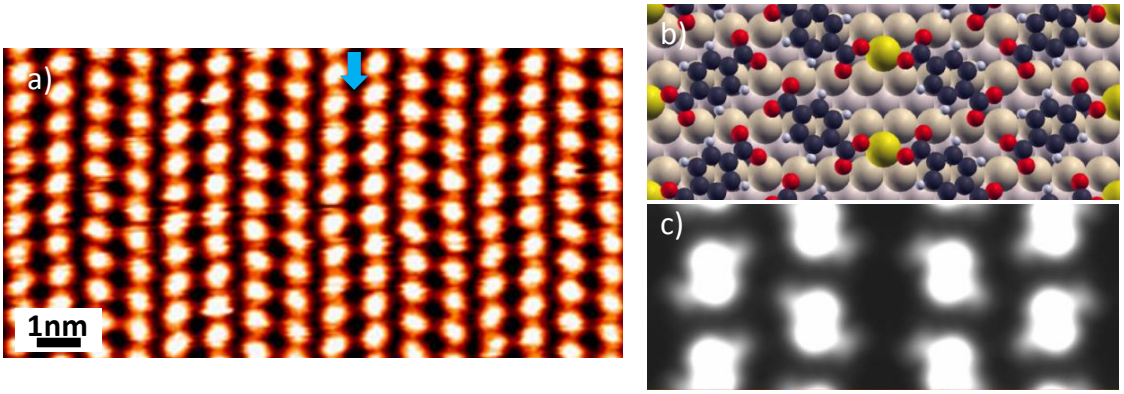

Figure 3.8 a), b) and c) STM image (I=800 pA, U=-1.2 V), model and simulated STM image of the (14×2) structure on Cu(110), respectively. The blue arrow in (a) shows the position of the Cu adatoms, imaged as a darker line.

3.1.2 The (14×2) structure

The STM image shown in Figure 3.8a reveals that this new film exhibits a different internal structure to the previous one. Instead of the alternating pattern of brighter and darker protrusions characteristic of the (10×2) phase, the new one exhibits more densely packed rows with uniform contrast. Moreover, the TP species, again imaged as elliptical features with the same ±50° orientation with respect to the [001] direction, are arranged in tightly packed double rows that are intercalated by darker lines (marked by the blue arrow in Figure 3.8a). The molecules within each double row are arranged in a herringbone motif. The distance between the centres of subsequent double rows or between the darker lines is 17.8±0.3 Å, corresponding to 7× Cu lattice spacings along the $[1\bar{1}0]$ direction. However, sequential rows are specular symmetric, and thus the actual periodicity is 14× that of the substrate. Along the [001] direction, the TP are again separated by 2× Cu lattice spacings, and thus the total unit cell is (14×2) with respect to the Cu(110) surface.

XPS measurements of this phase reveal spectra very similar to those obtained for the (10×2) phase; the C 1s spectrum contains two peaks for the aromatic and

carboxylate C atoms and the O 1s has only a singular narrow peak, indicating that the TPA C backbone is intact and that the carboxyl moieties are deprotonated.

This structure is usually observed coexisting with others, including the (10×2). Even within the same STM image, it can be possible to image multiple periodicities along the $[1\bar{1}0]$ direction. If the TPA coverage is finely controlled such that the molecular coverage is ~1.5 nm^{-2}, the (14×2) phase is obtained in majority. With this in mind, LEED characterisation of this phase is not exceptionally challenging and is not presented here; the diffraction pattern obtained in a LEED measurement is a superposition of all the structures within the LEED spot and, therefore, in this case the pattern would be highly complex and contain configurations corresponding to multiple periodicities.

DFT has also been used to determine the lowest energy atomistic configuration corresponding to the observed (14×2) phase and to ascertain the possible inclusion of adatoms. The configuration and the corresponding simulated STM image are shown in Figure 3.8b and c. The double rows consist of TP in a herringbone arrangement interacting via ionic H-bonds, reminiscent of the c(3×5) phase reported on Cu(001) [18]. The double rows are in turn separated by rows of Cu adatoms, which interact with the TP via coordination bonds. In contrast with the (10×2) superstructure, here only one of the carboxylate moieties per TP binds to adatoms, the other one being bound via ionic H-bonds to neighbouring molecules.

3.1.3 (The 6×2) structure

A second phase transition can be induced by further increasing the molecular coverage and annealing to 450 K. Figure 3.9 shows an example STM image of the new structure, again revealing [001]-aligned rows of TP. The bright features are

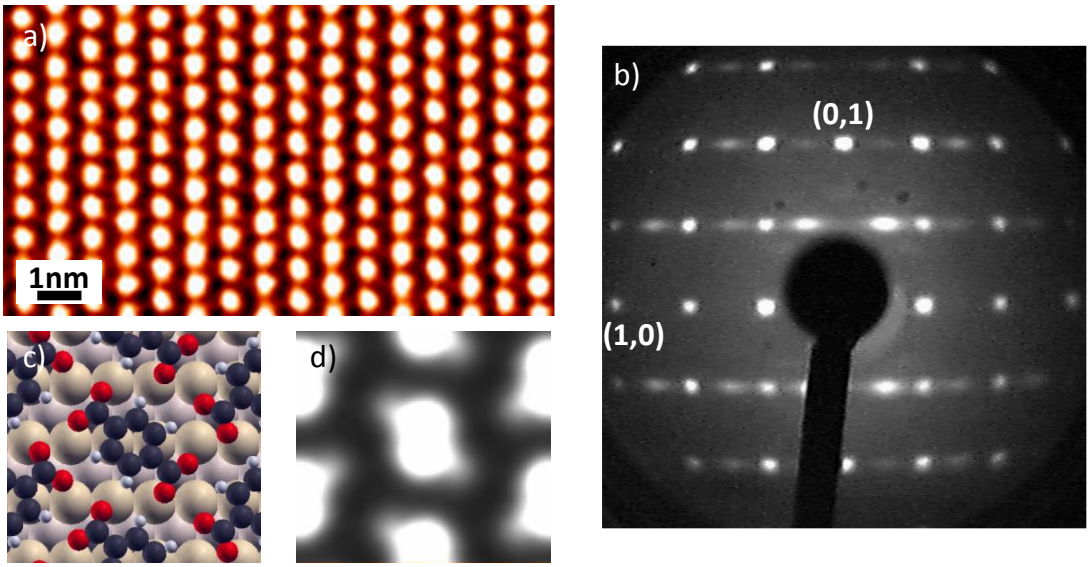

Figure 3.9 a) and b) STM image and LEED pattern of the (6×2) TP phase on Cu(110). a) I=800 pA, U=-1.2 V. b) E=61 eV. c) and d) DFT-calculated lowest energy structure and simulated STM image of the (6×2) film.

now less elliptical in shape, but retain the same orientation with respect to the chain direction. In contrast to the previous phase, the TP chains are now uniformly spaced along the $[1\bar{1}0]$ direction, exhibiting an inter-row periodicity of 7.7±0.3 Å or 3× Cu lattice spacings. As the in-row intermolecular separation is 2× Cu lattice spacings and subsequent rows exhibit specular symmetry, this new film has a (6×2) superstructure. The LEED pattern shown in Figure 3.9b is compatible with this assignment. XPS characterisation of this phase shows an unchanged chemical state to those in the previous films; both the C 1s and O 1s spectra indicate the molecules are deprotonated.

Figure 3.9c shows the DFT-calculated lowest energy configuration for a TP film with a (6×2) superstructure. Unlike the previous two structures, this phase contains no Cu adatoms. Instead, the (6×2) consists entirely of TP interacting via ionic H-bonds arrayed in the same herringbone motif observed for the double-rows

in the (14×2) phase. The simulated STM image, shown in 3.9d, supports this structural assignment.

Increasing the TPA coverage further and annealing does not result in additional phase transitions. It is therefore likely that the (6×2) is the most densely-packed structure possible for TP without reorientation into the perpendicular geometry previously indicated by RAIRS measurements [21]. A vertically standing phase has, however, proven difficult to reproduce with the current experimental conditions. This may be because, once adsorbed flat on the metal surface, the barrier towards molecular reorientation is very high. The observed carboxyl deprotonation enhances the molecule-substrate interaction, which further increases this energetic barrier. It is possible that the experimental parameters used here, such as the molecular flux and deposition lengths, or kinetic limitations play an important role, but this has not been extensively investigated.

3.1.4 Intact TPA on Cu(110)

To obtain reference spectra of intact TPA on the Cu(110) surface, a multiple layer thick film was prepared. A high molecular flux was used and therefore its thickness is not *a priori* known. Furthermore, the substrate was held at 190 K during deposition, resulting in a different, unknown sticking coefficient of the impinging molecules. The surface was held below RT to inhibit deprotonation and the sublimation of metal adatoms from steps [12]. The resulting XPS spectra are shown in Figure 3.10.

The C 1s spectrum in Figure 3.10a exhibits three distinct peaks. The largest is the aromatic peak, shifted ~1 eV lower in binding energy with respect to the monolayer films to 285 eV. The other peaks are located in the carboxyl region, at

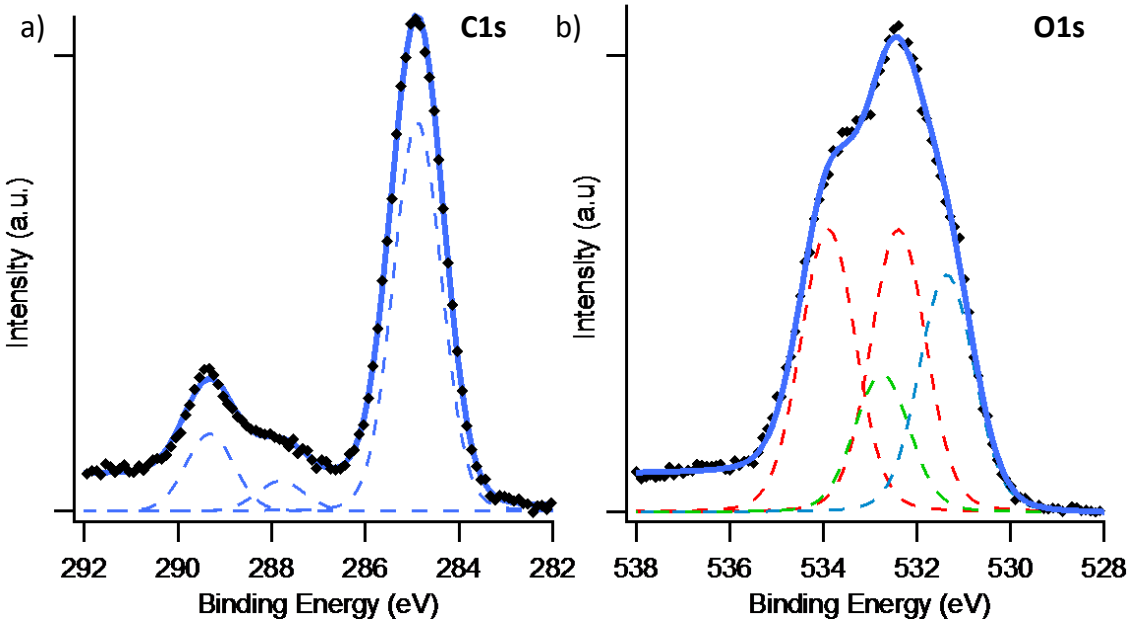

Figure 3.10 a) and b) C 1s and O 1s XPS spectra, respectively, of the TPA multilayer film, measured at 190K. In the O 1s spectrum, the carboxylic peaks have been coloured red, the carboxylate green and the contaminant peak green.

approximately 288 eV and 289 eV. The smaller of the two at 288 eV matches that described in the previous section and is therefore assigned as carboxylate. The larger peak at approximately 289 eV has no counterpart in the monolayer spectra and thus is assigned as the carboxylic acid moiety, in agreement with XPS measurements of other carboxyl species [10,11,29,30,32,33,35,36].

The O 1s spectrum, Figure 3.10b, is considerably complex and is ultimately deconvoluted into four distinct peaks. The first is at 531 eV, which, based on the monolayer spectra is assigned as carboxylate. The peaks at 532 and 533 eV are assigned as the alcohol and keto-functionalities, respectively, of the intact carboxylic acid moiety, in line with previous measurements [6,11,30,33]. The final, smallest peak is centred at 532.4 eV, which cannot be attributed to either TPA or TP. Instead, it is assigned to contaminants that have advantageously adsorbed onto the surface as a consequence of the low substrate temperature. These pollutants are most likely

species such as CO and CO_2, which are common residual background gases in vacuum systems and typically only adsorb on Cu at LT [37-39].

The XPS data, therefore, reveals that, even at 190 K, some degree of TPA deprotonation occurs. Assuming that the first layer is complete and is fully deprotonated, and that the TPA in subsequent layers remain intact, it is possible to estimate the thickness of the film by comparing the ratios of carboxylate:carboxylic signals in the two spectra. In both, the peak ratios are 1:2.4 (for the O 1s, the sum of the two carboxylic signals is used), suggesting the TPA film is 2-3 monolayers thick. However, this approximation that does not consider the potential for signal attenuation due to, for example, the limited electron escape depth.

3.1.5 Phase transitions of TPA on Cu(110)

The STM and LEED data presented above have highlighted a number of different TP structures, the nature of which is determined by the molecular coverage. The DFT-calculated free energies of formation per molecule for the three structures grant some insight into the observed phase transitions. The energies, summarised in Figure 3.11a, are reported in comparison to that of a gas-phase TP species and consider the contribution of the Cu adatoms using their calculated formation energy from steps. Critically, the energies *descend* with increasing TP density. This energy trend, depicted schematically in Figure 3.11b as a function of molecular coverage, can also be used to rationalise the two observed phase transitions. At sub-monolayer coverage, the TP species assemble into the (10×2) structure as it is the most energetically favourable, in line with the experimental data. As more TPA is added, the total energy of the system decreases linearly (i.e. becomes more favourable), as shown by the red line in Figure 3.11b. Once the monolayer is saturated, additional

a)	(10×2)	(14×2)	(6×2)
Formation energy / molecule (eV)	-5.8	-5.5	-5.2

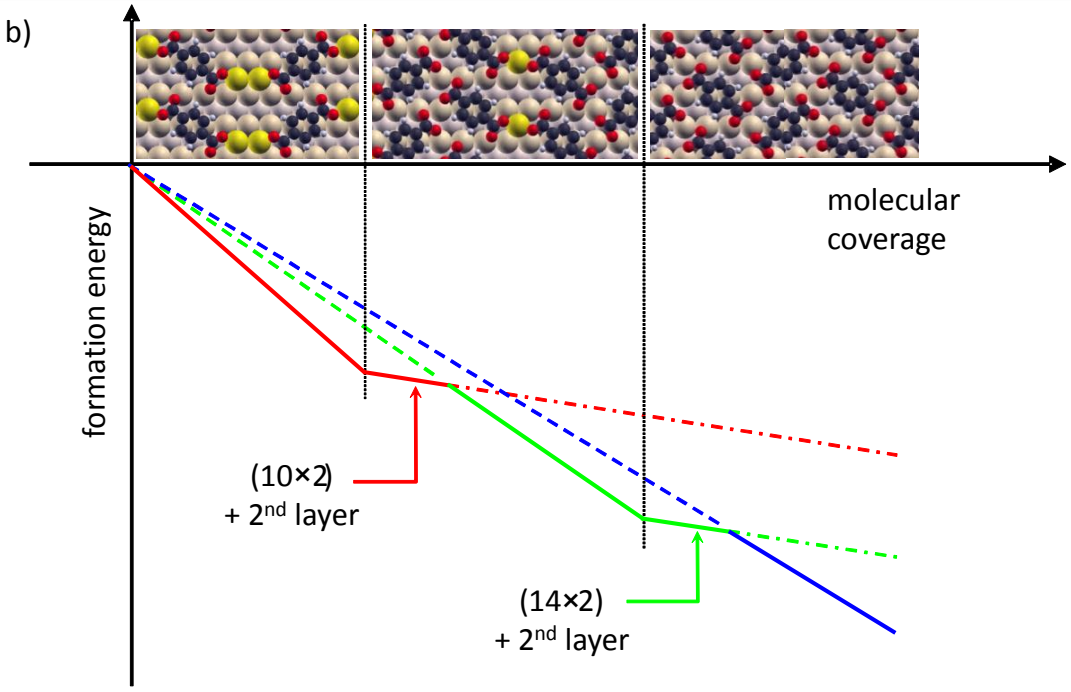

Figure 3.11 a) Summary of the DFT-calculated free energies of formation per molecule for the three TP structures obtained on Cu(110). b) Schematic of the total adsorption energy with increasing TPA coverage. The red, green and blue profiles show the adsorption energies for the (10×2), (14×2) and (6×2) phases respectively. Dashed lines represent the energy the system would have if all molecules were in the same phase. Dash-dotted lines are a tentative (not calculated) representation of the energy for second layer molecules. The full line indicates the actual supramolecular configuration adopted by the system.

molecules can only be adsorbed on top of the first layer, which, as indicated by the red dot-dashed line, is less favourable due to their weaker interaction with the metal surface. As the coverage increases, it becomes more energetically favourable for the multilayer film to reorganise and incorporate the additional species into the first layer. However, there is apparently some energetic barrier towards this reorganisation at RT, as otherwise it would occur spontaneously. By annealing to 450 K, this barrier is overcome and the (14×2) phase is formed. Whilst the DFT

reveals that this structure is less energetically favourable per molecule, the *total* energy is now reduced due to the greater TP density in the monolayer film. This argument is likely to also apply to the second phase transition between the (14×2) and (6×2) structures.

3.1.6 TPA on Cu(110) - summary

Using STM, LEED, XPS and DFT, three different TP phases have been characterised on Cu(110). They exhibit similar structures, albeit with varying numbers of incorporated Cu adatoms. These measurements illustrate that in, general, when adsorbed on reactive metal surfaces, molecular tectons can be strongly influenced by the innate chemical reactivity of the underlying metal, even at LT. Furthermore, it is a clear example of how assembly can be modified by the surface symmetry, strong adsorbate-substrate interactions and the inclusion of adatoms into the supramolecular structure.

3.2 TPA on Cu(111)

The following STM data has been obtained using a LT-UHV-STM purchased from Createc GmbH, which is described in more detail in Section 2.6. The theoretical work has been performed by Professor Alessandro Troisi and Dr Natalia Martsinovich. Additional details can be found in Section 2.5.

3.2.1 TPA H-bonded phase

When deposited onto a Cu(111) surface held at RT, STM measurements reveal that TPA assembles into narrow, elongated islands, as shown in Figure 3.12. These typically nucleate from steps and defects and exhibit preferential orientations with respect to the underlying metal: The long directions of the islands (see the blue

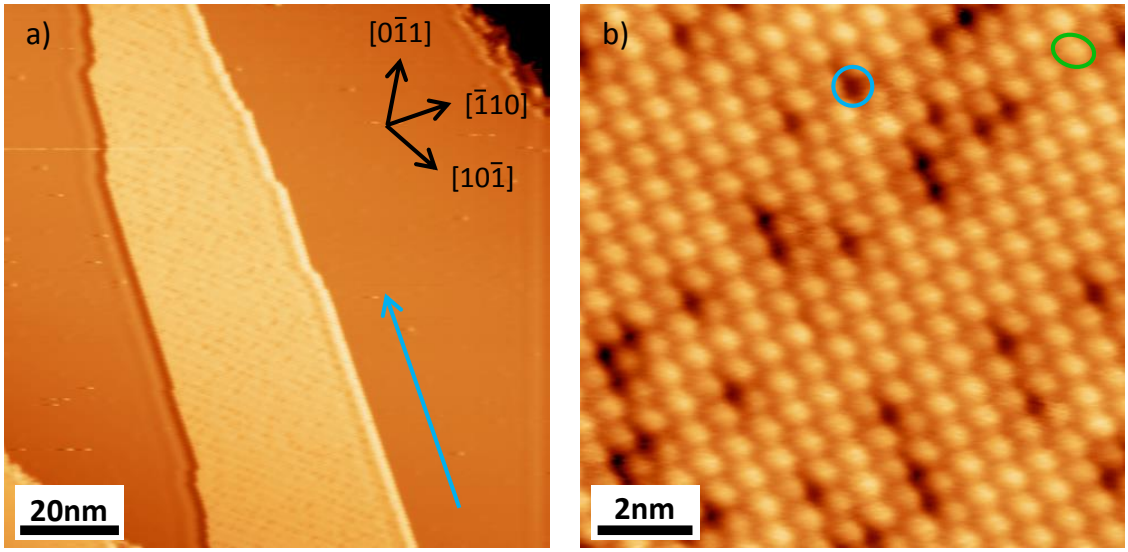

Figure 3.12 STM images of the TPA H-bonded network on the Cu(111) surface, after deposition onto a RT substrate. The blue arrow indicates the straight edge of the molecular island. a) I=50 pA, U=1.3 V. b) shows a zoomed-in image of the islands internal structure. The green oval highlights a single TPA molecule and the blue circle demonstrates a defect in the organic lattice. I=100 pA, U=-1.0 V.

arrow in Figure 3.12a) are aligned perpendicularly to the substrate crystallographic directions – i.e. along the [11$\bar{2}$], [1$\bar{2}$1] and the [$\bar{2}$11] directions.

Close inspection of the molecular islands (Figure 3.12b) reveals that their internal structure consists of a periodic array of oval protrusions that strongly resembles the brickwork motif observed previously [2-7]. As before with the Cu(110) surface, the elliptical protrusions are assigned as individual TPA in a flat-lying geometry (one is highlighted by the green oval in Figure 3.12b). Each molecule is aligned perpendicularly to the crystallographic directions.

The brickwork-like arrangement of protrusions could be taken as an indication that the TPA has adsorbed intact and that no deprotonation has occurred. However, as a similar structure has been reported on Pd(111) for fully deprotonated TP [10], further evidence is essential to support this conclusion. This is obtained by observing the effects of annealing treatments, which are described in more detail in Section 3.2.2. In short, annealing above 353 K results in a transformation of the TPA

superstructure, generating a plethora of different motifs, several of which are identified as MO complexes. As the formation of such complexes is not limited by the availability of Cu adatoms at RT [40-43], the annealing step must be critical for the formation of the carboxylate moiety. Therefore, in the STM images shown above, the TPA must still be protonated.

Even after a brief inspection, there are immediately obvious differences between the monolayer shown in Figure 3.12b and the previously reported brickwork structure. The blue circle highlights one of many dark spots in the organic lattice. These are only observed between the carboxyl moieties, not between neighbouring TPA chains; in other words, they are located in the approximate position of the dimeric H-bonds. The TPA-TPA separation across these defects is 10.4±0.4 Å, corresponding to a distance of ~3.4 Å between the O atoms in the TPA carboxyl moieties either side of the dark spot. This indicates that the defects are actually gaps in the organic lattice due to an increased molecular separation. Approximately 15% of the H-bonds are elongated in this manner.

There does appear to be some degree of correlation between the locations of these spots; often the defects are aligned in short lines oriented diagonally from the TPA chain orientation (see purple box in Figure 3.13a). However, the extent of this alignment appears to vary significantly between different sample preparations. For example, Figure 3.13 shows STM images of two TPA films from different preparations; in 3.13a, some limited, local-scale defect correlation is observed, but in general their distribution is largely random, whilst in the 3.13b, the defects are seemingly organised into longer rows that are uniformly separated in the organic lattice. Because of the apparent preparation-dependence, the arrangement of defects has not been analysed in detail.

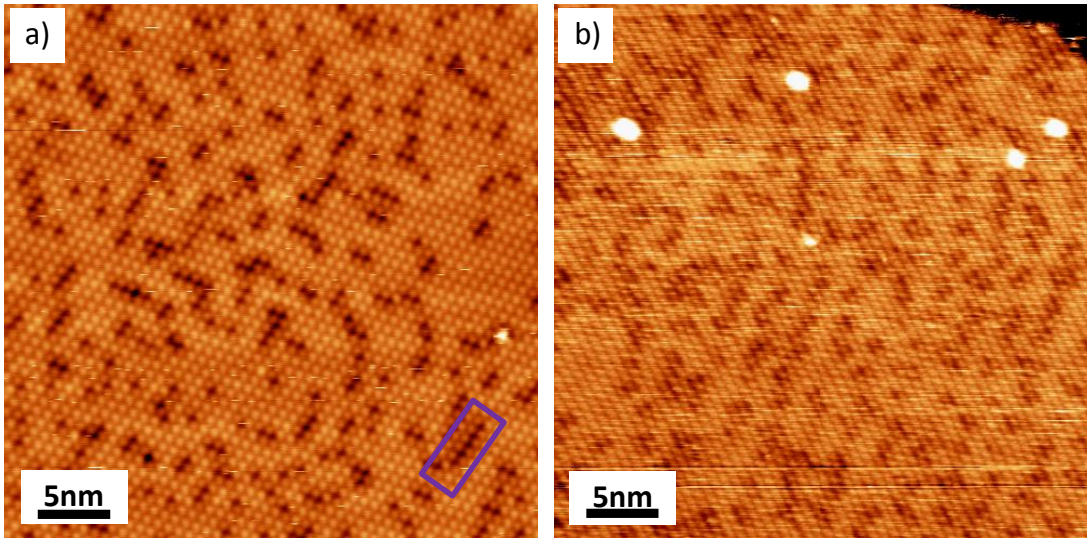

Figure 3.13 Two STM images showing a) weakly-correlated or randomly-arranged, and b) strongly-correlated distribution of defects in the TPA lattice. The two images have been obtained from different sample preparations. The purple box indicates a short chain of defects. a) I=210 pA, U=1.4 V. b) I=33pA, U=-0.9V.

A second important difference with respect to previous brickwork films is discovered when measuring the periodicity of the TPA where there are no defects. The intermolecular separation along the chains is 9.3±0.5 Å, corresponding to H-bond lengths of only 2.3 Å. Table 3.1 summarises the H-bonds lengths reported previously in other studies, revealing that the H-bond length measured here is considerably small; the typical TPA H-bond length is around 2.7-3.0 Å, implying that the separations observed on Cu(111) are approximately 10-25% smaller than those observed in similar films on weakly-interacting surfaces. They are also approximately 12-15% smaller than those observed in the bulk [44,45], suggesting that on Cu(111) the dimeric H-bonds are being significantly compressed from their ideal length.

To summarise, TPA adsorbs intact on Cu(111) at RT and assembles into a brickwork-like structure that is characterised by H-bonds that are either compressed or considerably extended. The reason for this unusual assembly, as mentioned in

Substrate	H-bond length (Å)	Reference
Au(111)	2.9 - 3.1	[2]
Ag(111)	3.0 *	[5]
Pd(111)	2.5	[10]
Pt(111)	2.6	[3]
Graphene / Pt(111)	2.8	[7]
Bulk	2.61 – 2.69	[44, 45]

Table 3.1 Summary of the dimeric H-bond lengths reported for TPA on a number of different weakly-interacting surfaces and in bulk TPA crystals. The * indicates a H-bond length that has been corrected to use a TPA molecular length of ~7Å.

essentially any publication dealing with supramolecular self-assembly at surfaces, is a 'subtle interplay' of intermolecular and adsorbate-substrate interactions [9,46,47]. In this particular example, the effect is relatively pronounced due to the strongly interacting nature of Cu(111). This interplay is, in general, poorly understood and is often used to justify unusual aspects of supramolecular assemblies without a detailed quantitative explanation of the exact cause or the effect. Moreover, it has not to date been studied in a manner that allows fundamental predictive models to be developed. With this in mind, TPA on Cu(111) is a perfect molecule-on-metal system with which to develop such a model. To achieve this, the characteristics of the two interactions and their resulting interplay have been investigated using a range of theoretical techniques, the results of which have been incorporated into a generalised algorithm that is capable of explaining the observed supramolecular assembly.

3.2.1.1 Theoretical investigation of TPA on Cu(111)

All of the theoretical work presented in this section has been performed by Dr Natalia Martsinovich and Professor Alessandro Troisi. Additional details can be found in Section 2.5.

The nature of the intra- and inter-chain interactions were first investigated using a series of MM calculations. Initially, the characteristics of the H-bonding were studied by calculating the total energy per molecule of TPA in isolated 1D chains as a function of the intermolecular separation (the **a** direction in Figure 3.14a). Details of the calculations can be found in Section 2.5.1, but in essence, a single TPA was located inside a periodic cell with dimensions **a**×**b**×**c**, as illustrated in Figure 3.14a. 1D chains were simulated using large **b** and **c** values. The intra-chain interactions were simulated by step-wise increasing the size of **a**, effectively increasing the length of the dimeric H-bonds, and calculating the total energy. The resulting potential energy profile is shown in Figure 3.14b, where the experimentally determined 'normal' molecular periodicity (green) and the TPA-TPA separation about the defects (blue) are also marked with dashed lines. The profile exhibits a Morse-like shape with a single energy minimum at 9.65 Å. This matches the periodicity reported for bulk TPA crystals [44, 45]. However, this is ~0.3 Å longer than the experimentally determined separation measured on the Cu(111) surface, confirming that the H-bonds are compressed. Moreover, no additional minimum is observed at larger separations, implying that there is an energetic penalty associated with the TPA-TPA distance observed around defects (~0.3 eV when compared with the ideal gas-phase H-bond length).

It may be that the proximity of neighbouring chains results in the formation of additional energy minima at larger intermolecular separations. This is thought

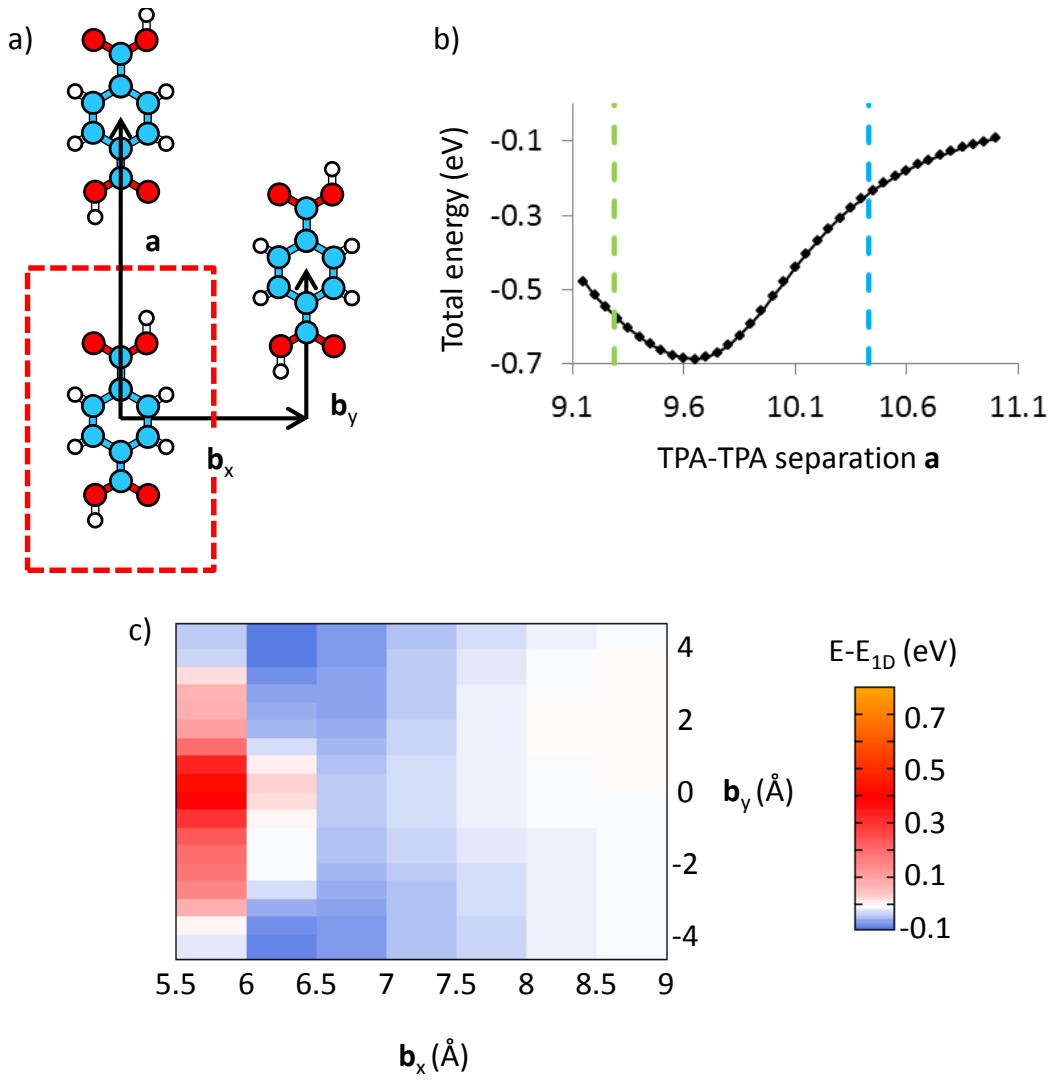

Figure 3.14 MM study of the TPA-TPA interactions. a) shows a schematic of the unit cell used in the MM calculations, revealing how the unit cell of the calculation was constructed to test the in-chain and inter-chain interactions. Vectors **a** and **b** define the size and shape of the unit cell which, for the case of a single TPA row, is shown by the red dashed lines. b) Potential energy profile calculated as a function of **a**. c) Potential energy surface as a function of $\mathbf{b}_x$ and $\mathbf{b}_y$ for a fixed value of **a**.

unlikely, as otherwise it would be expected on all solid surfaces and also in the bulk. However, to clarify whether this is the case, additional calculations have been performed whereby the dimensions of the unit cell where varied in a different manner. The **a** parameter was initially fixed at 9.65 Å, whilst the $\mathbf{b}_x$ and $\mathbf{b}_y$ parameters, which define the relative positions of neighbouring H-bonded TPA

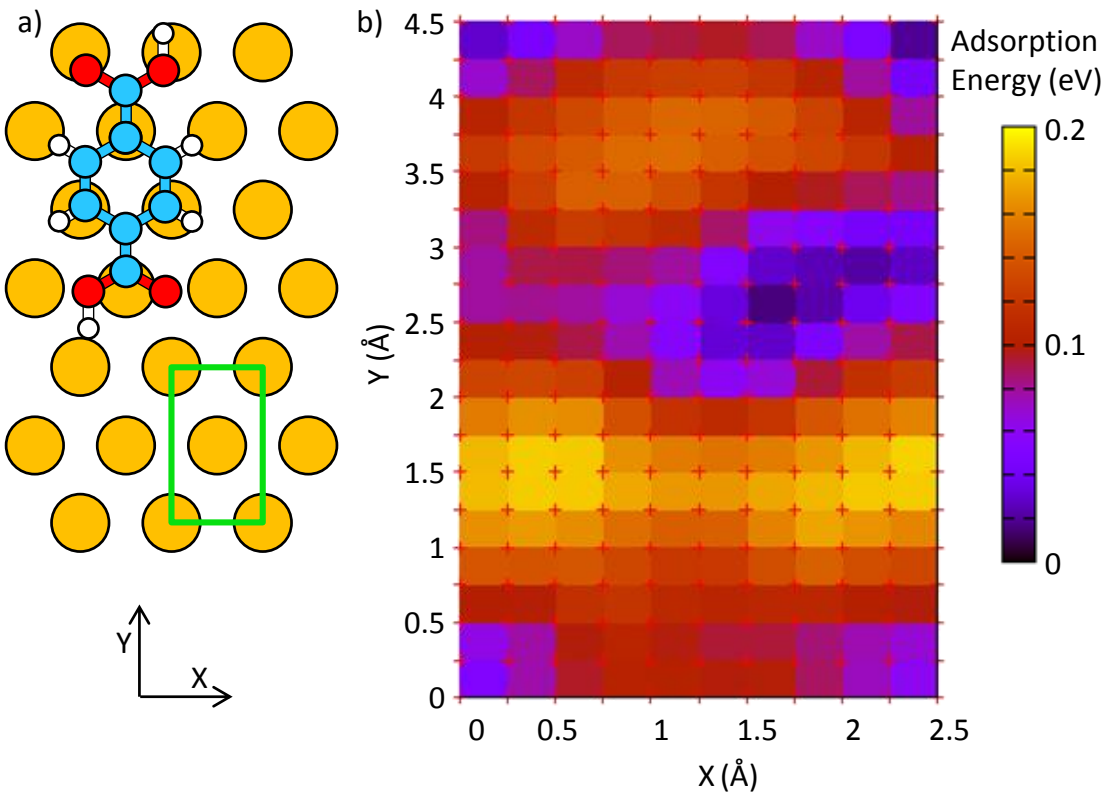

Figure 3.15 a) Model of the initial TPA arrangement on Cu(111) used in the DFT calculations. The green rectangle shows the space explored by the DFT calculations, corresponding to the DFT-calculated potential energy surface shown in (b).

chains, were varied. The corresponding potential energy surface (PES), shown in Figure 3.14c, reveals a single, clear minimum for the position of neighbouring molecules at $\mathbf{b}_x$~6 Å and $\mathbf{b}_y$~±4 Å. This is line with the experimentally-determined interchain separation of 5.5±0.3 Å. Critically, no second minimum is observed at different values of $\mathbf{b}_y$, indicating that inter-chain interactions are also not the cause of the experimentally observed defects. To confirm this conclusion, a third set of calculations were performed where **a**, $\mathbf{b}_x$ and $\mathbf{b}_y$ parameters were simultaneously varied about their lowest energy values. No additional energy minima were obtained in this manner, indicating that this is in fact the most energetically favourable structure based on intermolecular interactions alone.

The next step is to investigate the nature of the molecule-substrate interaction, which has been achieved using dispersion-corrected DFT calculations [48]. An isolated TPA molecule was initially placed on a 3-layer thick Cu(111) slab with the centre of its aromatic core located over a hexagonal close-packed hollow site. It is oriented with its long axis along the crystals $[11\bar{2}]$ direction, in line with the STM data, as shown in Figure 3.15a. The adsorbate was then moved laterally over the surface in 0.25 Å steps, such that the area shown by the green rectangle was explored. At each position, the adsorption energy was calculated, as defined in Equation 2.8. The resulting PES, shown in Figure 3.15b, reveals that the most energetically favourable adsorption site is actually that shown in Figure 3.15a, where the aromatic core is centred over the hexagonal close-packed hollow site. The darker pixels in the corners of the PES have approximately the same energy as this minimum as, due to the symmetry of the substrate, they correspond to similar adsorption sites. Deviation from the lowest energy position results in a rapid reduction of the adsorption energy by as much as 0.2 eV.

The shape of the PES is likely to be broadly similar for all (111)-terminated metal surfaces. However, the variations in the adsorption energy will significantly depend on the specific substrate material, with the case of Cu(111) being expected to cause considerably larger PES corrugation than other weakly interacting materials. For example, the corrugation of the Au(111) PES has been previously calculated to be as little as 0.05 eV [49]. It is therefore possible that on Cu(111) the molecule-substrate interaction could compete with that between adsorbates and may play a significant role in the assembly of TPA.

Calculating the effect of this adsorption energy variation requires both interactions and their resulting interplay to be simulated over a significant number of

adsorbates. This results in *ab initio* methods like DFT being unfeasibly expensive. Instead, a very general analytical method has been devised, which can predict molecular assembly based on the calculations of the intermolecular and molecule-substrate interactions described above. Moreover, the characteristics of the two can be reduced to two key parameters, which can, in a first approximation, be used to fully describe the molecular assembly. The current model is only applicable to self-assembly in 1D, but in principle can be readily expanded to also consider that in 2D.

The molecule-molecule and adsorbate-substrate interactions are first approximated using a Morse potential function, $\mathcal{F}(x)$, and a cosine function, $\mathcal{G}(x)$, respectively, as illustrated in Figure 3.16a. The characteristics of these functions, in particular the depth and positions of the energy minima are obtained from the MM and DFT calculations described above. As the functions have standard shapes, their *relative* characteristics can be described fully using just two parameters; $\mathcal{D}$, which is the ratio of the interaction strengths, and $\mathcal{L}$, which defines the ratio of molecular separations as defined by the intermolecular and adsorbate-substrate interactions. The latter of these is not necessarily the atomic periodicity of the substrate; for example, in this case it is the distance between hexagonal close-packed hollow sites along the $[11\bar{2}]$ direction of Cu(111). The specific values for TPA on Cu(111) obtained from the MM and DFT calculations described above are $\mathcal{D}$=3.45 and $\mathcal{L}$=2.07.

Once the two functions are established, a simple algorithm, shown in Figure 3.16b, can be used to determine the assembly of the organic film. First, a 'surface cell' is constructed from a 1D chain of P points along the x direction, whose separation is given by the periodicity of adsorption sites on the real metal surface. The molecules are simulated with a second chain of N points, referred to as the

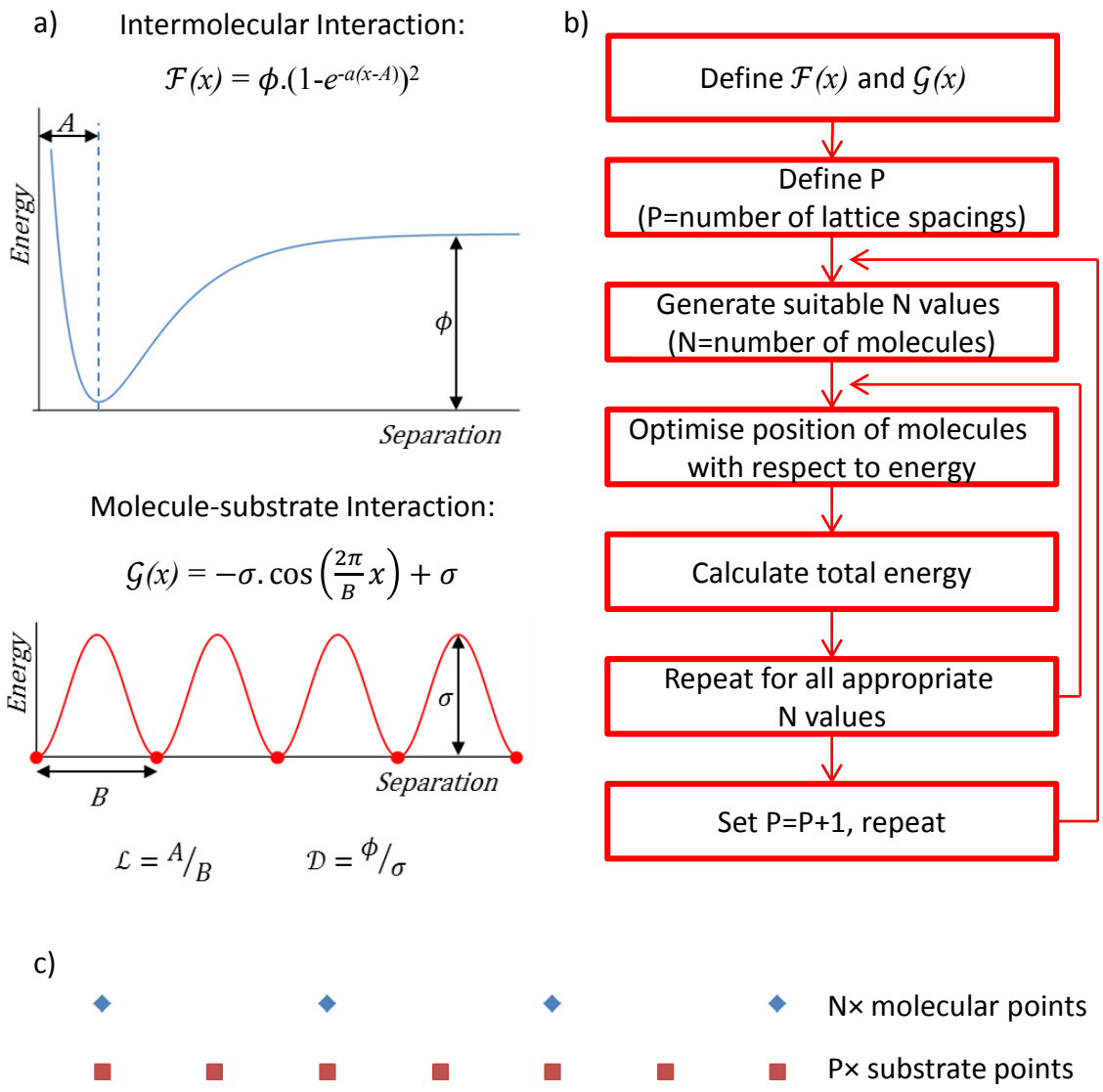

Figure 3.16 a) Derivation of the $\mathcal{D}$ and $\mathcal{L}$ parameters and the definition of the $\mathcal{F}(x)$ and $\mathcal{G}(x)$ terms used to simulate the different interactions. b) Flow diagram showing how the proposed analytical model can be used to predict the effects of the interaction interplay. c) Illustration of the two chains of points used to depict the substrate and molecules in the algorithm. The blue dots indicate the positions of molecules, the red of the substrate.

'molecular points'. The distribution of these points is initially set to match the gas-phase intermolecular separation or, to check that the results of the calculation are not specific to the starting arrangement, so that they are equally distributed over the length of the substrate cell. The two chains are shown schematically in Figure 3.16c. The positions of the points in the molecular chain are then varied depending on the

force each point experiences. The forces are evaluated using the functions $\mathcal{F}(x)$ and $\mathcal{G}(x)$, where $\mathcal{F}(x)$ is the force between the points in the molecular chain and $\mathcal{G}(x)$ is that between each point in the molecular chain and the substrate points. The positions of the molecular points are varied until the net force on each is zero, giving the most energetically favourable arrangement for that particular set of N and P values. The total energy of this arrangement is calculated, and then the entire algorithm is repeated using a range of different N and P values. In this way, the algorithm allows the lowest energy configuration of molecules to be readily assessed with little computational expense.

The $\mathcal{D}$ and $\mathcal{L}$ parameters are not explicitly included in the calculation. However, because they define all aspects of the assembly, it is in principle possible to use these as a reference for the molecule-on-metal system, and compare the parameters against previous performed calculations. With this in mind, the algorithm has been used to simulate the assembly for molecular systems with characteristic $\mathcal{D}$ and $\mathcal{L}$ values. Figure 3.17 shows the assemblies predicted for three systems with $\mathcal{D}$=0.5 and $\mathcal{D}$=5.0. Small values of $\mathcal{D}$ indicate a comparatively strong molecule-substrate interaction and thus a significant effect on the molecular assembly is anticipated. Figure 3.17a shows an example calculation using $\mathcal{D}$=0.5 and $\mathcal{L}$=0.4. The corresponding molecular assembly reveals the formation of tight pairs about the substrate lattice points. It is therefore immediately clear that in comparatively extreme conditions, the assembly is radically different from that given by the intermolecular interactions alone. It is important to note that the low $\mathcal{L}$ value plays a significant role in this particular case. Figure 3.17b shows the results of simulations using $\mathcal{D}$=0.5 and $\mathcal{L}$=1.2, revealing adsorbates that are uniformly separated, with each being situated directly over the lattice point. Thus, while the molecule-substrate

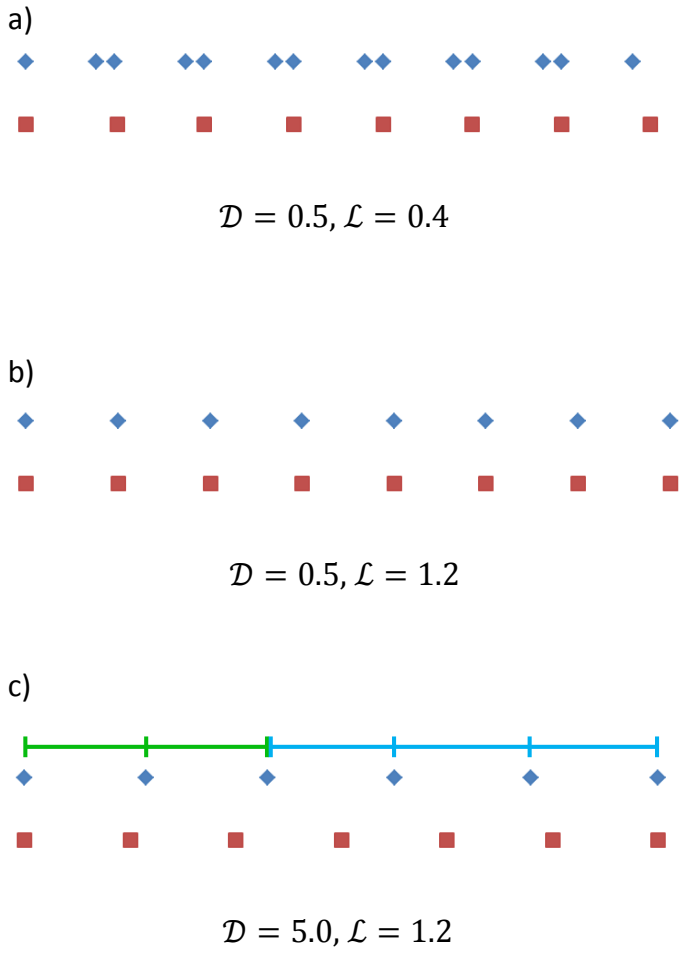

Figure 3.17 The results of simulations using model $\mathcal{D}$ and $\mathcal{L}$ values. The blue dots indicate the positions of molecules, the red of the substrate. The green and blue bars in c) indicate intermolecular separations that are smaller or longer than that expected from the $\mathcal{L}$ parameter, respectively.

interaction is strong in both calculations, the obtained assembly is only significantly modified by the surface when there is a substantial mismatch between the molecular and substrate lattice parameters; in general, the greater the mismatch of molecular and substrate periodicities (where $\mathcal{L}$ is far from an integer value), the greater the perturbation to the assembly.

Figure 3.17c shows the assembly predicted for $\mathcal{D}$=5.0 and $\mathcal{L}$=1.2. This $\mathcal{D}$ value is approximately that where the effects of the interaction interplay are expected to be apparent; for example, $\mathcal{D}$=3.45 for TPA on Cu(111). The calculations reveals

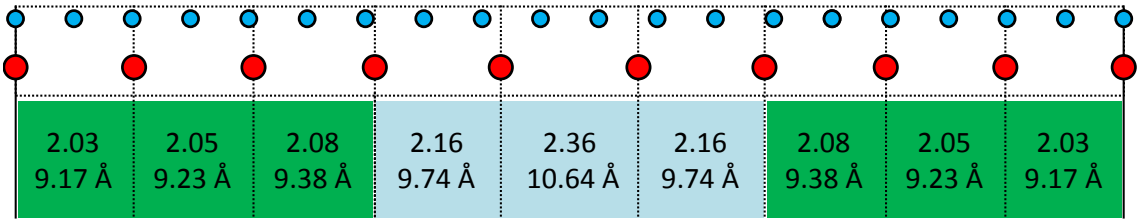

Figure 3.18 Calculated distribution of TPA molecules from the model described in the text. The red circles represent the positions of substrate lattice sites. The blue circles show the positions of the TPA molecules and define the lower boxes showing the intermolecular separations. These are reported in units of lattice parameters (top) and actual distances (bottom). The colour coding shows where the bonds are shorter (green) or longer (blue) than the separation predicted from the intermolecular interaction alone.

that the intermolecular spacing in not constant across the unit cell. Moreover, the separations are either compressed or elongated with respect to that defined by the intermolecular interactions, as is indicated by the green and blue bars, respectively.

Figure 3.18 shows the calculated lowest energy structure using the specific $\mathcal{D}$ and $\mathcal{L}$ values of TPA on Cu(111). The unit cell contains nine molecules spread over nineteen Cu lattice spacings. As was observed in Figure 3.17c, the intermolecular separation varies across the cell; the majority of the separations, depicted by the green boxes, are smaller than the 'ideal' periodicity of 9.65 Å. Within experimental tolerances, these match the 9.3±0.5 Å measured for the 'normal' H-bonding in the TPA chains. Other distances, highlighted by the blue box, are longer than that predicted from the $\mathcal{L}$ parameter. Critically, the algorithm is able to predict the most important feature of the TPA assembly; the centremost separation is considerably larger than even the other elongated distances, and thus this corresponds to the defects observed experimentally. Moreover, the calculated separation closely matches that measured for the STM data.

It is apparent therefore that the analytical method described above can both qualitatively and quantitatively predict the assembly of TPA on Cu(111). To test its versatility with respect to other molecule-on-metal systems, the algorithm has been performed with the parameters for TPA adsorbed on the Au(111) surface. In this case, the metal interacts only weakly with the adsorbate and has a larger atomic periodicity, resulting in $\mathcal{D}$=13.8 and $\mathcal{L}$=1.89 [49]. The model predicts that the TPA assemblies should exhibit equal intermolecular spacings of 10.22 Å, longer than the 9.65 Å predicted by the MM calculations. Critically, this value matches quite well the 9.9–10.3 Å reported previously [2]. Interestingly, this calculation reveals that even for weakly interacting surfaces the interplay of interactions is still in force, albeit that its effect is relatively small.

One critical note is that, taken at face value, the calculations of TPA on Cu(111) suggest that the defects in the lattice should repeat every nine TPA molecules. However, this is not observed experimentally, as the defects are, in a first approximation, spread in a seemingly random manner throughout the TPA lattice. In fact, many of the different molecular configurations (with respect to the substrate cell) have very similar energies to that shown in Figure 3.18. This is particularly true when the calculation incorporates a large number of molecules and lattice sites, whereby small variations in the number and positions of the molecules result in only small differences in the total energy. Consequently, more complex dispersions of defects are possible with only very small energetic differences. Nevertheless, the important result is that the model predicts both the short H-bonds and the defects observed experimentally in the H-bonded TPA monolayer on Cu(111).

In conclusion, the analytical model developed here is capable of describing the effects of the ‘subtle interplay’ of intermolecular and adsorbate-substrate

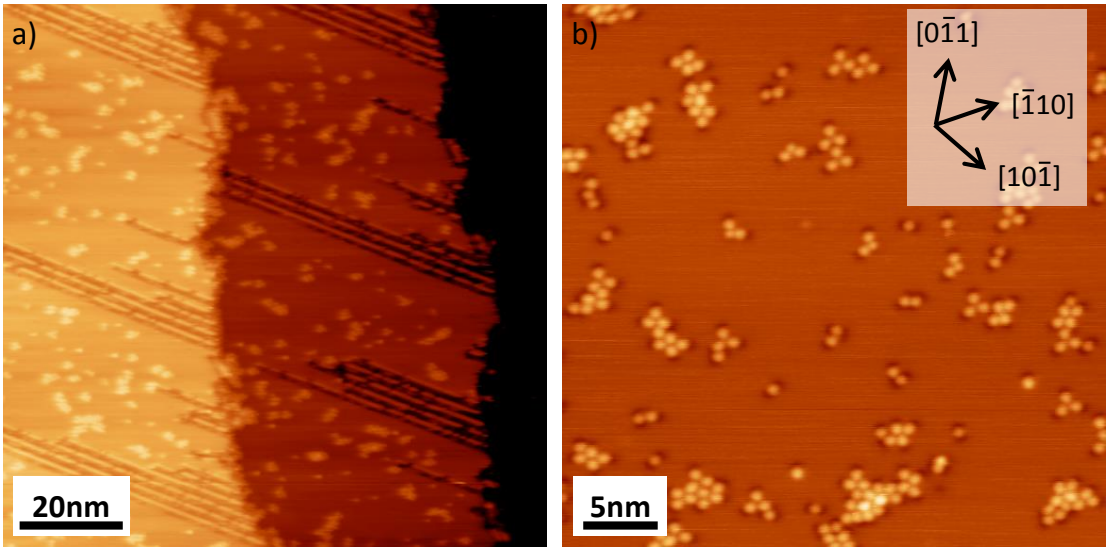

Figure 3.19 STM images of the TP structures fabricated by annealing the H-bonded TPA phase to 353K. a) shows an overview of the features found, including the terrace-bound structures and the 2D stripes observed at steps. I=70 pA, U=1.6 V. b) Zoomed in view of the terrace-bound structures, demonstrating the variety of motifs observed. I=40 pA, U=-1.4 V.

interactions in a manner not previously achieved. Moreover, given the relatively low computational cost of the algorithm, it should be possible to use it to calculate the effects of the interaction interplay so as to include them when designing molecular nanostructures. As proof of its efficacy, the algorithm has been used to characterise the unusual assembly of TPA on Cu(111), where it has proven capable of predicting both the quantitative and qualitative aspects of the molecular film. It is anticipated that this model can be readily expanded for more complex assemblies, including other materials, more complex tectons and surfaces, and ultimately 2D assembly.

3.2.2 Effect of annealing on the TPA brickwork film

Annealing the H-bonded phase above 353 K results in a radical transformation of the molecular film, as shown in the large-area STM images in Figure 3.19. As briefly mentioned in the previous section, this is expected to arise due to deprotonation of the TPA to TP. Some of the following structures appear MO

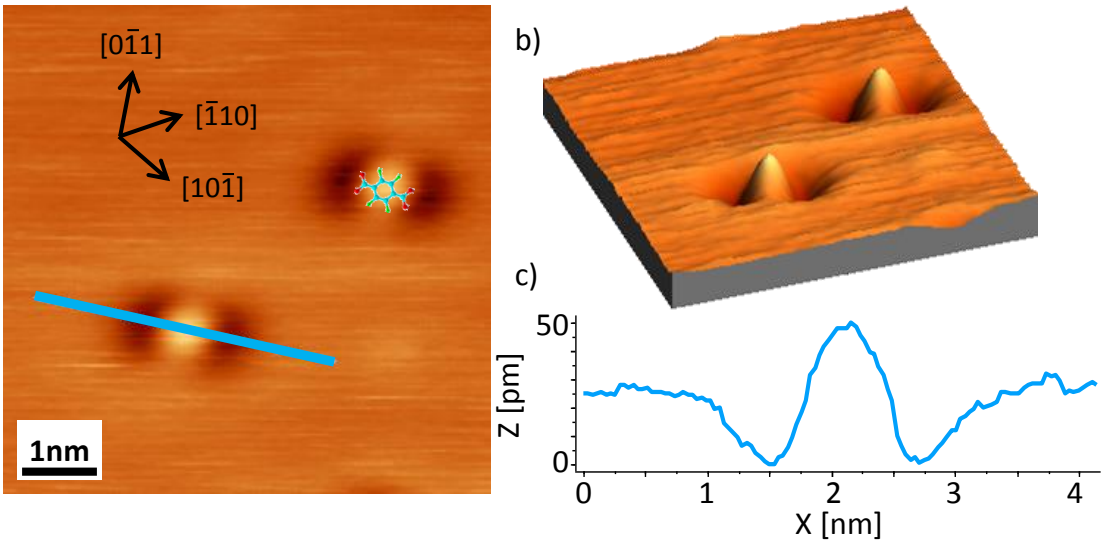

Figure 3.20 a) STM image of two TP monomers. The blue line illustrates the position of the line profile shown in c). A TP model has been overlaid on the upper feature. I=40 pA, U=-1.4 V. b) 3D representation of the image in a) to highlight the depressions at the ends of the TP molecules.

in nature, and given that there is a significant density of Cu adatoms even at RT [40-43], the annealing step is most likely necessary to trigger the deprotonation of the carboxyl moieties required for MO complexes to form. Two main types of assembly are observed, which have been loosely categorised as either 'terrace-bound' or 'step-bound'. The former, highlighted in Figure 3.19b, consists of a variety of different compact TP aggregates, including ordered trimers and tetramers, alongside a plethora of disorganised structures. The latter, which are currently not well understood, exhibit a 2D row-like motif and are usually observed nucleated from substrate steps. Both are described in more detail in the following sections.

3.2.2.1 TP on Cu(111) – terrace-bound structures

Approximately 40% of the terrace-bound objects exist as single monomers (single TP ellipses that have no immediate neighbours), two of which are shown in Figure 3.20. This quantity is only an approximate value, as the exact proportion of each structure observed on the surface is likely to depend on a number of factors,

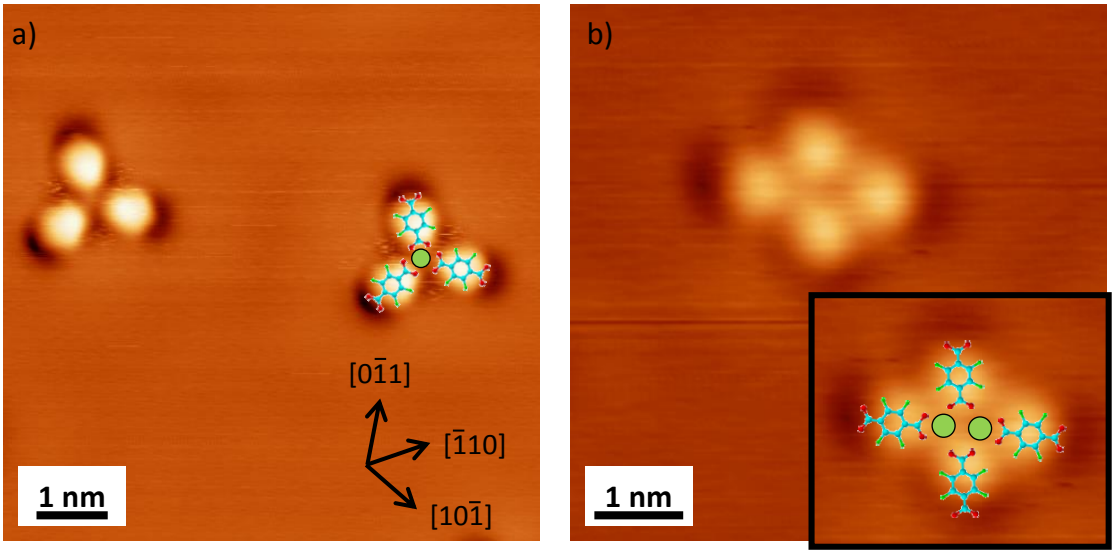

Figure 3.21 a) STM image of two TP trimers. The trimer on the right is overlaid with a structural model including a single Cu adatom. I=50 pA, U=-1.9 V. b) STM image of a TP tetramer and, inset, the same image with an overlay of a tentative model with two Cu adatoms. I=30 pA, U=-1.9 V.

including the molecular coverage and the characteristics of the annealing step. The molecules are all aligned with their long axis perpendicular to the main substrate crystallographic directions. The adsorbates exhibit characteristic dark 'halos' at the O termini, as illustrated by the 3D image and line profile in Figures 3.20b and c. As these halos appear darker than the underlying metal and extend beyond the TP length, they cannot be due to just a topographic effect induced by bending of the carboxylate towards the surface [9]. Instead, it is more reasonable to think that they arise from a partial charge on the carboxylate moiety, arising from its deprotonated chemical state. A similar effect has been observed for other carboxylic acids on Cu(111) [50].

In addition to the monomeric TP, small ordered conglomerates are also observed. Figure 3.21a shows two trimers, which are a particularly common motif (accounting for approximately 25% of all terrace-bound objects). Each TP in a trimer is aligned perpendicular to one of the principal crystallographic directions of the

substrate and exhibits the same characteristic halos at it's outermost termini as the monomers. These structures are believed to be MO in origin, with one or multiple Cu adatoms located at the centre of the trimer. Adatoms are required to stabilise these aggregates, as the dipole generated at the carboxylate moiety should repel other TP species if not compensated for [51]. This repulsion is mediated by bonding to metal adatoms, possibly through charge transfer to and from the metal centre. However, a residual overall negative charge could be the reason for the distribution of these complexes over the entire terrace. A tentative model for this structure is overlaid onto the right-most trimer in Figure 3.21a.

Tetrameric motifs are also occasionally observed, as shown in Figure 3.21b. These are less common and number only around 15% of all terrace-bound features. Previous work revealed a similar motif when Fe or Co is co-deposited with TPA [5,14,16,17], whereby the tetramers were reported to contain pairs of adatoms. The model overlaid in the inset image reveals that, unlike those observed previously, these structures appear to be slightly distorted from the 'ideal' 2-fold symmetry. Unfortunately, their limited occurrence and low image quality prevents an exact quantification of the extent of this perturbation. It is likely due to a mismatch in the structures of the substrate and the MO complexes; in essence, the 3-fold symmetry of the surface cannot readily support the formation of a 2-fold symmetric MO complex. It is also interesting to note that, unlike the previous examples, these complexes do not form long-range networks [5,14,16,17].

3.2.2.1 TP on Cu(111) – step-bound structures

Figure 3.22a and b highlight the assemblies that nucleate from steps and defects such as, for example, screw dislocations and contaminants. The two features

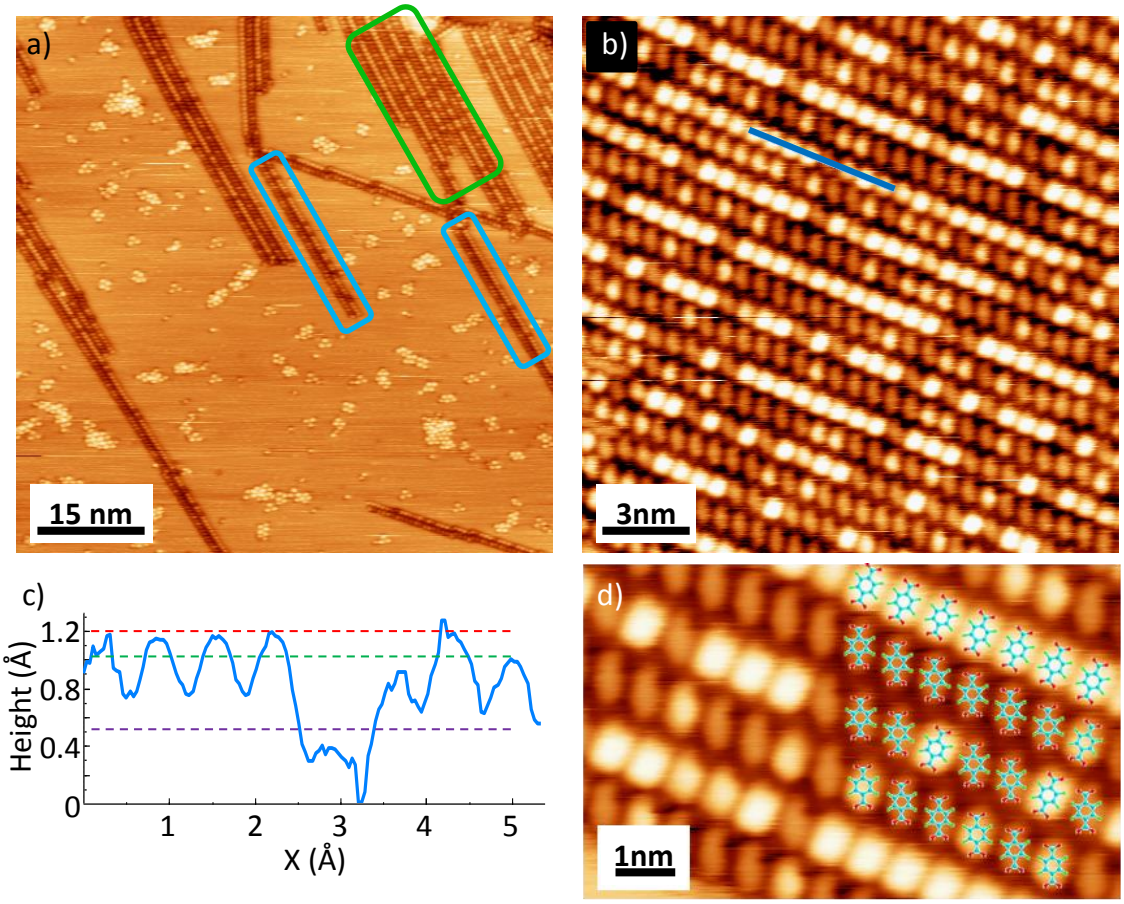

Figure 3.22 a) Large-range STM image, showing 1D stripes (highlighted by blue boxes) and 2D islands (highlighted by green boxes). I=100 pA, U=-1.0 V. b) Zoomed in image of a 2D island; the profile along the blue line is shown in c). d) Zoomed in STM image, overlaid with TP models. c) and d) I=110 pA, U=-1.0 V.

are in essence the same, only differing in whether the structure is extended in 1D (blue box) or 2D (green box). They both contain a core double-row motif of TP-like features, with one row on average brighter than the surrounding Cu(111) substrate and the other darker. Interestingly, the relative position of the row contrast is always the same within a single image; in Figure 3.22a, the bright rows are always above the dark ones.

Assignment of the structure of these rows has proven difficult, due to the complexity of the STM images. A variety of contrasts is observed even within a single row, as demonstrated by the line profile in 3.22c. Moreover, the shapes of the individual molecular features are not consistent; the darkest ones are elliptical while

the brightest are approximately rectangular. All of the features match the dimensions of TP (Figure 3.22d), and are thus tentatively assigned as such. This phase could also possibly contain Cu adatoms that are not resolved in the STM images; adatoms typically originate from kinks in steps during annealing [12], and therefore the nucleation of this assembly from steps suggests the involvement of adatoms. A precise identification of this complex structure will require extensive theoretical support and additional experimental data, which is also not necessarily limited to STM measurements and, thus, has not been attempted.

3.2.3 Fe-TP structures

Many studies have focused on the potential of incorporating extrinsic metal adatoms – metal atoms not of the same material as the substrate – into organic networks, particularly given their potential in, for example, magnetic data storage applications [52-55]. In this regard, metal-TP complexes are possible candidates, leading to a number of studies investigating the assembly of TPA with magnetic metals [14,16,17]. Previous work has reported two-fold symmetric tetramer structures, which, in some cases, can also extend into long-range porous networks. This is believed to be the most energetically favourable structural motif for metal-TP complexes, possibly due to optimisation of the MO bonding [16]. To assess whether this is also true on the Cu(111) surface, where the strong molecule-substrate interaction could play a significant role in the assembly process, the formation of Fe-TP complexes has been investigated.

The growth of Fe thin films on clean Cu(111) is controlled by the substrate temperature during deposition [56,57]. When deposited onto a Cu(111) surface held at 90 K, 3D pyramidal islands are formed, whereas between 200 K and 300 K, Fe

bilayer islands are obtained. If the sample is at RT or above, the Fe induces a reorganisation of the Cu(111) surface, resulting in the formation of 1-layer deep holes in the terraces. Of these three different growth modes, the intermediate bilayer growth is the most suited to this study; it should provide readily accessible Fe adatoms without modifying the shape of the Cu terraces. The Fe packing in these islands is dependent on their size; small islands are exclusively face-centred cubic (fcc)-packed, whilst larger ones are a mixture of fcc and body-centred cubic (bcc). This is clearly resolved in STM images as a sharp contrast change [56]. This complexity arises from the structural mismatch of the fcc Cu(111) surface and the bcc packing of the Fe crystal structure.

To optimise the Fe coverage, depositions were performed onto a clean Cu(111) surface held at 248 K. The STM data in Figure 3.23 reveals that Fe islands nucleate both at steps and on the terraces, and that there is no reorganisation of the Cu substrate. The majority of the islands exhibit a uniform contrast, suggesting they consist of only fcc packed Fe. The islands also exhibit a uniform height of 3.86±0.14 Å, revealing they are two atomic layers thick, in line with previous STM measurements [56]. Some islands, two of which are highlighted with green circles in Figure 3.23a, exhibit brighter regions that may be indicative of additional Fe layers.

Figure 3.23b show a STM image of a single Fe island where what appears to be the atomic structure can be resolved. Figure 3.23c shows the current image of the same island, allowing the corrugation to be better visualised. As only a limited amount of data has been taken, it cannot be confirmed that this is true atomic resolution or otherwise. Regardless, the protrusions are clearly packed in a (111)-like arrangement, in line with previous measurements [56].

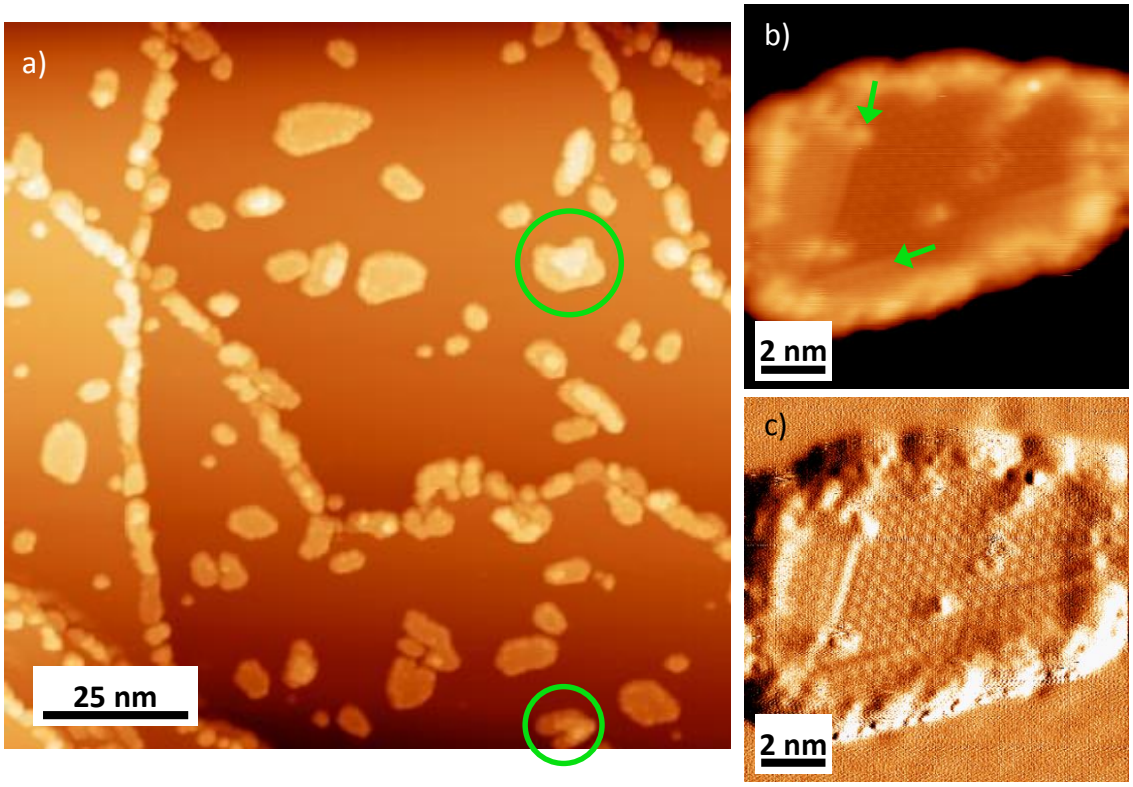

Figure 3.23 a) Large-range STM image of Fe islands grown on the Cu(111) surface held at 248 K during deposition. I=100 pA, U=1.0 V. The green circles highlight multilayer-high Fe islands. b) and c) Zoomed in topography and current images of a single Fe island, respectively. The current image is shown to highlight the resolution within the island, suggesting a (111)-like arrangement of the protrusions. The green arrows in b) shows the locations of steps within the island. I=1.3 nA, U=45 mV.

3.2.3.1 Deposition of Fe onto the TPA brickwork-like film

When Fe is deposited onto a pre-prepared TPA brickwork-like film held at 248 K, STM measurements (Figure 3.24a) show the nucleation of Fe islands at step edges and on the substrate terraces. The peripheries of the molecular islands also act as nucleation sites, particularly at their curved edges, which project a high number of un-bonded carboxyl moieties onto the terrace.

The internal structure of the TPA islands, shown in Figure 3.24b, exhibit a similar arrangement as that observed prior to Fe deposition; the molecules are assembled into a brickwork-like structure with both compressed and elongated H-

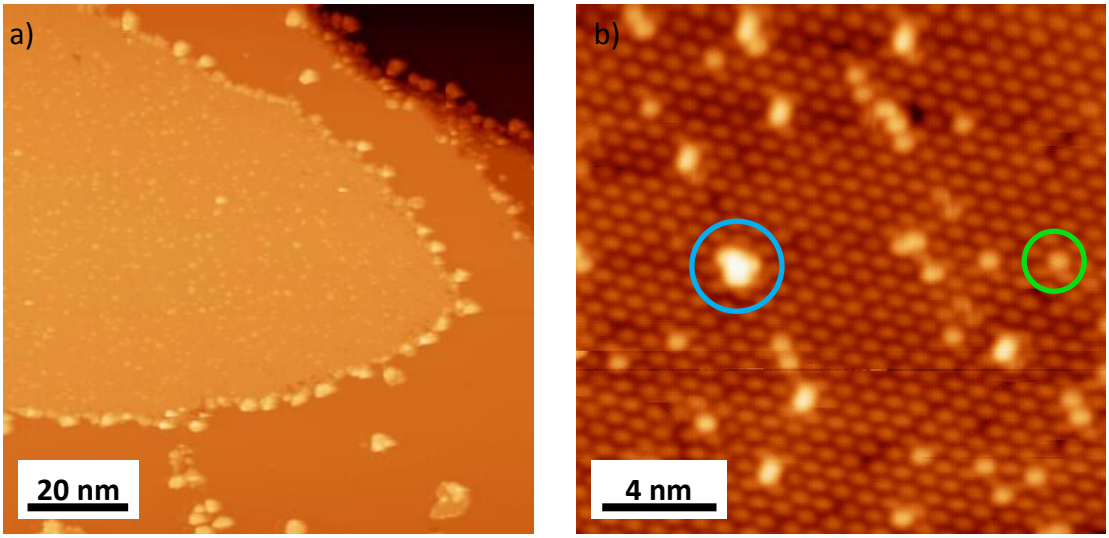

Figure 3.24 a) Large-range STM image of Fe deposited onto H-bonded TPA/ Cu(111) held at 248 K. I=40 pA, U=1.4 V. b) Zoomed in STM image of a TPA island after Fe deposition. Some protrusions consist of Fe adsorbed either on top or penetrating into the TPA lattice (blue circle), others correspond to single TPA molecules with enhanced contrast (green circle). I=40 pA, U=1.4 V.

bonds in the organic lattice. Two additional brighter features are also observed, which are highlighted by the blue and green circles. The blue circle indicates an example of an irregular shaped protrusion, which is thought to be a Fe cluster adsorbed either on top of the organic film or within it, directly on the metal surface. Such features are rather random in size and shape and their total number density is quite small. The green circle points out a TPA molecule with brighter contrast. Others appear slightly different in shape, but still fit within the organic lattice. These are expected to be some form of Fe-TPA complex, although their exact nature with respect to deprotonation state and MO bonding is not clear.

Figure 3.25 shows the results of annealing the previously described films to 317 K, which generates a significant transformation of the TPA monolayer. The molecular packing within the islands is seemingly disordered, as shown in Figure 3.25b. However, close inspection reveals that the disordered areas actually contain small motifs similar to those observed for Cu-TP. For example, the two circles in

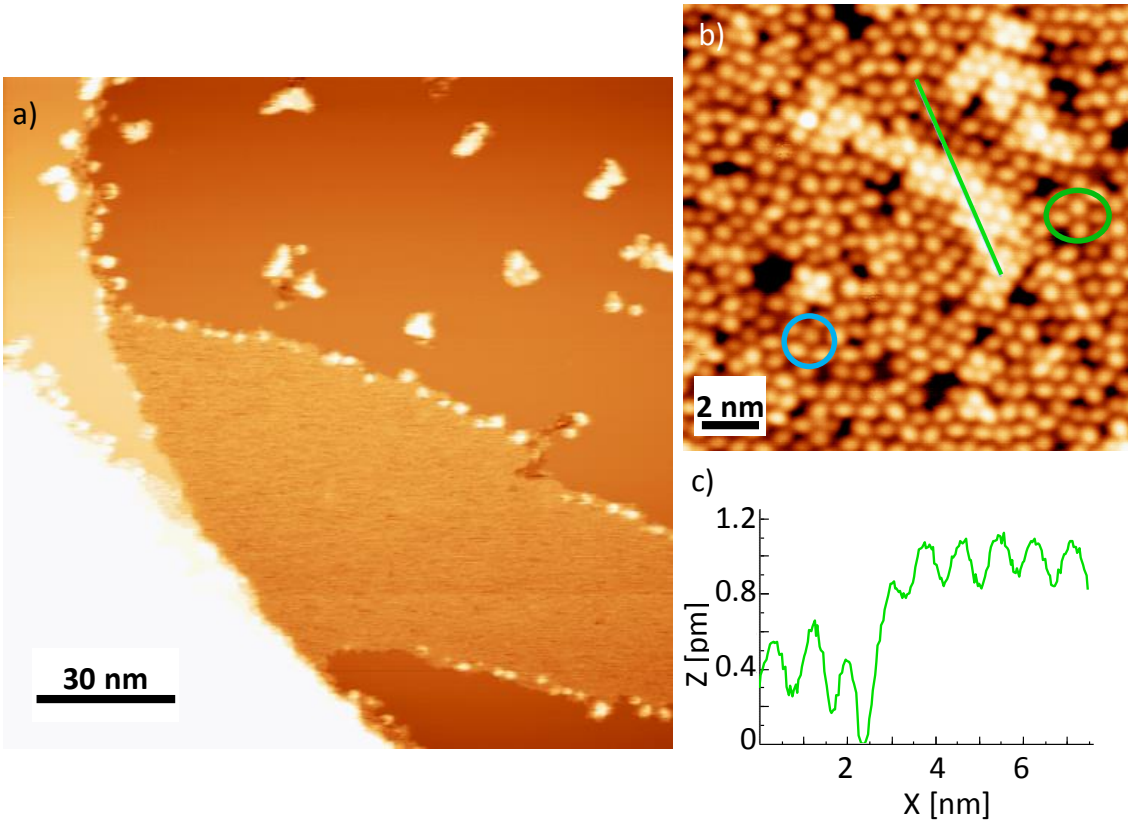

Figure 3.25 a) Large-range and b) zoomed in STM images of the films in Figure 3.24 after annealing to 317 K. a) I=58 pA, U=-0.3 V. b). I=33 pA, U=0.4 V. The blue and green circles highlight trimer and tetramer motifs, respectively. The green line shows the line profile in c).

Figure 3.25b highlight apparent trimers and tetramers. It may be that this disordered phase therefore corresponds to densely packed Fe-TP complexes.

In addition to the proposed MO TP complexes, some regions within the molecular islands exhibit brighter contrast and appear to contain TPA-like protrusions in a brickwork structure. These may be intact molecules that have not undergone deprotonation or interaction with the Fe. The origin of their relative brighter contrast, illustrated by the line scan in Figure 3.25c, may be due to their chemical state or to a true topographic effect; the reorganisation of the molecules induced by Fe-TP complexation may result in some of the TPA being lifted on top of

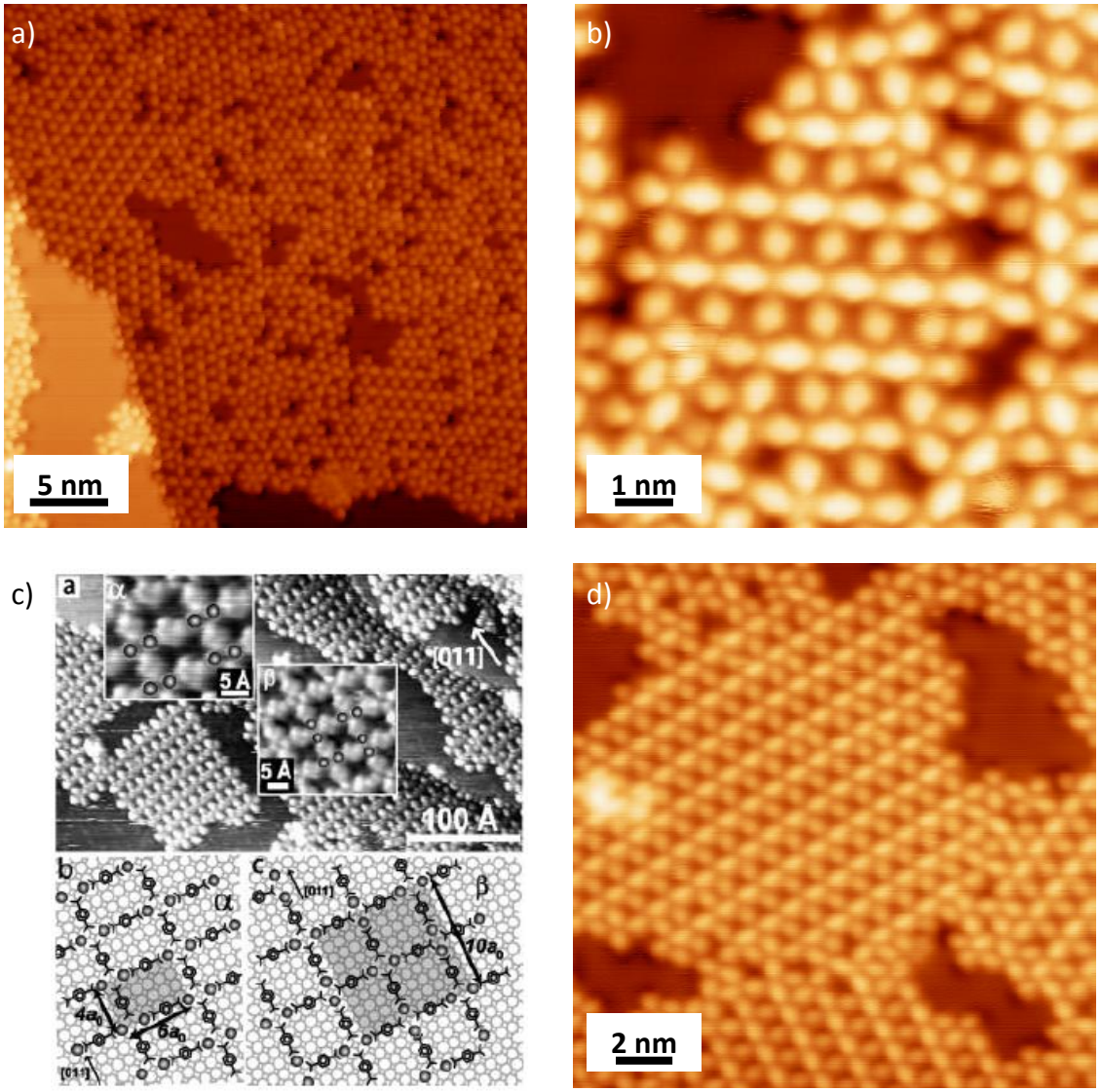

Figure 3.26 a) Large-range STM image of the films in Figure 3.24 after annealing to 383 K. I=33 pA, U=1.7 V. b) Zoomed-in STM image of the same sample, highlighting the apparent similarity to the MOCN-II structure shown in c) (figure taken from reference [15]). I=40 pA, U=-0.7 V. d) STM image of the same Fe-TPA structure after annealing to 403 K. I=58 pA, U=-0.5 V.

the MO film, possibly through the onset of in-plane pressure from the surrounding Fe-TP complexes [18,20,25].

Figure 3.26a and b show example STM images after further annealing to 383 K. In direct contrast to the Cu-TP complexes fabricated at this temperature (see Section 3.2.2.1), the adsorbates are only observed in large islands. Within these islands, ordered domains with a rectangular superstructure can be clearly resolved,

which strongly resemble the Fe-TP and Co-TP MO networks reported previously [14,16,17]. Furthermore, the rectangular dimensions of the cavity reveal the arrangement of the adatom dimers in the MO phase. Studies of Fe-TP on Cu(001) (Figure 3.26c) reported that when subsequent dimers are aligned perpendicular to one another, the pore is square in shape, whereas if they are oriented parallel to one another the hole is rectangular [17]. Thus, in the Fe-TP phase identified here, the adatom dimers are aligned parallel to one another. Annealing the sample to even higher temperatures results in the ordered Fe-TP domains growing larger, as illustrated in Figure 3.26d. This structure is therefore likely to be to be most energetically favourable one.

In summary, when Fe is deposited onto the TPA brickwork-like structure, a long-range porous Fe-TP network, similar to those reported previously [14,16,17], is ultimately obtained. This phase is only formed after annealing to high temperature, suggesting the presence of kinetic limitations on the formation of the MO network. The 2-fold symmetry of the assembly illustrates the enhanced strength of the carboxyl-Fe bond with respect to that with Cu; the templating effect of the substrate apparent in the Cu-TP complexes has been overcome, allowing the 'ideal' Fe-TP porous structure to be formed.

3.3 Summary of TPA on Cu surfaces

The investigations presented in this chapter reveal that any attempt to describe and understand the assembly of molecular tectons on Cu surfaces based on intermolecular interactions alone is likely to fail. In the case of Cu(110), the intrinsic reactivity of the substrate results in complete deprotonation of the TPA at RT, which in turn assembles into a range of MO or all-organic networks, depending on the

coverage. These exhibit approximately rectangular symmetry, indicating a strong templating effect from the underlying metal. Similarly, the Cu(111) surface also plays a strong role in defining molecular assembly; a brickwork-like structure is obtained at RT, which exhibits both uncharacteristically short and long molecular separations due to an interplay of intermolecular and molecule-substrate interactions. Annealing results in the formation of different compact Cu-TP complexes on terraces and an as-yet unidentified long-range phase mainly nucleating from steps. These motifs are to-date exclusive to this surface. By co-depositing Fe and annealing, a long-range porous assembly can also be obtained, which is believed to be the most favourable for metal-TP complexes by virtue of the stronger Fe-TP bond.

3.4 Chapter 3 references

1. Barth, J.V., *Fresh perspectives for surface coordination chemistry.* Surface Science, 2009. **603**(10–12): p. 1533-1541.
2. Clair, S., et al., *STM Study of Terephthalic Acid Self-Assembly on Au(111): Hydrogen-Bonded Sheets on an Inhomogeneous Substrate.* The Journal of Physical Chemistry B, 2004. **108**(38): p. 14585-14590.
3. Kim, Y.-G., S.-L. Yau, and K. Itaya, *In Situ Scanning Tunneling Microscopy of Highly Ordered Adlayers of Aromatic Molecules on Well-Defined Pt(111) Electrodes in Solution: Benzoic Acid, Terephthalic Acid, and Pyrazine.* Langmuir, 1999. **15**(22): p. 7810-7815.
4. Lackinger, M., et al., *Self-Assembly of Benzene−Dicarboxylic Acid Isomers at the Liquid Solid Interface: Steric Aspects of Hydrogen Bonding.* The Journal of Physical Chemistry B, 2004. **108**(36): p. 13652-13655.
5. Suzuki, T., et al., *Substrate effect on supramolecular self-assembly: from semiconductors to metals.* Physical Chemistry Chemical Physics, 2009. **11**(30): p. 6498-6504.
6. Carrera, A., et al., *Controlling Carboxyl Deprotonation on Cu(001) by Surface Sn Alloying.* Journal of Physical Chemistry C, 2013. **117**(33): p. 17058-17065.
7. Addou, R. and M. Batzill, *Defects and Domain Boundaries in Self-Assembled Terephthalic Acid (TPA) Mono layers on CVD-Grown Graphene on Pt(111).* Langmuir, 2013. **29**(21): p. 6354-6360.
8. Martsinovich, N. and A. Troisi, *Modeling the Self-Assembly of Benzenedicarboxylic Acids Using Monte Carlo and Molecular Dynamics Simulations.* The Journal of Physical Chemistry C, 2010. **114**(10): p. 4376-4388.
9. Fuhr, J.D., et al., *Interplay between Hydrogen Bonding and Molecule–Substrate Interactions in the Case of Terephthalic Acid Molecules on Cu(001) Surfaces.* The Journal of Physical Chemistry C, 2012. **117**(3): p. 1287-1296.
10. Canas-Ventura, M.E., et al., *Coexistence of one- and two-dimensional supramolecular assemblies of terephthalic acid on Pd(111) due to self-limiting deprotonation.* Journal of Chemical Physics, 2006. **125**(18): p. 184710.
11. Stepanow, S., et al., *Deprotonation-driven phase transformations in terephthalic acid self-assembly on Cu(100).* Journal of Physical Chemistry B, 2004. **108**(50): p. 19392-19397.
12. Brune, H., *Thermal dynamics at surfaces.* Annalen der Physik, 2009. **18**(10-11): p. 675-698.
13. Classen, T., et al., *Hydrogen and Coordination Bonding Supramolecular Structures of Trimesic Acid on Cu(110).* The Journal of Physical Chemistry A, 2007. **111**(49): p. 12589-12603.
14. Clair, S., et al., *Monitoring Two-Dimensional Coordination Reactions: Directed Assembly of Co−Terephthalate Nanosystems on Au(111).* The Journal of Physical Chemistry B, 2006. **110**(11): p. 5627-5632.
15. Tait, S.L., et al., *Metal-Organic Coordination Interactions in Fe-Terephthalic Acid Networks on Cu(100).* Journal of the American Chemical Society, 2008. **130**(6): p. 2108-2113.

16. Wang, Y., et al., *Tertiary Chiral Domains Assembled by Achiral Metal−Organic Complexes on Cu(110).* The Journal of Physical Chemistry C, 2010. **114**(30): p. 13020-13025.
17. Lingenfelder, M.A., et al., *Towards Surface-Supported Supramolecular Architectures: Tailored Coordination Assembly of 1,4-Benzenedicarboxylate and Fe on Cu(100).* Chemistry - A European Journal, 2004. **10**(8): p. 1913-1919.
18. Tait, S.L., et al., *First layer compression and transition to standing second layer of terephthalic acid on Cu(100).* Physical Chemistry Chemical Physics, 2012. **14**(22): p. 8217-8223.
19. Tseng, T.-C., et al., *Charge-transfer-induced structural rearrangements at both sides of organic/metal interfaces.* Nat Chem, 2010. **2**(5): p. 374-379.
20. Liu, J., et al., *Structural Transformation of Two-Dimensional Metal–Organic Coordination Networks Driven by Intrinsic In-Plane Compression.* Journal of the American Chemical Society, 2011. **133**(46): p. 18760-18766.
21. Martin, D., R. Cole, and S. Haq, *Creating a functionalized surface: The adsorption of terephthalic acid onto Cu(110).* Physical Review B, 2002. **66**(15): p. 155427.
22. Atodiresei, N., K. Schroeder, and S. Blügel, *Density-functional theory study on the arrangement of adsorbed formate molecules on Cu(110).* Physical Review B, 2007. **75**(11): p. 115407.
23. Frederick, B.G., et al., *Evolution of Lateral Order and Molecular Reorientation in the Benzoate/Cu(110) System.* Surface Review and Letters, 1996. **03**(04): p. 1523-1546.
24. Perry, C.C., et al., *Face specificity and the role of metal adatoms in molecular reorientation at surfaces.* Surface Science, 1998. **409**(3): p. 512-520.
25. Wang, Y., et al., *Varying molecular interactions by coverage in supramolecular surface chemistry.* Chemical Communications, 2012. **48**(4): p. 534-536.
26. Dougherty, D.B., P. Maksymovych, and J.T. Yates, Jr., *Direct STM evidence for Cu-benzoate surface complexes on Cu(110).* Surface Science, 2006. **600**(19): p. 4484-4491.
27. Messina, P., et al., *Direct observation of chiral metal-organic complexes assembled on a Cu(100) surface.* Journal of the American Chemical Society, 2002. **124**(47): p. 14000-14001.
28. *Simulated using the LEEDpat3.0 free software. http://www.fhi-berlin.mpg.de/KHsoftware/LEEDpat. Obtained November 2013*.
29. Lin, N., et al., *Two-dimensional adatom gas bestowing dynamic heterogeneity on surfaces.* Angewandte Chemie-International Edition, 2005. **44**(10): p. 1488-1491.
30. Faraggi, M.N., et al., *Role of Deprotonation and Cu Adatom Migration in Determining the Reaction Pathways of Oxalic Acid Adsorption on Cu(111).* The Journal of Physical Chemistry C, 2011. **115**(43): p. 21177-21182.
31. Payer, D., et al., *Ionic Hydrogen Bonds Controlling Two-Dimensional Supramolecular Systems at a Metal Surface.* Chemistry – A European Journal, 2007. **13**(14): p. 3900-3906.
32. Jones, G., et al., *The local adsorption geometry and electronic structure of alanine on Cu(110).* Surface Science, 2006. **600**(9): p. 1924-1935.

33. Baumann, P., et al., *Long-range ordered acetate structure on Cu(110).* Chemical Physics Letters, 1996. **260**(1–2): p. 215-222.
34. Baber, A.E., et al., *Assisted Deprotonation of Formic Acid on Cu(111) and Self Assembly of 1D Chains.* Physical Chemistry Chemical Physics, 2013. **15**(29): p. 12291-12298.
35. Immaraporn, B., P.P. Ye, and A.J. Gellman, *The transition state for carboxylic acid deprotonation on Cu(100).* Journal of Physical Chemistry B, 2004. **108**(11): p. 3504-3511.
36. Zhang, W., et al., *Molecular orientation of terephthalic acid assembly on epitaxial graphene: NEXAFS and XPS study.* Physical Chemistry Chemical Physics, 2012. **14**(29): p. 10125-10131.
37. Nakamura, J., J.A. Rodriguez, and C.T. Campbell, *Does CO2 Dissociatively Adsorb on Cu Surfaces?* Journal of Physics-Condensed Matter, 1989. **1**: p. SB149-SB160.
38. Rasmussen, P.B., P.A. Taylor, and I. Chorkendorff, *The Interaction of Carbon Dioxide with Cu(100).* Surface Science, 1992. **269**: p. 352-359.
39. Kirstein, W., B. Kruger, and F. Thieme, *CO Adsorption Studies on Pure and Ni-Covered Cu(111) Surfaces.* Surface Science, 1986. **176**(3): p. 505-529.
40. Giesen, M., *Scaling transition of the time dependence of step fluctuations on Cu(111).* Surface Science, 1999. **442**(3): p. 543-549.
41. Pawin, G., et al., *A Surface Coordination Network Based on Substrate-Derived Metal Adatoms with Local Charge Excess.* Angewandte Chemie International Edition, 2008. **47**(44): p. 8442-8445.
42. Matena, M., et al., *Aggregation and Contingent Metal/Surface Reactivity of 1,3,8,10-Tetraazaperopyrene (TAPP) on Cu(111).* Chemistry – A European Journal, 2010. **16**(7): p. 2079-2091.
43. Sirtl, T., et al., *Control of Intermolecular Bonds by Deposition Rates at Room Temperature: Hydrogen Bonds versus Metal Coordination in Trinitrile Monolayers.* Journal of the American Chemical Society, 2012. **135**(2): p. 691-695.
44. Bailey, M. and C.J. Brown, *The Crystal Structure of Terephthalic Acid.* Acta Crystallographica, 1967. **22**(3): p. 387-391.
45. Sledz, M., J. Janczak, and R. Kubiak, *New crystalline modification of terephthalic acid.* Journal of Molecular Structure, 2001. **595**(1-3): p. 77-82.
46. Stepanow, S., et al., *Surface-Assisted Assembly of 2D Metal–Organic Networks That Exhibit Unusual Threefold Coordination Symmetry.* Angewandte Chemie, 2007. **119**(5): p. 724-727.
47. Kuhnle, A., et al., *Growth of unidirectional molecular rows of cysteine on Au(110)-(1x2) driven by adsorbate-induced surface rearrangements.* Physical Review Letters, 2004. **93**(8): p. 086101.
48. Grimme, S., *Semiempirical GGA-type density functional constructed with a long-range dispersion correction.* Journal of Computational Chemistry, 2006. **27**(15): p. 1787-1799.
49. Mura, M., N. Martsinovich, and L. Kantorovich, *Theoretical study of melamine superstructures and their interaction with the Au(111) surface.* Nanotechnology, 2008. **19**(46): p. 465704.
50. Vitali, L., et al., *Portrait of the potential barrier at metal-organic nanocontacts.* Nature Materials, 2010. **9**(4): p. 320-323.

51. Ishii, H., et al., *Energy level alignment and interfacial electronic structures at organic metal and organic organic interfaces.* Advanced Materials, 1999. **11**(8): p. 605-625.
52. Gambardella, P., et al., *Supramolecular control of the magnetic anisotropy in two-dimensional high-spin Fe arrays at a metal interface.* Nature Materials, 2009. **8**(3): p. 189-193.
53. Otero, R., et al., *Molecular Self-Assembly at Solid Surfaces.* Advanced Materials, 2011. **23**(44): p. 5148-5176.
54. Ruben, M., et al., *Grid-type metal ion architectures: Functional metallosupramolecular arrays.* Angewandte Chemie-International Edition, 2004. **43**(28): p. 3644-3662.
55. Classen, T., et al., *Templated Growth of Metal–Organic Coordination Chains at Surfaces.* Angewandte Chemie International Edition, 2005. **44**(38): p. 6142-6145.
56. Biedermann, A., et al., *Coexistence of fcc- and bcc-like crystal structures in ultrathin Fe films grown on Cu(111).* Physical Review B, 2006. **73**(16): p. 165418.
57. Klaua, M., et al., *Strain-driven formation of two-dimensional holes on Cu(111) after the deposition of Fe.* Surface Science, 1997. **381**(2–3): p. 106-116.

Chapter 4

Oxalic acid on Cu(110) and Cu(111)

This chapter describes the extensive efforts that have been made to understand the adsorption and assembly of OA on the Cu(110) and Cu(111) surfaces. This has been attempted using an extensive array of different characterisation techniques and theoretical simulations. In both cases, the assembly has been readily obtained and is clearly determined by the substrate symmetry. Conversely, the adsorption geometry has proven extremely difficult to characterise; the small size and high symmetry of OA make its orientation impossible to discern from STM measurements alone. This is particularly true for its assembly on the Cu(110) surface, where a range of different complementary experimental and theoretical

techniques, including STM, XPS, NEXAFS and DFT, have been required to fully characterise the adsorption geometry. On Cu(111), it is possible to infer the molecular orientation from the obtained STM data and through comparison to previous measurements [1,2].

In the following, the results from these different characterisation methods are presented. On Cu(110), OA is fully deprotonated and adsorbs in a flat lying geometry, in contrast to that reported previously from the RAIRS measurements of Martin *et al*. [1]. An open, rectangular oxalate superstructure is obtained, but the driving force behind its formation over others that are apparently more favourable is not currently understood. Furthermore, STM characterisation reveals local-scale aspects of the superstructure that will prove to have a significant impact on its suitability as a decoupling layer, which is expanded upon in Chapter 5. On Cu(111), a densely-packed OA superstructure is obtained. Because of its high molecular density, this structure is inferred to contain mono-deprotonated OA in an upright adsorption geometry.

4.1 OA on Cu(110)

Exposure of a clean Cu(110) surface to approximately 5 Langmuirs (1 Langmuir=1×10^{-6} mbar s^{-1}) of OA vapour typically generates a molecular film that is multiple layers thick. An example STM image is shown in Figure 4.1a. The substrate terraces appear largely disordered, except for small regions where some periodic structures can be resolved. Annealing the sample to 398 K results in the removal of these disordered regions, and the formation of the highly ordered monolayer shown in Figure 4.1b. It is not clear whether this crystalline first layer was already present underneath the multilayer film, or whether the annealing is an important step in its

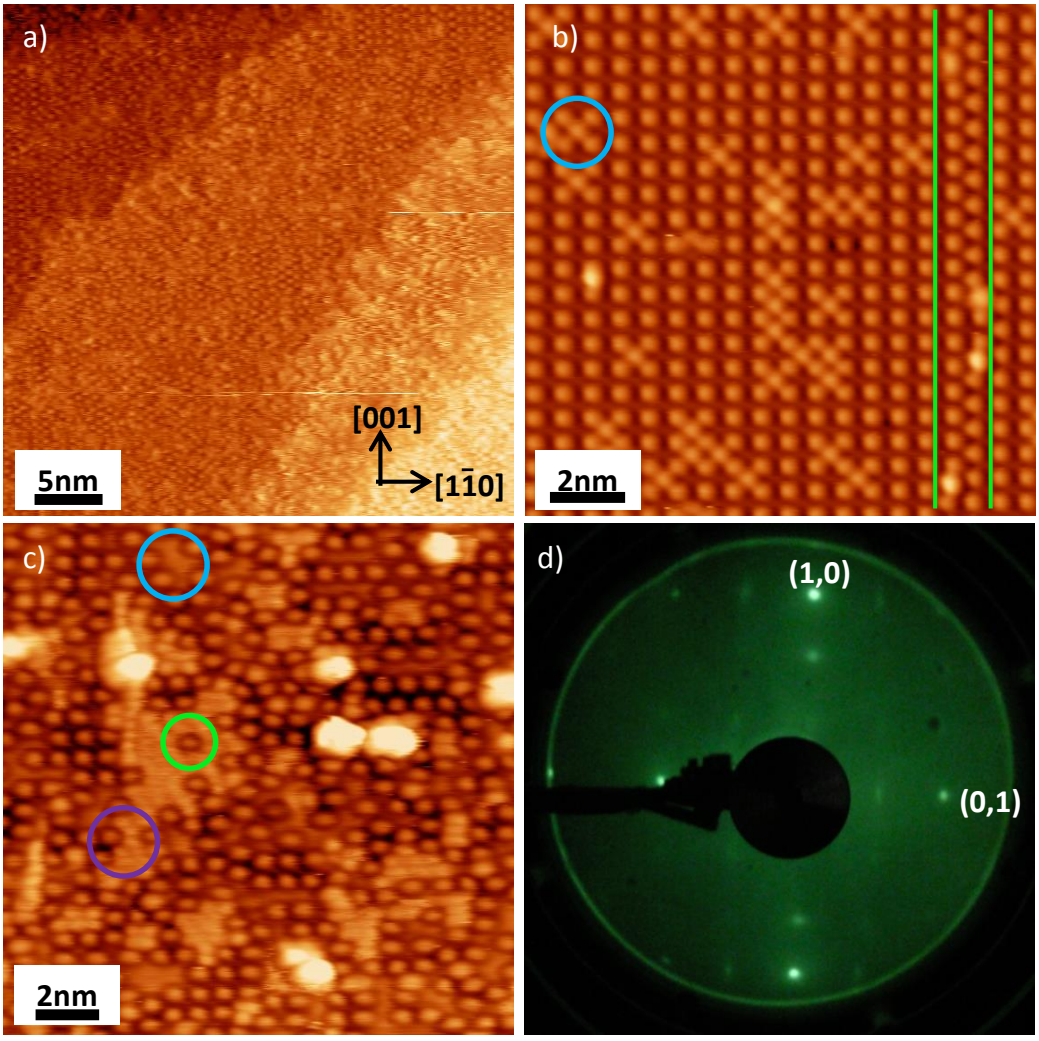

Figure 4.1 a) STM image of the OA film on the Cu(110) surface prior to annealing. Small ordered regions can be found amidst non-resolvable areas. I=120 pA, U=-1.1 V. b) STM image of the OA film after annealing to 398 K, showing the long-range (3×2) ordering. The blue circle highlights an interstitial OA molecule and the green lines highlights a domain boundary between two (3×2) domains. I=180 pA, U=-1.1 V. c) STM image of the OA film after annealing to 423 K, demonstrating clean areas (blue circle), potential decomposition products (purple circle) and isolated OA features (green circle). I=100 pA, U=1.1 V. d) LEED image of the (3×2) OA film. E=148eV, T≈RT.

generation. In either case, this suggests that the fuzzy regions in 4.1a probably correspond to areas with multilayer coverage.

The STM image in Figure 4.1b shows that the OA monolayer film obtained after annealing is highly ordered, consisting of a rectangular array of circular protrusions. Based on their lateral dimensions, it is tempting to immediately assign

these as individual OA molecules adsorbed on the surface. However, some caution should be taken in this, as the adsorbates do not necessarily have to appear as protrusions on the surface [3]. For example, it may be that the dark regions between the circular features actually correspond to the OA molecules. Confirmation can be achieved by annealing the sample to 423 K, which results in a complex transformation of the OA monolayer. The STM image in Figure 4.1c reveals a number of different features, including what appears to be bare substrate (blue circle) and potential decomposition products (purple circle). However, the sample still contains a large number of protrusions with similar size, shape and assembly to those observed prior to annealing. Critically, some of these features are observed to be isolated from others, such as that indicated by the green circle in Figure 4.1c. This indicates that the discrete OA units in the complete monolayer are, in fact, the circular protrusions, and are thus assigned as such.

The molecular assembly can be characterised by its periodicity along the two crystallographic directions. The OA intermolecular separations along the $[1\bar{1}0]$ and $[001]$ directions are 7.5±0.2 Å and 6.6±0.3 Å, respectively, which correspond to 3× and 2× the Cu lattice spacings in the two respective directions. There is a 10% error in the $[001]$ direction with respect to the 'ideal' $[001]$ separation, but the overall structure is confirmed by the LEED pattern shown in Figure 4.1d. Thus, the entire structure has (3×2) symmetry. This superstructure is in line with previous measurements of similar molecules on Cu(110); for example, both formate and methoxy assemble into superstructures with a 2× periodicity along the $[001]$ direction [4,5], whereas succinic acid forms a phase with a 3× periodicity along the $[1\bar{1}0]$ [6].

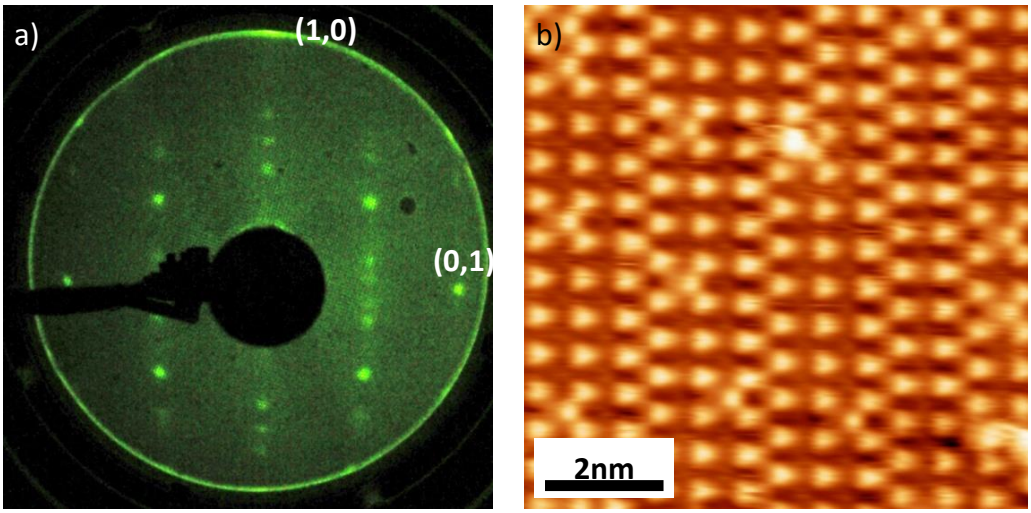

Figure 4.2 a) LEED image of the 'disordered (3×2)' OA phase. E=63eV, T≈RT. b) Corresponding STM image. I=300 pA, U=-1.0 V.

It is also worth noting that, in some cases, a different LEED pattern is obtained, such as that shown in Figure 4.2a. The 2× [001] periodicity is maintained, but along the $[1\bar{1}0]$ direction numerous spots are observed that correspond to a number of different periodicities. Figure 4.2b shows an example STM image of such a film, revealing that whilst the film is still locally ordered with (3×2) symmetry, the domains are actually extremely narrow along the $[1\bar{1}0]$ direction. The width of these domains varies typically between two to four OA molecules wide, resulting in LEED patterns with fractional-order spots corresponding to 6-12× the substrate periodicity. It may be that this 'disordered (3×2) phase' is similar to or matches one previously observed by Martin *et al.*, which was reported to develop after exposing the c(2×2) OA film to the LEED electron beam [1]. Carboxylate films are known to be sensitive to low-energy electrons [7] and in the case of OA on Cu(110), it is proposed that the LEED beam results in a partial removal of OA and the formation of a different superstructure. Martin *et al.* reported that this new phase had a c(10×2) symmetry, which is approximately in line with the periodicity measured in the STM and LEED measurements in this work. However, further confirmation of this link is required.

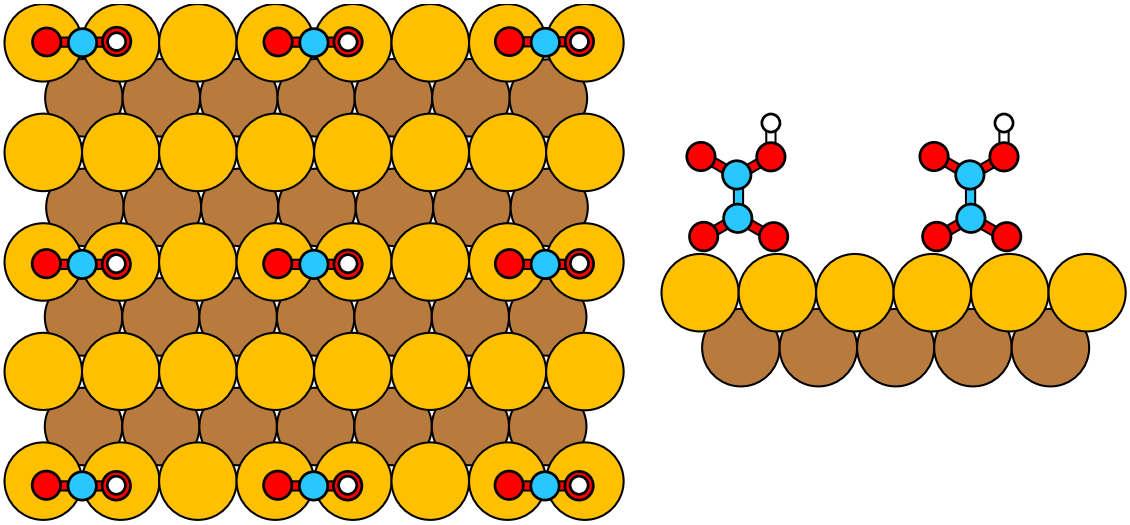

Figure 4.3 Initially-assumed OA structure, viewed from above and along the [001] direction, based on the (3×2) structure found using STM and LEED and the upright orientation suggested in reference [1] from RAIRS studies.

Previously, Martin *et al*. presented the results of RAIRS measurements that indicated that OA adsorbs in an upright orientation on Cu(110), forming bidentate bonds to the surface [1]. With this in mind, the model shown in Figure 4.3 was initially suggested as a tentative working model, whereby the OA is adsorbed in an upright orientation in a (3×2) superstructure. The O atoms that bind to the surface are adsorbed on top of the Cu atoms, resulting in a bridging geometry, in line with previous measurements of other adsorbed carboxylates [8-11].

4.1.1 Local-scale structural features of OA on Cu(110)

Close inspection of the OA (3×2) structure reveals a number of local-scale features – those that can only be observed in a spatially localised probe technique like STM - that warrant further discussion. One such feature is highlighted by the blue circle in Figure 4.1b, where an extra protrusion is observed at the centre of the indicated (3×2) cell. This ‘interstitial’ species appears identical in shape to those that surround it, which, in a first approximation, is thought to be an additional OA

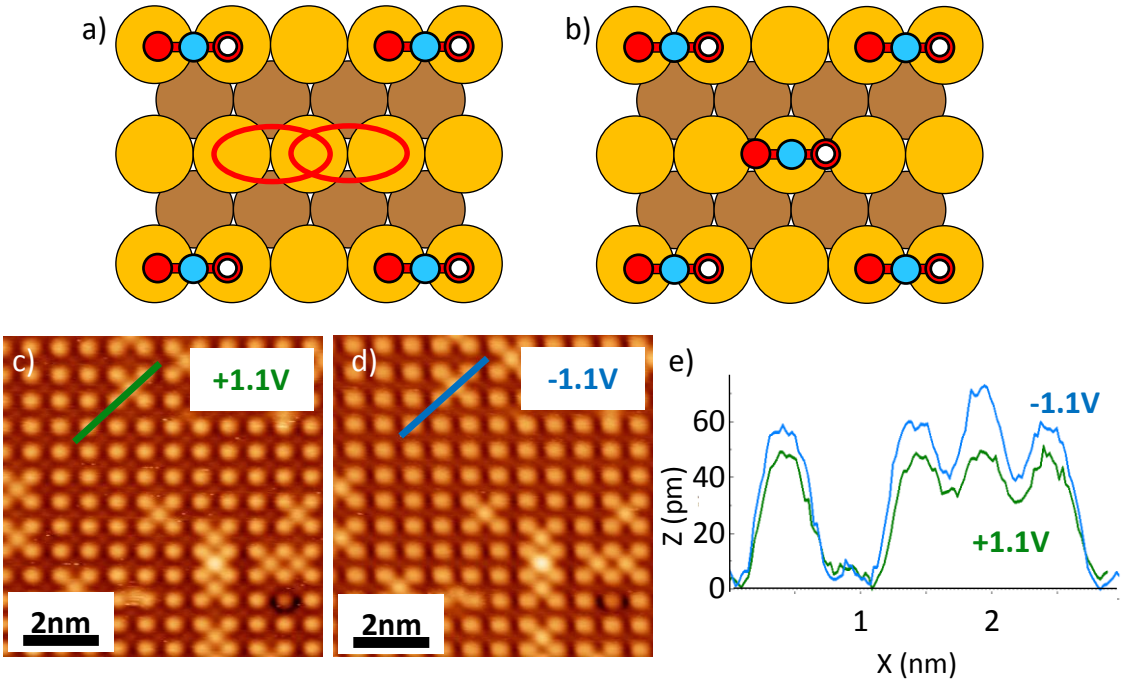

Figure 4.4 a) Possible positions of the interstitial OA if it maintains the same adsorption site as the surrounding OA molecules. In either of the two positions, the molecule is no longer centred within the (3×2) cell. b) Alternative adsorption site compatible with the a symmetric c(3×2) configuration. c) and d) STM images of the OA (3×2) structure, imaged at positive and negative bias voltages, respectively. I=180 pA. e) Profiles of the two lines in a) and b), highlighting the apparent height differences in empty and filled state imaging.

adsorbed in the centre of the (3×2) unit cell, which also has a comparable adsorption geometry.

Regardless of its exact molecular orientation, the 3× periodicity of the OA superstructure along the $[1\bar{1}0]$ direction means that the interstitial species cannot have the same adsorption site as the rest. For the interstitial molecule to be adsorbed in the same geometry as the surrounding molecules, for example in the bridging adsorption site shown in Figure 4.4a, the interstitial molecule has to be localised in one of the two positions shown by the red ovals. Consequently, it cannot do so whilst maintaining the experimentally observed centred locale within the (3×2) cell. Instead, the STM images imply that the interstitial molecules have different adsorption geometries to the surrounding OA, as illustrated in Figure 4.4b. Some

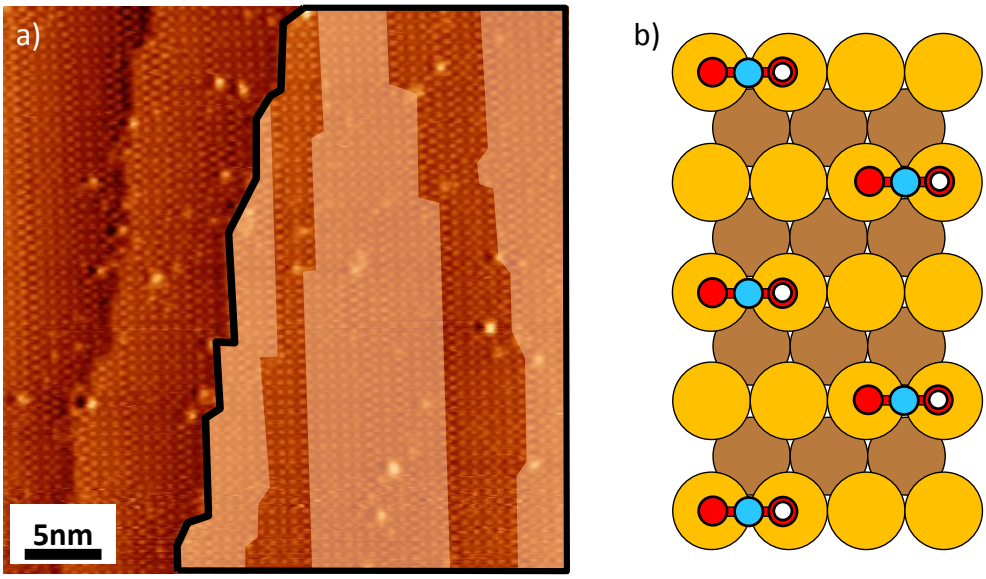

Figure 4.5 a) Large scale STM image of the OA monolayer films. In the top terrace, the OA domains have been coloured to highlight the [001] orientation of the domain boundaries. I=210 pA, U=1.0 V. b) Model of the domain boundary shown in Figure 4.1b, demonstrating the staggered arrangement of the OA molecules.

support for this is gained from STM data taken at different bias voltages, which are shown in Figures 4.4c and d. When imaging with a positive bias (tunnelling into unoccupied sample states), the interstitial species appears to have the same height as those in the surrounding lattice. However, when imaged with a negative bias (from occupied sample states), the interstitial OA appear slightly higher than the surrounding ones. The effect can be seen clearly in the line profiles in Figure 4.4e. This bias-dependent imaging is likely to arise from different binding sites on the Cu(110) surface, such as that suggested in Figure 4.4b.

A second important feature observed in Figure 4.1b is the domain boundary highlighted by the green lines. A statistical analysis over a large number of images showed that these domain boundaries are always oriented along the [001] substrate direction. For example, in the STM image in Figure 4.5a the top terrace has been coloured to reflect the different OA domain boundaries, all of which extend beyond the length of the STM image (37×37 nm^2). Moreover, many of the domain

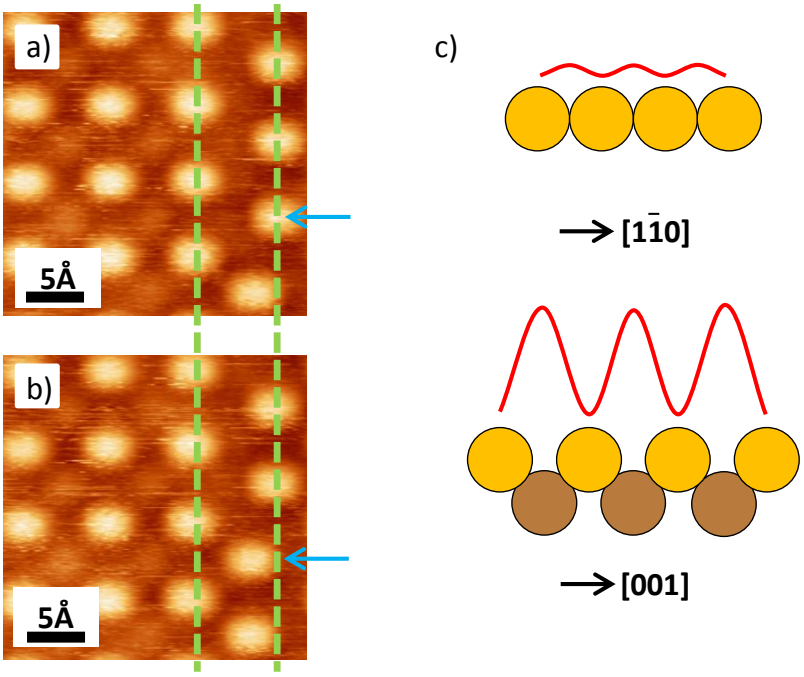

Figure 4.6 a) and b) Sequential STM images of a domain boundary with a 3× periodicity along the [1$\bar{1}$0] direction. The OA molecule highlighted with the blue arrow is seen to move one Cu lattice spacing to the left between the two scans. I=110 pA, U=1.2 V. c) Schematic representation of the diffusion barriers along the two principal crystallographic directions of the Cu(110) substrate.

boundaries, including that in Figure 4.1b, show a greater local OA density than in the (3×2) regions. As is illustrated in Figure 4.5b, by staggering the OA along the [001] direction, the OA is able to pack more compactly, forming a 2× periodicity in the [1$\bar{1}$0] direction, giving a density of 2.65 nm^{-2}. This is a ~50% increase over the 1.8 nm^{-2} observed for the (3×2) phase. This suggests that the interaction between neighbouring molecules is based more on steric constraints than on actual intermolecular forces; this is discussed in more detail in Section 4.1.2.

Sequential STM images taken of wider domain boundaries (those with a 3× or greater periodicity along the [1$\bar{1}$0] direction) reveal a process that may explain why only [001]-oriented grain boundaries are obtained. Figure 4.6a and b show two consecutive STM images taken at a domain boundary with a 3× periodicity along the [1$\bar{1}$0] direction. In the two images, one OA molecule, highlighted by the blue arrow,

moves one Cu lattice spacing along the $[1\bar{1}0]$ direction. Further images reveal that these movements can occur back and forth and also for other OA molecules at this grain boundary. However, no movement has ever been observed along the [001] direction, suggesting that the diffusion barriers along the two crystallographic directions are very different. This is readily justified by consideration of the surface structure; the [001] direction has a much greater corrugation that the close-packed $[1\bar{1}0]$ direction, and thus the corresponding potential barrier that an adsorbate must overcome is comparatively larger. The two barriers are depicted schematically in Figure 4.6c. To understand how these barriers result in the anisotropic OA domain growth, it is important to consider the way in which the molecules have to organise to generate long range ordering. For example, to pack in the [001] direction, the OA must move along the $[1\bar{1}0]$ direction. The opposite is true for ordering along the other direction. As the $[1\bar{1}0]$ diffusion barrier is much lower than the [001] one, long range ordering along the [001] is more easily achieved.

Despite these insights, a number of open issues still remain regarding the exact nature of this film; what is the chemical state of the OA molecules (mono- or doubly-deprotonated, or indeed still intact)? What is the precise orientation of the OA molecules? Why is only the (3×2) structure obtained, instead of the previously-reported c(2×2)? In an attempt to rationalise the observed structure and gain some insight into the remaining questions, DFT calculations have been performed, which are outlined below.

4.1.2 DFT of OA on Cu(110)

The following DFT calculations have been performed by Dr Sara Fortuna and Dr Stefano Fabris. Details of the calculations can be found in Section 2.5.2.

	Chemical State	Adsorption energy/mol (eV)
a) 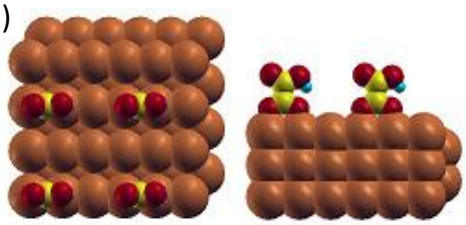	Mono-deprotonated	-0.599
b) 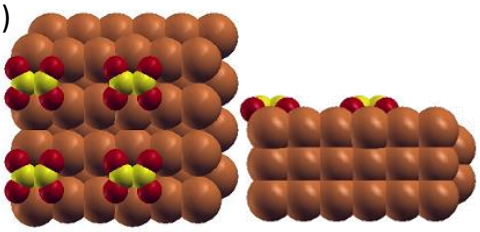	Fully deprotonated	-0.319
c) 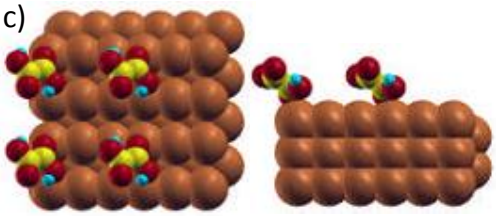	Intact	-0.151

Table 4.1 The most favourable geometries for the a) mono-deprotonated, b) fully-deprotonated and c) intact OA molecules with a (3×2) superstructure on the Cu(110) surface, as predicted by DFT simulations.

The first set of calculations was performed whilst maintaining the experimentally-determined (3×2) superstructure, but varying the chemical state (intact, mono- or doubly-deprotonated) and adsorption geometry (for example, flat-lying, twisted or upright) of the adsorbed OA. Table 4.1 shows the most favourable adsorption geometries for the three different chemical states available to OA. Of these, the lowest energy configuration corresponds to one with mono-deprotonated OA molecules adsorbed in an upright geometry, matching that reported in previous RAIRS measurements [1]. The energy difference between these configurations is of sufficient magnitude that the mono-deprotonated state should be strongly favoured.

When in an upright orientation, the molecules in a (3×2) superstructure are too far apart to be stabilised by intermolecular H-bonds; instead, the H-atom in the

	Structure	Adsorption energy/mol (eV)
a) 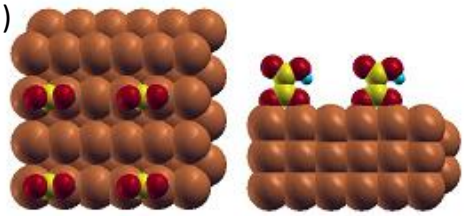	(3x2)	-0.599
b) 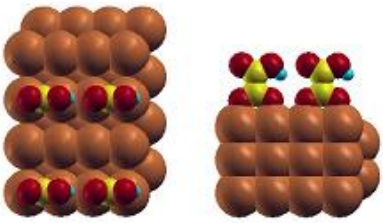	(2x2)	-0.760
c) 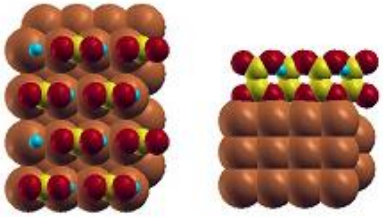	c(2x2)	-0.740

Table 4.2 Total adsorption energies, as predicted by DFT, of mono-deprotonated OA adsorbed in an upright geometry on the Cu(110) surface, using different molecular packings.

remaining carboxylic moiety forms an intramolecular H-bond with the carboxylate moiety that is bonded to the surface. Thus, it is not clear at this stage why the molecules are separated by the experimentally-observed 3× $[1\bar{1}0]$ periodicity, when a 2× periodicity should allow the formation of intermolecular H-bonding. Calculations in this direction, shown in Table 4.2, in fact reveal that the (3×2) superstructure is not the most energetically favourable assembly for the mono-deprotonated upright geometry. By reducing the $[1\bar{1}0]$ periodicity by one Cu lattice spacing, a (2×2) superstructure is formed, which is 0.16 eV more favourable than the (3×2) phase. Furthermore, by also packing the molecules twice as densely along the [001] direction, giving the c(2×2) phase, the total energy per molecule is the same as that calculated for the (2×2) superstructure. However, as this phase has twice the

number of molecules in the unit cell, the total energy per surface unit is now nearly 2.5× more favourable than that of the experimentally observed (3×2). In short, DFT predicts that, if the OA were mono-deprotonated and adsorbed in an upright orientation, they would instead pack into the c(2×2) structure identified from LEED measurements by Martin *et al*. [1].

It is thus clear that DFT cannot accurately predict the experimental adsorption geometry and chemical state of the (3×2) film by considering only the presence of OA molecules. It is likely, therefore, that the OA molecules experience a much more complex chemical environment. This could involve the inclusion of Cu adatoms into the organic lattice, as has been demonstrated in the previous chapter [12] and for other carboxylic acid systems [13-16]. Alternatively, it may be that OA adsorption induces a local (2×1) reconstruction of the substrate, which may explain the observed 2× periodicity along the [001] direction. (110) surfaces of several fcc crystals are well-known to undergo a (2×1) reconstruction, which is driven by the formation of small (111)-facets [17]. Although Cu(110) is stable in its (1×1) structure, the reconstruction is known to be triggered by the deposition of strongly-interacting adsorbates [18,19]. However, given the numerous positions adatoms can reside in, it is not easy to unambiguously identify the presence of adatoms or of a reconstruction with DFT. With this in mind, further experimental data has been obtained; in particular, as the STM data provided no indication of the OA chemical state or adsorption geometry, XPS and NEXAFS measurements have been performed, which are outlined below.

4.1.3 Photoelectron spectroscopy of OA on Cu(110)

The XPS and NEXAFS measurements discussed in this section were done in collaboration with Professor Phil Woodruff and Dr David Duncan. The experiments were performed at the I09 beamline at the Diamond Light Source, UK. As the I09 end-station does not include a STM, LEED was used to confirm the (3×2) structure of the monolayer film after sample preparation.

Figures 4.7a and c show XPS spectra of the oxalic acid monolayer film, whilst in b and d those of the multilayer film is displayed. The O 1s spectrum of the OA (3×2) monolayer, Figure 4.7a, exhibits a singular, narrow peak centred at 531.4 eV. As was the case for TPA on Cu(110) in the previous chapter, such a peak in the O 1s spectrum indicates a fully-deprotonated species; in this case, oxalate. In comparison, the O 1s spectrum of the OA multilayer, Figure 4.7b, shows a peak in the same position, but now with a shoulder at higher binding energy. This shoulder is fitted with two further peaks for the keto- and alcohol moieties of the protonated acid group using a fixed separation of 1.3 eV, as was reported for OA on Cu(111) by Faraggi *et al.* [2].

The C 1s spectrum for the OA monolayer, shown in Figure 4.7c, appears to confirm what is shown by the O 1s core levels. The spectrum is fitted with three separate peaks, centred at 284.3, 287.7 and 289.7 eV. The peak at 287.7 eV is assigned to the oxalic carboxylate moiety, based on its relative intensity and binding energy [2,12,20]. The remaining peaks are harder to identify, as their binding energies lie outside those normally observed for carboxylic species. Faraggi *et al*. reported similar peaks in their investigation of OA on the Cu(111) surface [2], which they identified as CO_2 adsorbed at Cu steps. This seems unlikely, given that CO_2 desorbs from Cu surfaces well below RT [21,22]. Regardless of their exact cause,

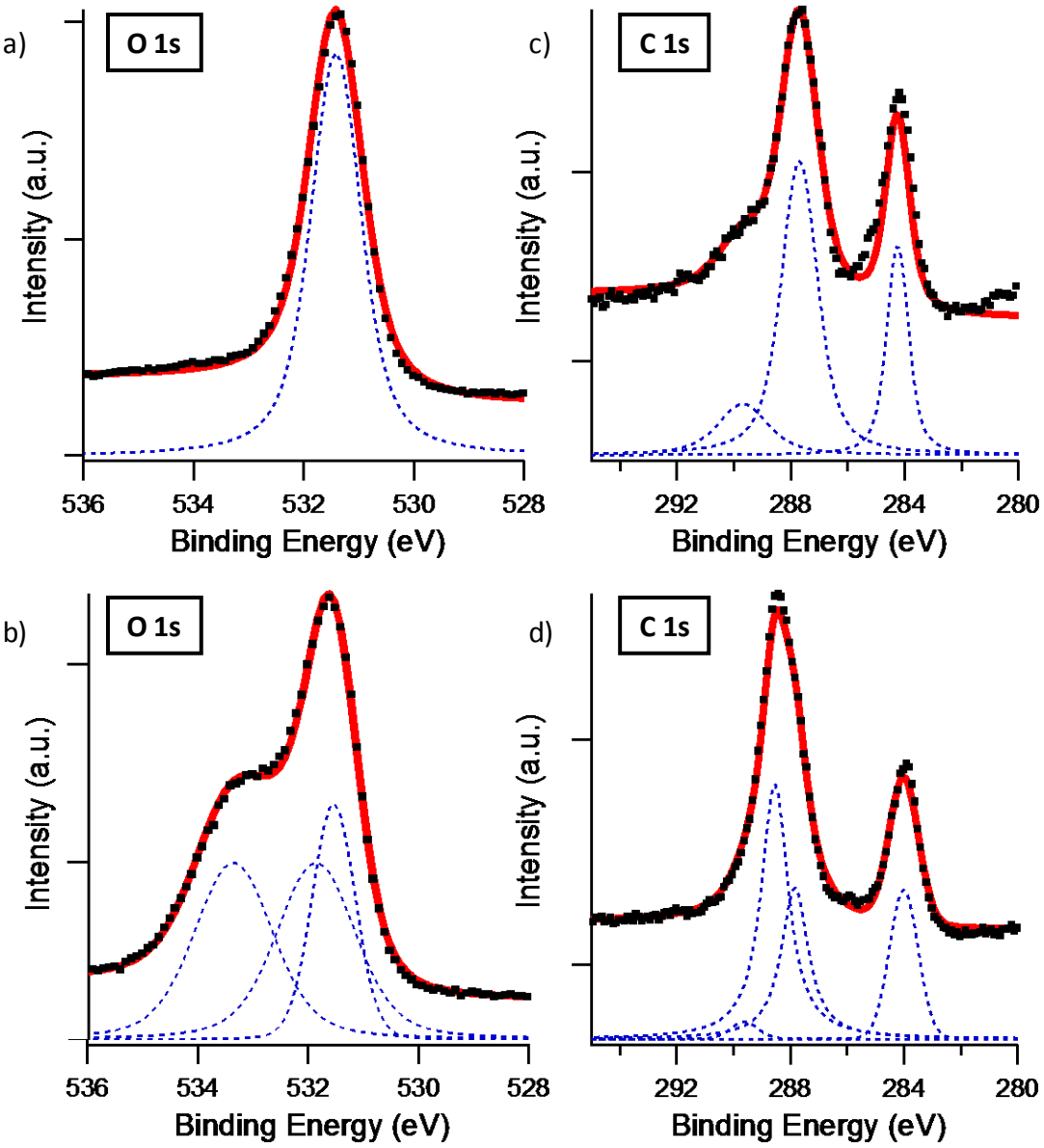

Figure 4.7 a) and b) O 1s spectra of the OA monolayer and multilayer films, respectively. c) and d) C 1s spectra of the OA monolayer and multilayer films, respectively. The peak assignment is discussed in the text.

these two peaks appear to be an intrinsic feature of OA adsorbed on Cu surfaces, but for now, as they cannot be assigned, they will be neglected.

The multilayer C 1s spectrum, shown in Figure 4.7d, shows a broadly similar structure but is in fact considerably more complex. The unidentified peak at 284.3 eV remains, but the equivalent peak at higher binding energy is smaller and is now obscured by the increased broadness of the oxalate peak. The broader oxalate peak

now also appears to be shifted towards a higher binding energy of 288.3 eV. This peak can be ultimately fitted with three separate peaks of different intensities. The first is the small peak at 289.6 eV, which matches the high binding energy unidentified signal observed in the C 1s monolayer spectrum. The second peak, centred at 287.8 eV, is assigned to oxalate in the first molecular layer. The only new peak is that at 288.5 eV, which is assigned to carboxylic C from intact OA that is adsorbed on top of the oxalate film. The ratio of carboxylic to carboxylate signals is fixed at 2.6:1, which matches that obtained in the O 1s spectrum in 4.7c.

The XPS measurements reveal that the previous working model presented in Figure 4.3, where the (3×2) monolayer consists of mono-deprotonated OA, is incorrect. Moreover, it gives a strong indication that the OA is in a flat-lying orientation; it is unlikely that an upright orientation is compatible with a fully deprotonated chemical state. To confirm this, NEXAFS remains the most powerful tool to unambiguously define the molecular orientation.

The relative orientations of the σ- and π-states of OA are shown in Figure 4.8a. The NEXAFS spectra of OA on the Cu(110) surface, taken for a number of different photon polarisation angles with respect to the surface plane, are shown in Figure 4.8b and c. When the photons polarisation vector is aligned parallel to the surface (i.e. incoming light is perpendicular to the sample), the resulting NEXAFS spectrum, shown in pink in both spectra, reveal that the σ-transitions (green band) are favoured over those to π* states (orange band). In the opposite case, where the polarisation vector is close to the surface normal, the π-resonances are strongly favoured. This unambiguously demonstrates that the OA is adsorbed in an approximately flat-lying orientation, as suggested from the XPS data. Moreover, this

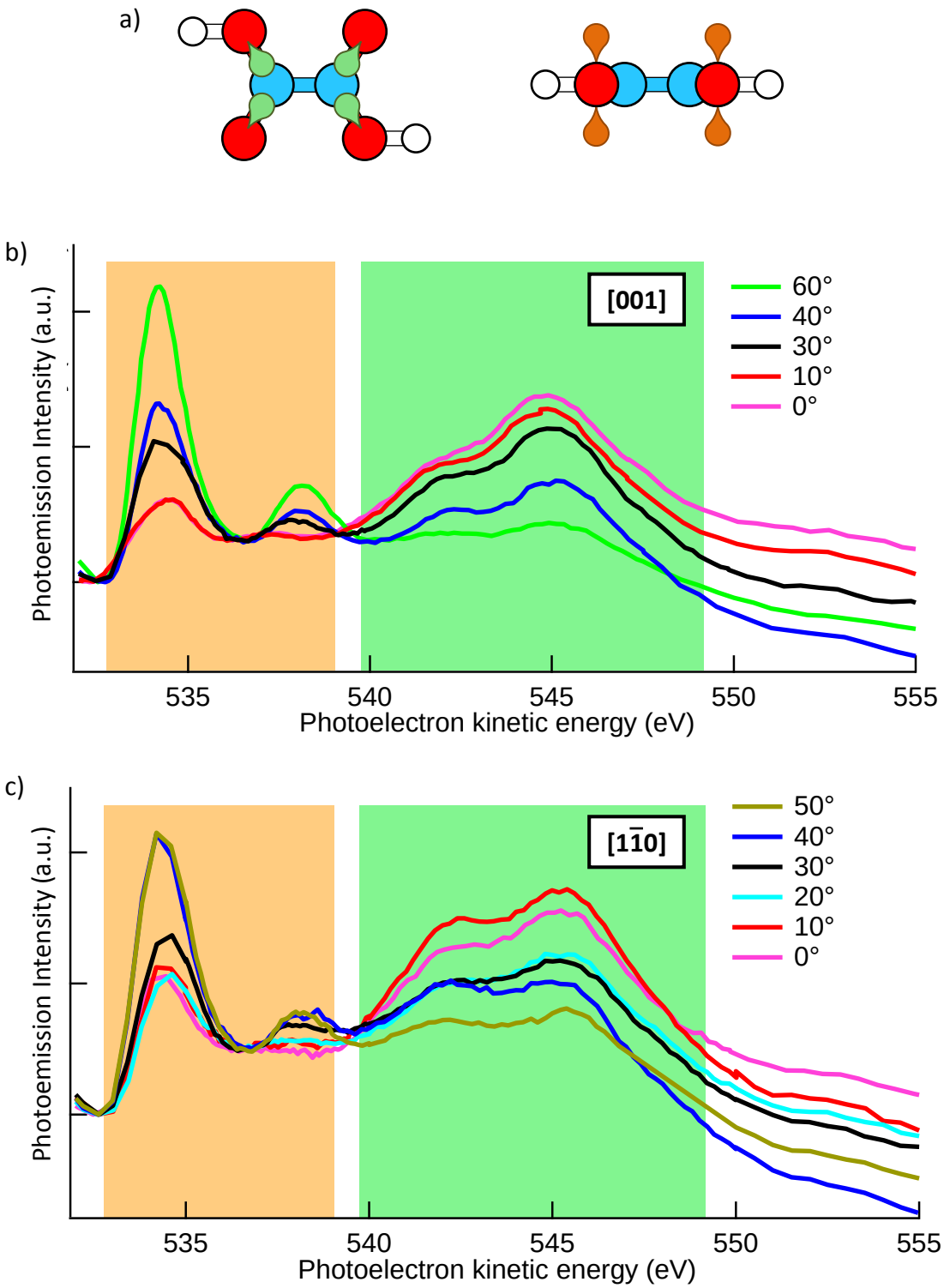

Figure 4.8 a) Top and side views of OA, showing the relative orientations of the σ- and π-states (orange and green, respectively). The NEXAFS spectra of the OA (3×2) monolayer, acquired with the photon incidence angle oriented along b) along the [001] direction and c) along the [1$\bar{1}$0] direction. The photon polarisation vector of each scan are given with respect to the surface plane. In the two spectra, the σ- and π-transitions are highlighted by the green and orange bands, respectively.

further confirms that the tentatively-suggested working model shown in Figure 4.3 was incorrect.

In addition to the flat-lying geometry, it could in principle be possible to identify the orientation of the molecules with respect to the substrate crystallographic directions. This can be achieved by comparing the spectra obtained along the two crystallographic directions. For example, if the spectra taken at the 40° angle along the $[1\bar{1}0]$ or the $[001]$ axes are significantly different, some conclusions about the molecular orientation in the plane of the surface can be drawn. However, in this case, the NEXAFS signal does not appear to vary between the two spectra, and thus it is not possible to extract any information about the orientation of the OA with respect to the two substrate directions.

4.1.4 Summary of OA on Cu(110)

A range of different experimental techniques has been used to characterise the adsorption and assembly of OA on the Cu(110) surface. Initial STM and LEED measurements revealed a low density (3×2) structure, contrary to the densely-packed c(2×2) phase reported previously by Martin *et al*. [1]. To understand the adsorption geometry of the OA molecules in the (3×2) structure, extensive DFT simulations were performed. These revealed that the most favourable geometry for the (3×2) superstructure appears to be one where the OA is mono-deprotonated and is aligned along the surface normal. However, further calculations demonstrated that in this orientation, the OA should in fact pack more densely. Consequently, further experimental measurements were performed to identify the chemical state and adsorption geometry of the OA; XPS and NEXAFS revealed that the molecules were actually fully deprotonated and adsorbed parallel to the surface. The OA geometry is

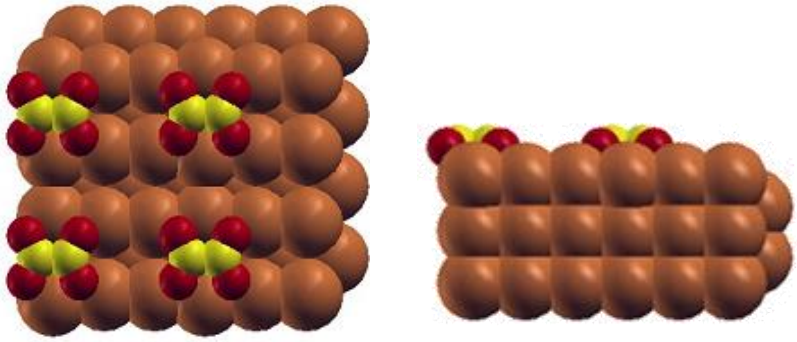

Figure 4.9 Proposed adsorption geometry of the OA molecules, based on the results of the STM, LEED, DFT, XPS and NEXAFS measurements.

therefore most likely similar to that shown in Figure 4.9. However, as the DFT calculations revealed that this structure is less energetically favourable than the upright one, there must be some additional factor, such as a substrate reconstruction, which makes the flat-lying geometry ultimately more energetically favourable. The above data should provide an excellent starting point for further DFT calculations and experimental determination of the exact molecular adsorption geometry, such as that obtained from photoelectron diffraction [23]. These further studies should be able to identify any possible substrate reconstruction or the inclusion of Cu adatoms into the organic matrix.

Alongside a more detailed structural characterisation, another important remaining challenge to be addressed is to understand why only this flat-lying phase has been obtained, instead of the vertically-standing one reported by Martin *et al*. [1]. Attempts to reproduce the upright phase by Martin *et al*. with the deposition setup used in this work have not proven successful. For example, exposures of >100 Langmuirs have been attempted, whereby only multilayer films have been obtained. One possibility is that the c(2×2) observed using LEED by Martin *et al*. may not have been a monolayer film. Instead, it may be that subsequent layers (i.e. the second or third layers) on the surface exhibit a c(2×2) superstructure *on top* of a flat-lying

(3×2) templating layer, similar to what is observed for benzoate and TPA on Cu(110) [24,25]. The first flat-lying layer would not be detected by RAIRS, due to the intrinsic selection rules associated with this experimental technique [26]. Thus, it may be possible that the c(2×2) structure may have been present in the multilayer films shown in Figure 4.1a. STM is not, however, suited to characterising multilayer structures; the potential for high molecular mobility, even at LT, and the reduced tunnelling current in multilayer films can make their resolution with STM challenging, albeit not impossible. Further experiments, such as combined STM and RAIRS measurements, might be needed to further investigate this possibility and to ultimately elucidate the exact cause of the different structures.

4.2 OA on Cu(111)

The adsorption of OA has also been explored on Cu(111), where two intrinsically different OA phases have been obtained. The first has been reported previously by Faraggi *et al.* [2] but has been reproduced and re-evaluated throughout the course of this work. The second, which exhibits a greater molecular density (5.9 nm^{-2} in comparison to the 3.9 nm^{-2} of the flat-lying phase). The two films exhibit completely different molecular adsorption geometries, with the first being flat-lying and the second vertically-standing.

4.2.1 Flat-lying OA phase on Cu(111)

Given its importance in this work, the findings of reference [2] will be briefly presented in tandem with the STM data obtained in this work. When small amounts of OA are deposited onto the Cu(111) surface, dark triangular features are first observed localised at steps, as shown in Figure 4.10a and b. Based on their appearance and the results of XPS characterisation, these were inferred to be formate

[28], generated by the decomposition of OA when adsorbed at steps. Further support for this assignment is achieved in this work, where the internal structure of the dark stripes has been resolved; the chains consist of circular protrusions separated by 2× the substrate close-packed periodicity, matching that reported previously for formate on the Cu(110) [4] and the Cu(111) surfaces [29]. However, further evidence is required for this conclusion, perhaps through NEXAFS characterisation.

As the OA coverage is increased, a phase with rhomboidal symmetry develops on the terraces (Figure 4.10c-f). XPS characterisation by Faraggi *et al*. revealed a complex array of signals, including formate, OA and 'CO_2 contaminants' (as discussed in Section 4.1.3). Critically, the O 1s spectrum contains only a singular sharp peak, indicating that the OA is fully deprotonated. NEXAFS measurements reveal that the oxalate is adsorbed parallel to the surface [27], similarly to that described above for the Cu(110) surface.

A structural characterisation of this phase has proven difficult, as the STM image shown in Figure 4.10f and those reported in reference [2] by Faraggi *et al*. are incredibly difficult to interpret. Faraggi *et al*. previously argued that the fully deprotonated OA should not remain stable on a metal surface; in fact, electron transfer into the surface would render the OA neutrally-charged, which in turn results in decomposition of the OA into CO_2 that then mostly desorbs [21,22]. Consequently, they propose that the oxalate structure is stabilised by coordination to Cu adatoms. The authors also present a DFT-predicted structure that is considerably complex. This structure, shown in Figure 4.11, is unlikely to be completely correct; the dimensions of the proposed structure do not match those of the rhomboidal features in the STM data, contrary to the image shown in Figure 4.11 taken from reference [2].

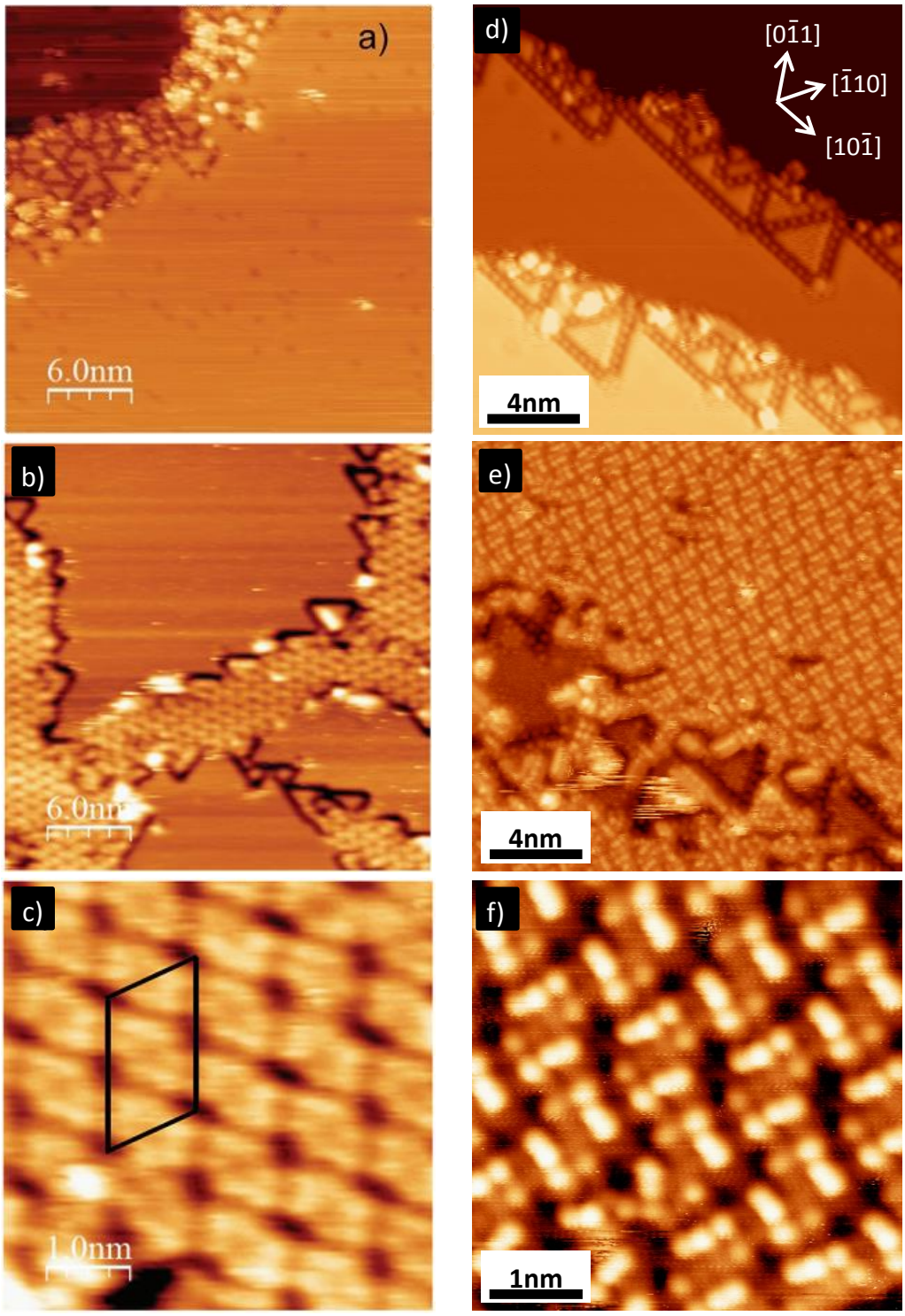

Figure 4.10 STM images showing the adsorption of OA on Cu(111) as a function of coverage. a-c) are adapted from reference [2], performed at 100 K. d-f) were obtained in this work. a) and d) show formation of formate. b) and e) The coexistence of the OA rhomboidal phase and formate. c) and f) Zoomed in STM images of the rhomboidal structure of the OA phase. d) I=100 pA, U=1.0 V. e) I=140 pA, U=-1.7 V. f) I=140 pA, U=-1.7 V. The crystallographic directions inset into d) only apply to d-f).

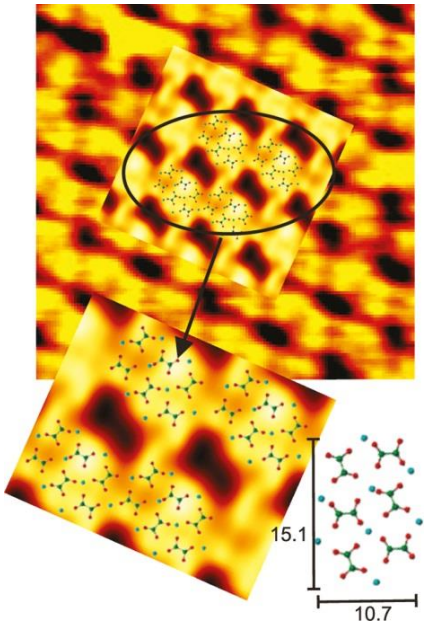

Figure 4.11 Model of the Cu-OA structure on Cu(111) as proposed by Faraggi *et al*. Image taken from reference [2].

This phase has proven generally extremely difficult to reproduce with the current fabrication system. In particular, this is thought to be due to the different rate of deposition used in these experiments when compared to that of Faraggi *et al*. In reference [2], a differentially-pumped OMBE source was used, allowing a fine control over the amount of deposited OA, due to a comparatively slow deposition rate. In contrast, the dosing system used in this work was characterised by a very fast deposition rate, resulting in an OA film that is multiple layers thick within only a few minutes of exposure time. Deposition rate has already been demonstrated to be a particularly important parameter in the fabrication of MO structures [30]; in fact, for a MO species to be formed, the metal and organic components have to meet and interact on the surface. If the organic molecule deposition rate is sufficiently high, the formation of MO structures can be suppressed, due to the reduced probability that an adsorbed molecule and adatom will interact prior to self-assembly of the adsorbates. In the specific case examined here, this effect is amplified, owing to the

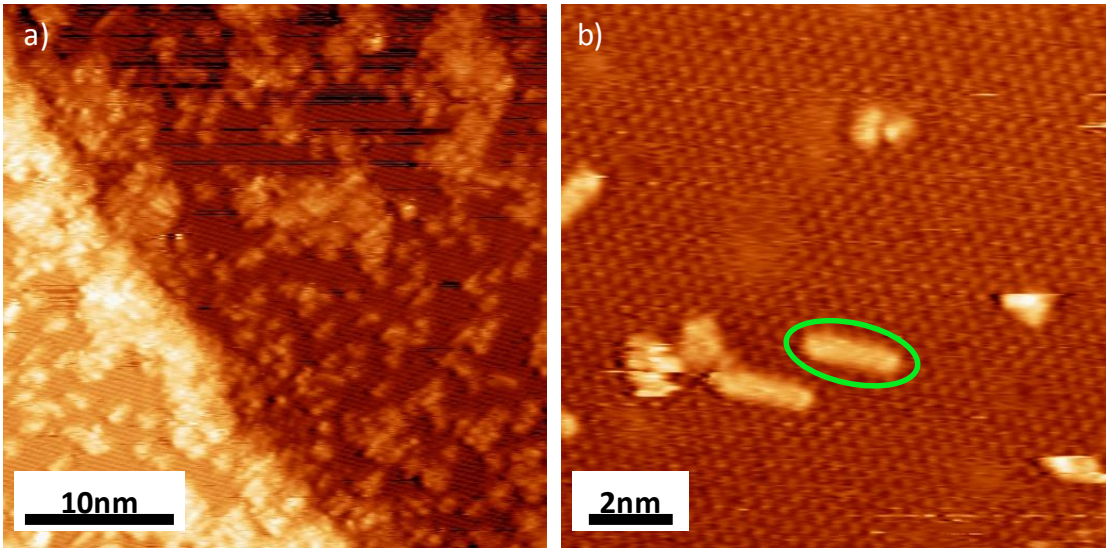

Figure 4.12 a) STM image of the Cu(111) surface after exposure to 30 Langmuirs of OA. I=100 pA, U=-1.0 V. b) STM image acquired after annealing the sample shown in a) to 398 K. The green oval highlights a chain of second layer OA. I=57 pA, U=1.0 V.

comparatively low density of adatoms on the Cu(111) surface at RT [31]. The net result is likely an incomplete deprotonation of the OA molecules, leading to the formation of a novel high density phase, which is described in the next section.

4.2.2 Vertically-standing OA phase on Cu(111)

Figure 4.12a shows a representative STM image obtained after exposure of the Cu(111) surface to approximately 30 Langmuirs of OA vapour. As was the case with the Cu(110) surface, STM images taken immediately after exposure reveal regions of a disordered phase alongside areas that contain an ordered array of protrusions. The disordered regions can be removed by annealing the sample to 398 K; however, on the Cu(111) surface, this tends to leave a small amount of second layer OA, as highlighted in Figure 4.12b. These are organised into 1D stripes, which appear relatively broad. No molecular resolution of these could be achieved. To completely remove the stripes, the sample had to be annealed to temperatures higher

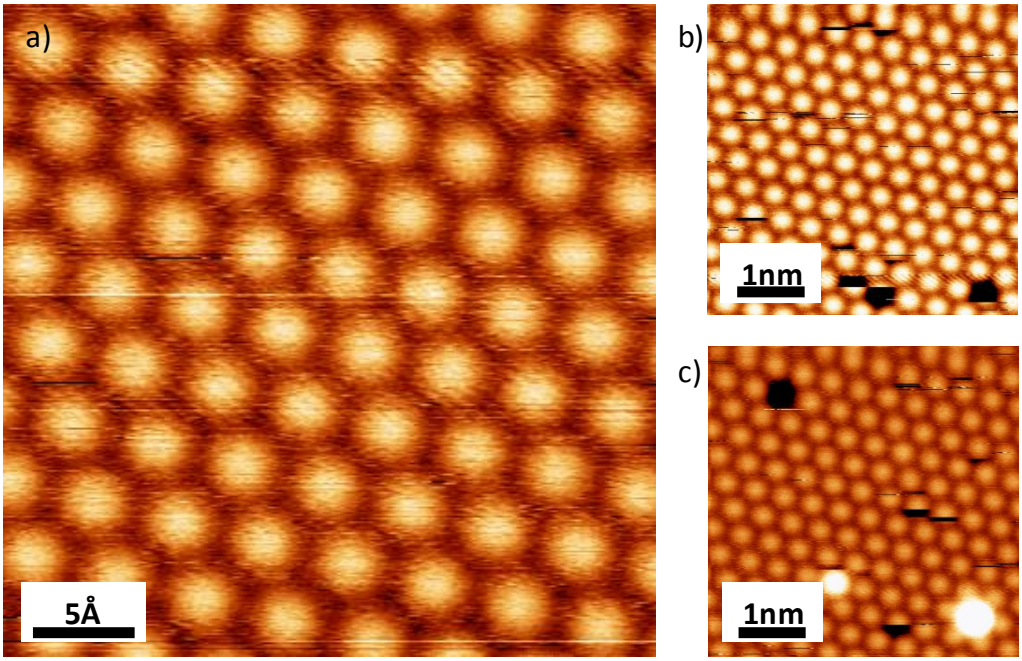

Figure 4.13 a) Zoomed in STM image of the OA (√3×√3)R30° monolayer phase on the Cu(111) surface. I=190 pA, U=-1.4 V. b) and c) Two sequential STM images of the same area, highlighting removal of individual molecules by the tip in b) and deposition of OA molecules onto the OA monolayer in c). The contrast in b) and c) been selected so that the on-top OA molecules could be better resolved. b) and c) I=19 pA, U= -1.4 V.

than 473 K. The resulting OA monolayer, shown in Figure 4.15a, appears to be stable to at least 523 K, which is considerably higher than the 423 K desorption/decomposition temperature determined on the Cu(110) surface and the decomposition temperature reported for the flat-lying phase [2,27].

The monolayer consists of circular protrusions arranged with a hexagonal symmetry. As on the Cu(110) surface, these protrusions are assigned to individual OA molecules. Under particular tip conditions it has occasionally been possible to remove and redeposit individual OA molecules from the monolayer film, as shown in Figures 4.15b and c. This demonstrates that each protrusion is a separate, discrete species and can therefore be safely assigned as single OA molecules.

The OA monolayer was also characterised by LEED, resulting in the pattern shown in Figure 4.14. By measuring the periodicities between molecules in the STM

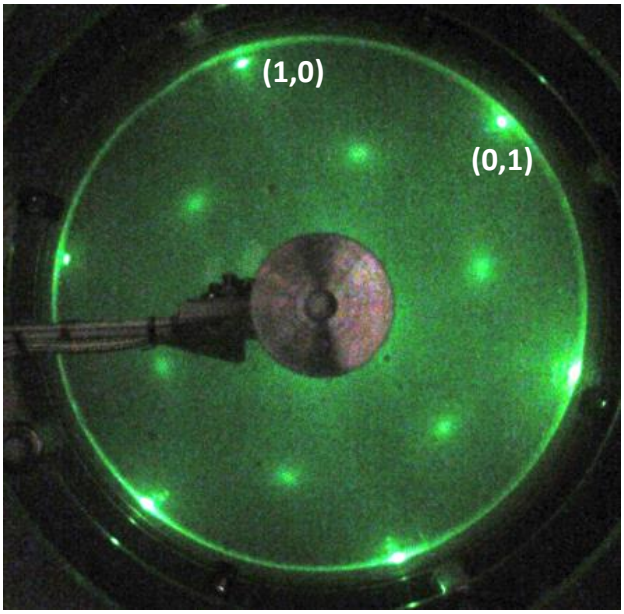

Figure 4.14 LEED image of the OA (√3×√3)R30° structure. E=105 eV, T=207 K.

images, and by thorough inspection of the LEED pattern, it was possible to determine that the OA molecules are adsorbed in a $(\sqrt{3}\times\sqrt{3})$R30° superstructure. Interestingly, the fractional-order spots in the LEED pattern corresponding to the supramolecular phase only appear when the sample is cooled below approximately 208 K. Above this temperature, the molecular spots become gradually more diffuse until they completely disappear, leaving only the substrate (1×1) pattern. This suggests that the OA is mobile on the surface above this threshold temperature, which is perhaps unsurprising given the close-packed nature of the substrate and its expected small diffusion barriers.

The above STM and LEED data allow the exact adsorption configuration of the OA to be inferred. The models in Figure 4.15a and b show two possible adsorption geometries for OA in a $(\sqrt{3}\times\sqrt{3})$R30° superstructure. In the flat-lying motif in Figure 4.15a, the OA molecules are fully deprotonated, in line with the measurements of OA on Cu(110). The resulting O-O separations are ~1.3 Å, which is believed to be highly unfavourable, particularly given the potential for a partial

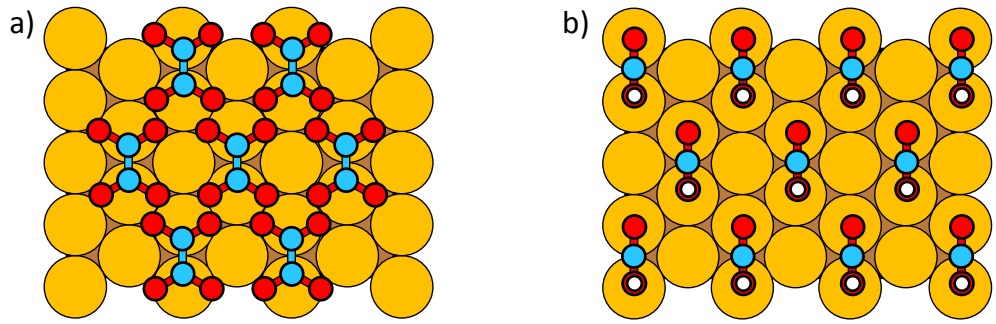

Figure 4.15 Schematics of a potential a) flat-lying and b) vertically-standing OA monolayer on Cu(111) with a (√3×√3)R30° superstructure.

charge or dipole being located on the O atoms as a consequence of deprotonation [32]. In addition, it is unlikely that there is sufficient space for the inclusion of adatoms, which were reported to be a necessary component for the stabilisation of fully deprotonated OA [2]. Instead, it is much more reasonable to believe that OA is adsorbed in an upright geometry, such as that depicted in Figure 4.15b. This geometry is in line with the fabrication method used in this work; rapid deposition favours limited OA deprotonation. In this model, the carboxylate is bonded to the surface in a bridging geometry, as reported previously for formate on Cu(111) [33]. An upright orientation is likely restricted to mono-deprotonated OA, resulting in an 'organic surface' consisting of intact carboxyl moieties. Whilst this structure is believed to be the most likely, further verification is still required.

4.2.2.1 Local-scale structural features in the OA $(\sqrt{3}\times\sqrt{3})$R30° film

Unlike the OA film on Cu(110), the $(\sqrt{3}\times\sqrt{3})$R30° film on Cu(111) is very uniform, exhibiting a very low density of individual missing molecules. Only one type of additional local-scale feature was determined and only very rarely, thereby not being overly significant for the ultimate use of OA films as decoupling layers.

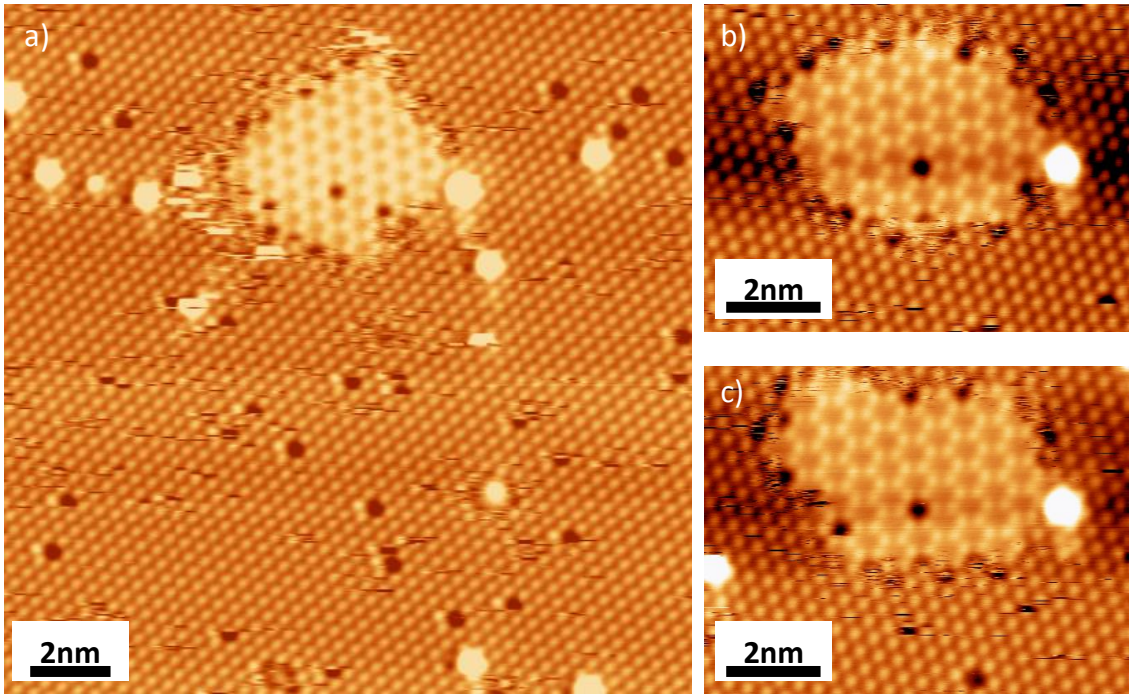

Figure 4.16 Successively-acquired STM images of unidentified features obtained after OA monolayer preparation. a) Large area STM image I=140 pA, U=-1.4 V. b) and c) Sequential STM images of the porous OA structure, showing the dynamic nature of the structure. I=58 pA, U=-1.4 V.

Figure 4.16 shows a series of successive STM images where this feature appears as an inclusion within a regular OA film. Its structure consists of dumbbell-shaped protrusions set in a low density brickwork motif. The gaps between dumbbells appear to have a lower apparent height and, in some cases, a darker hole is visible between the dumbbells. These holes appear approximately similar in size to a single OA molecule (or, as can be observed in Figure 4.16, a single OA vacancy), and thus may be in some way related.

It is not clear at this stage what these features are actually comprised of. The dimensions of the dumbbells do not appear to match those of an upright or flat-lying OA molecule, nor does the structure match that of either of the two OA phases described above. However, the features must be in some way contain OA molecules; in fact, the two images in Figure 4.16b and c were taken sequentially, and it is clear

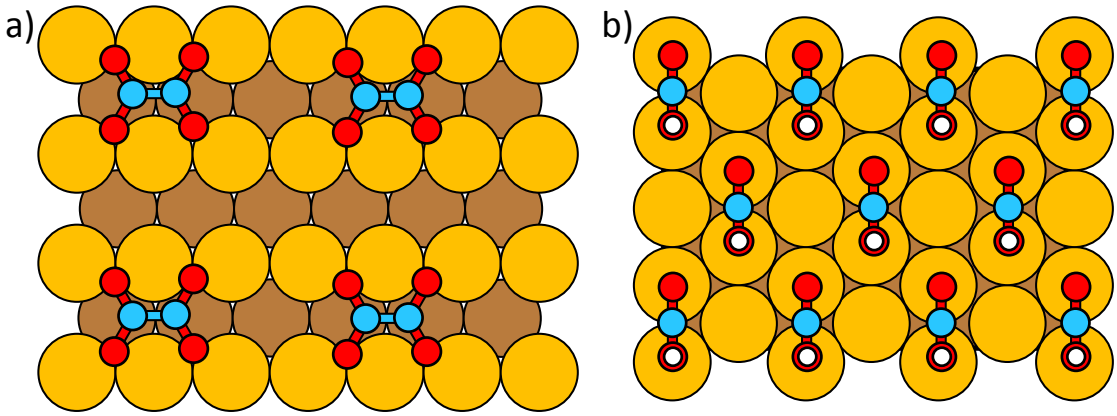

Figure 4.17 Top-view models of a) the flat-lying OA film on the Cu(110) surface and b) the vertically-standing OA on the Cu(111) surface.

that the shape of the bright islands change between the two scans. This 'brickwork' structure must therefore be in some kind of dynamic equilibrium with the surrounding upright OA molecules. A further point of interest is found in Figure 4.16c, where a hole is observed to be forming, suggesting that these also are an integral part of the brickwork phase.

In summary, OA seems to form two different structures when deposited onto the Cu(111) surface. The first is a flat-lying, doubly deprotonated phase reported to contain Cu adatoms; the second is a presumed vertically-standing, mono-deprotonated phase of closely-packed OA molecules. Further experiments are planned to determine the precise OA adsorption geometry and chemical state.

4.3 Comparison of OA films on Cu(110) and Cu(111)

If based only on the STM data, an initial comparison of the monolayer formed by OA on the two copper surfaces could conclude that the molecules adsorb in identical bonding geometries, but with differing superstructures. However, a number of different measurements have proven that this is not the case. On the Cu(110) surface, OA is fully deprotonated and adsorbs in a flat-lying geometry

(Figure 4.17a). Conversely, on the Cu(111) surface, phases with either flat-lying or upright orientations (Figure 4.17b) have been found. These different films have very different packing densities; 1.8, 3.7 and 5.9 nm^{-2} for (3×2) film on Cu(110), and the flat-lying and vertically-standing films observed on Cu(111), respectively.

The ultimate aim of this work is to evaluate the suitability of OA films as decoupling layers. While it is still necessary to experimentally determine their effectiveness, which is explored in the next chapter, certain conclusions can already be drawn here. The (3×2) OA film is not particularly well suited, due to its low molecular density and flat-lying orientation; with a flat-lying film, the interaction between the overlayer and the decoupling film is likely to be complex, as the overlayer molecules could interact with the O or C atoms, or, in this particular case, even the underlying substrate in between the molecules. Conversely, the $(\sqrt{3}\times\sqrt{3})$R30° film on the Cu(111) surface is an ideal model decoupling layer, as the dense-packing and upright geometry should limit penetration through the film and results in a well-defined overlayer-decoupling layer interaction.

4.4 Chapter 4 references

1. Martin, D., R. Cole, and S. Haq, *Investigating the adsorption of oxalic acid onto Cu(110) to create a chemically functionalised surface.* Surface Science, 2003. **539**(1-3): p. 171-181.
2. Faraggi, M.N., et al., *Role of Deprotonation and Cu Adatom Migration in Determining the Reaction Pathways of Oxalic Acid Adsorption on Cu(111).* The Journal of Physical Chemistry C, 2011. **115**(43): p. 21177-21182.
3. Lang, N.D., *Apparent size of an atom in the scanning tunneling microscope as a function of bias.* Physical Review Letters, 1987. **58**(1): p. 45-48.
4. Poulston, S., et al., *STM study of formic acid adsorption on Cu(110).* Physical Review B, 1997. **55**(19): p. 12888-12891.
5. Kreikemeyer Lorenzo, D., et al., *The structure of methoxy species on Cu(110): A combined photoelectron diffraction and density functional theory determination.* Surface Science, 2011. **605**(1–2): p. 193-205.
6. Liu, N., G.R. Darling, and R. Raval, *Dynamic chiral flipping within strongly chemisorbed molecular monolayers at surfaces.* Chemical Communications, 2011. **47**(40): p. 11324-11326.
7. Frederick, B.G., et al., *Electron-stimulated disordering in c(8x2) benzoate/Cu(110): a combined STM, LEED and HREELS study.* Surface Science, 1997. **394**(1-3): p. 26-46.
8. Hayden, B.E., et al., *An iras study of formic acid and surface formate adsorbed on Cu(110).* Surface Science, 1983. **133**(2–3): p. 589-604.
9. Pascal, M., et al., *Quantitative structural determination of the high coverage phase of the benzoate species on Cu(1 1 0).* Surface Science, 2001. **492**(3): p. 285-293.
10. Floate, S., et al., *An in-situ infrared spectroscopic study of the adsorption of citrate on Au(111) electrodes.* Journal of Electroanalytical Chemistry, 2003. **542**: p. 67-74.
11. Atodiresei, N., K. Schroeder, and S. Blügel, *Density-functional theory study on the arrangement of adsorbed formate molecules on Cu(110).* Physical Review B, 2007. **75**(11): p. 115407.
12. Wang, Y., et al., *Varying molecular interactions by coverage in supramolecular surface chemistry.* Chemical Communications, 2012. **48**(4): p. 534-536.
13. Dougherty, D.B., P. Maksymovych, and J.T. Yates, Jr., *Direct STM evidence for Cu-benzoate surface complexes on Cu(110).* Surface Science, 2006. **600**(19): p. 4484-4491.
14. Classen, T., et al., *Hydrogen and Coordination Bonding Supramolecular Structures of Trimesic Acid on Cu(110).* The Journal of Physical Chemistry A, 2007. **111**(49): p. 12589-12603.
15. Wang, Y., et al., *Programming Hierarchical Supramolecular Nanostructures by Molecular Design.* The Journal of Physical Chemistry C, 2013. **117**(7): p. 3440-3445.
16. González-Moreno, R., et al., *Role of the Anchored Groups in the Bonding and Self-Organization of Macrocycles: Carboxylic versus Pyrrole Groups.* The Journal of Physical Chemistry C, 2013. **117**(15): p. 7661-7668.
17. Binnig, G., et al., *(111) facets as the origin of reconstructed Au(110) surfaces.* Surface Science Letters, 1983. **131**(1): p. L379-L384.

18. Kern, K., et al., *Long-range spatial self-organization in the adsorbate-induced restructuring of surfaces - Cu(110)-(2x1)O.* Physical Review Letters, 1991. **67**(7): p. 855-858.
19. Koch, R., et al., *Reconstruction behavior of FCC(110) transition-metal surface and their vicinals.* Applied Physics a-Materials Science & Processing, 1992. **55**(5): p. 417-429.
20. Stepanow, S., et al., *Deprotonation-driven phase transformations in terephthalic acid self-assembly on Cu(100).* Journal of Physical Chemistry B, 2004. **108**(50): p. 19392-19397.
21. Nakamura, J., J.A. Rodriguez, and C.T. Campbell, *Does CO2 Dissociatively Adsorb on Cu Surfaces?* Journal of Physics-Condensed Matter, 1989. **1**: p. SB149-SB160.
22. Rasmussen, P.B., P.A. Taylor, and I. Chorkendorff, *The Interaction of Carbon Dioxide with Cu(100).* Surface Science, 1992. **269**: p. 352-359.
23. Woodruff, D.P., *Adsorbate structure determination using photoelectron diffraction: Methods and applications.* Surface Science Reports, 2007. **62**(1): p. 1-38.
24. Frederick, B.G., et al., *Evolution of Lateral Order and Molecular Reorientation in the Benzoate/Cu(110) System.* Surface Review and Letters, 1996. **03**(04): p. 1523-1546.
25. Tait, S.L., et al., *First layer compression and transition to standing second layer of terephthalic acid on Cu(100).* Physical Chemistry Chemical Physics, 2012. **14**(22): p. 8217-8223.
26. Greenler, R.G., et al., *The metal-surface selection rule for infrared-spectra of molecules adsorbed on small metal particles.* Surface Science, 1982. **118**(3): p. 415-428.
27. Otero, R., et al., *Molecular Self-Assembly at Solid Surfaces.* Advanced Materials, 2011. **23**(44): p. 5148-5176.
28. Nakamura, J., et al., *X-ray photoelectron spectroscopy and scanning tunnel microscope studies of formate species synthesized on Cu(111) surfaces.* Journal of Vacuum Science & Technology A, 1997. **15**(3): p. 1568-1571.
29. Fujitani, T., et al., *Scanning Tunneling Microscopy Study of Formate Species Synthesized from CO2 Hydrogenation and Prepared by Adsorption of Formic Acid over Cu(111).* The Journal of Physical Chemistry B, 2000. **104**(6): p. 1235-1240.
30. Sirtl, T., et al., *Control of Intermolecular Bonds by Deposition Rates at Room Temperature: Hydrogen Bonds versus Metal Coordination in Trinitrile Monolayers.* Journal of the American Chemical Society, 2012. **135**(2): p. 691-695.
31. Perry, C.C., et al., *Face specificity and the role of metal adatoms in molecular reorientation at surfaces.* Surface Science, 1998. **409**(3): p. 512-520.
32. Ishii, H., et al., *Energy level alignment and interfacial electronic structures at organic metal and organic organic interfaces.* Advanced Materials, 1999. **11**(8): p. 605-625.
33. Sotiropoulos, A., et al., *A structural study of formate on Cu(111).* Surface Science, 2000. **444**(1–3): p. 52-60.

Chapter 5

Terephthalic acid on oxalic acid monolayers

,

This chapter addresses the capability of OA films to support molecular overlayers. TPA has been chosen as a test molecular species to assess the effect of the decoupling layer on the *assembly* of overlayer species. It's carboxyl functionalities make it an interesting prototype overlayer species as it can form H-bonds with other TPA molecules and also, in principle, with the underlying OA layer. In addition to this, the assembly of TPA on the bare metal substrates in now well understood (see Chapter 3), and thus any observed superstructures on the decoupling films can be readily compared to that in the non-decoupled case.

In the following, the adsorption and assembly of TPA on the OA (3×2) and $(\sqrt{3}\times\sqrt{3})$R30° monolayer films has been investigated with STM, with a particular focus on whether it is adsorbed on top of the decoupling layer or not. On the flat-lying (3×2) OA monolayer, TPA assembles into [001]-oriented 1D chains. A number of observations indicate that, instead of adsorbing on top of the decoupling layer, the TPA displaces the OA so as to be in direct contact with the metal surface. However, by cooling the sample OA film to LT prior to TPA deposition, this can be prevented. In contrast, the densely packed $(\sqrt{3}\times\sqrt{3})$R30° OA film acquired on Cu(111) is not displaced at RT, and thus the TPA adsorbs on top and is therefore decoupled from the metal surface. The overlayer species assembles into 1D chains and 2D brickwork islands, which, through a detailed structural analysis, reveal that the underlying decoupling layer also plays a significant role in the TPA assembly.

5.1 TPA on the OA (3×2) monolayer

It was concluded in Chapter 4 that the OA (3×2) monolayer fabricated on the Cu(110) surface, shown in Figure 5.1a, is not likely to be the best candidate for a decoupling layer, for a number of reasons. The superstructure has a low-density, which may provide access for overlayer molecules to the underlying substrate. In addition, the OA is adsorbed in a flat-lying geometry, which could result in a poorly defined interaction between the OA and the overlayer. Finally, the decoupling film is relatively thin in comparison to a vertically standing organic monolayer and therefore, even if adsorbed on top, the overlayer may still undergo some electronic interaction with the metallic substrate. Regardless of these potential limitations, the adsorption of TPA on the OA (3×2) monolayer has been investigated with STM.

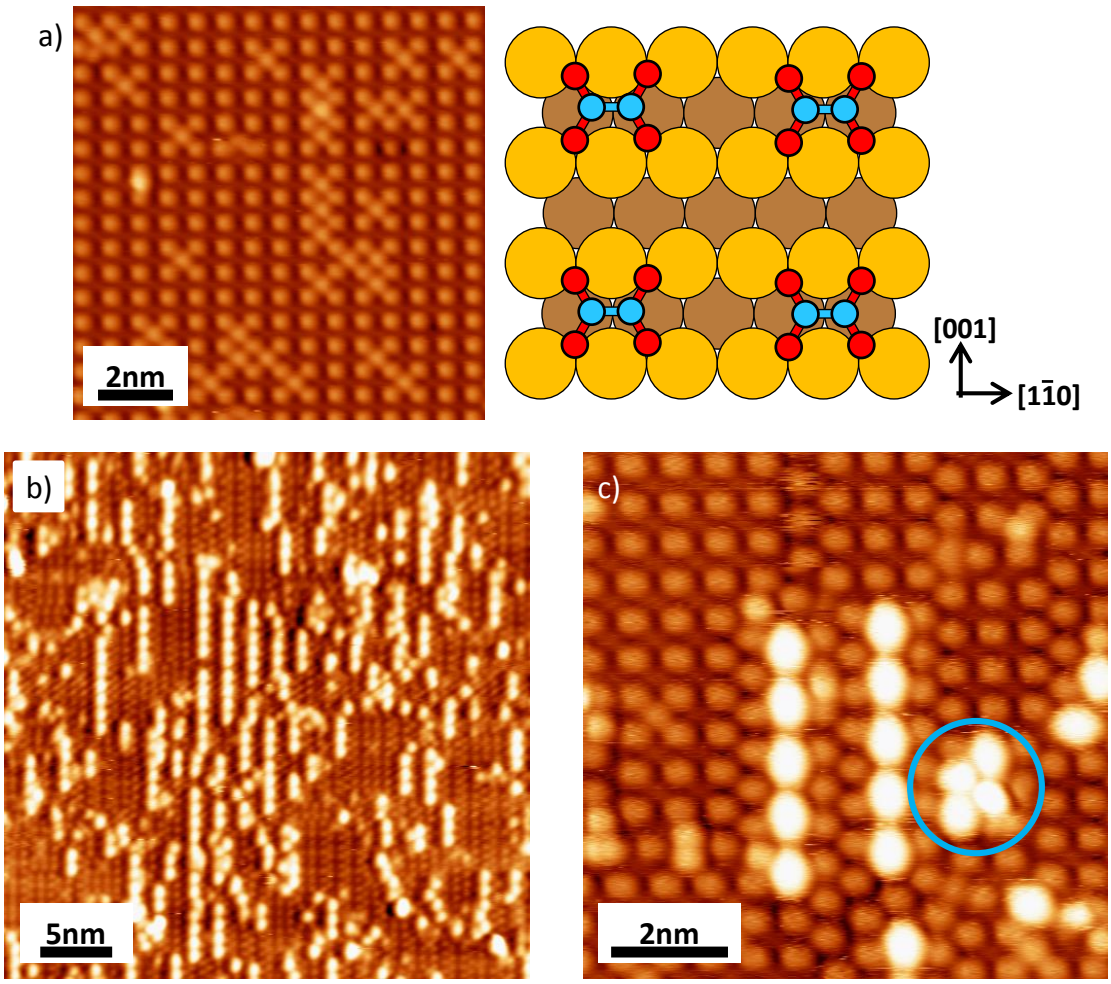

Figure 5.1. a) STM image and model of the OA (3×2) monolayer film obtained on the Cu(110) surface. I=180 pA, U=-1.1 V. b) and c) STM images taken after TPA deposition onto the OA (3×2) film held at RT, showing the formation of [001]-oriented TPA stripes. The blue circle in c) indicates an unordered TPA structure. b) I=210 pA, U=-1.0 V. c) I=110 pA, U=-1.0 V.

Figure 5.1b and c show characteristic STM images obtained after depositing TPA onto the (3×2) OA phase. The sample is held at RT during deposition, after which it is cooled to 77 K for imaging. The TPA molecules are imaged as bright, elliptical protrusions and are mostly assembled in [001]-oriented chains. They appear significantly brighter than the surrounding OA, possibly suggesting they are adsorbed on top of the OA monolayer. Occasional small, randomly-arranged TPA structures and isolated species are also observed, such as that highlighted by the blue

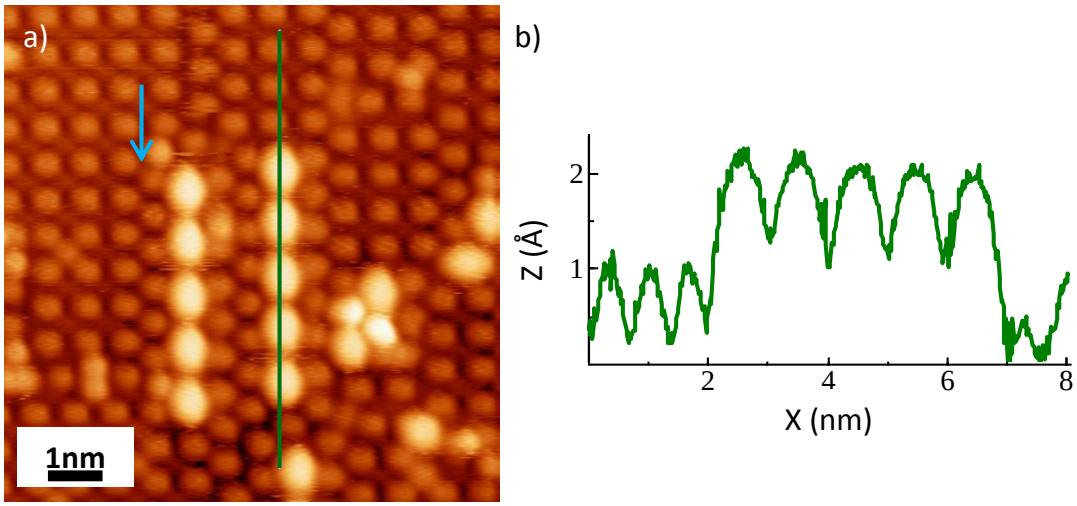

Figure 5.2 a) STM image of two TPA chains on the OA (3×2) film. The green line marks the position of the profile shown in b). The blue arrow in a) highlights the local disorder in the OA film. I=110 pA, U=-1.0 V.

circle in Figure 5.1c, but these are comparatively rare and were therefore not characterised in detail.

Close inspection of the TPA chains, Figure 5.1c, shows that the TPA long molecular axis is always aligned along the chain direction – i.e. along the [001] crystallographic direction of Cu(110). This suggests that the molecules interact via H-bonding of the carboxyl moieties and are therefore not deprotonated. Further verification of this is given by the intermolecular periodicity, 9.7±0.3 Å, which gives an average H-bond length of 2.7 Å that matches those typically obtained for H-bonded TPA [1-7] (see table 3.1). The STM data also indicates that there are no observable changes to the structure after annealing up to 398 K.

5.1.1 TPA adsorption geometry: on top of the OA?

Figure 5.2 reveals that the apparent height of the TPA appears to be ~1 Å greater than the decoupling layer. This could be taken as an indication that the TPA is adsorbed on top of the OA film. However, this is not conclusive evidence due to

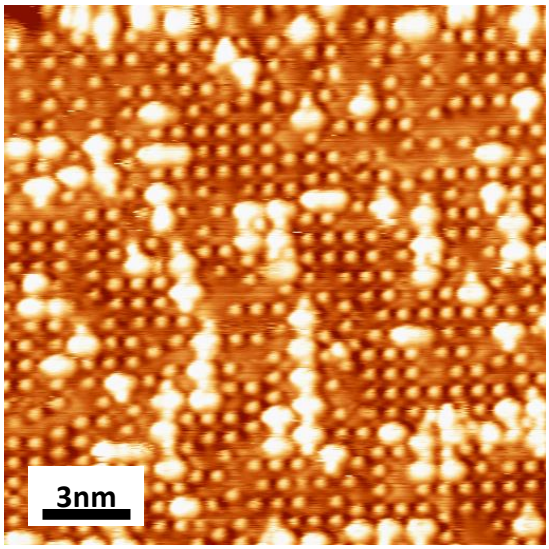

Figure 5.3 STM image of TPA on the OA (3×2) film after annealing to 423 K. Gaps are now found in the OA lattice, whilst the TPA have maintained the same apparent brightness with respect to the OA molecules. I=65 pA, U=-0.9 V.

the well-known fact that STM-determined heights can be strongly influenced by electronic effects [8], and thus do not necessarily reflect 'true' topographic heights.

In an attempt to further clarify the cause of the observed contrast, a sample such as that shown in Figure 5.1b has been annealed to 423 K. As was observed in Section 4.1, this results in decomposition and possibly desorption of some of the OA, in turn exposing regions of the underlying metal surface. Even if initially adsorbed on top of the OA, the TPA would be expected to have moved into these vacancies after annealing, as this would allow them to have a direct and more energetically favourable interaction with the metal surface. The effects of this treatment are demonstrated in Figure 5.3; the 1D chains are mostly dispersed and the individual molecules are all reoriented along the $[1\bar{1}0]$ direction. These observations are taken as proof that, regardless of their initial adsorption location, the TPA is now adsorbed directly on the metal surface. The TPA still appear brighter than the surrounding OA, revealing that their enhanced contrast is not just due to their topography, but instead to an electronic effect. Although DFT calculations might be

required to elucidate the precise origin of the tunnel current enhancement, this will most probably be due to the high electron density of the TPA phenyl ring.

This result is backed by further evidence that indicates that, directly upon deposition, TPA penetrates through the OA film and adsorbs directly on the metal surface. The blue arrow in Figure 5.2 highlights that, in the area immediately surrounding the TPA chain, the OA superstructure exhibits a denser structure than the (3×2) observed prior to deposition. In these regions, neighbouring [001]-oriented OA rows are only separated by 2× Cu lattice spacings and are offset by 1× the lattice spacing along the [001] direction. This results in a local OA density of 2.65 nm^{-2}, in comparison to 1.80 nm^{-2} for the unperturbed OA (3×2) lattice. This reorganisation is observed around all TPA chains, indicating that it is a fundamental consequence of TPA adsorption.

There are two plausible reasons for this rearrangement; in the first, TPA, adsorbed on top of the OA, reorganises the underlying decoupling layer to optimise its own adsorption geometry. However, for this to be true, the locally increased OA density should be offset by a corresponding reduction in other areas. As no vacancies or OA superstructures with reduced density are observed after TPA deposition, this is assumed to not be the case. Instead, it is much more reasonable to believe that the OA restructuring is induced by a different mechanism, one where the TPA displaces the underlying OA film to adsorb directly onto the metallic surface, as is depicted in Figure 5.4. In this way, the locally higher molecular density is generated without the need to reduce it in other areas.

This model may also explain why the TPA assembles into [001]-oriented chains. In Section 4.1.1, it was noted that only [001]-oriented grain boundaries are observed in the OA superstructure, whilst no $[1\bar{1}0]$-oriented boundaries are

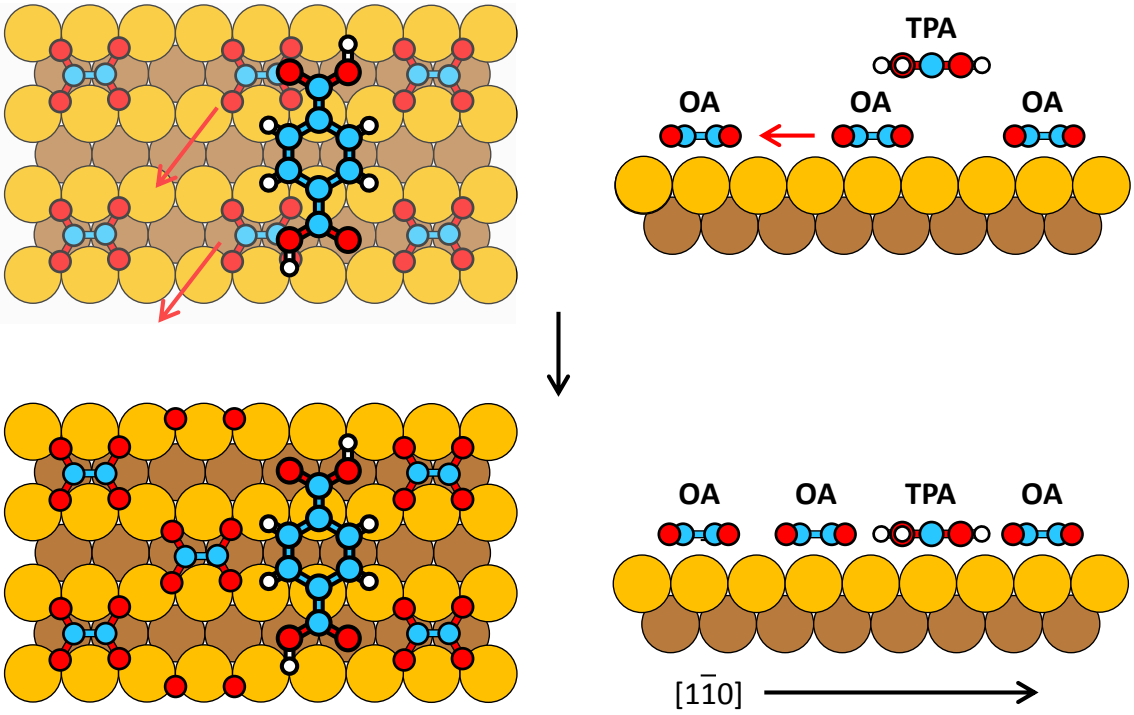

Figure 5.4 Schematic of the TPA molecules penetrating through the OA film to adsorb on the bare surface. The TPA initially adsorbs on top of the OA film (top). The OA is then displaced, so that the TPA can adsorb directly on the metal surface (bottom). The increased local OA density is a consequence of the TPA 'squeezing' the OA out of the way. The OA molecules and Cu(110) substrate have been faded in the top left panel, to clarify the TPA molecule.

identified. Many of these domain boundaries exhibit a similar staggered geometry to that observed about the TPA chains. It is likely that, when arranged in this manner, the OA does not experience a significant energetic penalty in comparison to the (3×2) molecular arrangement, due to the intercalation of the molecular rows. In other words, this structure most likely represents the least energetically unfavourable arrangement that also grants a denser OA packing. By assembling into [001]-oriented rows, the TPA spatially optimises the formation of this higher-density OA structure. Conversely, if the TPA were to form, for example, [1$\bar{1}$0]-oriented structures, the OA would have to be displaced along the [001] direction. As no [1$\bar{1}$0]-oriented grain boundaries are observed in the pristine film, this is assumed to be considerably energetically unfavourable.

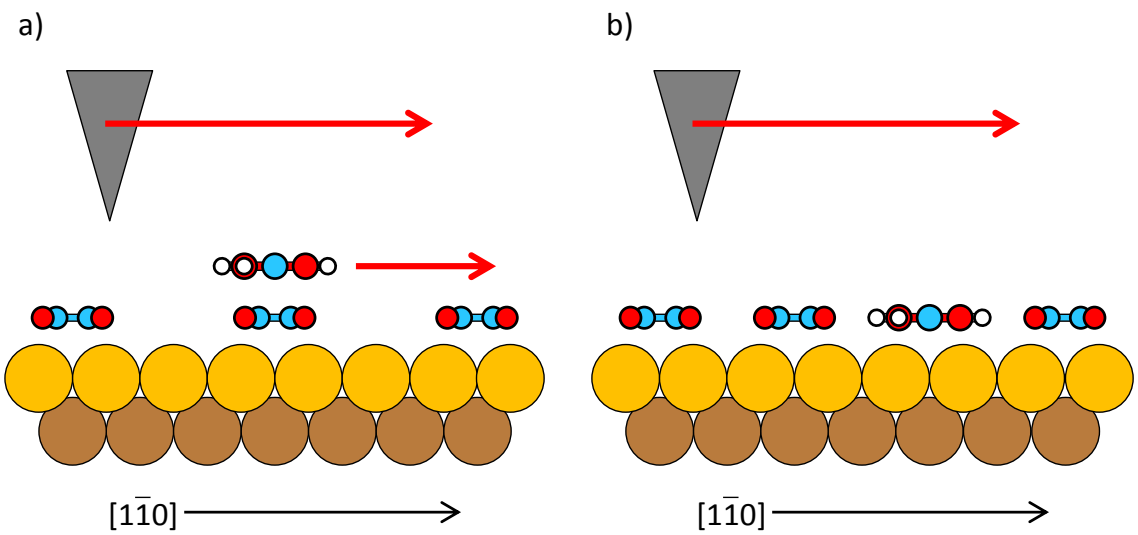

Figure 5.5 a) Schematic of proposed TPA manipulation on-top of the OA film by the STM tip. b) Model demonstrating how the lack of TPA mobility fits a model where OA is displaced and TPA is directly adsorbed onto the copper substrate.

Further support for this second TPA adsorption model comes from efforts to manipulate the TPA using the STM tip. Controlled manipulation of adsorbates with the STM was first demonstrated in the seminal work of Eigler *et al*. in the early 1990's [9,10], whereby tip-adsorbate interactions were utilised to manipulate single atoms on the surface and fabricate a range of nanostructures. These procedures can be extremely complex and usually require the mechanical stability only achieved with liquid He-cooled STMs. However, it is possible to perform manipulations in a coarse manner, even at 77 K, by imaging the surface with small tip-surface separations (see Section 5.2.1). If the TPA was adsorbed on top of the OA, as illustrated in Figure 5.5a, its anticipated weak binding to the organic layer and its corresponding low diffusion barrier should allow it to be readily manipulated. Numerous attempts have been made to move the TPA in this way, but no evidence of translation has been observed. Consequently, the scenario illustrated in Figure 5.5b is anticipated, whereby the TPA is effectively immobilised by the strong molecule-substrate interactions and, possibly, OA-TPA lateral interactions.

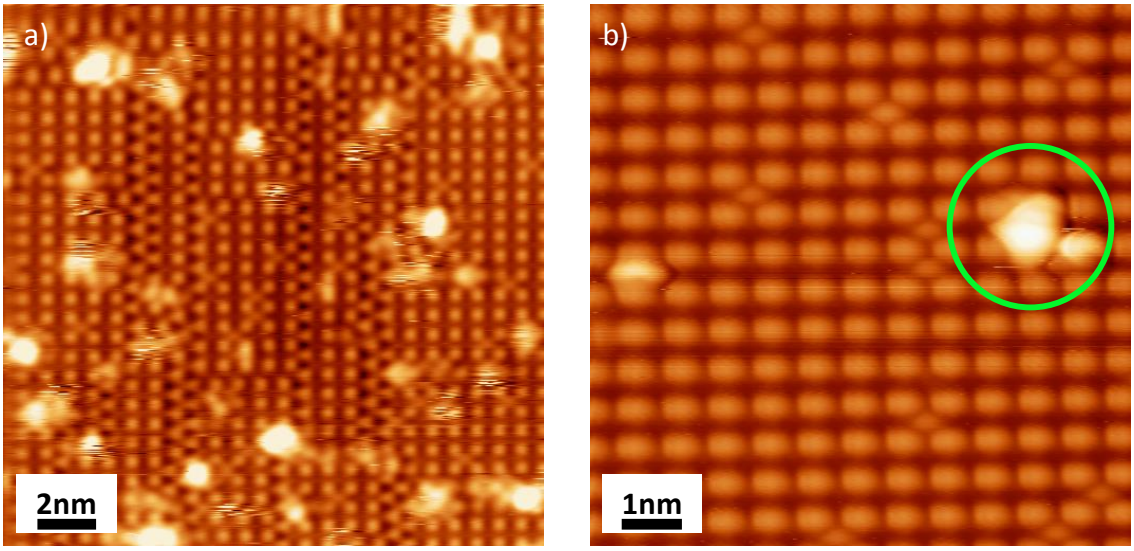

Figure 5.6 STM images of TPA on the OA (3×2) film, held at approximately 140 K during TPA deposition to limit OA mobility. a) Large range STM image. I=83 pA, U=1.4 V. b) Zoomed-in STM image of what is thought to be a single TPA molecule, circled, highlighting that there is no disruption to the OA lattice. I=58 pA, U=-1.8 V.

5.1.2 Deposition of TPA onto a OA film held at LT

As molecular motion is inhibited at LT, it may be possible to prevent TPA penetrating the OA film by cooling it prior to overlayer deposition. Figure 5.6 shows characteristic STM images obtained after depositing TPA onto an OA (3×2) film held at approximately 140 K. It is immediately apparent that the TPA H-bonded chains are no longer formed. Instead, the surface now contains only isolated, randomly placed bright protrusions that exhibit no uniform shape.

Crucially, the OA layer is still highly ordered and no regions with a local higher OA density are observed in the proximity of the TPA molecules. This reveals that the TPA has adsorbed on top of the OA film, which has therefore effectively worked as a decoupling layer. The irregular appearance of the individual adsorbates might be due to a variety of different adsorption geometries, which is made possible

by the low substrate temperature and the weaker interaction of the TPA with OA, with respect to the Cu substrate.

While successful, this approach is far from ideal. By pre-cooling the OA film, the overlayer species cannot adopt their most thermodynamically favourable adsorption geometry with respect to the OA film. As an adsorbate's local environment can play a significant role in determining its functional properties, this may be undesirable for certain applications [11]. In addition, the lack of molecular mobility precludes the formation of self-assembled structures on top of the decoupling layer. Consequently, this strategy has not been explored further.

In summary, the STM measurements described above reveal that the OA (3×2) film is not an ideal decoupling layer. However, it may be of potential use to modify the molecular assembly of benzyl carboxylic acids; in this example, the TPA forms isolated 1D chains that have previously only been obtained on Pd(111) [5]. Moreover, it also appears that by pre-treating the Cu surface with OA, the TPA chemical state is preserved, as evidenced by the formation of intermolecular H-bonds in the TPA structure, similar to that recently demonstrated by using Sn [12].

5.2 TPA on the OA $(\sqrt{3} \times \sqrt{3})$R30° film

To recap, two distinctly different superstructures have been observed when OA is deposited onto the Cu(111) surface. The first, originally reported by Faraggi *et al*. [13], consists of fully-deprotonated, flat-lying OA molecules. The proposed supramolecular assembly is considerably complex and contains Cu adatoms, which were reported to be necessary to stabilise the deprotonated molecules against decomposition. This monolayer has proven generally difficult to reproduce with the

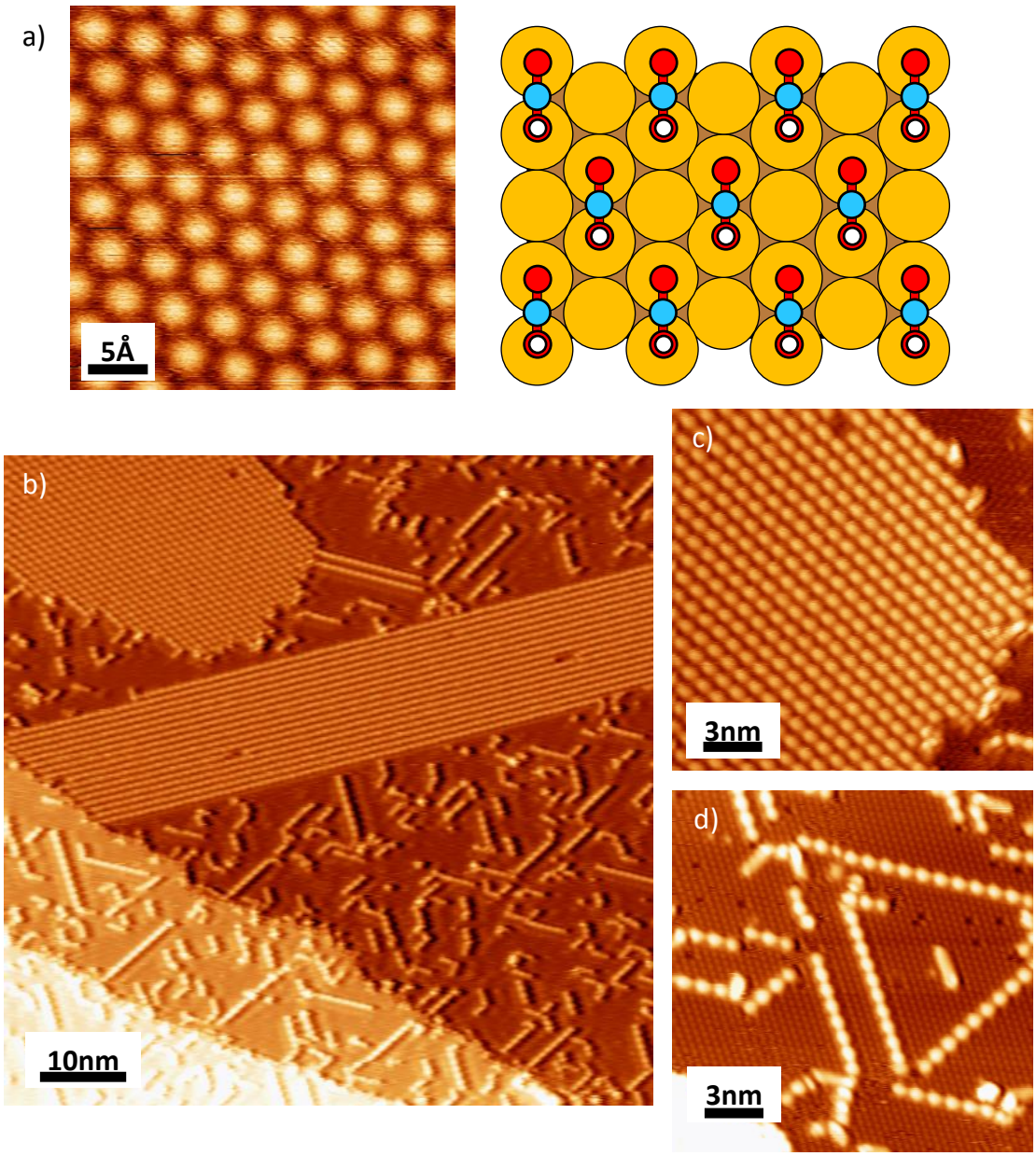

Figure 5.7 STM images and model of the $(\sqrt{3} \times \sqrt{3})R30°$ OA structure obtained on the Cu(111) surface. I=90 pA, U=-1.4 V. b-d) STM images acquired after TPA deposition onto the OA film held at RT. c) and d) show zoomed in images of the overlayer 2D islands and the 1D chains, respectively. b-c) I=14 pA, U=1.8V. d) I=100 pA, U=-0.9 V.

current deposition setup and its structure is currently not well understood, so it has not been used in this part of the investigation.

The second assembly, shown in Figure 5.7a, is thought to consist of mono-deprotonated OA molecules arranged in an upright geometry in a densely-packed

$(\sqrt{3}\times\sqrt{3})$R30° superstructure. Consequently, this phase is anticipated to be a much more appropriate choice for a decoupling layer; in particular, no exposed Cu (except in rare cases) and no mobility of the OA molecules have ever been observed, making the displacement mechanism outlined in Section 5.1.1 for the OA (3×2) phase very unlikely. Furthermore, as the film is terminated with carboxylic moieties, it is anticipated to have a strong effect on the assembly of overlayer species.

Figure 5.7b-d shows a series of STM images obtained after depositing TPA onto an OA $(\sqrt{3}\times\sqrt{3})$R30° film held at RT. The TPA again appears brighter than the surrounding OA lattice. Two different TPA superstructures are observed, which are highlighted in the Figures 5.7c and d. The first, Figure 5.7c, consists of 2D islands that have internal structures reminiscent of the brickwork motif obtained on weakly-interacting materials [2,4,6]. Interestingly, the defects that characterise the brickwork structure on Cu(111) (see Section 3.2) are not observed. The second, highlighted in Figure 5.7d, consist of 1D chains similar to those observed on the OA (3×2) film. The two phases are oriented perpendicularly from one another, which will be expanded upon in Section 5.2.2.

In both cases, the head-to-tail arrangement of the TPA ellipses strongly suggests that the molecules are intact and interact via H-bonding. However, the two superstructures exhibit uncharacteristically short H-bonds; 2.2±0.3 Å and 1.9±0.5 Å for the 2D islands and the 1D chains, respectively. In contrast, the separation between neighbouring chains in the 2D islands are abnormally large at 8.4±0.1 Å, in comparison to the ~6 Å and ~5 Å observed on Au(111) and Ag(111) [4,6], and the 5.5±0.3 Å identified on bare Cu(111).

5.2.1 TPA adsorption geometry

As was the case for the OA (3×2) film, the STM data presented above contains sufficient information to infer the adsorption site of the TPA. Initial inspection of the two structures might suggest a displacement model. For example, the existence of 1D stripes on the (3×2) OA phase on Cu(110) is most likely a consequence of the TPA being adsorbed directly on the metal surface. Moreover, the observed lack of defects in the 2D islands might be due to in-plane pressure from the surrounding OA molecules [14] that compresses the TPA film and inhibit the formation of longer H-bonds. Whilst this would also be in line with the particular small H-bond lengths, it would, however, be in conflict with the increased separation between neighbouring chains in the 2D islands. These observations could also be explained by a strong templating effect of the OA layer, and more importantly, there is also a significant body of evidence supporting the opposite scenario of an actually decoupled TPA film.

When deposited onto the OA (3×2) film on the Cu(110) surface, TPA displaces the decoupling film, generating localised disruption of the OA monolayer in the areas immediately surrounding the TPA chains. In contrast, the STM images shown in Figure 5.7 reveal that in this case the OA is not disrupted. It could be that, instead of adsorbing as an overlayer, the TPA has again displaced the OA but has not generated a new OA superstructure. For this to be true, the displaced OA would have to be removed from direct contact with the metal by being lifted on top of other OA molecules. However, there is no evidence of this, and thus the lack of disruption is taken as a strong indication that the TPA is adsorbed on top of the decoupling layer.

In addition to this, and perhaps more importantly, tip-induced movement of the TPA (similar to that described in Section 5.1.1) has proven successful on this

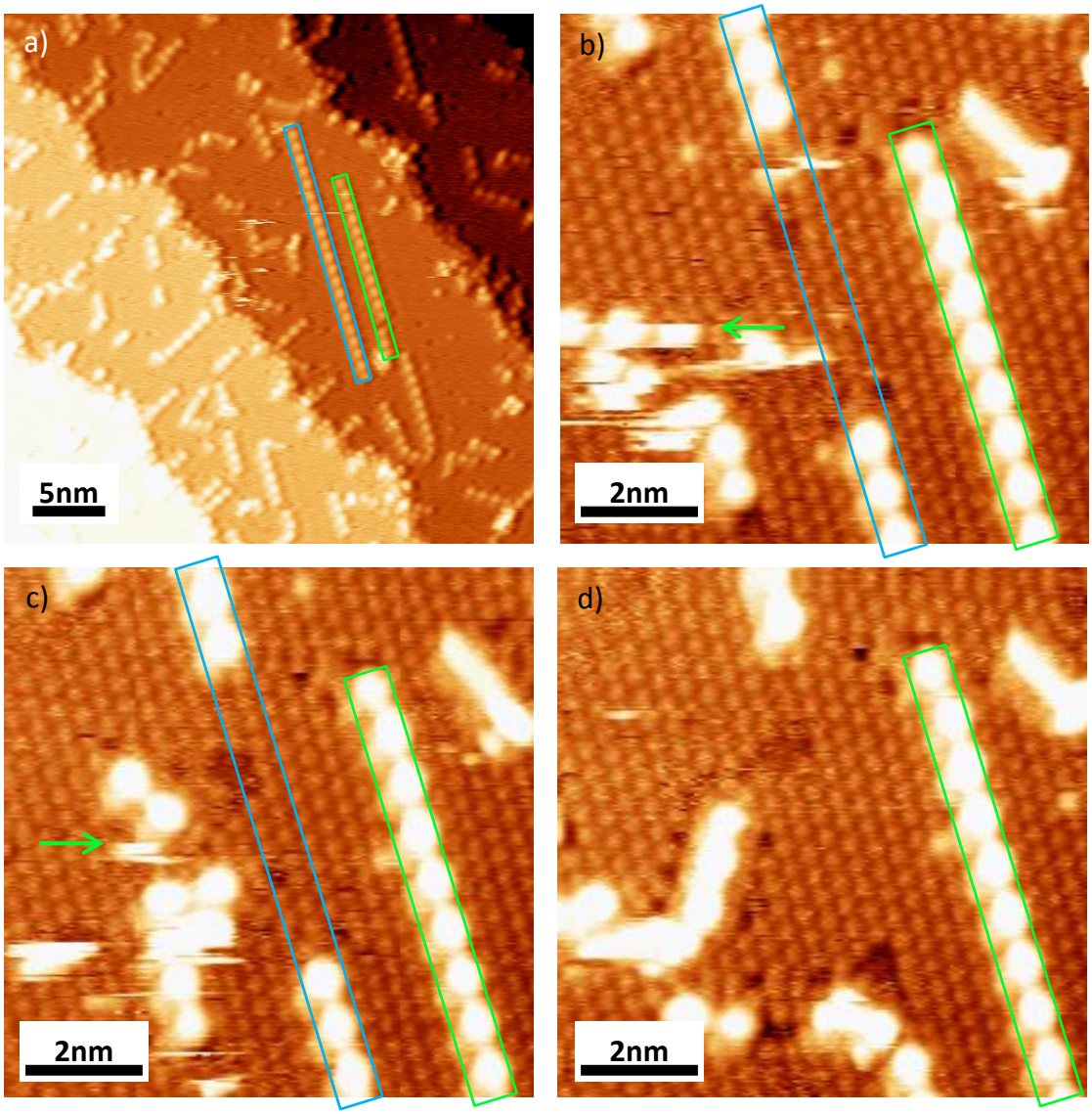

Figure 5.8 a-d) Sequentially-acquired STM images of two 1D TPA chains on the OA/Cu(111) film. The chain highlighted in blue is disassembled by its interaction with the scanning tip, whilst that in green remains intact and can be used as a reference marker. The green arrows in b) and c) indicate the positions of the displaced TPA. All STM images taken at I=100 pA, U=-1.8 V.

decoupling layer. Surprisingly, these manipulations were already possible with relatively mild tunnelling conditions, often occurring even when using routine imaging conditions. Figure 5.8 shows a series of successive STM images of two TPA chains, highlighted by blue and green boxes. The chain indicated by the blue box starts to be disrupted between the images in 5.8a and b, with some of the molecules appearing to have been displaced to the left of the image, as indicated by

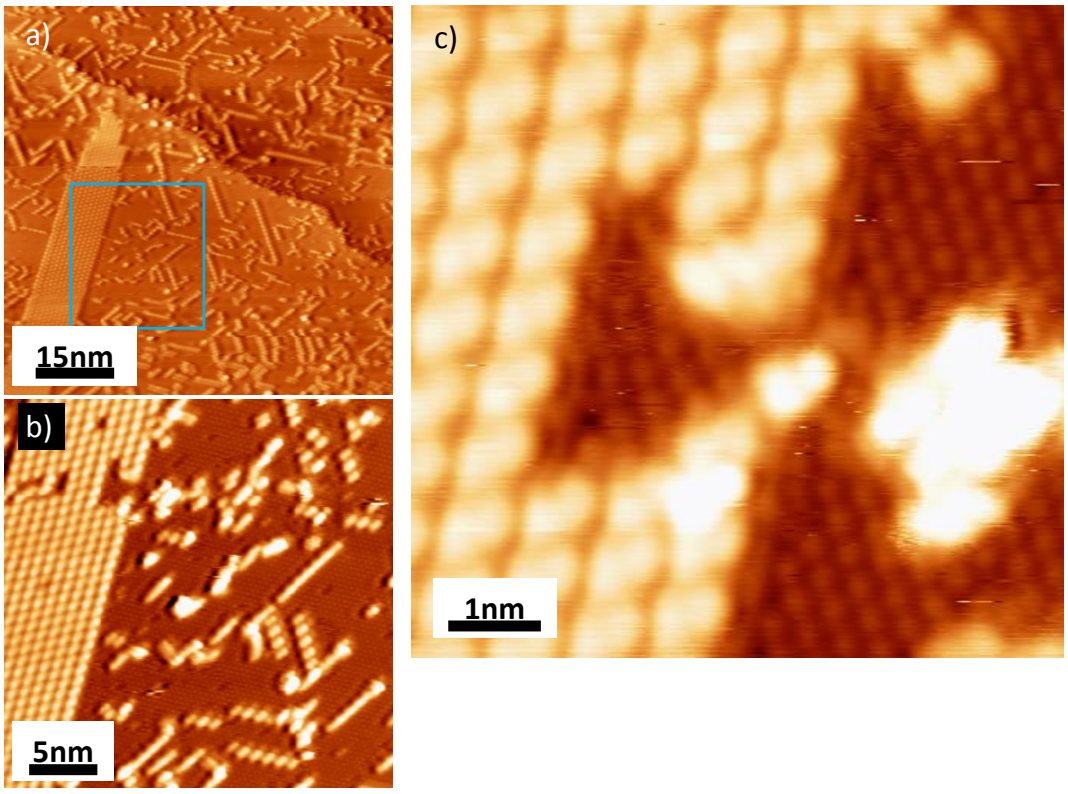

Figure 5.9 a) Large area STM image of TPA deposited onto the OA/Cu(111) monolayer. The blue box corresponds to the approximate area shown in panel b). A line-by-line flattening is applied to this image due to tip-switching events. I=100 pA, U=1.8 V. b) Zoomed in image of the 2D TPA island after manipulation of the TPA molecules. c) Zoomed-in image showing the OA exposed after TPA manipulation. b) and c) I=40 pA, U=-1.8 V.

the green arrow in b. The disassembly carries on in the image in c and is completely removed in d. Critically, by displacing the TPA it is possible to image the underlying OA film located underneath the overlayer structures. The OA molecules appear no different to that in the surrounding decoupling film, indicating no chemical or conformational modifications to the OA from the overlayer. Moreover, their supramolecular arrangement is still synchronised with the surrounding $(\sqrt{3}\times\sqrt{3})$R30° film, revealing that the decoupling film is structurally unperturbed by OA adsorption.

Molecular manipulation of the TPA in the 2D islands has also proven successful, as illustrated in Figure 5.9. In 5.9a an extended 2D island is shown,

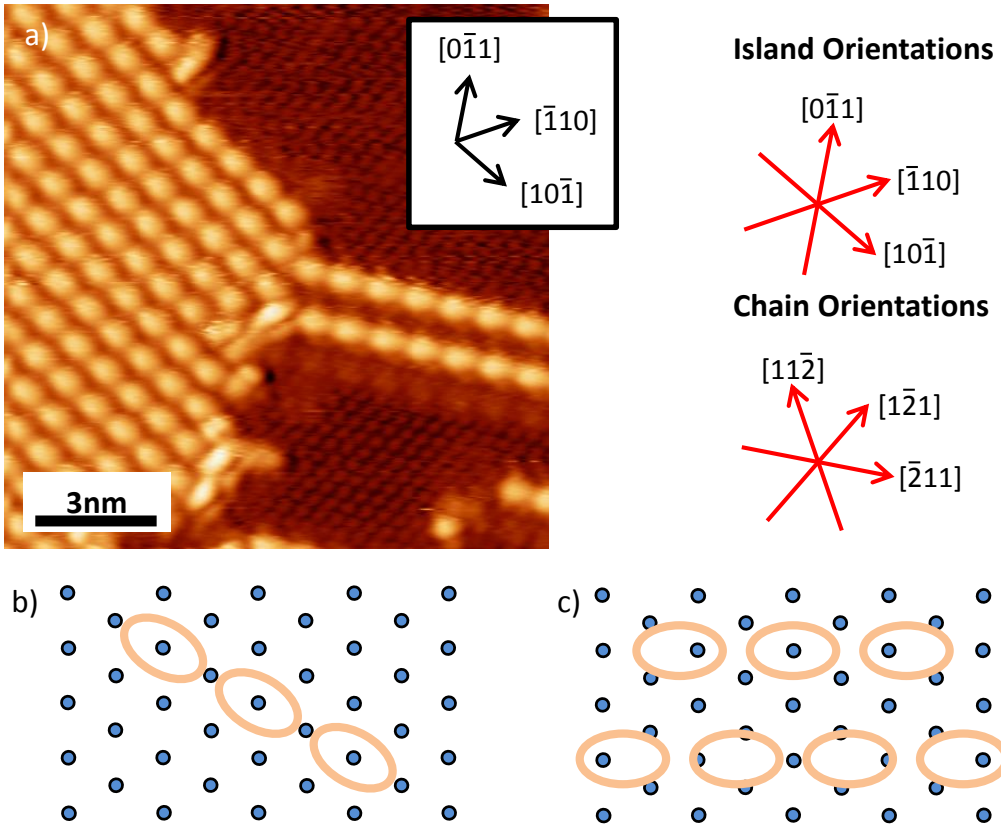

Figure 5.10 a) STM image of TPA on the OA/Cu(111) film, demonstrating the perpendicular orientations of the 2D islands and 1D chains. Inset are the substrate crystallographic directions. I=14 pA, U=1.8 V. The directions of the 2D islands (upper) and 1D chains (lower) are also shown. b-c) Proposed models for the TPA 1D chains and 2D islands on the OA lattice, based on the observed orientation and periodicity of the TPA. OA is shown as blue circles, TPA as orange ovals.

which undergoes partial fragmentation during a subsequent image. In c, it is possible to directly observe the hole left by the tip-induced manipulations; the OA appears unchanged by TPA adsorption and displacement, and the superstructure is again structurally in-phase with the rest of the OA monolayer.

5.2.2. Assembly of the 'on-top' TPA structures

The OA appears to exhibit a significant degree of influence over the assembly of overlayer TPA, as evidenced by the formation of two different

structures, the abnormally short H-bonds in both, and the relatively large separation of the chains in the 2D islands. Understanding the cause of this may provide some future strategies to modify molecular assembly on organic decoupling layer, and thus an extensive analysis of the overlayer structure and its correlation to that of the OA film has been attempted.

A tentatively proposed structural model of the 1D overlayer chains with respect to the OA substrate is shown in Figure 5.10b. The chains are oriented perpendicularly to the substrate crystallographic directions, in line with the experimental data. Each TPA molecule is assumed to have an identical adsorption site and to extend over three OA molecules. This is considered to be a particularly low energy configuration because of the possible intermolecular interactions that it allows: H-bonds could occur between the TPA and the three underlying OA molecules. Additionally, there are four further OA molecules in close proximity that could undergo some interaction. In both cases, the bonding could be both through the carboxylic moieties of TPA and OA, and between the OA carboxyl groups and the protons of the TPA phenyl rings. A consequence of this adsorption configuration is that the TPA-TPA dimeric H-bonds that keep the 1D rows together must be significantly shorter than normal [1-7]. For all TPA to have the same adsorption configuration on the OA in this direction, the dimeric H-bonds between the overlayer species must be only 1.8 Å in length, closely matching the experimentally determined 1.9±0.5 Å.

Analysis of the 2D islands structure reveals a number of observations that are yet to be explained. By aligning along the Cu(111) close-packed directions (i.e. perpendicular to the close-packed directions of the OA film), the TPA molecules likely undergo a reduced number of interactions with the underlying OA film; the

tentative model presented in Figure 5.10c seems to indicate that each molecule is positioned over a singular OA molecule and up to a further four that are in close proximity. Thus, this adsorption geometry is probably less favourable than that observed for the 1D chains. Additionally, the model also shows that the individual TPA molecules cannot have the same adsorption configuration with respect to the underlying OA. As a consequence, it would be expected that the molecules should be able to 'adjust' their relative positions so as to attain a more favourable TPA-TPA separation and thus, differently to what is actually observed, should form dimeric H-bonds that are not so unusually short. Finally, it is also not understood why this specific orientation allows the chains to stack into a brickwork structure while the other perpendicular orientation, observed for the isolated 1D chains, should not. In principle, if the 1D TPA chains were to stack, an inter-chain separation of 7.69 Å would allow the TPA to maintain the same adsorption configuration. Whilst this is slightly larger than the ~5 Å observed on metal surfaces [9,11], it is shorter than the 8.4±0.1 Å observed experimentally in the 2D chains. In other words, 2D stacking seems more favourable for the molecular orientation observed in the 1D chains than in the 2D islands. Thus, it is not clear at this stage why the TPA chains in the 2D islands are separated by 2× the OA lattice spacing in this direction, as shown in Figure 5.10c.

In summary, the OA decoupling layer has a significant effect on the assembly of TPA overlayers. While there are still many unanswered questions, it is clear that the interaction between the OA and the TPA is comparatively strong and thus may provide a potentially powerful tool with which to control molecular overlayer assembly.

5.3 Summary of TPA on OA decoupling films

The STM data presented above reveals that both the OA (3×2) and $(\sqrt{3}\times\sqrt{3})$R30° monolayer films are capable of supporting TPA overlayers, which are believed to be some of the first non-alkanethiol examples of organic decoupling films. When deposited onto the (3×2) film at RT, TPA penetrates through the film to adsorb directly onto the metal surface, evidenced by the resulting disruption of the OA monolayer and assembly of the TPA. This can be prevented by cooling the decoupling layer to LT prior to TPA deposition, but this prevents the assembly of the overlayer on top of the OA film. Conversely, the OA $(\sqrt{3}\times\sqrt{3})$R30° film is capable of supporting TPA overlayers at RT, perhaps by virtue of its more densely-packed and robust supramolecular structure. The on-top adsorption configuration is evidenced by the unperturbed OA film about the TPA structures and, through tip-controlled manipulation of the overlayer, by direct observation of the decoupling layer underneath the overlayer. The OA film plays a significant role in the overlayer assembly, resulting in the formation of 1D stripes and 2D brickwork-like islands. In both cases, the TPA lattice parameters are significantly different from those observed previously. It is hoped that, through further study of the effect of the underlying OA film on overlayer assembly, it may be possible to use organic decoupling layers such as these as a tool with which to facilitate and/or manipulate self-assembly processes.

It is important to note that it has not been possible to characterise the degree of electronic coupling between the decoupled TPA and the metal surface. Perhaps one of the most suitable technique for such characterisation is STS [11,15,16], as it allows simultaneous elucidation of an adsorbates local environment and its electronic properties [17]. However, such measurements would be extremely difficult for this particular investigation; to interpret STS measurements in a meaningful way, it is

important that the DOS of the tip in the required bias range is *a priori* well understood, which is usually achieved by measuring the STS spectrum of the clean metal surface [18]. In an ideal case, the tip should have a featureless DOS, which is indicative of a metallic tip apex without adsorbed molecular species. However, this is a particular difficult challenge in this work. First, the complete monolayer of OA prevents the characterisation of the tip DOS on clean areas of the surface. In addition, the most common approach for tip forming is to crash it into clean areas of the substrate in a controlled manner, depositing or picking up atoms onto or from the sample [19]. The OA monolayer also prevents this. With this in mind, STS measurements have not been attempted here, but should be the focus of future work.

5.4 Chapter 5 references

1. Bailey, M. and C.J. Brown, *The Crystal Structure of Terephthalic Acid.* Acta Crystallographica, 1967. **22**(3): p. 387-391.
2. Kim, Y.-G., S.-L. Yau, and K. Itaya, *In Situ Scanning Tunneling Microscopy of Highly Ordered Adlayers of Aromatic Molecules on Well-Defined Pt(111) Electrodes in Solution: Benzoic Acid, Terephthalic Acid, and Pyrazine.* Langmuir, 1999. **15**(22): p. 7810-7815.
3. Sledz, M., J. Janczak, and R. Kubiak, *New crystalline modification of terephthalic acid.* Journal of Molecular Structure, 2001. **595**(1-3): p. 77-82.
4. Clair, S., et al., *STM Study of Terephthalic Acid Self-Assembly on Au(111): Hydrogen-Bonded Sheets on an Inhomogeneous Substrate.* The Journal of Physical Chemistry B, 2004. **108**(38): p. 14585-14590.
5. Canas-Ventura, M.E., et al., *Coexistence of one- and two-dimensional supramolecular assemblies of terephthalic acid on Pd(111) due to self-limiting deprotonation.* Journal of Chemical Physics, 2006. **125**(18): p. 184710.
6. Suzuki, T., et al., *Substrate effect on supramolecular self-assembly: from semiconductors to metals.* Physical Chemistry Chemical Physics, 2009. **11**(30): p. 6498-6504.
7. Addou, R. and M. Batzill, *Defects and Domain Boundaries in Self-Assembled Terephthalic Acid (TPA) Mono layers on CVD-Grown Graphene on Pt(111).* Langmuir, 2013. **29**(21): p. 6354-6360.
8. Lang, N.D., *Apparent size of an atom in the scanning tunneling microscope as a function of bias.* Physical Review Letters, 1987. **58**(1): p. 45-48.
9. Eigler, D.M. and E.K. Schweizer, *Positioning Single Atoms with a Scanning Tunneling Microscope.* Nature, 1990. **344**(6266): p. 524-526.
10. Crommie, M.F., C.P. Lutz, and D.M. Eigler, *Confinement of Electrons to Quantum Corrals on a Metal Surface.* Science, 1993. **262**(5131): p. 218-220.
11. Nilius, N., T.M. Wallis, and W. Ho, *Influence of a Heterogeneous Al_2O_3 Surface on the Electronic Properties of Single Pd Atoms.* Physical Review Letters, 2003. **90**(4): p. 046808.
12. Carrera, A., et al., *Controlling Carboxyl Deprotonation on Cu(001) by Surface Sn Alloying.* Journal of Physical Chemistry C, 2013. **117**(33): p. 17058-17065.
13. Faraggi, M.N., et al., *Role of Deprotonation and Cu Adatom Migration in Determining the Reaction Pathways of Oxalic Acid Adsorption on Cu(111).* The Journal of Physical Chemistry C, 2011. **115**(43): p. 21177-21182.
14. Liu, J., et al., *Structural Transformation of Two-Dimensional Metal–Organic Coordination Networks Driven by Intrinsic In-Plane Compression.* Journal of the American Chemical Society, 2011. **133**(46): p. 18760-18766.
15. Heinrich, A.J., et al., *Single-Atom Spin-Flip Spectroscopy.* Science, 2004. **306**(5695): p. 466-469.
16. Repp, J. and G. Meyer, *Scanning tunneling microscopy of adsorbates on insulating films. From the imaging of individual molecular orbitals to the manipulation of the charge state.* Applied Physics a-Materials Science & Processing, 2006. **85**(4): p. 399-406.
17. Hipps, K.W., *Scanning Tunneling Spectroscopy (STS)*, in *Handbook of Applied Solid State Spectroscopy*, D.R. Vij, Editor. 2006, Springer US. p. 305-350.

18. Wahl, P., et al., *Background removal in scanning tunneling spectroscopy of single atoms and molecules on metal surfaces.* Review of Scientific Instruments, 2008. **79**(4): p. 043104.
19. Melmed, A.J., *The art and science and other aspects of making sharp tips.* Journal of Vacuum Science & Technology B, 1991. **9**(2): p. 601-608.

Chapter 6

Summary and outlook

The aim of this work has been to investigate the consequences of strong molecule-substrate interactions on the assembly of molecular tectons on metallic surfaces, and to develop a novel, all-organic approach towards decoupling these nanostructures from the substrate. The main results of this work, obtained from a combination of experimental methods, such as STM, XPS and NEXAFS, and theoretical simulations, including MM and DFT, are recapped in the following sections. First, the modification of molecular self-assembly on two strongly-interacting surfaces has been demonstrated. After this, the adsorption and assembly of a prototype organic molecule was investigated, with a focus on its potential use as

a decoupling layer. In the final chapter, the efficacy of the two different decoupling films was evaluated through the deposition of an organic overlayer. Both films were ultimately proven to be capable at decoupling the overlayer, although their suitability to the task was substantial different and depended on their intrinsic properties.

6.1 TPA on Cu(110) and Cu(111)

Chapter 3 focused on efforts to investigate the effects of strong molecule-substrate interactions on the self-assembly of adsorbed molecular tectons. This was achieved through a detailed analysis of the assembly of TPA on Cu(110) and Cu(111). On the former, TPA is readily deprotonated to form TP. The TP is revealed to assemble into row-like superstructures that, depending on the molecular coverage, are characterised by MO or ionic H-bonds. The symmetry of the different phases is a direct consequence of the two-fold symmetry and strong atomic corrugation of the underlying metal surface. Thus, through a combination of experimental and theoretical methods, this study highlights the potential importance of the substrate reactivity, its density of adatoms, and also the molecular coverage on the assembly of carboxylic-based tectons on solid surfaces.

The Cu(111) surface is less reactive than Cu(110), and thus TPA adsorbs intact at RT. This has allowed the investigation of how strong molecule-substrate interactions can affect the assembly of intact benzyl carboxylic tectons. STM reveals a brickwork-like structure, where the TPA intermolecular separations along the chain direction are either considerably compressed or elongated compared to those obtained on weakly interacting surfaces. This unusual assembly is a consequence of the often-cited ‘subtle interplay’ between molecule-molecule and adsorbate-substrate interactions. To characterise this interplay, the results of MM and DFT calculations

have been combined into a simple analytical algorithm, which is capable of assessing the effect of the two interactions on the assembly of many molecules. This model, which is thought to be the first to quantify the nature of the interaction interplay, is able to both quantitatively and qualitatively simulate the unusual assembly of TPA on Cu(111) and others. Furthermore, this model can be readily expanded to explore other molecular systems, and is expected to become an important framework for studying molecular assembly on strongly-interacting surfaces.

The reactivity of Cu(111) can be enhanced with annealing treatments, which allow the assembly of adsorbed TP on Cu(111) to be characterised. As was the case when adsorbed on Cu(110), TP forms a range of Cu-TP MO complexes, whose symmetry reflects that of the underlying metal surface. In contrast, when Fe is deposited, the resulting long range Fe-TP MO complexes exhibit two-fold symmetry as a consequence of the much stronger bonding between the carboxylates moieties and Fe, in comparison to that with Cu. This study reveals the potential for tuning the assembly of molecular tectons through the deposition of metal adatoms with different interaction strengths.

In summary, the assembly of TPA and TP on Cu surfaces reveals that surface engineering with molecular tectons is a highly complex undertaking. In particular, it is not feasible to consider just the structure and interactions of the tectons, as is usually possible in solution-phase supramolecular chemistry. Moreover, it is essential to also include the substrate and its effects on assembly in the design process. For this to be possible, further work is needed to characterise, for example, the effects of substrate reactivity and strong molecule-surface interactions.

6.2 OA on Cu(110) and Cu(111)

Chapter 4 described the fabrication and characterisation of OA monolayers on Cu(110) and Cu(111), with the ultimate aim being to use these films use as novel, non-alkanethiol organic decoupling layers. OA was selected as a suitable prototype molecule due it being previously reported to only adsorb in an upright geometry on Cu(110). Furthermore, it is reported to form a densely-packed film at surface saturation without the need for a complex fabrication process (e.g. pre-dosing the surface with O). However, an extensive experimental and theoretical characterisation of its adsorption and assembly on Cu(111) revealed that it adsorbs parallel to the surface and forms a low-density (3×2) supramolecular structure. Additional further experimental and theoretical work will be needed to elucidate the nature of this phase; for example, the structure may include Cu adatoms, or may be the result of a reconstruction of the underlying Cu(110) surface.

A similar adsorption geometry had been previously reported on Cu(111). This was reproduced in the course of this work, but the presently-used deposition setup almost exclusively produced a different phase that exhibited an upright adsorption geometry. Moreover, in this configuration the OA assembles into a dense $(\sqrt{3}\times\sqrt{3})$R30° assembly that appears, as was demonstrated in Chapter 5, to be well suited to the task of an organic decoupling layer. Future experiments should focus on further characterisation of this film; in particular to confirm the adsorption geometry and chemical state of the OA molecules.

6.3 TPA overlayers on the OA monolayer films

In Chapter 5, the efficacy of the OA monolayers characterised in the previous Chapter is investigated. To achieve this, TPA was deposited onto the OA (3×2) and $(\sqrt{3}\times\sqrt{3})$R30° films obtained on the Cu(110) and Cu(111) surfaces, respectively.

When deposited onto the OA monolayer obtained on Cu(110) at RT, TPA displaces the underlying molecules so as to adsorb directly on the metal. This is evidenced by local disordering of the otherwise crystalline OA film, the assembly of the TPA into [001]-oriented chains, and the robustness of the chains with respect to STM tip-induced manipulations. By cooling the OA film to LT prior to TPA deposition, this displacement can be prevented. However, this inhibits the assembly of the overlayer molecules into ordered structures, which may ultimately limit the applicability of this particular decoupling layer.

In contrast, when deposited onto the $(\sqrt{3}\times\sqrt{3})$R30° OA film at RT, TPA remains on top of the decoupling layer. This is demonstrated by a number of observations, including STM tip-induced molecular manipulations that allow the underlying, intact OA to be exposed and imaged. The TPA overlayer assembles into one of two different structures; 1D chains or 2D brickwork islands. The latter lack the defects observed on the bare surface, but both motifs demonstrate abnormally short H-bonds. This most probably occurs to facilitate a better periodicity match with the decoupling layer. Such short H-bonds have only been observed on Cu(111), revealing that the adsorption potential of TPA on top of the OA film is likely to be similarly corrugated. In all, these measurements indicate that the templating effect of an organic decoupling layer can be significantly strong if appropriate functional moieties are utilised. Future studies should focus on the use of differently-terminated

decoupling films so as to further develop the use of such films in directing self-assembly.

In conclusion, it is clear that the central aims of this thesis, to explore the characteristics of the molecule-substrate interaction and to develop an all-organic approach towards preventing it, have been achieved. In addition, it is apparent that organic decoupling layers could be an extremely fruitful tool with which to modify and tune the self-assembly of functional tectons into desired nanostructures in ways not necessarily possible through intermolecular interactions alone. It is expected that the results presented here will lead to further study of organic decoupling layers and, in particular, their use in surface engineering.

List of Publications

The following is a list of publications that have resulted from the work in this thesis:

"Varying molecular interactions by coverage in supramolecular surface chemistry"
Yeliang Wang, Stefano Fabris, Thomas W. White, Federico Pagliuca, Paolo Moras, Marco Papagno, Dinesh Topwal, Polina Sheverdyaeva, Carlo Carbone, Magalí Lingenfelder, Thomas Classen, Klaus Kern and Giovanni Costantini
Chemical Communications 48, 534 (2012)

"Addressing the 'subtle interplay' in molecular self-assembly on metal surfaces"
Thomas W. White, Natalia Martsinovich, Alessandro Troisi and Giovanni Costantini
(in preparation)

"Structural investigation of oxalic acid on Cu(110)"
Thomas W. White, David A. Duncan, Ben Moreton, D. Phil Woodruff, Tien-Lin. Lee, Sara Fortuna, Stefano Fabris and Giovanni Costantini
(in preparation)